The University Of Sheffield.

The Study of Fire Spread on an Inclined Wooden Surface by Multiple Spectrum Imaging Systems and Diagnostical Techniques

Mr Yufeng Lai

Combustion and Flow Diagnostics Research Group

Department of Mechanical Engineering

2021

This thesis is submitted to the University of Sheffield for the degree of Doctor of Philosophy in the faculty of Engineering.

Declaration

The work presented in this thesis is that of the Author and has not been submitted for any other award or degree at the University of Sheffield or any other university or institution.

Acknowledgements

First of all, I would like to express my sincere gratitude to my supervisor, Professor Yang Zhang, for his constant encouragement and guidance. I am deeply grateful for his help in all stages of the writing of this thesis. Without his consistent and illuminating instruction, this thesis could not have reached its present form.

Second, I want to show my gratitude to my parents, Mr Xudong Lai and Mrs Guangxia Xie, who supported and encouraged me throughout the PhD studies and before. Brave, honest and persevering, these characters they taught me always help me get through the hard time.

I would also like to thank my beloved wife Mrs Yunbai Wang for the constant accompanying and believing. It is her who made me become a better man. She is also the best teammate of me, and always give me a hand whenever I need it, both in life and work. The numerous difficulties we have surmounted together, will not be forgotten.

My truthful love is dedicated to my lovely daughter, Miss. Yitong Lai. She is the warmest sunshine of my life. She has brought me happiness, love, and hope. I must thank my daughter for letting me understand the meaning of responsibility.

Also, I would like to thank my colleagues. Particularly, to Dr Hangxu Zhou, who has always helped and accompanied me during my PhD studies, our friendship will not fade away; to Mr Xiao Wang for his generous help of my experiments and for the enjoyable time we spend together in the lab and pubs; and to Mr Ahmed Albadi for his selflessly help and useful suggestions. I would also be thankful to all my colleagues in Combustion and Flow Diagnostics Research Group, Dr Zhen Ma, Mr Shuida Ji, Dr Lukai Zheng, Dr Yiran Wang, Dr Songyang Yu, Dr Ahmad Fuad, Dr Houshi Jiang, Miss Muyi Pan, Mrs Jing Zhang, Mr Yuchen Zhang, Mr Haibo

Zhou and Mr Xuanqi Liu. It is an enjoyable and memorable time worked with them.

Finally, I want to show my sincere gratitude to Dr Jon Willmott for supporting me with the equipment and technique for my experiments. Also, I would like to thank the colleagues in his group, Dr Chengxi Zhu and Dr Thomas BO Rockett for sharing their expertise in emissivity and thermal metrology. Their help is acknowledged.

Publications

[1] **Y. Lai**, X. Wang, T. B. O. Rockett, J. R. Willmott, H. Zhou, and Y. Zhang, The effect of preheating on fire propagation on inclined wood by multi-spectrum and schlieren visualisation, Fire Safety Journal, vol. 118, 2020.

[2] **Y. Lai**, H. Zhou, and Y. Zhang, Experimental investigation of the fire spread on inclined wooden rods, 27th ICDERS, Beijing, China, 2019.

[3] H. Zhou, **Y. Lai**, Y. Li, and Y. Zhang, Modelling the propagation of one-end-burning cylindrical firebrand based on the measured regression rates, 27th ICDERS, Beijing, China, 2019.

Under Preparation Papers

[1] **Y. Lai**, X. Wang, T. B. O. Rockett, J. R. Willmott and Y. Zhang, The investigation of the effects of cross-wind on the fire spread on horizontal direction and inclined wooden rods by multi-imaging systems and temperature.

[2] **Y. Lai**, X. Wang, T. B. O. Rockett, J. R. Willmott and Y. Zhang, The study of the effects of inclination on the motion of fire plume by multi-imaging systems and motion estimation.

Abstract

Fire disaster, as an unavoidable threat around the world, caused millions of loss of living beings and properties. To minimise the damage that fire disaster causes, the prediction of fire spread is significant. Due to the burning of wood is a series of complicated processes, the study of fire spread along the wood surface is far from complete. To comprehensively understand the mechanism of wood combustion as well as the fire spread, a systematically study is necessary. With the development of digital cameras and computer science, the vision systems based on the digital camera become a useful tool for measurement and visualisation.

In this work, the fire spread on inclined wooden rod surface is systematically studied based on the vison systems. An original designed imaging system that synchronises visible, schlieren, and thermal imaging systems is developed. The various diagnostical techniques, including the temperature measurements by two-colour method and thermal imaging, optical flow motion estimation, and selective enhancement technique are developed along with the imaging system. Rely on the imaging system that developed in this study, the burning ability, temperature of the wooden surface and flame, the dim blue flame and the invisible hot gas flow can be visualised simultaneously.

The first contribution of this work is the developed pyrometers which are based on two methods: the first one is the two-colour method, which relies on the response ratio between two selected wavelengths. This method is used for measuring the soot flame temperature. The second pyrometer is based on thermal imaging, which uses a narrow band wavelength thermal image with known emissivity. It is used for reading the temperature of the wood surface. With the instruments developed in this work, the flame temperature and surface

temperature of the burning wood can be monitored at the same time.

Based on the imaging system and diagnostical techniques, the fire spread on wooden rods surface that inclined at various angles is investigated. It is first found in this work both the flame and fire plume would have geometry change at the inclination surface. Besides, with the help of the optical flow method, the minor fluctuate (<2mm/s) of the flame and hot flow can be detected and used to analyse the burning phenomena.

Another finding is the essential role of underneath preheating on sustaining the burning and spreading the fire. The pyrolysis zone, as well as the preheating zone, have been illustrated and visualised by synchronising the blue flame with the schlieren image by the first time. Furthermore, with involving the thermal imaging system, the preheating length underneath the burning rod is calculated and shows a monotonically increase with the increasing angle. Moreover, this work introduces a novel method to measure the flame attachment phenomenon quantitatively by using enhanced thermal image.

The effects of cross-wind on the burning of wood are investigated systematically with the imaging system. The main finding is that under the low speed of cross-wind, the burning and fire spread are enhanced, while they are decreased under the high speed of the wind. With the help of the multiple spectrum imaging, the mechanisms of the wood combustion under wind condition has been studied and visualised.

This new imaging system with developed diagnostical techniques is a useful tool for investigating the burning of wood and fire propagation. The findings in this works could help enhance the understanding of the fire protection and optimise the strategy both in fire protection and fire extinction.

Table of Contents

DECLARATION II

ACKNOWLEDGEMENTS III

PUBLICATIONS V

ABSTRACT VI

TABLE OF CONTENTS VIII

LIST OF FIGURES XII

LIST OF TABLES XX

NOMENCLATURE XXI

1. INTRODUCTION 1

1.1. Motivation 1

1.2. Objectives 3

1.3. Outline of the thesis 4

2. LITERATURE REVIEW 7

2.1. Introduction 7

2.2. Combustion and flame 7

2.2.1. Introduction 7

2.2.2. Background knowledge of combustion 8

2.2.3. Flame classification 9

2.2.4. Mechanism of heat transfer 11

2.3. Background of the digital vision system 16

2.3.1. Introduction 16

2.3.2. Light 17

2.3.3. Digital cameras 23

2.4. Temperature 29

2.4.1. Introduction 29

2.4.2. True, colour and brightness temperature 30

2.4.3. Review of techniques of temperature measurement 32

2.5. Wood combustion 36

2.5.1. Introduction 36

2.5.2. Background of wood combustion 37

2.5.3. Critical factors which influence the burning of wood 40

2.5.4. Fire spread 43

3. THE METHODOLOGY OF COMBUSTION DIAGNOSTICS 47

3.1. Introduction 47

3.2. Temperature measurement methods 47

3.2.1. Two-colour method 47

3.2.2. Thermal imaging temperature measurement 64

3.3. Schlieren imaging system 74

3.4. Optical flow method for motion estimation 77

4. THE EFFECTS OF THE INCLINED ANGLE AND THE DIAMETER OF WOODEN ROD ON THE FIRE PLUME 79

4.1. Introduction 79

4.2. Experiments and Methods 81

4.2.1. Experimental setup 81

4.2.2. Imaging system 84

4.2.3. Data processing 85

4.3. Results and Discussion 86

4.3.1. The fire plume at the beginning of self-sustained burning 87

4.3.2. The properties of flame spread 89

4.3.3. The flame attachment phenomenon 93

4.3.4. The heated flow 97

4.3.5. The flame velocity distribution 100

4.3.6. The distribution of the heated flow velocity 104

4.4. Conclusion 110

5. THE EFFECT OF THE UNDERNEATH PRE-HEATING ON THE FIRE SPREAD 111

5.1. Introduction 111

5.2. Experiment setup and methodology 114

5.2.1. Experiment setup *114*

5.2.2. Imaging systems *115*

5.2.3. Data processing *116*

5.3. Results and Discussion 119

5.3.1. The general combustion status *120*

5.3.2. The effect of underneath hot gas parcel *123*

5.3.3. The effect of flame attachment phenomenon *136*

5.3.4. Observation on the impact point of piloted impinging heat flux *138*

5.4. Conclusion 140

6. THE STUDY OF THE FIRE SPREAD UNDER DIFFERENT CROSS-WIND CONDITIONS 142

6.1. Introduction 142

6.2. Experiments method and setup 145

6.2.1. Sample setup *145*

6.2.2. Imaging system *147*

6.2.3. Data processing *148*

6.3. Results and discussion *149*

6.3.1. The cross-wind effects on the self-sustained burning at 0^o *150*

6.3.2. The cross-wind effects on the self-sustained burning at 30^o *167*

6.3.3. The comparisons of the cross-wind speed effects between 0^o and 30^o *199*

6.4. Conclusions 201

7. CONCLUSIONS AND FUTURE WORKS 207

7.1. Conclusions of the thesis *207*

7.1.1. Developed optical pyrometers 207

7.1.2. The effect of the diameter of wooden rods and the inclination angle on the fire plume 209

7.1.3. The effect of the underneath preheating on the fire propagtion 210

7.1.4. The effects of the cross-wind on the self-sustained burning 212

7.2. Suggested future works in this field *215*

REFERENCES 220

List of Figures

Figure 2.1 The schematic of typical diffusion flame and premixed flame: a) is the diffusion flame; and b) is the premixed flame. 11

Figure 2.2 The typical example of different flow conditions. 16

Figure 2.3 The electromagnetic spectrum and the visible spectrum (shown as the colour) [26]. 18

Figure 2.4 The Response of Cone Cells in Human's Eyes[28]. 19

Figure 2.5 The traditional spectrum curve of the blackbody radiation[29]. 20

Figure 2.6 The Colours of Black Body Radiation. 21

Figure 2.7 An example of premixed (left), partly premixed (middle) and diffusion flame (right)[33]. 23

Figure 2.8 The Cube of RGB Colour Model. 24

Figure 2.9 The Structure of Bayer Filter. 25

Figure 2.10 The common materials for thermal camera sensors[40]. 28

Figure 2.11 The different layers of a typical InGaAs sensor[41]. 29

Figure 2.12 The colour temperature and the typical examples[43]. 31

Figure 2.13 Chemical and physical processes within a burning timber[57]. 38

Figure 2.14 The illustration of thermal pyrolysis process. 39

Figure 2.15 Schematic of heat transfer in the burning of wood[79]. 45

Figure 3.1 The LANDCAL R1500T black body furnace. 51

Figure 3.2 The Photron SA-4 high speed camera. 52

Figure 3.3 The response of Photron SA-4 high speed camera[105]. 53

Figure 3.4 The direct images of the black body furnace at different temperature: a), b) … k) represent in the temperature 500, 600… 1500℃ respectively. 54
Figure 3.5 The IR cut off images of the black body furnace at different temperature: a), b) … i) represent in the temperature 700, 800… 1500℃ respectively. 54
Figure 3.6 The grey level ratio against temperature of direct image case. 55
Figure 3.7 The instrument factor against RG ratio of direct image case at different temperature range left: 500°C to 1100°C; right 1200°C to 1500°C.....55
Figure 3.8 The instrument factor against RB/GB ratio of direct image case at different temperature range left: RB ratio; right GB ratio. 56
Figure 3.9 The grey level ratio against temperature of IR cut off image case. 57
Figure 3.10 The instrument factor against RG/GB ratio of direct image case at different temperature range left: RG ratio; right: GB ratio. 57
Figure 3.11 The comparisons between actual temperature with measured temperature calculated by different channel ratio in direct image case. (a) calculated by RG ratio; (b) calculated by RB ratio; and (c) calculated by GB ratio. 59
Figure 3.12 The comparisons between actual temperature with measured temperature calculated by different channel ratio in IR cut off image case. (a) calculated by RG ratio; and (b) calculated by GB ratio. 60
Figure 3.13 The value and percentage of infrared radiation effect in different channels. Left: pixel value against temperature; right: the percentage against temperature.....61
Figure 3.14 The Bunsen burner used in the experiments. 62
Figure 3.15 The flame temperature testing cases. Left: the flame image; middle: the

temperature map; right: the temperature distribution. (a) represents methane flow rate 0.2L/min; (b) represents methane flow rate 0.4L/min; (c) represents methane flow rate 0.6L/min 64

Figure 3.16 The Hamamatsu C12741-03 InGaAs camera. 67

Figure 3.17 The bandpass of the camera and filter combination. 67

Figure 3.18 The illustration of the calibration setup. 68

Figure 3.19 The size of source effect in the imaging system. 69

Figure 3.20 The radiometric calibration result using 16ms exposure time. 69

Figure 3.21 The residuals of the measured temperature in 16ms exposure time. 70

Figure 3.22 The radiometric calibration result using 32ms exposure time. 71

Figure 3.23 The residuals of the measured temperature in 32ms exposure time. 72

Figure 3.24 The 32ms exposure time testing case of burning wooden block impacted by a water droplet. Left: fully ignited. Middle: just impacted with the water droplet. Right: the moment after impact of the water droplet. 73

Figure 3.25 The 16ms exposure time testing case of burning wooden rod with/without cross-wind involvement. Left: fully ignited without the cross-wind. Right: the cross-wind involved. 74

Figure 3.26 Schematic representation of the schlieren system. 75

Figure 3.27 Example schlieren image of the burning wooden rod during the piloted ignition by a Bunsen burner. 76

Figure 4.1 Schematic representation of the experimental set-up. 82

Figure 4.2 The Setup of imaging systems. 84

Figure 4.3 The comparison between direct imaging and schlieren imaging at the same time of the wood just ignited. 87
Figure 4.4 The actual burning images of different diameter woods at different inclinations. 90
Figure 4.5 The Burning lifetime of different diameters burning wood at 0 degrees and -30 degrees. 92
Figure 4.6 The averaged charring rate and surface to volume ratio of different diameters wooden samples at different inclination angles. 92
Figure 4.7 An example of real-time charring rate at 30^{o} inclination angle at different diameter rods at the beginning of self-sustained burning. 93
Figure 4.8 The actual flame images of different diameters wooden rods which burned from the middle at different timing and inclination angles. 94
Figure 4.9 The demonstration of fire plume and surrounding air flow burned at horizontal direction. 95
Figure 4.10 The demonstration of fire plume and surrounding air flow burned at positive inclination angle. 96
Figure 4.11 The demonstration of fire plume and surrounding air flow burned at negative inclination angle. 97
Figure 4.12 The schlieren images of different diameter woods at a set of inclinations. 99
Figure 4.13 The illustration of flame velocity burned at different inclination angles. 103
Figure 4.14 The distribution of flame velocity burned at different inclination angles. 104
Figure 4.15 The illustration of buoyant heated flow velocity burned at different inclination angles. 108

Figure 4.16 The distribution of buoyant heated flow velocity burned at different inclination angles. 110

Figure 5.1 Schematic representation of the experimental set-up. 116

Figure 5.2 The Setup of imaging systems. 117

Figure 5.3 The typical burning images at different inclination angles at different time points. 121

Figure 5.4 The burning lifetime and charring length against inclination angle. 122

Figure 5.5 An example of the surrounding hot flow at different inclination angles at $t=20\ s$. 125

Figure 5.6 An example of the selectively enhanced blue flame at different inclination angles at $t=0$ s and $t=20\ s$. 126

Figure 5.7 The illustration of underneath preheating zone related to the selectively enhanced weak blue flame with schlieren imaging at $t=20\ s$. 127

Figure 5.8 An example of the temperature distribution of the burning surface at different inclination angles at $t=0$ s and $t=20\ s$. 128

Figure 5.9 The visualisation of bottom heated area at (a) the point when the piloted ignition is turned off ($t=0\ s$) and (b) 20s after piloted ignition is turned off ($t=20\ s$). For each time point, top: the schlieren images of different inclination angles; bottom: the corresponding thermal images. 130

Figure 5.10 The underneath hot gas flow length and the heated length against the inclination angle at the beginning of self-sustained burning. 133

Figure 5.11 The underneath hot gas flow length and the heated length against the inclination

angle at 20 s after the start of self-sustained burning. 133

Figure 5.12 The combustion process at 20^{o} inclination angle. 135

Figure 5.13 The thermal images at different inclination angles at 20 s after the turning off the burner, the original images (left column) and the enhanced images (right column) 137

Figure 5.14 Flame attachment length and flame tilt angle against inclination angles. 138

Figure 5.15 The comparison between 0 degrees and 30 degrees at 1 second before the piloted impinging heat flux is turned off. Top row: 0 degrees; Bottom row: 30 degrees. 139

Figure 5.16 Demonstration of the effect of inclination on impact spot. 140

Figure 6.1 Schematic representation of the experimental set-up. 147

Figure 6.2 The top view imaging system and experimental setup. 149

Figure 6.3 The direct images of self-sustained burning at the different timing at the 0 degrees inclination with different speed of cross-wind. 153

Figure 6.4 The averaged burning lifetime against different cross-wind set at 0 degrees. 155

Figure 6.5 The averaged charring rate against different cross-wind set at 0 degrees. 156

Figure 6.6 The time-dependant averaged flame temperature of 0 degrees group under different cross-wind speed during the first 20s. 157

Figure 6.7 The surface temperature map at the 0 degrees inclination with different speed of cross-wind and timing. 159

Figure 6.8 The illustration of the selected line position. 161

Figure 6.9 The selected-line temperature map against time at the 0 degrees inclination with different speed of cross-wind. (a) presents speed 0; (b) presents speed 1; (c) presents speed 2; (d) presents speed 3; (e) presents speed 4; (f) presents speed 5. 163

Figure 6.10 The illustration of underneath hot gas flow at 0 degrees inclination at different timing under different cross-wind speed set. 168
Figure 6.11 The illustration of the effect of the cross-wind on the underneath hot gas flow at horizontal direction. 168
Figure 6.12 The direct images of self-sustained burning at 10 s on the 30 degrees inclination. 169
Figure 6.13 The direct images of 20 s self-sustained burning at the 30 degrees inclination with different speed of cross-wind. 170
Figure 6.14 The averaged burning lifetime against different cross-wind set at 30 degrees..172
Figure 6.15 The averaged charring rate against different cross-wind set at 30 degrees. 173
Figure 6.16 The actual flame and temperature map of 10 s self-sustained burning at the 30 degrees inclination with different speed of cross-wind. Left: the actual flame; right: the temperature colour map. 175
Figure 6.17 The flame temperature distribution of 10 s self-sustained burning at the 30 degrees inclination with different speed of cross-wind. 177
Figure 6.18 The time-dependant averaged flame temperature of 30 degrees group under different cross-wind speed during the first 20s. 178
Figure 6.19 The surface temperature map and cross line position. 179
Figure 6.20 The surface temperature map and the cross-line temperature of 10 s self-sustained burning at the 30 degrees inclination with different speed of cross-wind. 182
Figure 6.21 The demonstration of the point temperature positions. 183
Figure 6.22 The first 20s from the self-sustained burning temperature at the point 0 (left) and

point 2 (right) with different cross-wind speed. 185
Figure 6.23 The first 10s from the self-sustained burning temperature at different positions with wind speed set 0, 3, 4 and 5. 188
Figure 6.24 The selected-line temperature map against time at the 30 degrees inclination with different speed of cross-wind. (a) presents speed 0; (b) presents speed 1; (c) presents speed 2; (d) presents speed 3; (e) presents speed 4; (f) presents speed 5.....192
Figure 6.25 The schlieren image matches the surface temperature map after 10 s of self-sustained burning started with different cross-wind speed. 195
Figure 6.26 The illustration of underneath hot gas flow at 30 degrees inclination at 0 s,10 s and 20 s under different cross-wind speed set.....197
Figure 6.27 The illustration of the convective heat transfer and the supply of the hot gas flow underneath. 200
Figure 6.28 The burned wooden rod examples from different cases: a) represents speed 0; b) represents speed 2 and c) represents speed 4. 203
Figure 7.1 An example of the validation of the sprectral emissivity of a SiC fibre. The colours represent the calculating channels: red is R channel; green is G channel and blue is B channel. 216
Figure 7.2 Some examples of the real-time emissivity/temperature measuring of electrical heated coils at different power (20w, 25w, 30w, 35w and 40w). The colours represent the results calculated by different colour channels: red indicates the R channel; green indicates the G channel and blue indicates the B channel. The black points represent the temperature measured by the two-colour method.....217

List of Tables

Table 2.1 The classification of flames and examples. 10

Table 2.2 The classification of infrared[39]. 27

Table 4.1 The properties of experimental sample 81

Table 4.2 The properties of experimental sample 82

Table 4.3 The properties of the premix fuel 83

Table 6.1 The parameters of experiment setup 148

Nomenclature

Symbol	Definition
A	Area of the object
b	Wien's displacement constant
bs	Scaling exponent
$B_v(v,T)$	Spectral radiance
c	Speed of light
C_1	The first Planck's radiation constant
C_2	The second Planck's radiation constant
CCD	Charge-coupled device
CFA	Colour filter array
CH_4	Methane
CO_2	Carbon Dioxide
CMOS	Complementary-metal-oxide-semiconductor
$E(\lambda,T)$	Intensity of radiation
F	Fraction of energy received by radiation
$Flow_l$	Underneath hot flow length
fps	Frames per second
$G(\lambda,T)$	Grey level
G_{RG}	Ratio between the greyscale in red and green channels
G_{RB}	Ratio between the greyscale in red and blue channels
G_{GB}	Ratio between the greyscale in green and blue channels
h	Heat transfer coefficient
h	Planck constant
H_2O	Water
Hz	Hertz
InGaAs	Indium Gallium Arsenide
InP	Indium phosphide
InSb	Indium Antimonide
IR	Infrared
ISO	Camera sensor sensitivity
k	Thermal Conductivity
k	Boltzmann constant
K	Kelvin
L	Linear dimension
MATLAB	Matrix Laboratory
MCT	Mercury Cadmium Telluride

MFOV	Measurement Fields of View
mm	Millimetre
ms	Millisecond
NIR	Near-infrared
nm	Nanometre
O_2	Oxygen
P_{rad}	Radiation power of a black body
Pre_l	Pre-heating length
Pyr_l	Pyrolysis length
ρ	Density of the fluid
$q_{cond}^{''}$	Rate of radiative heat transfer
$q_{conv}^{''}$	Rate of convective heat transfer
R	Camera constant
RGB	Red, Green and Blue colour model
ROIC	Readout integrated circuit
Re	Reynolds number
S	Instrument factor
S_λ	Imaging system sensitivity
$S_{S-H}(T)$	Response model for a narrow band thermal device
$S_m(T)$	Measured signal intensity of any individual pixel
SLS	Strained Layer Superlattice
SSE	Size of Source Effect
s	Second
T	Absolute temperature
T_s	Surface temperature
T_f	Flow temperature
$T_b(\lambda)$	Brightness temperature
v	Relative velocity of the fluid
v	Frequency of the electromagnetic radiation
3D	Three- Dimension
°	Inclined degree
°C	Celsius degree
°F	Fahrenheit degree
μ	Dynamic viscosity of the fluid
μm	Micrometre
λ	Wavelength
λ_{peak}	Peak wavelength
β	Transmission coefficient of the imaging system
ε	Spectral emissivity
φ	Equivalence ratio

θ	Inclination angle
σ	Stefan-Boltzmann constant

1. Introduction

1.1. Motivation

Fire disaster, as an inevitable challenge in the history of human civilisation, threatens millions of lives and properties. The development of civilisation of human beings is accompanied by the fight against fire, in both the wild and the city. Until today, tragedies by the fire disaster happen globally. In 2019 December, bushfires in Australia killed a billion life beings and made thousands of people homeless, recorded that 10,488 structures were damaged or destroyed. As another disaster, at least 31 fatalities were found in the fire disaster in California, in 2020 December. Moreover, the fire disaster not only threatens life beings directly but also the environment. The more carbon dioxide produced in the fire disaster inevitably attributes the global warming. Despite the efforts made by human beings, fire disaster is still an unavoidable threaten around the world.

In order to minimise the damage that fire disaster causes, the prediction of fire spread is significant. The estimation of fire spread includes two aspects[1]: predicting the spotting distance of small wooden particles and studying the fire propagation along the wooden surfaces. Regarding the fire spread along the wooden surface, such study could be challengeable due to the complexity of the combustion in the natural wood. Many important affecting factors have to be carefully considered, such as the species of the wood, the heat pyrolysis, the heat transfer, the combustion productions, the flame dynamics and so on. In addition, due to the very high temperature inside the fire disaster, it is hard to be close to the burning wood for the data acquisition, especially for the temperature which cannot be obtained by the conventional methods, for instance, the thermocouples.

With the development of the digital camera, the vision systems based on digital camera are wildly used as the measurement tool for its advantage that the camera could receive the absolute light information as a detector, unlike the human's eyes[2]. The light information including the radiation, wavelength, air density, and flow field can be processed by the computer and build a specific vison-base measuring system based on various circumstances. Such imaging system can be applied in various fields, such as industrial inspection[3], [4], medical diagnosis[5], metal processing[6], automobile industry[7] and combustion diagnostics[8]–[11]. Due to its non-induction property, the imaging systems based on the digital camera are suitable for the research of fire spread on burning wood surface. In addition, with the combination of a series of imaging systems, the comprehensive study of the mechanism of wood burning can be achieved.

For the purpose of systematically studied the mechanism of the fire propagation on the wooden surface, the various imaging systems, such as high-speed colour imaging, high-speed schlieren imaging, thermal imaging are synchronised and used together with various imaging-base diagnostical techniques, such as the two-colour method, thermal imaging metrology, optical flow motion estimation and selectively enhancement technique. A novel imaging system has been developed to comprehensively visualise the phenomenon of fire propagation on the wooden surface under different conditions. The visible flame, dim blue flame, invisible hot flow and the temperature can be measured and analysed.

As one of the most important parameters of wood combustion, the surface inclination angle affects the fire propagation on the wooden surface significantly. Since the inclined wooden elevator dramatically enhanced the fire propagation in King's Cross fire disaster[12], many

researchers started to focus on the burning behaviours at the inclined surface[13]–[15]. Considering the inclination angle is a worthfully study parameter, it is chosen for the main variate in the study of this thesis. In addition, the pre-dried wooden rods are used as the object of study for their good typicality relate to the building structure and the controllability in the laboratory scale.

By building an innovative imaging system, the study in this thesis focuses on the mechanism of the effects of various parameters, including diameters of the wooden rod, inclination angles and the cross-wind speed on the fire propagation on the burning wooden rod. This research is based on the visualisation and analyses from the velocity field, aerodynamics, heat transfer, flame temperature and surface temperature. The results achieved in this study could be utilised to develop the understanding of the fire safety field.

1.2. Objectives

According to the motivation of this thesis, the main objective is comprised as two aspects: firstly, build an imaging system which contains multiple spectrums and schlieren imaging, and develop the imaging-base combustion diagnostics for applying them into this work; secondly, study the mechanism of the fire propagation with the built imaging system. In details, the objectives can be listed as:

- **For establishing the imaging system**

  Design and build an imaging system which could systematically visualised the phenomena of burning wood. The temperature of flame, and burning wooden surface are required measured by image-base techniques. The surrounding hot gas flow would need to be

visualised by schlieren imaging. The combustion diagnostic techniques such as the optical flow, and selective enhancement are implied in this work for investigation the fundamental mechanisms.

- **For studying the mechanisms of fire propagation on wood surface**

By using the designed imaging system, this work aims to study the fundamental mechanisms of wood combustion, especially for the fire propagation. In details, the study aims to study the phenomena from the aspects below:

- The wood geometry effects on the fire propagation including the diameters and the inclination of the wood surface.
- The flame geometry effects on the fire propagation.
- The effects of flow flied around the burning wood on the fire propagation.
- The effects of the temperature including the flame and wooden surface on the fire propagation and thermal pyrolysis.
- The forced air effects on the burning ability and fire propagation.

1.3. Outline of the thesis

This thesis is comprised of seven chapters, including the introduction, the literature review, the methodology of combustion diagnostics, three chapters of the experimental results and the conclusions. The details are listed below:

In Chapter 1, the motivation of the research study is outlined, and the objectives of the work are highlighted.

In Chapter 2, the background knowledge related to this thesis has been introduced. The literature review contains four main aspects, including the fundamental knowledge of combustion and flame; the introduction of the vision-based measurements by the digital cameras; the different temperature measurement techniques and relevant applications; the reviews of the wood combustion, the definition of the firebrand and the fire spread mechanisms in the wildfire. This chapter focuses on the essential knowledge of this thesis, more details of the literature review of the insights and gaps for each application will be discussed in the introduction of the relative chapter.

In Chapter 3, the imaging-based combustion diagnostical techniques are developed and presented as results. The two-colour temperature measurement is introduced in the first section, including the theories, the calibration, the error analysis and the testing cases for validating the method. As well, the thermal imaging metrology is introduced in the second section, including the fundamentals, the calibration of both the size effect and the radiative response, the analysis of calculating residuals and the testing cases for its applicability. The third section introduces the high-speed schlieren imaging system and the setup, an example image is provided for illustrating the testing zone. At the end of this Chapter, the optical flow method is introduced.

In Chapter 4, the effects of inclination and diameters of wooden rods on fire propagation are studied. In detail, the general properties of burning lifetime and charring rate are calculated; the visualising analysis of the flame attachment and the fire plume have been focused on; the velocities of both flame and turbulence flow are estimated by the optical flow method.

In Chapter 5, the main objective aims to prove that the underneath convective preheating is

the crucial factor that influences fire propagation. The effects of underneath hot gas parcel are studied by synchronised schlieren-thermal imaging. In addition, the flame attachment is quantitatively studied by the enhanced thermal image system. At the end of this chapter, the impact point of the burning rods is analysed by the schlieren image, the thermal image and the selectively enhanced direct image.

In Chapter 6, a designed wind diffuser is applied to supply the cross-wind. The effects of cross-wind on sustaining burning are studied. The investigation bases on the analysis of the temperature of flame and surface and the visualisation of the surrounding heated flow have been developed. Two selected inclination angles burning are compared with horizontal burning for studying the effects of inclination on combustion. At the end of this chapter, the comparisons of burning between two selected inclined angles are presented as well.

In Chapter 7, the main conclusions of the studies in this thesis are presented, and the main contributions from the studies are concluded. In addition, the suggested future works are listed at the end of the chapter.

2. Literature Review

2.1. Introduction

This chapter introduces the essential background knowledge of this thesis which is consisted of four main aspects. The first section introduces the background of combustion, including the definition of combustion, the equivalence ratio, the different types of flame, flame colour and the different definitions of the temperature. The second part is the introduction of black body radiation and the digital camera. In this section, the fundamentals of radiation will be introduced at the beginning. Then, the digital camera will be reviewed with the introductions of the sensor, the image colour and the various digital camera types. The temperature measuring techniques are studied in the third section. Of which, the developed temperature measurement equipment will be classified into two parts: invasive temperature measurement and non-invasive temperature measurement. As well their applications will be reviewed. The last part of this chapter is the background of wood combustion. In this section, the combustion products of wood, the firebrands and the fire propagation in wood combustion are introduced. The literature review in this chapter is intended to cover the main background knowledge of this study, the insights and the research gaps of this field will be discussed in the introduction of its relative application chapter.

2.2. Combustion and flame

2.2.1. Introduction

Combustion, fire and flame, which play a crucial role in the development of human civilisation had been observed and utilised at a very early time. However, the concept of 'combustion' was not perceived until the late 18th century. With the increasing demand by industrialisation,

the research in the combustion field had explosively increased at the beginning of the 20th century. Nowadays, combustion as a comprehensive science field has been classified in detail to various subjects. Research fields emerged in thermodynamics, aerodynamics, transport phenomena, chemical kinetics, reaction mechanism, mathematical simulation and so on[16]. Due to combustion being a complicated subject, this section is not intended to cover all the fields related to the combustion process but the essential knowledge that relates to the study of this thesis. Topics included are the definition of the combustion process, the different types of flame, the introduction of temperature and the mechanism of heat transfer.

2.2.2. Background knowledge of combustion

Combustion is defined as a rapid exothermic process in which chemical energy is rapidly released into heat energy and radiant energy during the mutual redox chemical reaction between the reductant (fuel) and the oxidant. This reaction includes complex equations. And during the combustion, atoms (C, H, O and N) relevant to combustion are conserved. The atoms rearrange into the combustion products accompanied by the releasing of light and heat.

The combustion can be classified into various types. By associating with the completeness of chemical reactions, combustion is defined as: complete combustion and incomplete combustion. The complete combustion indicates that the fuel burns with sufficient oxidiser, while incomplete combustion is defined as the fuel burns in the condition with the insufficient oxidiser. The incomplete combustion always produces a greater number of products, such as the unburnt particles and partially oxidised compounds that are harmful to human beings. For most fuels in practice, such as diesel oil, coal, and wood, incomplete combustion occurs in the

natural condition. Complete combustion usually occurs by premixing the fuel and oxidiser. In order to define such premix status, the equivalence ratio, $\boldsymbol{\varphi}$, is utilised. The equivalence ratio is defined as the ratio of actual fuel/air ratio to the stoichiometric fuel/air ratio. The equivalence ratio > 1 indicates a rich fuel flame that is under incomplete combustion; and if the equivalence ratio < 1, the combustion is lean with excess air, namely premix flame or complete combustion. The equivalence ratio can be calculated by the equation 2.1 shown below:

$$\boldsymbol{\varphi} = \frac{\boldsymbol{fuel-to-oxidiser\ ratio}}{(\boldsymbol{fuel-to-oxidiser\ ratio})_{\boldsymbol{st}}} \tag{2.1}$$

2.2.3. Flame classification

Combustion does not always come with the flame, because a visible flame is dependent on whether the radiation emitted from the combustion products inside the flame appears within the visible range, but when it does, the flame indicates the reaction of combustion. The flame can be classified based on its premixing status as a non-premixed flame (diffusion flame), and premixed flame. As well, based on whether the fluid flow is laminar or turbulent, the flame can be sub-classified as a laminar flame or turbulent flame[17]. The different flame type is presented in table 2.1 with examples[16][18]:

Premix status	Flow type	Common examples
premixed	laminar	flame on Bunsen burner
	turbulent	gasoline engine
non-premixed	laminar	candle, wood flame
	turbulent	flame in diesel engine

Table 2.1 The classification of flames and examples.

- Diffusion flame: diffusion flame is produced by the combustion without pre-mix the fuel and oxidiser. In the diffusion flame combustion, the fuel and oxygen can be combined based on the molecule diffusion and turbulent diffusion with the concentration gradient[16]. As a result, the shapes and the burning speed of diffusion flames mainly depend on the mixing rate between the fuel and oxygen instead of the chemical reaction speed, the schematic of the diffusion flame is illustrated in Fig.2.1 (a). Diffusion flames tend to burn slower than premixed flames as the insufficient oxidiser for the reaction. Besides, the diffusion flames produce more soot particles due to incomplete combustion.
- Premixed flame: the fuel and oxidiser are mixed homogeneously and stoichiometrically before the combustion reaction in the premixed flames. The chemical reaction occurs in a narrowed interfacial region and propagates to the unburning pre-mixture with a certain speed, the schematic of the premixed flame is illustrated in Fig.2.1 (b). The normal velocity of the premixed flame interface propagation is known as the flame speed which is dependent on the properties of unburning pre-mixture. In the premixed flame, the reaction rate depends on the

chemical reaction.

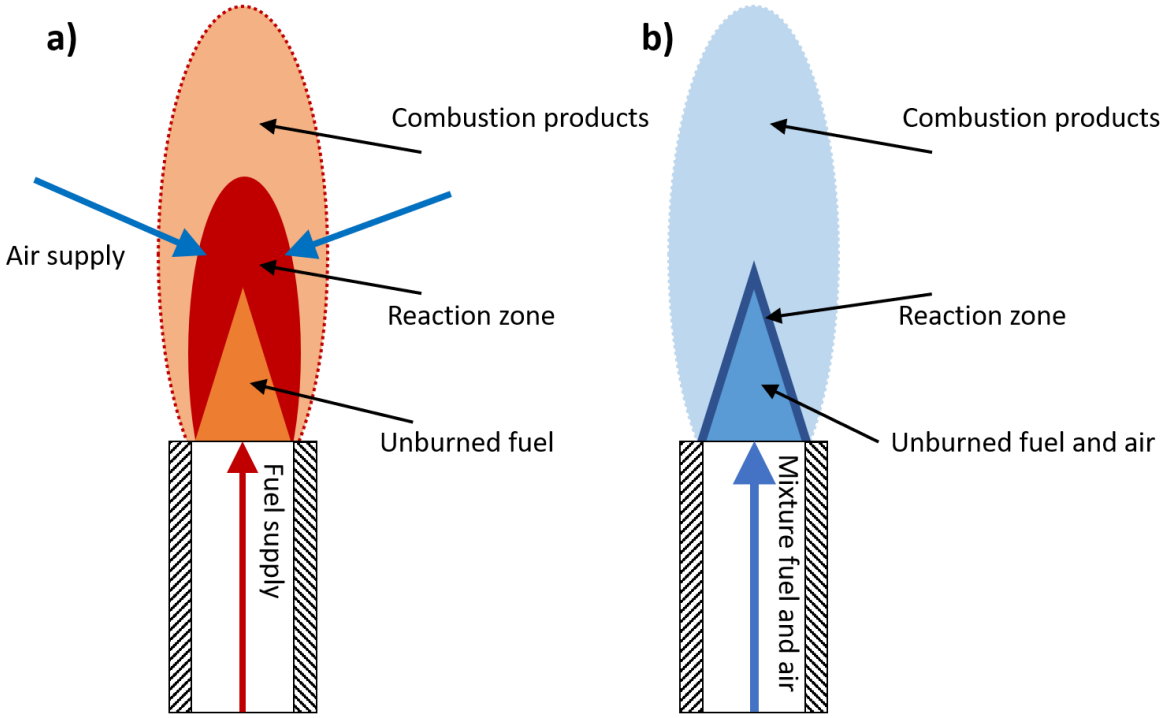

Figure 2.1 The schematic of typical diffusion flame and premixed flame: a) is the diffusion flame; and b) is the premixed flame.

2.2.4. Mechanism of heat transfer

As one of the most essential phenomena during the combustion process, heat transfer occurs every moment during the combustion reaction. Heat transfer is a common phenomenon in physics, caused by the temperature difference between the solid objectives or fluids. Heat transfer is measured by reading the change in the internal energy of a body. There are three main forms of heat transfer: thermal conduction, thermal radiation and thermal convection[19]. As long as there is a difference in temperature within or between bodies, heat inevitably transfers from high to low-temperature region. Heat transfer happens in one or more of these three ways according to the Second Law of Thermodynamics.

2.2.4.1. Conduction

Thermal conduction refers to the heat transfer phenomenon within a body with a temperature difference inside or between two bodies with different temperature when they contact directly. Thermal conduction takes place at the molecular level, and its essence is the energy transfer from the higher energetic molecules to those molecules which at a lower energetic level[19]. As well known, molecules are in the constant motion inside a body. The higher the temperature, the higher the kinetic energy of the molecule, which means the greater the energy of the vibration. When the molecules collide, energy is transferred from the higher energetic to the lower energetic molecules. Thus, when there is a temperature difference, the energy transfer through the heat conduction always proceeds in the direction from the high-temperature part to the low. The thermal conduction through solids is governed by Fourier's law, which is expressible as[20]:

$$\boldsymbol{q_{cond}}'' = -\boldsymbol{k}\frac{\boldsymbol{dT}}{\boldsymbol{dx}} \tag{2.2}$$

Where $\boldsymbol{q_{cond}}''$ represents the rate of heat transfer per unit area perpendicular to the direction of heat flow. It is proportional to the temperature gradient in the direction. The proportional coefficient $\boldsymbol{k}$ is the thermal conductivity of the material, which is one of the most basic physical properties of a material.

2.2.4.2. Radiation

Thermal radiation is a heat transfer method in which an object emits heat energy outward in the form of an electromagnetic wave. Since radiation does not depend on any external medium, therefore, it is the most efficient way of heat transfer in vacuum. No matter what kind of a substance is (solid, gas, or liquid), as long as its temperature is greater than absolute

zero, it would emit energy in the form of electromagnetic radiation. The emission of energy is caused by the change in the arrangement of electrons in the atoms or molecules that make up the material. The radiation power of an ideal radiator (blackbody) is based on the Stefan-Boltzmann law, which is given by equation 2.3:

$$\boldsymbol{P_{rad} = \sigma \cdot A \cdot T^4} \tag{2.3}$$

where $\boldsymbol{P_{rad}}$ is the radiation power of a black body, A is the body surface area (m^2), σ is the Stefan-Boltzmann constant which is $5.6704 \times 10^{-8} W \cdot m^{-2} \cdot K^{-4}$, T is the absolute (K).

when applying Eq.2.3 in a practical radiator, the equation can be modified as:

$$\boldsymbol{P_{rad} = \varepsilon \cdot \sigma \cdot A \cdot T^4} \tag{2.4}$$

where the term $\boldsymbol{\varepsilon}$ is called emissivity, which indicates the proportion of the radiation emits from a real object compared to the black body, the value of emissivity is between 0 to 1.

For the radiative transfer between two objects, the heat exchange is proportional to the temperature difference between the objects, the equation of exchange heat flux is given by:

$$\boldsymbol{q_{rad} = \varepsilon \cdot \sigma \cdot A \cdot F \cdot (T_a^4 - T_b^4)} \tag{2.5}$$

The $\boldsymbol{F}$ indicates the fraction of energy leaving from the body and received by body b, namely the view factor.

From equation 2.5, it can be seen that the radiative heat transfer depends on the temperature of the radiator, the higher the temperature, the more effective heat transfer emits from the thermal radiation.

2.2.4.3. Convection

Heat transfer between the fluids is dominated by thermal convection. The convective heat transfer takes place by the movement of fluids, the transfer of heat is essentially proceeded

via mixing the cold and hot fluids. The bulk motion of fluid enhances heat transfer in many physical situations, such as between a solid surface and the fluid[21]. The heat transfer from a solid surface to a low-velocity fluid can be calculated according to Newton's law of cooling, which is given by:

$$q_{conv}'' = h \cdot A \cdot (T_s - T_f)^{bs} \quad (2.6)$$

where h is defined as the heat transfer coefficient, A is the area of the object, bs is a scaling exponent, T_s indicate the surface temperature, and T_f is the flow temperature. According to the cause of thermal convection, it can be classified as natural convection or forced convection.

- Natural convection: in natural convection, fluid motion is caused by the difference of density which is attributed to the temperature gradients in the fluid. The heat transfer coefficient for the natural convection can be related to the buoyancy and the thermal properties of the fluid[20]. The upward heated flow above a fire or hot object is a common example of the natural convection.
- Forced convection: the forced convection takes place when the fluid is forced to flow on a surface by external devices, such as fans and pumps. The forced convection, as an artificially induced convection, could be used to control the heat transfer by mixing with the natural convection.

According to the types of fluid motion, the flow is divided as the laminar flow or the turbulent flow[22]. When the velocity of fluids is small, the fluids flow stratified, with each layer moving smoothly and the layers have no mixing, known as laminar flow; with the increase of the flow velocity, the boundary of flow begins to vibrate, and the frequency and amplitude increase

gradually. This flow condition is called the transition flow; when the flow velocity increases further, the streamlines of the fluid are no longer clearly discernible, and many eddies are appearing in the flow field, this flow condition is defined as turbulence flow[23]. This change of flow conditions can be quantified by Reynolds number which depends on the viscosity and density of the fluid and dimensions of the tunnel, which is defined as below.

$$\boldsymbol{Re} = \frac{\boldsymbol{\rho \cdot v \cdot L}}{\boldsymbol{\mu}} \tag{2.7}$$

where the $\boldsymbol{\rho}$ is the density of the fluid (kg/m3), $\boldsymbol{v}$ is the relative velocity of the fluid to the object (m/s), $\boldsymbol{L}$ indicates the linear dimension (m) and $\boldsymbol{\mu}$ is the dynamic viscosity of the fluid (kg/(m·s)).

When the Reynolds number is small, the main influence of flow field attributes to the viscous force, which is greater than the influence that comes from the inertial force, therefore, the velocity disturbance in the flow field has been attenuated by the viscous force, resulting in a smooth and laminar fluid flow. On the contrary, when the Reynolds number is large, the influence of inertial force becomes significant and greater than that of viscous force. The fluid flow is more unstable and turbulent, and the small change of velocity could be developed and strengthened, then form a chaotic and irregular turbulent flow field. In general condition inside the tube, the Reynolds number Re < 2100 is laminar flow, Re > 4000 is turbulent flow, and 2100 < Re < 4000 is transition state[23]. A typical example of the laminar, transition and turbulent flow is shown in Fig.2.2.

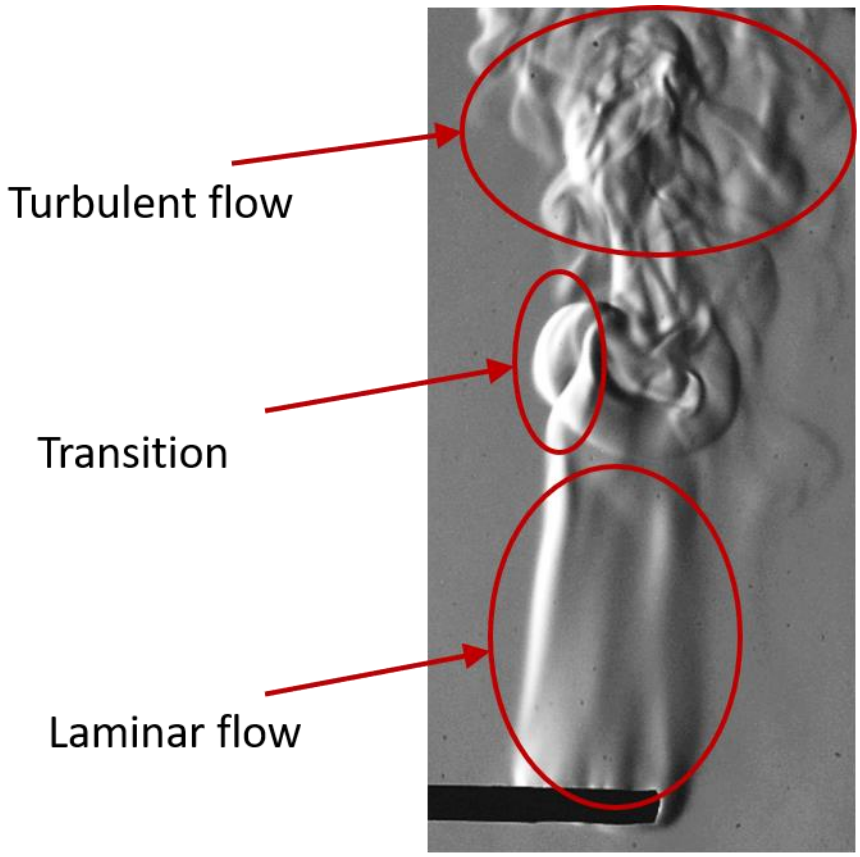

Figure 2.2 The typical example of different flow conditions.

2.3. Background of the digital vision system

2.3.1. Introduction

Vision, as one of the conscious senses of human beings, determines the ability of cognitive of the real world. Human receives the information from the world mainly from the vision represented by the eyes. The vision system of the human being can be seen as the most advanced imaging system, which could precisely represent the colour, shape, size and position of the observed objects by receiving the light in the visible range. The vision system helps human beings develop intelligence and cognitive ability in a sense. However, related visual deception tests reveal that what a person sees is related to what he or she wants to see. Therefore, the information received by the human vision system is subjective. With the help

of the development of digital camera and computer science, the vision system based on digital imaging becomes a powerful tool for visualising analysis and measurement. The digital imaging system is based on light emission from the real world. With the various purpose-built digital sensors, the request information from the objects can be captured, processed and analysed, which has an advantage over than directly received by human's eyes. In this section, the background of digital imaging systems is introduced, including the nature of light, the black body radiation and the digital camera sensors.

2.3.2. Light

Light is a physical term; its essence is widely known as the electromagnetic radiation within the specific electromagnetic spectrum. Seeking the nature of light is a long and hard journey. After the efforts of generations, physicists eventually reached a consensus that light could be characterised simultaneously as both a stream of particles and a wave[24]. This nature of light is known as the wave-particle duality. As human beings, the light received by our eyes is only a small portion of the electromagnetic spectrum, which is known as visible light. The visible light is usually defined as the wavelength between 400nm to 700nm[25]. However, there was various light emitting in other wavelength range, such as infrared, ultraviolet, gamma rays, X-rays, microwaves and radio waves. The overview of the spectrum of electromagnetic waves and the visible spectrum is given in Fig. 2.3.

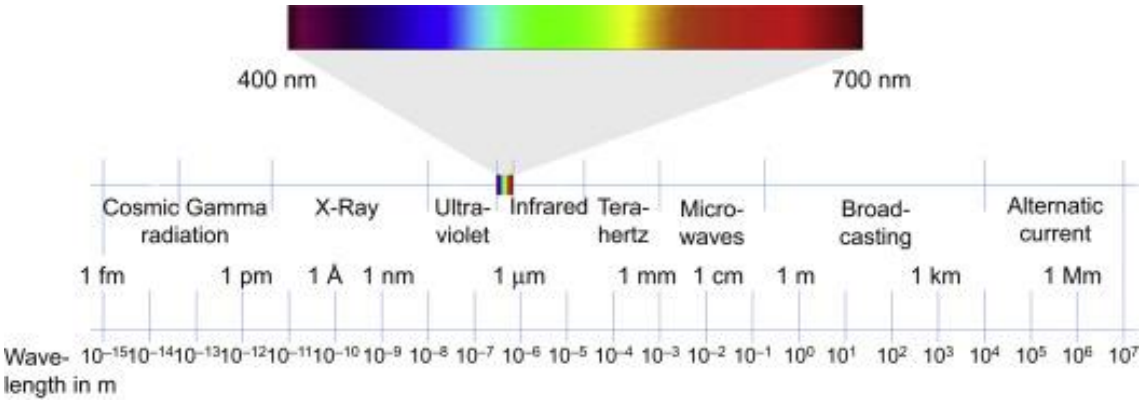

Figure 2.3 The electromagnetic spectrum and the visible spectrum (shown as the colour) [26].

The cone cells and rod cells in human's eyes have the ability to distinguish colours in the visible spectrum range, there are generally three kinds of cone cells in human's eyes: the first kind is mainly responsive to the light which is greenish-yellow colour, with the wavelength around 565 nm, sometimes this type of cones is called long-wavelength cones; the second kind is most sensitive to light of green colour, whose wavelength is around 535 nm, these cones are called as middle-wavelength cones; the last type of cone cells are generally called as short-wavelength cones with the most responsive wavelength in round 420nm which is perceived as bluish violet colour. There is just one type of rod cells whose most responsive wavelength is between the blue and green colours[27]. The response of cone cells in human's eyes is expressed as the Figure 2.4:

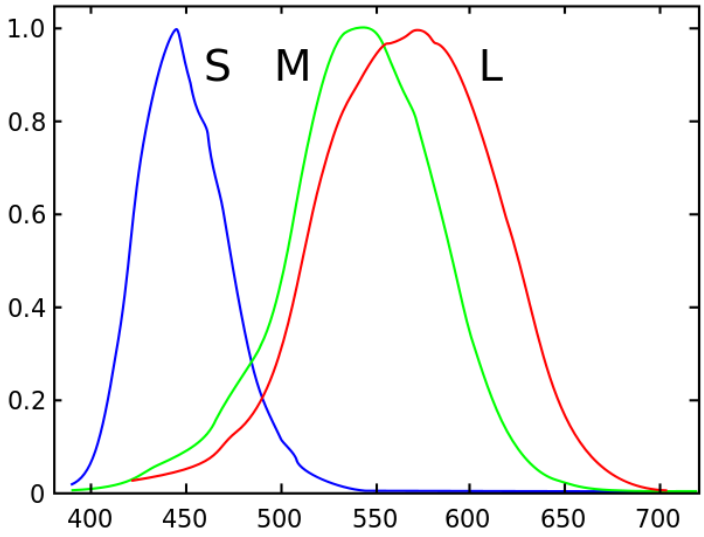

Figure 2.4 The response of cone cells in human's eyes[28].

2.3.2.1. Blackbody radiation

Every object whose temperature is higher than absolute zero has the ability which can constantly emit the electromagnetic wave. This kind of electromagnetic radiation is generated by the thermal motion of micro particles inside the object, known as thermal radiation. Its spectrum depends on the physical properties of the material and the temperature. In order to study the principle of thermal radiation independently of objects properties, physicists defined an ideal object which is known as the black body. The black body has the characteristics that its intensity only depends on the body's temperature, called the Blackbody radiation law or Planck's law. According to Planck's law, the spectral radiance $\boldsymbol{B_v(v,T)}$ can be expressed as:

$$\boldsymbol{B_v(v,T) = \frac{2h \cdot v^3}{c^2} \cdot \frac{1}{e^{h \cdot v/kT} - 1}} \tag{2.8}$$

where $\boldsymbol{h}$ is the Planck constant; $\boldsymbol{c}$ indicates the speed of light in a vacuum; $\boldsymbol{k}$ is the Boltzmann constant; $\boldsymbol{v}$ is the frequency of the electromagnetic radiation; $\boldsymbol{T}$ indicates the true temperature of the body.

The spectrum is peaked at a specific frequency that increases with the temperature. The visible light starts to reach an observable mount after about 500 degrees Celsius, when the temperature is lower than that degree, most of the emission is in the infrared region of the electromagnetic spectrum. Figure 2.5 shows the radiation curves with different temperature. When the temperature increases, the peaks of the curves move to higher intensities and shorter wavelengths.

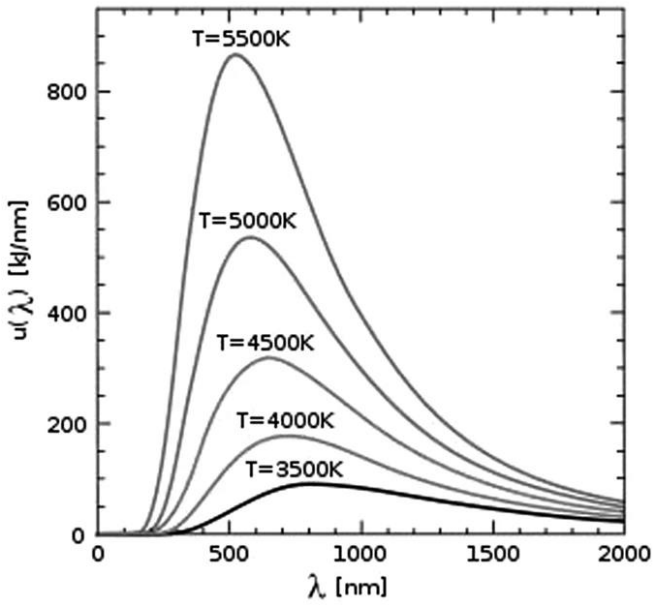

Figure 2.5 The traditional spectrum curve of the blackbody radiation[29].

Black body radiation can be seen as a function of wavelength for various absolute temperatures. Formally, Wien's displacement law indicates that the spectral radiance emitted by a black body radiation per unit wavelength has a peak wavelength $\boldsymbol{\lambda_{peak}}$ which is a function only depends on its absolute temperature, given by:

$$\boldsymbol{\lambda_{peak}} = \frac{\boldsymbol{b}}{\boldsymbol{T}} \tag{2.8}$$

where ***b*** is a constant of proportionality called Wien's displacement constant.

With the rising temperature, the peak $\boldsymbol{\lambda_{peak}}$ moves into a shorter wavelength, as a result, in

the visible spectrum, the colours of emission change from the dull red at the very first, then to yellow, and eventually to bluish-white. When the body appears white, it indicates that there is a large proportion of ultraviolet radiation. At very high temperatures, the colour eventually reaches bluish-white. The colours of blackbody radiation only depend on the temperature of the body, shown in Figure 2.6. The colour locus is known as the Planckian locus which is the path or locus that the colour of an incandescent black body would take in a particular chromaticity space with the temperature changes[30], the standard CIE XYZ colour space indicates directly to the corresponding chromaticity space specified by the two chromaticity coordinates known as x and y.

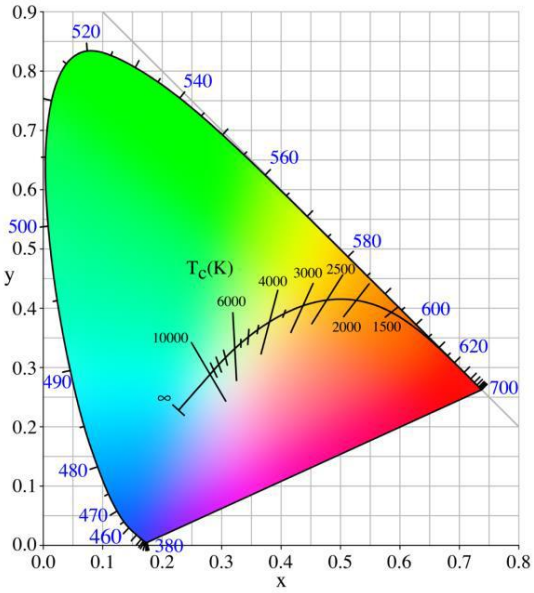

Figure 2.6 The colours of black body radiation[30].

2.3.2.2. Flame colour

The flame colour depends on several factors; the black body radiation and spectral band emission play the most important role in determining the flame colour. Temperature, or the black body radiation, determines the colours of a black body according to Fig.2.5, which also

influences the flame colour partly. For example, the combustion reaction mainly radiates the infrared at a temperature lower than 500 ^{o}C which is invisible to human's eyes. With the increasing temperature, the colour of emission changes from red to blue. This is a general trend of the colour changing with temperature. However, we cannot estimate the flame temperature by visualising its colour, because spectral band emission dominates the colour we received from the flame instead of black body radiation in practical (the temperature change is not significant according to the theory of black body radiation).

Due to the various emission spectrum of materials, the different combustion products have various peak emission wavelengths. For example, hydrocarbon flames, as the most common type of flame, extending the mixture of fuel and oxidiser can be the most significant factor to determine the flame colour. Because it could change the reaction paths which influences the colour. Generally, the flame which has no premixing of fuel and oxygen presents yellow colour. This is attributed to the incandescence of the soot particles produced in the flame. Considering that soot particles emit radiation above 500 nm, the in-complete combustion flame (no premixing) shows yellow colour in the visible range[31]. When the oxygen supply increases, less soot is produced since the more complete combustion reactions produce enough energy to excite and ionise gas molecules of the flame which leads to the appearance of blue colour. A blue colour flame only emerges when the blue emissions produced by the excited molecular becomes dominant, it can be obtained by a fully oxygen premixed flame which produces few soot particles. Then the flame colour is mainly determined by the molecular radicals of CH, which peak emission wavelength is around 430 nm[32]. A typical example for presenting three types of flame is shown in Fig.2.7.

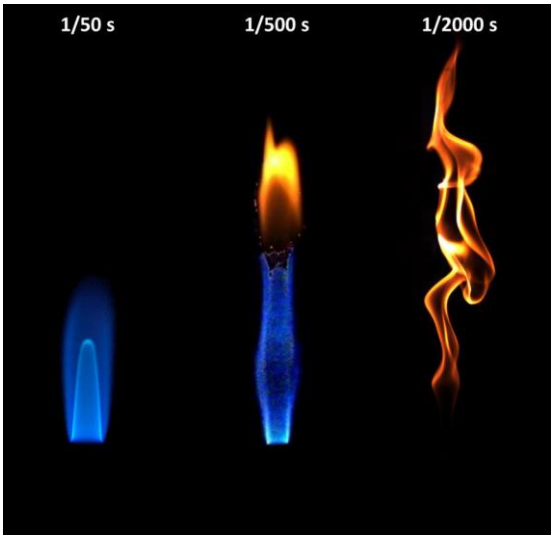

Figure 2.7 An example of premixed (left), partly premixed (middle) and diffusion flame (right)[33].

2.3.3. Digital cameras

The digital camera, as the most used kind of several, has the advantage that converts the optical image into electronic data which can be stored in digital memory. Digital cameras are different from traditional cameras which record the images by the chemical transformation produced in the negative plate by the light. The image sensors in digital cameras are used to replace the negative film for the function of the chemical sensitivity of light in the traditional camera. The captured image data can be stored in the memory device of the camera after a specific algorithm coding by the integrated microprocessors.

2.3.3.1. Colour cameras

Colour models are abstract mathematical models which divide the colours into different channels of value or colour components. They are commonly applied in colour reproduction in computer graphics representation and display. The main colour models utilised nowadays are RGB, CMYK, and HSB models. Comparing with other models, the RGB colour model is more widely used as the basic model of digital camera sensors for the physiological reason of human

beings. Even though the cone cells of human beings are not most sensitive to red, green, and blue, the light of these three colours can stimulate the cone cells independently[34].

Meanwhile, the RGB model is a device-dependent colour model, which means that different devices can detect the different colour values since the sensors have an unequal response to a light source. The RGB colour model is produced by combining three light channels (red, green, and blue) in various proportion. Zero intensity for each component indicates the dark colour while a full intensity of each presents the white colour. The distribution of colours in the RGB model can be expressed in a cubic space as shown in Figure 2.8:

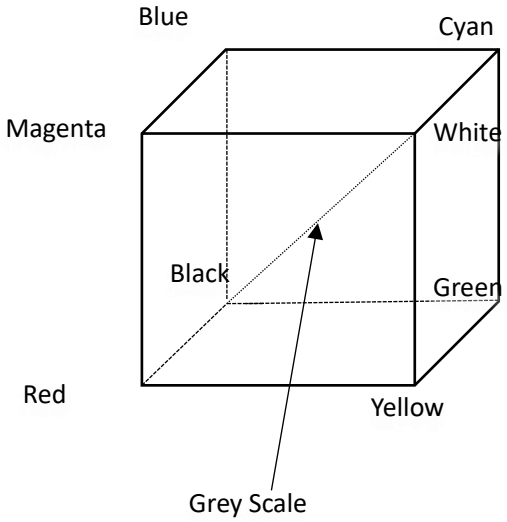

Figure 2.8 The cube of RGB colour model.

The Bayer filter is a colour filter array (CFA) for arranging the RGB colour filters in the front of the photo sensors. Digital cameras, camcorders, and scanners that use single-chip digital image sensors are mainly replying to the Bayer filters for colour image production. Figure 2.9 shows the structure of the Bayer filter, each unit of the RGB filter has four pixels composed of 50% green, 25% red, and 25% blue. The reason behind such uneven colour distribution is to

match the biological human vision which in a higher collection of G signal than other colours[35].

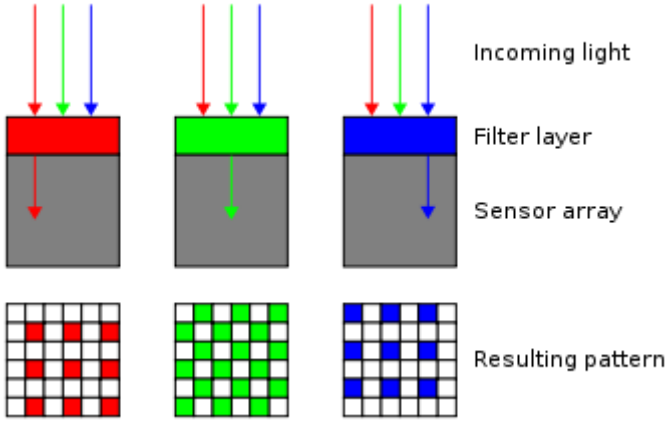

Figure 2.9 The structure of Bayer filter.

A camera sensor, commonly called as image sensor, is an electronic element that captures and converts the light information directly into colour images. The image sensors are used in digital cameras, medical imaging equipment, radar, sonar, and others. Currently, the most common types of image sensors are charge-coupled device (CCD) and complementary-metal-oxide-semiconductor (CMOS).

A CCD image sensor is a device that is based on the analogue signal. When light reaches the surface of a CCD sensor, a small electrical charge is produced in each capacitor. Each line of the capacitor will convey its charges into the nearest one. The last capacitor in the array transfers its charges into a charge amplifier, converting the charges into a voltage signal. By repeating this process, the charges of the sensor can be transferred into a sequence of the voltage signal. In the digital camera, this voltage signal will be transferred into a digital signal and processed in a microprocessor.

In comparison with the CCD sensor, the CMOS sensor does not involve electrical charges. A CMOS sensor has an amplifier in each pixel, the light energy thus can transfer into a voltage signal directly. However, more amplifiers in the sensor mean there is less area available for capturing photons, which led to part of the light lost, resulting in the reduction of the overall sensitivity of each unit. Currently, this problem has been overcome by using micro-lenses in front of each photodiode. By this technique, the light which would normally be wasted is now collected by the photo sensor[36]. As advantages, CMOS sensors implement has fewer components, costs less power, and provides faster readout speed than CCD sensors[37].

2.3.3.2. Thermal cameras

Thermal camera, or known as infrared camera, focuses on utilising the infrared radiation to create digital images. Unlike the colour camera which is sensitive to the visible light (400 nm – 700 nm), the thermal camera is sensitive to the wavelength above 1000 nm (1μm) and up to 14000 nm (14μm). According to the theory of wave propagation, the electromagnetic wave with a longer wavelength can propagate more effectively [38]. Therefore, infrared radiation could be more efficient than visible light for measuring the object from a distance or in total darkness. Besides, the thermal camera is more effective for capturing the low-temperature radiator than the colour camera. This is because the visible light only appears when the radiator temperature is higher than 500^{o}C, while the infrared radiation exists even at the low temperature. The infrared radiation can be divided by its wavelength, the common classification with the temperature range according to Wien's displacement law is presented in the table.2.2:

Division Name	Wavelength	Frequency	Temperature
Near-infrared	0.75-1.4 μm	214-400THz	2070-3864K
Short-wavelength infrared	1.4-3 μm	100-214THz	966-2070K
Mid-wavelength infrared	3-8 μm	37-100THz	362-966K
Long-wavelength infrared	8-15 μm	20-37THz	193-362K
Far-infrared	15-1000 μm	0.3-20THz	3-193K

Table 2.2 The classification of infrared[39].

Be different from the colour cameras which apply the Bayer filter to create the colour images, the thermal cameras mainly use the monochrome to indicate the intensity of radiation by grey-level. This is because the image sensors of generally-use cameras are unable to distinguish different wavelengths of infrared radiation. Another difference between the colour cameras is the focusing lenses. The focusing lenses of thermal cameras usually use germanium, calcium fluoride, or crystalline silicon instead of glass due to that glass would block the infrared radiation. In addition, most thermal camera lenses have antireflective coatings. That is one of the reasons why the thermal camera is much more expensive than the colour camera. There is another restriction of thermal cameras which is the resolution. Generally, the thermal camera generally has a low resolution. This is because a larger pixel size sensor is required for sensitisation.

In order to receive infrared radiation at various wavelengths, several different materials are

used for the camera sensors. In details, shortwave near-infrared and short-wavelength infrared sensors are typically composed of Indium Gallium Arsenide (InGaAs); middle-wavelength infrared sensors are generally made by Indium Antimonide (InSb); in the long-wavelength range, Mercury Cadmium Telluride (MCT) and Strained Layer Superlattice (SLS) are used for the camera sensors. The common materials for thermal camera sensors are presents in Fig.2.10.

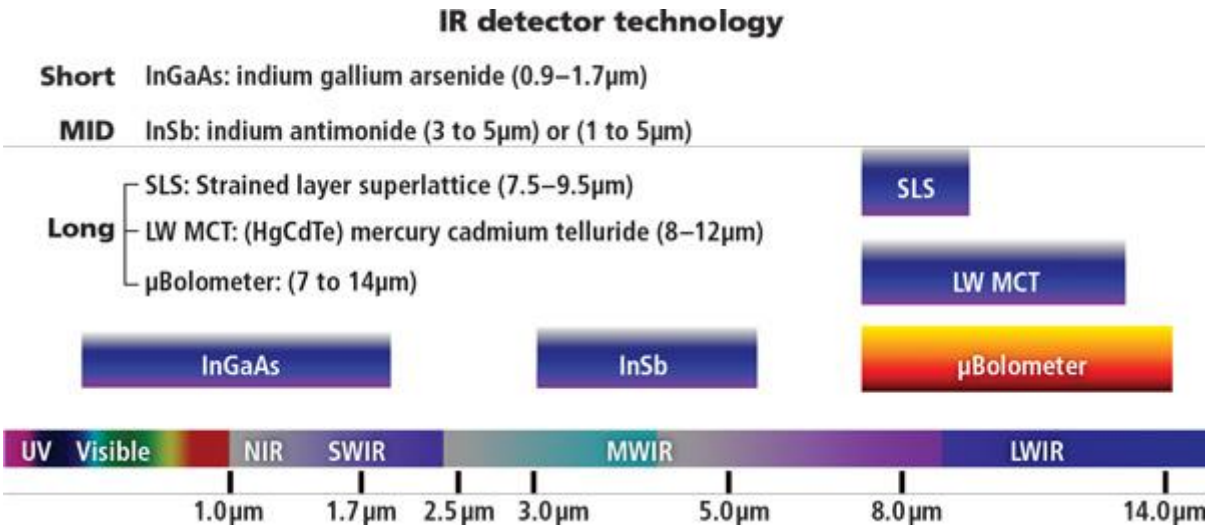

Figure 2.10 The common materials for thermal camera sensors[40].

From Fig. 2.10, it can be seen that the camera sensor made by the InGaAs is more suitable for measuring the object which emits near-infrared and short-wavelength infrared radiation. It can be a useful tool for industrial application, physical science and fire safety study. Comparing with the silicon-based CCD cameras which have good sensitivity in the visible range but insufficient sensitivity over 1100 nm, the InGaAs camera sensor has high sensitivity over the 900-1700 nm wavelength range due to its lower bandgap. An InGaAs array is made of a two-dimensional photodiode array. This array consists of an indium phosphide (InP) substrate, an InGaAs absorption layer and an ultrathin InP cap that has been bonded to a readout integrated

circuit (ROIC)[40]. An example of the InGaAs sensor layers is illustrated in Fig.2.11.

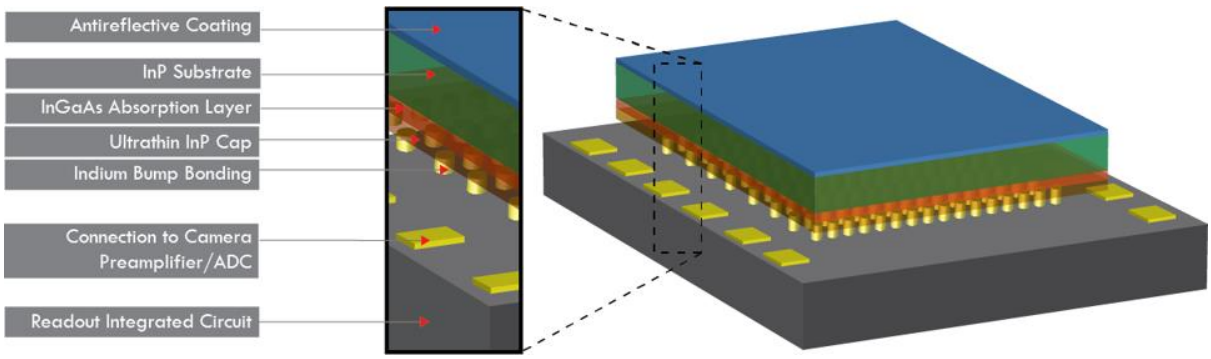

Figure 2.11 The different layers of a typical InGaAs sensor[41].

2.4. Temperature

2.4.1. Introduction

Temperature is one of the most important parameters in the physical world, it is essential for a wide range of technologies and all fields of natural science including physics, chemistry, biology and so forth. Temperature is a physical quantity that expresses the extent of cold and hot of objects. Specifically, temperature is the macroscopic expression of the intensity of the molecular thermal motion. Based on the theory of molecular kinetics, temperature is the representation of average kinetic energy of the microscopic particles' motions of objects, including molecules, atoms, and electrons. Due to temperature is an expression of all microscopic particles, it is based on statistics. Therefore, for a single microscopic particle, there is no meaning of the concept of temperature.

Temperature can be indirectly measured by the physical properties of objects. In history, temperature had been calibrated in various temperature scales, the common temperature scales are the Celsius scale, the Fahrenheit scale, and the Kelvin scale[42]. The theoretically minimum temperature is called absolute zero, as assuming all the particles of an objective

stop moving with no kinetic energy. Based on the third law of thermodynamics, the absolute zero cannot be reached by a finite temperature declining process. Absolute zero is denoted as 0 K in the Kelvin scale, -273.15 ^{o}C in the Celsius scale, and -459.67 ^{o}F in the Fahrenheit scale. In this section, the reviews about temperature which relate to the study of this thesis are introduced, including the concepts of true, colour and brightness temperature in section 2.4.2, and the reviews of temperature measurement methods in section 2.4.3.

2.4.2. True, colour and brightness temperature

Temperature is the expression of the thermal motion of microscopic particles, the temperature of objects is called absolute temperature or true temperature. According to the theory of black body radiation, the temperature is related to the colour of the object and the radiation emitted by the radiator. Therefore, two concepts are introduced for representing the properties of the object: colour temperature and brightness temperature.

- Colour temperature is a physical property that defines the colour of light, it is widely applied in physics, photography, manufacturing, astrophysics, and other fields. Colour temperature is defined as a temperature of an ideal black-body radiator whose emissions colour is the same as the colour of the light. Theoretically, with the increasing temperature, the black body will gradually show the colour in red, yellow, white, and finally glow blue colour. At a certain temperature, the spectrum emitted by the black body, known as the colour temperature at this temperature. Colour temperature is conventionally expressed in Kelvin, using the symbol ***K***. In colour temperature, the 'warm colours' are defined as colour temperatures under 3300 K, while the colour temperatures over 5000 K are called 'cool colours'. The colour and typical examples of colour temperature are shown in

Fig.2.12 below.

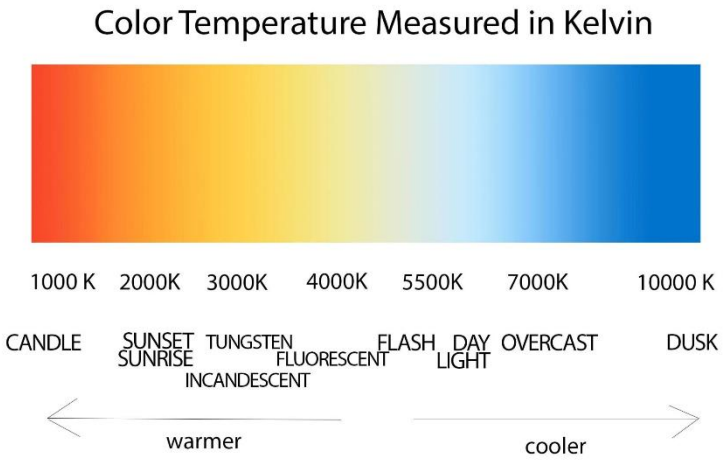

Figure 2.12 The colour temperature and the typical examples[43].

- Obviously, it is not reliable to estimate the temperature of objects by observing the colour or brightness of the objects as the colour is influenced by many factors such as the black body radiation, spectral band emission of the object itself and the transmission of light, for example, the Rayleigh scattering in the sky. Therefore, the brightness temperature is introduced to correlate the temperature of the object with its emitted radiation. The brightness temperature of a practical object is defined as the temperature of an ideal black-body radiator which radiates the equivalent radiation with the practical object at a certain wavelength[43]. The brightness temperature is extensively applied in various fields, especially in determining the true temperature in temperature diagnostic scope.

For a practical body, the radiation emitted is a portion of the black body radiation, determined by the spectral emissivity, $\boldsymbol{\varepsilon}$. At the low frequency and high-temperature range, the brightness temperature can be simplified as[44]:

$$\boldsymbol{T_b(\lambda) = \varepsilon(\lambda) \cdot T(\lambda)} \tag{2.9}$$

where $\boldsymbol{T_b(\lambda)}$ indicates the brightness temperature of the object, while $\boldsymbol{T(\lambda)}$ is the true

temperature of the object.

Combine with Planck's law in the Eq.2.8, the brightness temperature of the object can be expressed as:

$$T_b = \frac{2h\cdot\lambda}{k}\cdot ln^{-1}\cdot(1+\frac{2h\cdot\lambda^3}{B_\lambda\cdot c^2}) \quad (2.10)$$

At low frequency and high temperature, when $h\cdot\lambda \leqslant k\cdot T$ we can use the Rayleigh-Jeans Law to simply the equation, given by:

$$T_b = \frac{B_\lambda\cdot c^2}{2k\cdot\lambda^2} \quad (2.11)$$

As electromagnetic radiation is widely used for determining the temperature of objects, therefore, the brightness temperature is an important parameter when the calibration source is not an ideal black body. In the part of temperature metrology study of this thesis, a black body furnace which has 0.99 emissivity is used for the calibration process, therefore, its brightness temperature can be considered as true temperature approximately.

2.4.3. Review of techniques of temperature measurement

As temperature is important in all fields of natural science, engineering, and manufacturing, the measurement of testing the object's temperature is essential and crucial. To meet the rising standard of temperature measurement, a large number of sensors and devices have been developed. Most of them read the temperature by measuring the physical properties which will be varied with temperature. The common temperature measuring techniques can be classified into three types: invasive temperature measurement; semi-invasive temperature measurement; and non-invasive temperature measurement[45].

2.4.3.1. Invasive temperature measurement

The installation of a physical sensor within the component is the main feature of invasive

temperature measurement. There is a wide range of invasive instruments which can be classified by the varying properties of the instruments such as thermal expansion devices, thermoelectric devices, electrical resistance devices, semiconductor devices, and fibre optic probes. There is always a disturbance produced when the invasive equipment is installed. As a result, there is a difference between the measured temperature and the temperature of the object without the invasive devices.

- Thermal expansion devices. The thermal expansion of materials can be utilised to measure temperature. The devices include gas thermometry which based on the ideal gas law; liquid-in-glass thermometers that usually comprise a reservoir and capillary tube; and solids thermometry (usually are metals)[46].
- Thermoelectric devices. A thermocouple is an electrical device consisting of two dissimilar electrical conductors, producing a temperature-dependent voltage due to the thermoelectric effect. Thermocouples are widely used as temperature measuring devices. Thermocouples can be categorised by their materials as noble metal, base metal, high-temperature metal, and non-metal.
- Electrical resistance devices. The motion of free electrons is a temperature-dependent factor. Therefore, the electrical resistance of a conductor can be utilised to measure the temperature. The commonly used electrical resistance devices are platinum resistance thermometer with high precision but only used in laboratory conditions and the thermistors, which is cheaper than the platinum resistance thermometer but has lower precision.
- Semiconductor devices. As the semiconductor devices, such as transistors and diodes, are

sensitive to temperature change. Such characteristics can be utilised for temperature measuring. These devices have a decent accuracy of measuring and can utilise in a narrow temperature range[47].

2.4.3.2. Semi-invasive Temperature Measurement

In semi-invasive temperature measurement, a temperature-sensitive material has been applied to the surface coating. When the temperature changes, the variation in properties of the surface coating can be observed remotely. As there is also some disturbance when the coating is applied, this kind of methods can be classified as semi-invasive temperature measurement. The common techniques are thermochromic liquid crystal, thermographic phosphors and heat-sensitive paints.

- Thermochromic liquid crystals. Liquid crystals are composed of a molecular structure intermediate between a crystalline solid and an isotropic liquid. They are particularly sensitive to heat transfer. When the temperature changes, they would react to the changes with varying colours.
- Thermographic phosphors. It can be used for temperature measuring as the materials of phosphors are temperature sensitive. The variation of the surface coating with the temperature change can be observed by optical devices remotely. This technique has very high accuracy and thermal sensitivity. In addition, it is independent on the surface emissivity.
- Heat sensitive paints. These heat-sensitive paints have particular melting points which can indicate the maximum temperature attained[48].

2.4.3.3. Non-invasive temperature measurement

Invasive or semi-invasive instrumentations for temperature measuring could change the actual temperature of the measured sample or even affect the sample in itself. Besides, the temperature measured by invasive can be a time delay parameter, which is not suitable to the fluctuating temperature measuring such as flames or plasmas. Compared with invasive or semi-invasive methods, the main advantage of non-invasive temperature measurement is keeping the testing sample intact. In addition, the non-invasive methods generally read the temperature in real-time. Most non-invasive temperature measurement depends on the electromagnetic radiation, except the acoustic temperature measurement which relies on the velocity of the sound. The common types of non-invasive temperature measurement are listed below:

- Thermal radiation metrology. It is used for temperature measuring in the ranges from 50 to 6000K based on the captured thermal radiation in the infrared spectrum or visible light. The principle of thermal radiation metrology is based on Planck's distribution. The narrow band filter is often used to minimise the influence of the emissivity variation[49]. The thermal radiation metrology is well developed for various uses, such as engineering, manufacturing, metal processing, medical, fire safety and combustion. Based on whether the spectral emissivity of the testing sample is known, it can be classified as single-wavelength pyrometer and multiple-wavelength pyrometer[50], [51].
- Temperature measurement by refractive index. As the fluid density changes with temperature according to the Ideal Gas Law, the refractive index can be related to the temperature. Thus, it is used for temperature measuring. Schlieren is a common method

for observing the density variation and it can be utilised for reading the temperature distribution by pre-calibrating the pixel intensity with a standard temperature source[52].

- Laser-induced fluorescence. This method is used to measure flame temperature by exciting the molecules and atoms with a laser radiator. The flame temperature can be calculated by analysing the number and type of the excited molecules and atoms.
- Acoustic thermography. This method is designed for measuring the temperature of the fluid or solid surface. This technique was often used for the low-temperature range between 2.5-30K, currently, it can be used around 800K in temperature. For gas, this technique is based on the principle of thermodynamics which indicates the correction between the velocity of sound and the temperature of the gas. The velocity of sound can be obtained by recording the transit time of a sound signal between a pair of acoustic transducers at a known distance[53].

2.5. Wood combustion

2.5.1. Introduction

Wood combustion or burning of wood, as a kind of solid-fuel combustion based on the pyrolysis of wood materials, such as firewood, charcoal, chips, sheets, pellets, and sawdust, has been known and utilised since the beginning of human's civilisation. The attainability of wood and other cellulosic materials has provided human beings with abundant renewable energy resource. Although other kinds of fuel replace wood as a fuel with higher thermal efficiency, for example, diesel, gasoline, hydrogen, methane and so forth, the combustion of wood still affects human's life in a various way such as diesel, gasoline, hydrogen, methane,

and so forth, the combustion of wood still affects human life in various ways. The particular effect of wood combustion is the resultant fire disaster. As many cities are surrounded by forest, the wildfire generated from wood combustion significantly threatens the life and property of human beings.

Wood combustion is comprised of a series of physical and chemical processes which is very complicated. That is the reason why the study of the mechanisms of the wood burning process is still far from complete. However, with extensive knowledge of the physical and various techniques, now many details of the wood combustion process can be clarified. This chapter aims to introduce the fundamentals of wood combustion by illustrating the process of wood combustion in section 2.5.2, the key factors that influence the burning behaviours are introduced in section 2.5.3, and the fire spread mechanisms in the wildfire are reviewed in section 2.5.4.

2.5.2. Background of wood combustion

Like many other types of fuel, the wood burns 'indirectly' which means the combustion takes place as a series chain reaction between the oxidiser and the combustible gases that released from the wood material, instead of the wood material itself. The burning of wood is based on thermal decomposition, which is called pyrolysis, the gas-phase products are released into the air and reacted with the oxygen. In order to create a self-sustaining reaction, the combustion of these gases must generate sufficient heat to perpetuate the production of volatiles[54]. During the thermal pyrolysis, wood material produces inert and combustible gases, liquid tars, solid char layer, and inorganic ash[55][56]. Wood combustion is involved with a series of complicated processes, including dehydration, thermal pyrolysis, charring and oxidation[57].

The details of each stage are illustrated as the Figure 2.13:

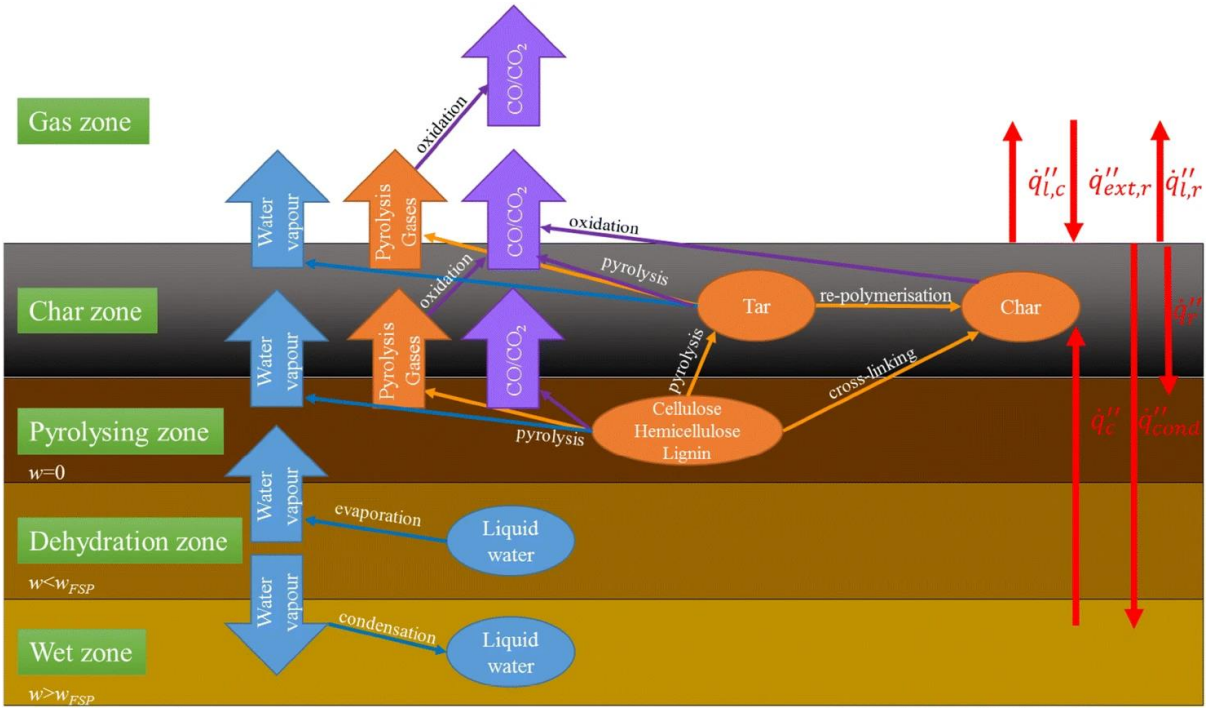

Figure 2.13 Chemical and physical processes within a burning timber[57].

- **Dehydration.** Before the pyrolysis proceeds, the water begins to evaporate when the temperature arises to 100 °C. Moisture removal is the previous process of pyrolysis. Generally, the virgin wood can be heated by the adjacent burning area by the means of heat transfer. When the heat rate is low, it is assured that all the free water has been evaporated before the thermal pyrolysis occurs[58]. Comparatively, when there is a high heat flux, dehydration and pyrolysis can occur simultaneously. The moisture usually delays the process of pyrolysis due to the evaporation of water content takes up the heat supply then delays the temperature increase.
- **Pyrolysis.** The wood material is essentially composed of cellulose molecules and lignin molecules, these kinds of molecules are arranged by the growing tree into a cellular form[59]. Wood is mainly composed of carbon, hydrogen and oxygen atoms, like other

types of fuel. These microparticles are held together by interatomic forces. When the external heat applies to the wood surface, the increasing temperature indicates the atoms vibrate more and more vigorously. Eventually, the atoms separate from each other and the molecules of cellulose and lignin come apart, called thermal pyrolysis. Typically, very slow pyrolysis occurs at around 200 ^{o}C which usually along with dehydration, rapid pyrolysis would occur when the temperature is higher than 300 ^{o}C[57][59][60]. The illustration of the pyrolysis processes and their products are shown in Fig.2.14. Cellulose is mainly decomposed by two means of processes: the first way is breaking the link of carbon ring, which occurs in the low-temperature range, produces mainly the non-flammable products such as char alongside carbon monoxide, carbon dioxide, and H_2O; the second is called as chain scission which occurs when the temperature is higher than 300 ^{o}C, in which the levoglucosan molecules can break away and produce the combustible gases[58][60][61]. It is worth distinguishing pyrolysis with combustion, the nature of pyrolysis is the thermal motion of the molecules, it can occur without any oxidiser while combustion is the reaction between the fuel and oxidiser.

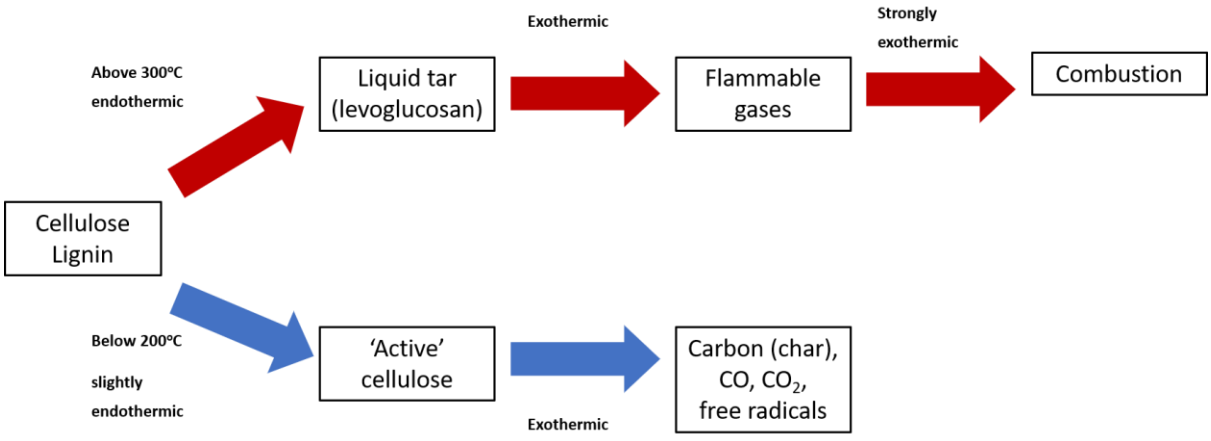

Figure 2.14 The illustration of the thermal pyrolysis process.

- **Charring.** It is a common phenomenon that the wood quickly turns in black with the burning process. The pyrolysis of wood generates a layer of char which is comprised of carbon and ash. The char forms a layer that prevents the interior virgin wood from direct heating from outside. The charring mainly occurs during the slow pyrolysis process. The mass loss attributed to the pyrolysis process slowly at the temperatures below 200°C, along with producing the non-combustible volatiles such as carbon dioxide, formic acids, and acetic acids, leaving cellulose largely unreacted[56]. With constantly heating at low temperature, the hemicellulose (active cellulose) can be converted into a carbonaceous char[62].
- **Oxidation.** The gas-phase products of wood pyrolysis are consisted of a wide range of compounds, specifically, 213 different compounds[59]. Some combustible gas-phase products mix with the surrounding air then produces flaming combustion and releases a large amount of heat, which could further induce pyrolysis and combustion reactions. The chain of the gas-phase combustion forms. The rate of combustion is mainly determined by the rate of pyrolysis, due to mostly all the flammable gases produced by thermal pyrolysis are directly transferred into the reaction zone[63]. Meanwhile, the oxidation occurs with the solid-phase products (mainly the char), and produces the solid particles, for example, the soot, this kind of process is called smouldering combustion[57].

2.5.3. Critical factors which influence the burning of wood

In practical, the wood combustion behaviours are varied with many properties, including the various species of wood, which contains the material properties such as the density, moisture content, Permeability and so on; the different burning conditions, which contains the

orientations of the wood samples, the size of the testing wood, and the grain direction; besides, the external heat flux and oxygen concentration play important roles to influence the wood combustion as well[57]. The charring rate is a typical characteristic that could represent the burning properties of wood. Besides, the lifetime of burning also used for evaluating the sustainability of the burning of wood which cannot self-sustain. The details of the main properties influencing wood combustion are listed below:

- **Density.** The density of wood materials is one of the most significant factors that influence the burning of wood. Many researchers have studied the effect of density as a key variable on the charring rate of wood[64]–[66]. It has been proved that low-density wood (soft wood) has a larger charring rate than which of high-density wood (hard wood)[67]. This is because the low-density wood has a higher void volume and a relatively low thermal conductivity, thus produces localised heating and heat accumulation, then resulting in a higher flame spread rate [68]. In addition, the wood with higher density generally has a lower charring rate due to the more energy is required for pyrolyzing the greater mass of material.
- **Moisture content.** The greater moisture content in the wood material could retard the pyrolysis which has been proved by many researchers[57][59][68]. It is an understandable mechanism due to the heat sink effect that the larger amount of free water inside the wood material, the greater energy is required for evaporating the water, thus less energy can be utilised for the thermal pyrolysis.
- **Species of wood.** Besides the factors of different density and moisture in various species of wood, the chemical composition can be another important factor influencing the

charring rate[57][62]. It is difficult to quantitatively analyse the effect of species of wood on the charring rate due to there is a considerable variation between species, nevertheless, some conclusions have been made by researchers. In Friquin's work[56], he concluded the effect of species mainly attributes to the lignin content. In details, higher lignin contents would lead to a higher char yield. Collier[69] states that the effects of chemical composition on charring rate mainly attributes to its effects on kinetics and energetics of pyrolysis.

- **Orientations.** The orientations of the sample influence the combustion of most materials, including the wood, by changing the fire dynamics and aerodynamics. In an upward direction fire, the buoyancy would drive the convective heat transfer along with the sample, thus the charring rate becomes larger[70]. In addition, the flame attachment phenomenon occurs on the inclined surface, this is attributed to the imbalance pressure on the flame sides due to the confinement of air entrainment[71].
- **Grain direction.** The direction of the wood grain is considered as an important factor that influences the burning of wood. This is mainly attributed to the permeability of wood is paralleled to the grain direction[57]. Even small changes of grain direction could significantly affect the way the free water and oxygen move, as well as affects the way flammable gases escape. In addition, the thermal conductivity is tended to be paralleled to the grain direction rather than perpendicular to it[57]. Therefore, the fire spread along the grain direction is considered as the most effective direction which has the largest charring rate.
- **External heat flux.** When the wood is burning under a sustaining external heat flux, the

behaviours of burning obviously change. The additional radiative heating from an external heat source could increase the energy using for dehydration and thermal pyrolysis. It has been demonstrated that the charring rate increases with increasing heat flux in a nearly linear function[72].

- **Oxygen concentration.** Like other types of combustion, the wood combustion process relies on the supply of oxidiser. The lower oxygen concentration generally presents in a low rate of solid-phase combustion (the char oxidation). Thus, a greater volume of char appears along with reducing heat transfer into the deep layer of wood samples. The charring rate decreases at lower oxygen concentration consequently.

2.5.4. Fire spread

Generally, in a wildfire, the fire spread in two ways which depending on far the spread is from the main fire. Fire spread for a long distance away from the primary fire, usually by the lofted firebrands named as the spotting ignition[73]. The second type is that when a fire spread along any individual wood element, the fire spread by the means of heat transfer[1]. In this section, the definition of firebrands is introduced, and the spotting phenomenon of firebrands is demonstrated then. The fundamentals of the fire spread along the individual fuel element are introduced at the end of the section.

2.5.4.1. Spotting ignition

- **Firebrands.** The firebrands in a wildfire play a crucial role in spreading the fire to a long distance away from the initial burning zone, which is the general terms of any small wooden pieces under burning that generated by the wildfire. The size and shape of firebrands are hard to be predicted due to their occasionality and complex burning

conditions. Many researchers have collected the results of naturally generated firebrands[74][75][76]. It has been reported that the density of a firebrand typically ranged from 250 kg/m^3 to 950 kg/m^3[77]. From the study, it is shown that the density of a firebrand also depends on its combustion status and the burning time.

- **Spotting phenomenon.** The strong wind in a wildfire is very dangerous considering the spotting phenomenon. The spotting ignition dramatically increases the range where under the threatening of fire. In addition, spotting ignition usually makes fire spread unpredictably fast, significantly increase the hardness of fire extinction and evacuation. Typically, the spotting phenomenon can be divided into three stages, which are generation, transport, and ignition[78]. Thus, it is a series of complicated processes for fire spotting. To understand the mechanism of the spotting phenomenon, various topics are required, such as ignition, thermal pyrolysis, combustion, fire dynamics, and so forth. The study of fire spread by an individual objective is essential for better understanding the mechanism of spotting ignition. In the practice circumstances, the flying firebrands generally have various angles of attack and resulted in different spotting distance and burning lifetime. Besides, the different wind speed and direction would dramatically affect the intensity of burning and the ability of fire propagation.

2.5.4.2. Fire spread along the individual fuel element

Every large-scale fire disaster including the city fire or wildfire is comprised by the burning of each individual element. The study of fire spread could help us improve the understanding of the fire safety and control the nonstationary fire. The fire spread is based on the concept of ’burning’ and ‘nonburning’[1]. To define this concept more precise, the term of fire

inception surface is introduced.

- **Surface of fire inception.** The term is defined as the boundary of the burning and nonburning surface. The fire spread is essentially transporting the heat or active molecular to the surface of fire inception. It is hard to define the ignition temperature for the surface of fire inception due to the wood combustion is comprised by a series process. Generally, the rapid pyrolysis temperature of 300 ^{o}C is considered as the ignition temperature which spread the fire into the adjacent virgin surface.

The fire can spread by the means of heat transfer, which are conduction, convection and radiation. The typical heat transfer schematic inside a wood burning system is shown in Fig.2.15.

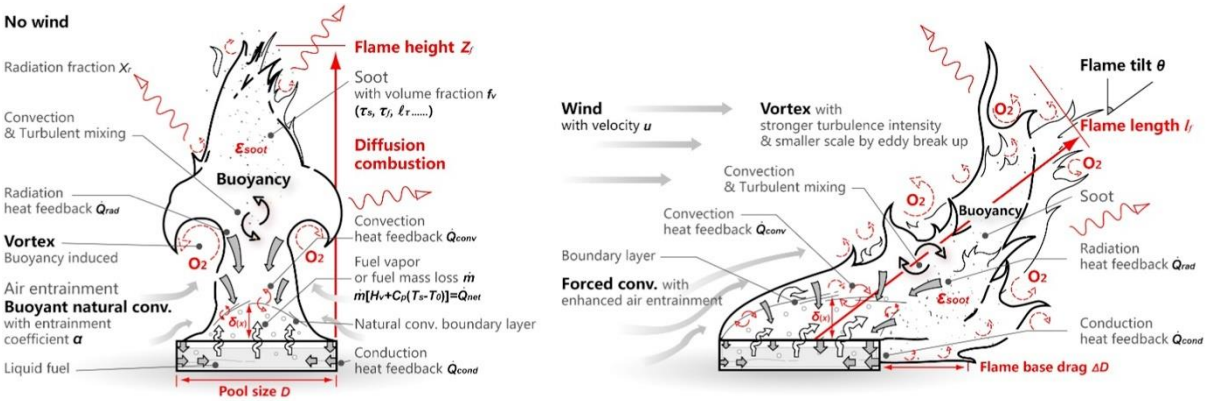

Figure 2.15 Schematic of heat transfer in the burning of wood[79].

- **Convection.** Convection is the most dangerous way that the fire spread in fire disasters. The heat generated by the exothermic reactions of combustion moves along with the gas-phase combustion products and forms a layer that encloses the fuel element. The convection can be transferred along the fuel element or travel upward due to the buoyancy and ignites the virgin fuel. Convection is the most common way of fire spread, especially in domestic and commercial buildings.

- **Conduction.** The fire spread by conduction in wood combustion mainly attributes to the transferring of the active molecules into the adjacent virgin fuel. Due to the low thermal conductivity of wood material, the conduction may be insignificant for the fire spread.
- **Radiation.** The radiative heat transfer also plays an important role in fire spread. Regarding the burning of wood, the radiative heat transfer occurs between the flame and the fuel surface. The flame could transfer the energy by electromagnetic waves and impacts the virgin fuel. For small-scale fire, the radiation heat transfer is insignificant. However, in a large-scale fire such as the wildfire, the radiation is intense and becomes the key factor that influences the fire spread as an additional heat flux for heating the wood surface.

3. The methodology of Combustion Diagnostics

3.1. Introduction

One aim of this thesis is to develop the techniques and methods of combustion diagnostics and to apply them in combustion diagnosis. For this purpose, various methodologies and imaging systems are employed including two-colour temperature measurement, thermal imaging metrology, schlieren imaging system, and optical flow method.

Since temperature is one of the most important parameters in this study, the temperature measurement in this thesis is developed by two different methods, including the two-colour method for measuring the flame temperature and the single wavelength in the near-infrared (NIR) range for measuring the temperature on the wood surface. Including the theoretical fundamentals, technique specifics, calibration, and error analysis, the details of both measurements will be introduced in section 3.2.

Meanwhile, the schlieren imaging system is built for visualising the invisible heated flow surrounded a burning wood rod, which will be introduced in section 3.3 including the setup and the example case.

The optical flow method has been used to calculate the velocity of the surrounding flow and the flame edge, the method of optical flow will be shown in section 3.4.

3.2. Temperature measurement methods

3.2.1. Two-colour method

The two-colour method is an non-contact temperature measurement metrology, as introduced in the Section 2.4.3.3, the principle of this technique is based on the blackbody radiation, and by well calibrating the ratio between two channels response of the detector

against temperature, the temperature of any grey body can be calculated. The two-colour method was firstly introduced in the paper by Hottel and Broughton et al. in 1932[80]. Since then, the two-colour method has been developed and widely used in various fields. As it has good feasibility of a large surface, the two-colour method was most frequently used in surface temperature measuring such as wall temperature measuring [81], monitoring the carbon steel temperature[82], measuring brake disc surface temperature[83], and so on. As the soot particle can be seen as a grey body whose emissivity keeps consistent with wavelength, the two-colour method has been well applied in the analysis of the diesel engine combustion[84]–[87] and wood combustion [88]–[90], [90]–[94]. In addition, the soot concentration can be calculated by the two-colour method which had been studied in the previous studies [88], [95]–[98]. It has been proved that the flames from both the diesel[84], [87], [99] and the wood combustion [88], [92]–[94], [100] can be measured by the two-colour method because the soot particles can be considered as homogenously distributed inside the flame[101]. By capturing the radiation intensity from the soot particles, the flame temperature can be measured then.

In this study, the two-colour method with a high-speed colour camera will be used to calculate the flame temperature distribution of the burning wood. In section 3.2.1.1, the fundamental of the two-colour method will be introduced. Then, the calibration results of the camera will be presented in section 3.2.1.2 with two different optical settings. In section 3.2.1.3, several testing cases will be presented to show the calibration results.

3.2.1.1. Background of two-colour method

The fundamental principle of the two-colour method is based on Planck's law, which described the energy emitted by a perfect black body[102]. The equation of Planck's law can be shown as:

$$\boldsymbol{E(\lambda, T) = \frac{C_1}{\lambda^5}(e^{\frac{C_2}{\lambda T}} - 1)^{-1}} \quad (3.1)$$

Where $\boldsymbol{\lambda}$ represents the wavelength, $\boldsymbol{T}$ is the true temperature of the object (K), $\mathbf{E(\lambda, T)}$ represents the unit area intensity of radiation emitted at the wavelength λ of the object and $\boldsymbol{C_1}$ and $\boldsymbol{C_2}$ are the first and second Planck's radiation constant.

The perfect black body does not exist in the real world, and every object emits a certain percentage of radiation of the black body. The emissivity **ε** is used to represent the ratio of the radiation emitted by a practical object over a black body, resulting in the value of emissivity is always less than 1, $\boldsymbol{\varepsilon}$ <1. The grey body is an ideal object as well, which is defined as an object whose emissivity keeps consistent in different wavelengths. The grey body is widely used to simplify the practical model, it is reliable when the effect of wavelength on the emissivity can be ignored.

Combined with the definition of the grey body, Planck's law can then be presented as:

$$\boldsymbol{E(\lambda, T) = \varepsilon \frac{C_1}{\lambda^5}(e^{\frac{C_2}{\lambda T}} - 1)^{-1}} \quad (3.2)$$

Where **ε** is the emissivity of a grey body. In this study, the temperature will be applied in the range from 1000K to 2600K and in the visible light wavelength range between 400nm – 700nm. Due to $\frac{\boldsymbol{C_2}}{\boldsymbol{T\lambda}} \gg 1$ within this region, the equation can be described by Wien's radiation law:

$$\boldsymbol{E(\lambda, T) = \varepsilon \frac{C_1}{\lambda^5} e^{\frac{-C_2}{\lambda T}}} \quad (3.3)$$

The radiation can be captured using a digital camera system, and the intensity of radiation

can be converted into the grey level $\boldsymbol{G(\lambda, T)}$, the equation of the grey level is given by:

$$\boldsymbol{G(\lambda, T) = R * S_{\lambda} * \varepsilon * \frac{C_1}{\lambda^5} e^{\frac{-C_2}{\lambda T}}} \quad (3.4)$$

Where the R represents the camera constant which depends on the imaging system, camera sensor sensitivity (ISO), the aperture of the lens and so on. In the equation, $\boldsymbol{S_{\lambda}}$ is the imaging system sensitivity of the wavelength. Then, the ratio of two grey levels at selected wavelengths $\boldsymbol{\lambda_2}$ and $\boldsymbol{\lambda_2}$ can be given as:

$$\boldsymbol{\frac{G(\lambda_1,T)}{G(\lambda_2,T)} = \frac{S_{\lambda_1}}{S_{\lambda_2}} * (\frac{\lambda_2}{\lambda_1})^5 * exp\left[\frac{C_2}{T} * \left(\frac{1}{\lambda_2} - \frac{1}{\lambda_1}\right)\right]} \quad (3.5)$$

And the temperature $\boldsymbol{T}$ can be obtained by rearranging Equation 3.5, shown as:

$$\boldsymbol{T = \frac{C_2 * (\frac{1}{\lambda_2} - \frac{1}{\lambda_1})}{In\frac{G(\lambda_1,T)}{G(\lambda_2,T)} + In\frac{S_{\lambda_2}}{S_{\lambda_1}} + In(\frac{\lambda_1}{\lambda_2})^5}} \quad (3.6)$$

The ratio of the camera sensitivity of two selected wavelengths $\boldsymbol{\frac{S_{\lambda_2}}{S_{\lambda_1}}}$ is named as the instrument factor $\boldsymbol{S}$ which can be obtained in a pre-calibration process by using a black body furnace. As the grey body is an ideal object which does not exist in the real world, it should be noted that the emissivity is not consistent in different wavelengths. However, it has been proved that when the two selected wavelengths are close, the difference of emissivity between the two selected wavelengths can be ignored[103].

3.2.1.2. Calibration

The accuracy of a pyrometer is based on the calibration process with a certain temperature source. The calibration process aims to obtain the correlation between the temperature with the input parameter. Regarding the theory of two-colour method, the calibration process needs to establish the correlation between the temperature and the grey level ratio of two selected wavelengths. According to Equation 3.6, it is found that the temperature can be

calculated with the input grey level ratio if the ratio of the camera sensitivity between two selected wavelengths (instrument factor) has been obtained.

In this study, a black body furnace (LANDCAL R1500T) is used as the standard temperature source for the calibration process, which is shown in Fig 3.1. The LANDCAL R1500T furnace is a highly stable and transportable black body, which can be heated up to 1500℃. The emissivity of radiation emitted by the furnace is approximately 0.99 at short wavelengths[104]. The emissivity of two wavelengths can be considered as constant in the visible light.

Figure 3.1 The LANDCAL R1500T black body furnace.

According to the properties of the Bayer filters on the CMOS sensor of a digital camera, the signals received by the camera are in the visible range and split into three channels: red (R), green (G) and blue (B). The grey level ratios among the R, G and B channels are applicable for the temperature measurement by the two-colour method. In this study, a Photron SA-4 high-speed camera is set in the front of the black body furnace to capture the radiations from the furnace, shown in Fig.3.2. The spectral response of the camera is shown in Fig.3.3. The red line in the Figure indicates the red channel response, the blue and the green lines

indicate the blue and green channel responses, respectively. The Blue signal rises to its maximum intensity around 470 nm, the green signal has a peak at 540 nm, and the red signal has a maximum response at 620 nm.

Figure 3.2 The Photron SA-4 high-speed camera.

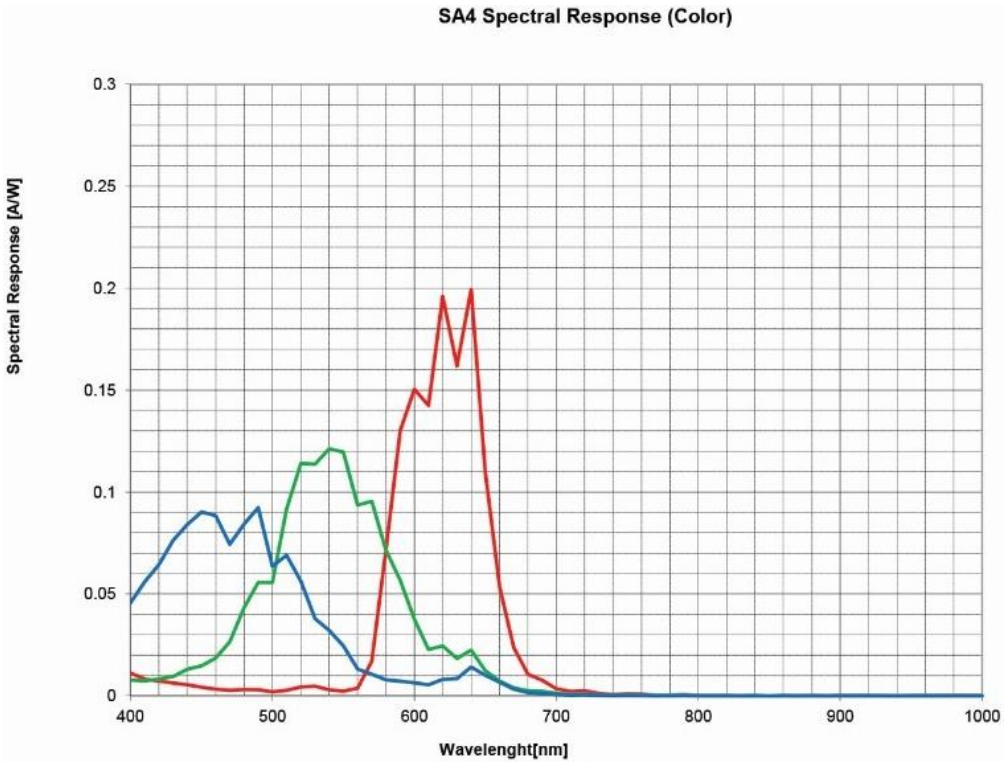

Figure 3.3 The response of Photron SA-4 high-speed camera[105].

In the calibration process, the camera was used a build-in shading process with a lens cap to eliminate the dark noise. Since the Bayer filter can be easily influenced by near-infrared radiation, an infrared cut off filter is used to eliminate the effect of infrared and improve the accuracy. A comparison between camera responses with and without IR cut off filter is listed in the results. The black body furnace will be heated from 700°C to 1500°C, while the images will be captured every 100°C after 20 mins passed since the furnace had reached every temperature step.

According to Eq. 3.6, the ratio of camera sensitivity between two selected wavelengths (instrument factor $\boldsymbol{S}=\frac{S_{\lambda_2}}{S_{\lambda_1}}$) can be obtained from the calibration process. By re-arranging Eq. 3.6, the instrument factor is given by:

$$\boldsymbol{S}=\frac{S_{\lambda_2}}{S_{\lambda_1}}=\frac{e^{\frac{C_2}{T}\left(\frac{1}{\lambda_2}-\frac{1}{\lambda_1}\right)}}{\frac{G(\lambda_1,T)}{G(\lambda_2,T)}\cdot\left(\frac{\lambda_1}{\lambda_2}\right)^5} \tag{3.7}$$

The wavelengths $\boldsymbol{\lambda_1}$ and $\boldsymbol{\lambda_2}$ are selected to present the peak wavelengths of the red, green, or blue colour channels.

The results of direct images (no filter applied, similarly hereinafter) at different temperatures are shown in Fig.3.4. As the signal of 500°C (Fig.3.4 (a)) is too weak, the calibration range in this case is selected from 600°C to 1500°C. It should be noted that the bluish colour can be found in the direct image in the low-temperature range. According to the black body radiation theory[102], the blue colour should not appear at such low temperature. Therefore, it can be ensured that the infrared radiation has a strong influence on the camera sensor, even if an IR block filter has been installed in the front of the camera sensor.

To eliminate the effect from the infrared, the IR cut off filter was applied, where the results are shown in Fig.3.5. By comparing Fig. 3.4 and Fig. 3.5, it can be seen that the blue colour almost disappeared. As the filter blocked a part of the radiation from the furnace, the images at very low temperature became unobservable. Therefore, in order to avoid such disadvantage, the calibration range was chosen from 700°C to 1500°C.

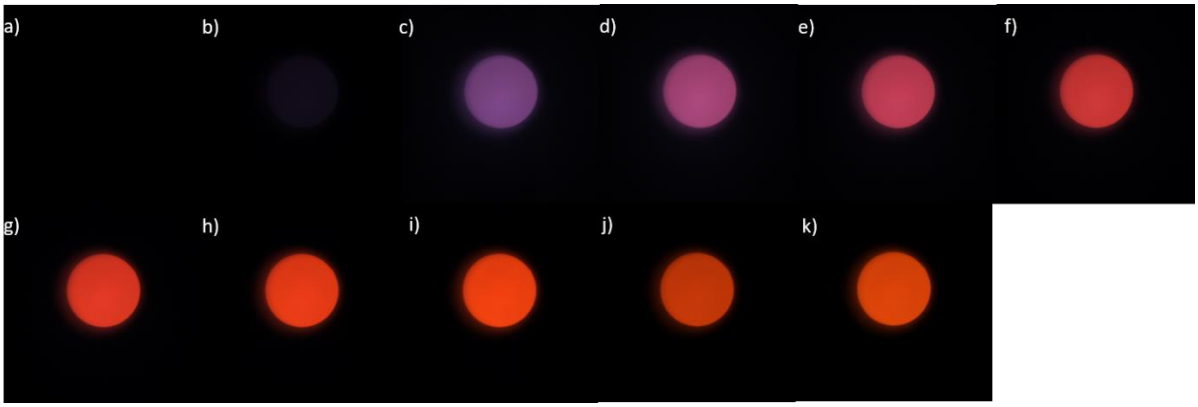

Figure 3.4 The direct images of the black body furnace at different temperature: a), b) … k) represent in the temperature 500, 600… 1500℃ respectively.

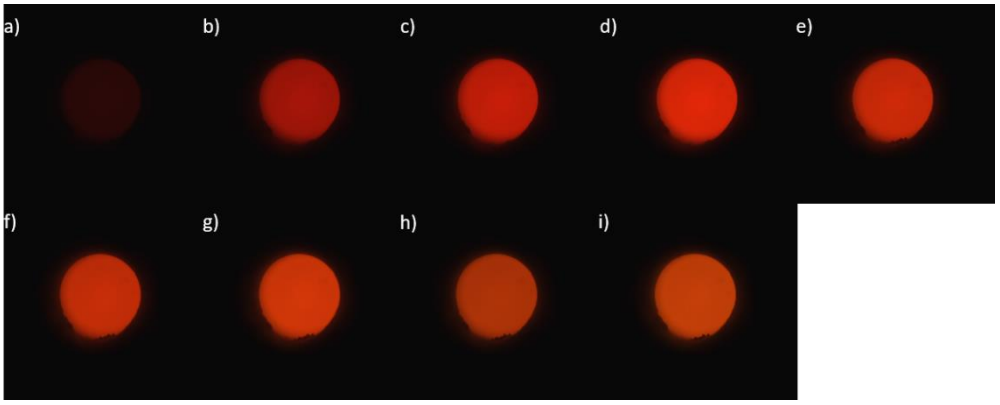

Figure 3.5 The IR cut off images of the black body furnace at different temperature: a), b) … i) represent in the temperature 700, 800… 1500℃ respectively.

The images in this study were processed by the MATLAB software with a specially written algorithm to convert them into three independent grey levels of R, G and B channels. The

grey level ratios against temperature in the direct image case are presented in Fig.3.6. It should be highlighted that the RG ratio shows non-monotonicity in the temperature range from 500ºC to 1500ºC. This means that the measuring range needs to be divided into two temperature range: 500ºC – 1100ºC and 1200ºC – 1500ºC.

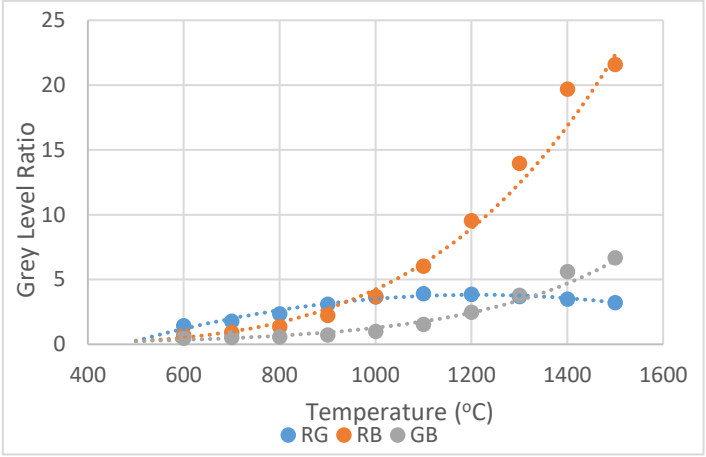

Figure 3.6 The grey level ratio against the temperature of the direct image case.

The instrument factor S can be calculated by Eq. 3.7. The results of the instrument factor are shown in Fig.3.7 below:

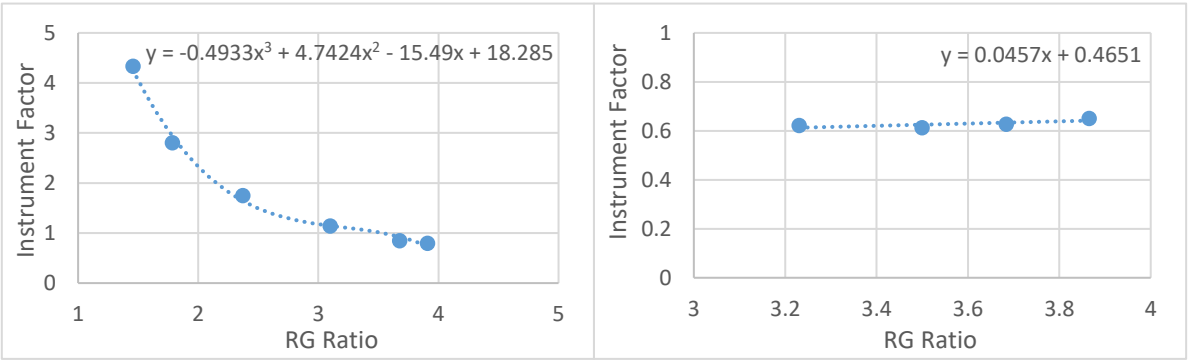

Figure 3.7 The instrument factor against RG ratio of direct image case at different temperature range left: 500ºC to 1100ºC; right 1200ºC to 1500ºC.

The fitting equation of instrument factor S can be expressed as:

In 600-1100℃

$$S_{RG} = \frac{S_{\lambda_G}}{S_{\lambda_R}} = -0.4933{G_{RG}}^3 + 4.7424{G_{RG}}^2 - 15.49G_{RG} + 18.285 \quad (3.8)$$

In 1200-1500℃

$$S_{RG} = \frac{S_{\lambda_G}}{S_{\lambda_R}} = 0.0457G_{RG} + 0.4651 \tag{3.9}$$

where the G_{RG} represents the ratio between the greyscale in red and green channels; similarly, the G_{RB}, and G_{GB} represent the ratio between red and blue; and green and blue respectively.

Meanwhile, the instrument factor related to RB ratio and GB ratio can be calculated and shown in Fig.3.8.

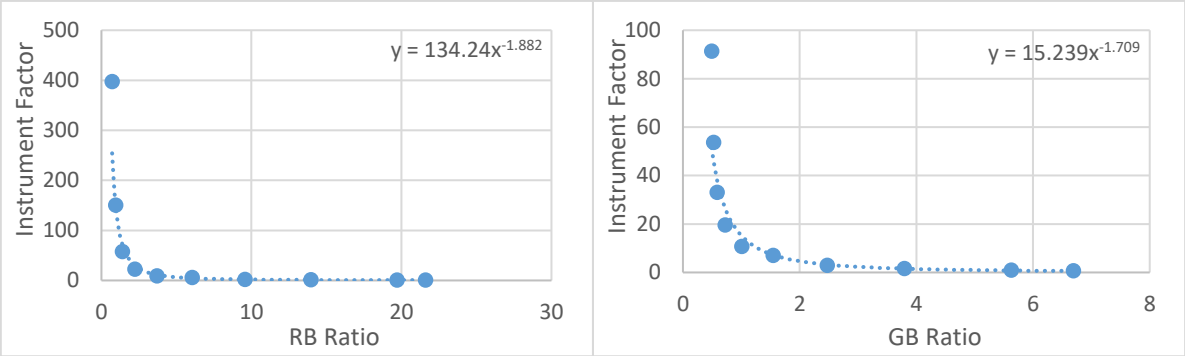

Figure 3.8 The instrument factor against RB/GB ratio of direct image case at different temperature range left: RB ratio; right GB ratio.

And, the fitting equation of instrument factor S can be expressed as:

RB ratio:

$$S_{RB} = \frac{S_{\lambda_B}}{S_{\lambda_R}} = 134.24G_{RB}^{-1.882} \tag{3.10}$$

GB ratio:

$$S_{GB} = \frac{S_{\lambda_B}}{S_{\lambda_G}} = 15.239G_{GB}^{-1.709} \tag{3.11}$$

As discussed before, the infrared affects significantly in the camera sensor, especially at the low-temperature range. The infrared radiation can be blocked by the IR cut off filter. Similar to the results of the direct image case, the grey level ratios from the IR cut off image case is

shown in Fig.3.9. The red line, the green and the blue line indicate the ratio of red/green channels, red/blue channels and green/blue channels respectively.

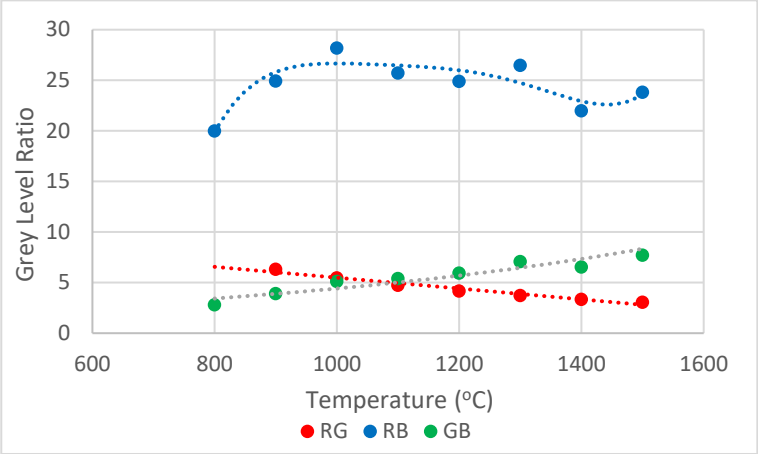

Figure 3.9 The grey level ratio against the temperature of the IR cut off image case.

Be different from the direct image case, the RG ratio from the IR cut off image case shows linear in the temperature range 800°C to 1500°C. According to its good monotonicity, the temperature beyond 1500°C can be logically speculated. Due to the IR cut off filter blocked the majority of infrared radiation, the signal of the blue channel became weak. Since the small amount of blue value, the RB ratio becomes fluctuate and unreliable. Therefore, the RB ratio was abandoned in this case.

The curves of instrument factor against RG and GB ratios can be fitted as below:

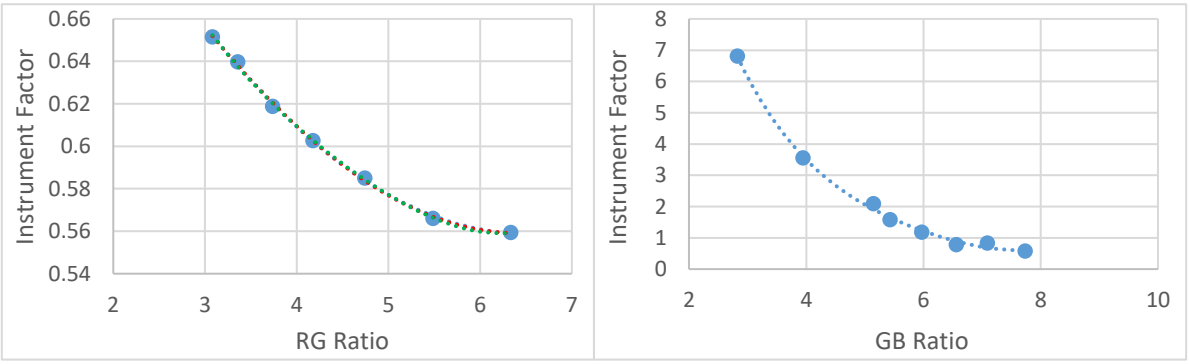

Figure 3.10 The instrument factor against RG/GB ratio of direct image case at different temperature range left: RG ratio; right: GB ratio.

It is worth noting that the RG ratio has the best fitting curve, the curves match together in different fitting equations. The equation can be concluded as:

$$S_{RG} = \frac{S_{\lambda_G}}{S_{\lambda_R}} = 0.0006{G_{RG}}^4 - 0.0109{G_{RG}}^3 + 0.0803{G_{RG}}^2 - 0.3105G_{RG} + 1.1125 \quad (3.12)$$

Similarly, the fitting equation of GB ratio is given by:

$$S_{RG} = \frac{S_{\lambda_G}}{S_{\lambda_R}} = 0.0154{G_{GB}}^4 - 0.3801{G_{GB}}^3 + 3.668{G_{GB}}^2 + 32.999 \quad (3.13)$$

The temperature then can be calculated by the Eq. 3.6 with combining the different instrument factor equation which was obtained from the calibration. The error is analysed by comparing the difference between the black body temperature (actual temperature) with the calculated temperature. In the direct image case, the comparisons between actual temperature with measured temperature by RG, RB and GB ratios are shown in Fig. 3.11 (a), (b) and (c) respectively.

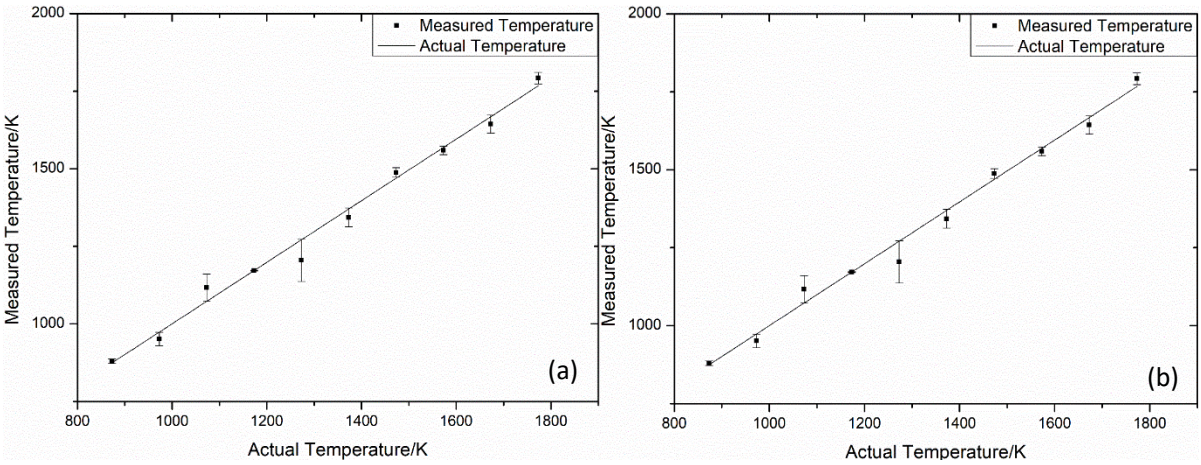

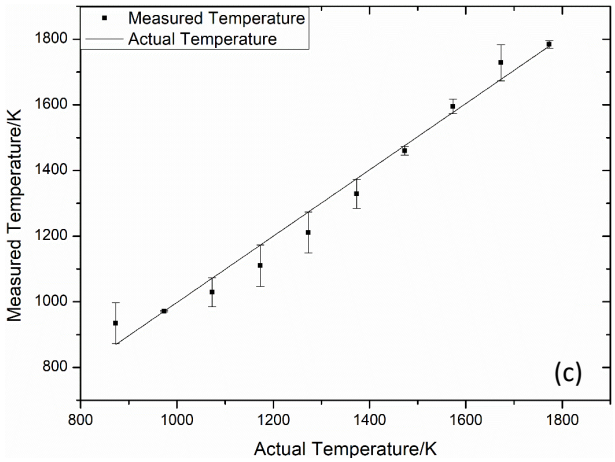

Figure 3.11 The comparisons between actual temperature with measured temperature calculated by different channel ratio in direct image case. (a) calculated by RG ratio; (b) calculated by RB ratio; and (c) calculated by GB ratio.

In the results shown in Fig.3.11 (a), the maximum error of 68K occurred at the actual temperature of 1273K, corresponding to a relative error of 5.3%. The average error of this case is 24.9K, with a relative error of 1.9% in the whole temperature range.

Regarding the results calculated by RG ratio (Fig.3.11 (b)), the maximum error in this case is 63K occurred in the actual temperature 1173K with a relative error of 5.4%, and the average error of the case is 37.9K with an average relative error 3.1%.

And, from the results of GB ratio (Fig.3.11 (c)), the maximum error is 127K in the actual temperature of 1273K with a relative error of 10.0%. And the average error in this case is 82.5K with an average relative error of 6.6%.

Thus, in the case of direct image case, the results from the RG ratio have the smallest error. However, due to its non-monotonicity, it can only be used when the approximate temperature range of the testing object is known. Comparatively, the RB ratio could be a better choice with a relatively low error and good monotonicity with temperature. The temperature can be speculated beyond 1500^{o}C by the method of extrapolation. From the

results if Figure.3.11, it can be seen the residual is relatively high, this is because the effect of the infrared leaking cannot be ignored, in order to eliminate this effect, the infrared cut off filter is used.

Similarly, the measured temperature is compared with the actual temperature in the case of IR cut off image case to analyse the error. The comparisons are shown in Fig.3.12.

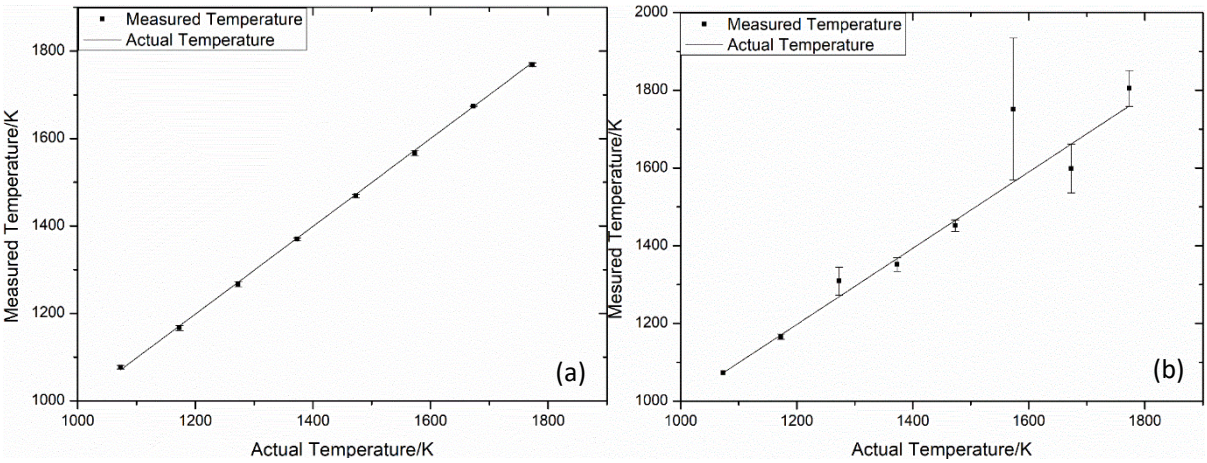

Figure 3.12 The comparisons between actual temperature with measured temperature calculated by different channel ratio in IR cut off image case. (a) calculated by RG ratio; and (b) calculated by GB ratio.

As shown in Fig. 3.12 (a), the error with RG ratio can be controlled under 10 K, the maximum error of 6K occurred around the actual temperature 1173K to 1273K, corresponding to a relative error of 0.5%. The average error of this case is 4.3K with a relative error of 0.3% in the whole temperature range. Similarly, the error with GB ratio is shown in Fig 3.12 (b), which has a maximum error of 176K in the actual temperature 1573K, with a relative error of 11.2%. The average error of this case is 45.1K, corresponding to a relative error of 2.9%. Compared to the error analysis from the direct image case with the IR cut off case, it can be concluded that the accuracy of temperature measurements can be significantly improved by

applying the IR cut off filter. In most situation, using the IR cut off filter and RG ratio will be the best choice for this study which has a temperature range from 800°C to 1500°C, and the higher temperature can be estimated by the interpolation. For the objective at a lower temperature than 800°C, the temperature measurement by direct image is more suitable, since the direct image can capture more radiation signal than the IR cut off image at a lower temperature. The RG ratio can be used if the approximate temperature range is known; otherwise using the RB ratio instead. In this study, the two colour method with the IR cut off filter will be applied to image burning wood rods. Based on the imaging results, the RG channels ratio will be utilised to estimate the temperature of the soot flame.

Furthermore, in order to analyse the influence on infrared radiation by the camera sensor, the intensity of pixel for the direct image was compared with those after applying the IR cut off filter. The results are shown in Fig.3.13 in actual value and percentage.

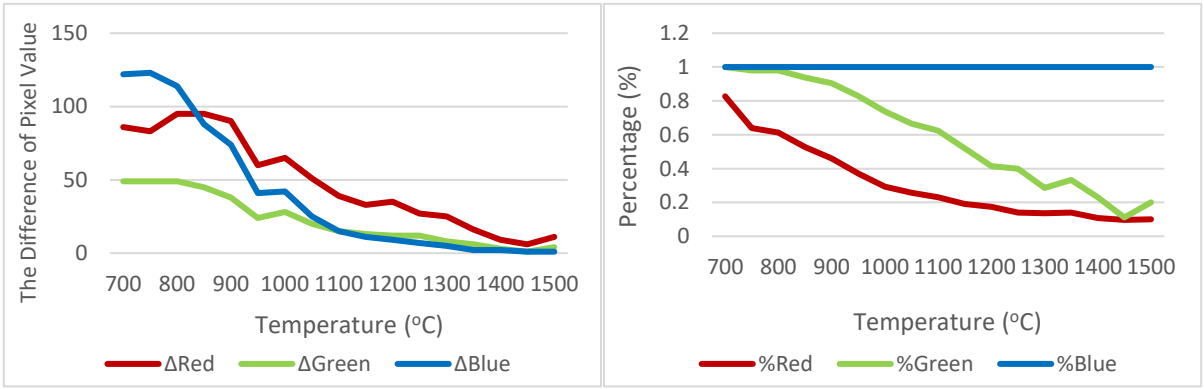

Figure 3.13 The value and percentage of infrared radiation effect in different channels. Left: pixel value against temperature; right: the percentage against temperature.

From Fig. 3.13, it can be seen that the infrared significantly affects the camera sensor at a low-temperature range such as 700 - 1000 degrees, then dropped fast when the temperature increased to 1100°C. Such trend can be explained by the black body radiation

curve, that the peak of radiation is in the infrared wavelength at the low-temperature range. With the increasing temperature, the peak of radiation moves into the visible light range, lower value of infrared would be emitted by the object. Besides, from the right panel of Fig.3.13, it is found the blue channel is most likely affected by the infrared radiation, followed by the green channel. This is because the G and B channel in the camera sensor is more sensitive to the infrared radiation, resulting in a higher pixel value increment in these two channels [106].

3.2.1.3. Testing cases

The calibrated optical pyrometer system was tested with a Bunsen Burner which is shown in Fig. 3.14. The methane was used as the fuel to test the flame temperature. The flow rate was controlled by a flowmeter whose maximum flow rate was 1.1 L/min. The flow rates were set as 0.4L/min, 0.6L/min and 0.8L/min. And the IR cut off filter was installed in the front of the camera lens and the ratio of RG channel was used to calculate the soot flame temperature.

Figure 3.14 The Bunsen burner used in the experiments.

The technique in this work is able to measure the temperature range from 853 ^{o}C to 1843 ^{o}C based on the camera dynamic range. A centre line is selected to show the temperature change with the different distance. The measured soot flame temperature is shown with its centre line temperature in the Figure 3.15. It can be seen from the Figure, the soot flame temperature range is from 870 ^{o}C to 1800 ^{o}C, and the temperature increased with the distance increased and reached the maximum when the fuel and oxidiser in the stoichiometry then decreased at its edge. In order to validate this technique is able to measure the soot flame temperature, the measured results are compared with the existed work in other literatures. The measured temperature range and its trend with the distance are well matched with the work from other researchers[107][108].

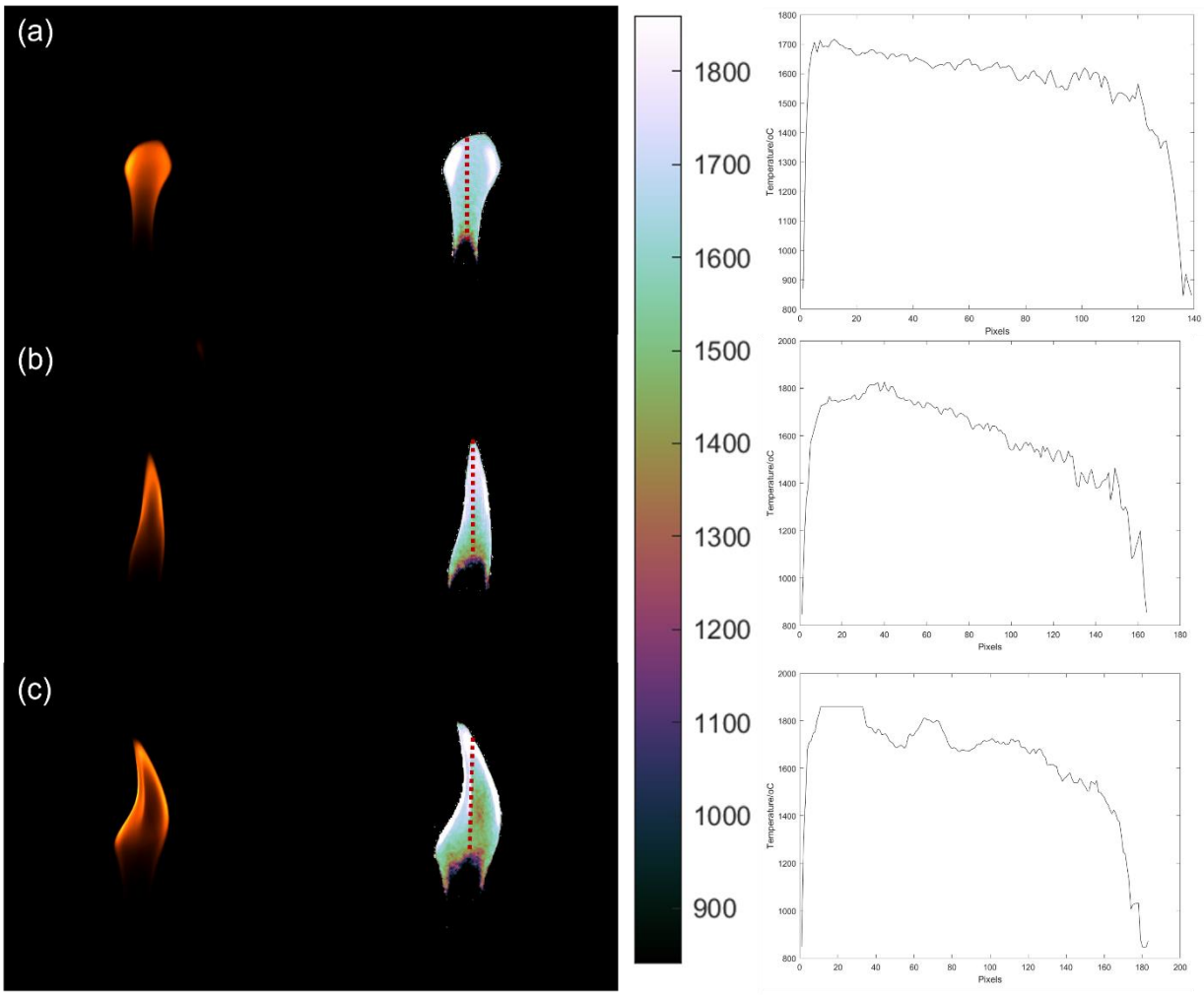

Figure 3.15 The flame temperature testing cases. Left: the flame image; middle: the temperature map; right: the centre line temperature. (a) represents methane flow rate 0.4L/min; (b) represents methane flow rate 0.6L/min; (c) represents methane flow rate 0.8L/min

3.2.2. Thermal imaging temperature measurement

As discussed in the previous section, the two colour method can be widely used based on its advantage when the emissivity of the object can be neglected. Alternatively, when the emissivity of the object is known, the temperature can be obtained by the radiation intensity of an object at one selected wavelength, according to Eq. 3.2 by the Planck law. The thermal

imaging system has a higher sensitivity than the colour imaging system especially in the low-temperature range, which means that the thermal imaging is more suitable for measuring the objective at a low temperature. In addition, as the fewer distractions of the thermal imaging system, it could usually get a smaller error. As well, the thermal imaging system was highly developed and widely used for temperature measuring in many fields, such as the industry of metal[109]–[111], semiconductor[112]–[115], and plastics[116], [117]. In this study, the Hamamatsu C12741-03 InGaAs camera is used for temperature measurement of burning wood surface. The fundamental of single wavelength temperature measurement was introduced in the section 3.2.2.1. As well the calibration procedures, including the size of source effect (SSE) and radiometric calibration, will be introduced. Then, the results of calibration will be presented in section 3.2.2.2. Before the end, the water droplet impacted on a burning wood will be used as the testing case to validate the applicability of the study in this thesis and shown in section 3.2.2.3.

3.2.2.1. Background of the thermal imaging temperature measurement

The fundamental of the thermal imaging temperature measurement is based on the calibration to a blackbody radiator which follows Planck's law. For a narrow band thermal imaging system, the most popular method for the calibration is based on the Sakuma Hattori equation[118], which is given by:

$$\boldsymbol{S_m(T) = \beta \cdot \varepsilon \cdot S_{S-H}(T)} \tag{3.14}$$

Where the $\boldsymbol{S_m(T)}$ is the measured signal intensity of any individual pixel at a certain temperature; $\boldsymbol{\beta}$ represents the transmission coefficient of the imaging system; $\boldsymbol{\varepsilon}$ is the

spectral emissivity of the measured object; and the $S_{S-H}(T)$ is the response model for a narrow band thermal device to a black body radiator, which is given by:

$$S_{S-H}(T) = \frac{C}{exp\left(\frac{C_2}{AT+B}\right)-1} \tag{3.15}$$

Where the C_2 is the second Planck's radiation constant; A, B and C represent the fitting coefficients which can be obtained by the calibration procedure with an ideal blackbody radiator. As assuming the transmission coefficient of this imaging system is constant, the transmission coefficient β can be cancelled under this condition. During the calibration process, the black body furnace which has an emissivity of 0.99 and is assumed as an ideal black body radiator. Therefore, the following equation is giving during the calibration process:

$$S_m(T) = S_{S-H}(T) \tag{3.16}$$

After calibrating the device, the temperature T can be obtained by combining the Eq. 3.14 and 3.15:

$$T = \frac{C_2 \, ln\left(\frac{C}{S_{S-H}(T)}\right)+1}{A} - B = \frac{C_2 \, ln\left(\frac{C \cdot \varepsilon}{S_m(T)}\right)+1}{A} - B \tag{3.17}$$

As the commercial thermal imaging device has a relatively poor Measurement Fields of View (MFOV)[119], and the Size of Source Effect (SSE) which indicates the sensitivity of the capturing radiation of the device relating to the radiator size[120], [121]. In this study, a size adjustable aperture is set in the front of the furnace to find out the minimum size of an object for a more accurate temperature measuring.

3.2.2.2. Calibration

The device utilised in this study for the thermal imaging metrology is the Hamamatsu C12741-03 InGaAs camera, which is shown in Fig. 3.16. For the properties, the camera has a resolution of 640 x 512, a frame rate of 60 and an output of 14-bit images. The used Thorlabs FEL1500

long-pass filter can be combined within the response range of the camera to form a suitable bandpass from 1550nm – 1670nm, shown in Fig. 3.17. The choice of this bandpass of wavelength is because of its high sensitivity to the temperature range of the measuring wood surface. In order to get a larger temperature measuring range for different cases, the two different exposure time of 16ms and 32ms are used to get low-temperature range and high-temperature range respectively. The black image was captured with the lens cap on to reduce the background noise.

Figure 3.16 The Hamamatsu C12741-03 InGaAs camera.

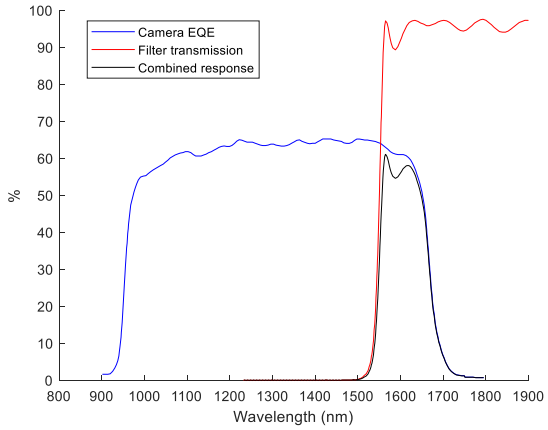

Figure 3.17 The bandpass of the camera and filter combination.

In order to find out the Size of Source Effect (SSE), an adjustable aperture was set in the front of the furnace, which is illustrated in Fig. 3.18. The signal in the central pixel was recorded by

the adjustable aperture with a changing aperture size, where the results are shown in Fig. 3.19. From the results, it is found that the signal intensity was increased sharply with increasing aperture size, then tended to be constant when the aperture was increased to 3 mm. Therefore, the 3 mm aperture was defined as the '100% signal'. The increased signal above '100% signal' was due to the glare of the imaging system, but it was under an acceptable range. Also, the 95% energy (red line) received at 1.42 mm aperture while the 90% energy (green line) at 0.92 mm of aperture. Therefore, it can be concluded that the measured hot object should be larger than 1.4 mm in order to get an accurate temperature result. In addition, the 3 mm aperture will be used during the radiometric calibration process.

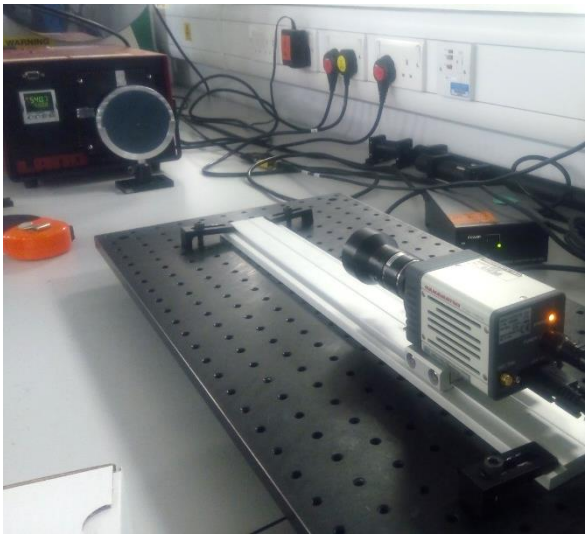

Figure 3.18 The illustration of the calibration setup.

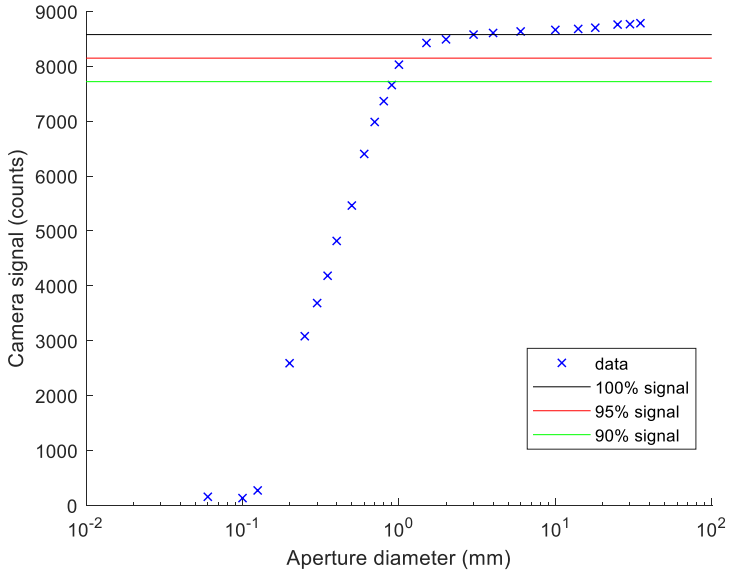

Figure 3.19 The size of source effect in the imaging system.

According to Eq. 3.15, the parameters of ***A***, ***B*** and ***C*** can be obtained in the calibration procedure. In this study, two different exposure time were set to match the different temperature range. In details, the exposure time was 16 ms for the temperature range 300°C to 750°C while 32ms for the temperature from 200°C to 550°C. The radiometric calibration result for the 16ms exposure time is shown in Fig. 3.20 below.

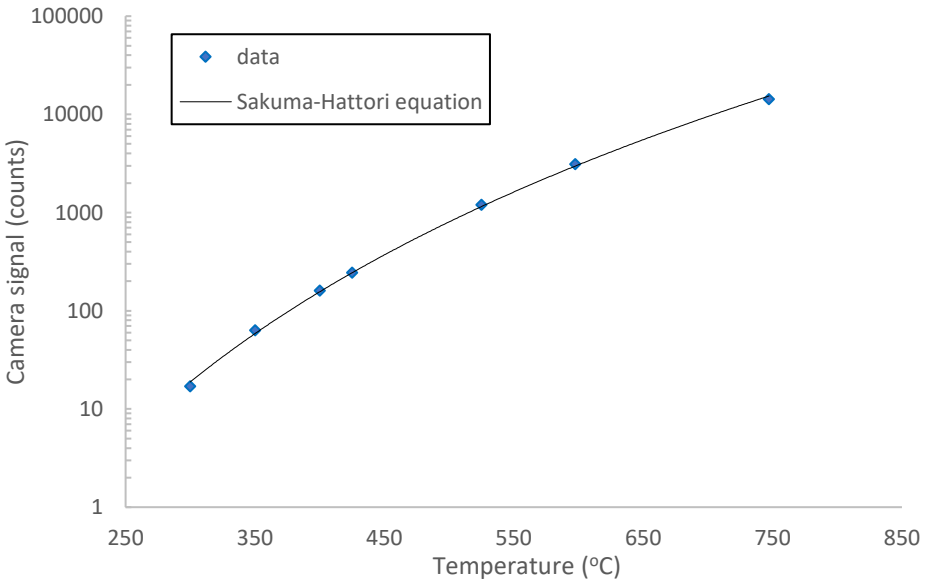

Figure 3.20 The radiometric calibration result using 16ms exposure time.

The results show a good fitting with the Sakuma-Hattori equation. From the calibration results, the fitting coefficients can be obtained as:

$$\boldsymbol{A} = 1.386 \times 10^{-6}$$

$$\boldsymbol{B} = 9.202 \times 10^{-5}$$

$$\boldsymbol{C} = 2.000 \times 10^{8}$$

Then, according to Eq. 3.17, the temperature can be calculated by the fitting curve. The imperfection of the results can be quantified by using the difference between the calculated temperature and the furnace temperature, which is shown in Fig.3.21 below:

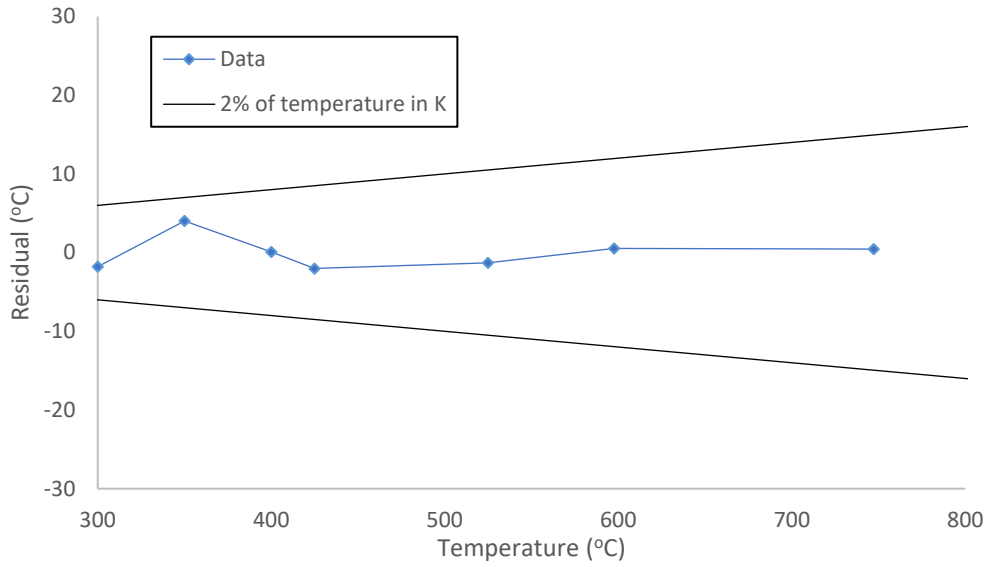

Figure 3.21 The residuals of the measured temperature in 16ms exposure time.

The uncertainly of the measuring results can be caused by many factors, including the spectral emissivity, the radiometry calibration process, the curve fitting, the optical transmission of the device and the noise of this imaging system. However, the residuals of temperature performed fairly good in this temperature range, and the maximum error was around 4°C at 350°C which. Overall, the residuals were under 2% (black lines) which was in an acceptable range.

The exposure time of 32ms was used for the radiometry calibration to read the lower temperature. The calibration temperature range was from 200°C to 550°C. Similarly, the results fitted with the Sakuma-Hattori equation are shown in Fig. 3.22 below.

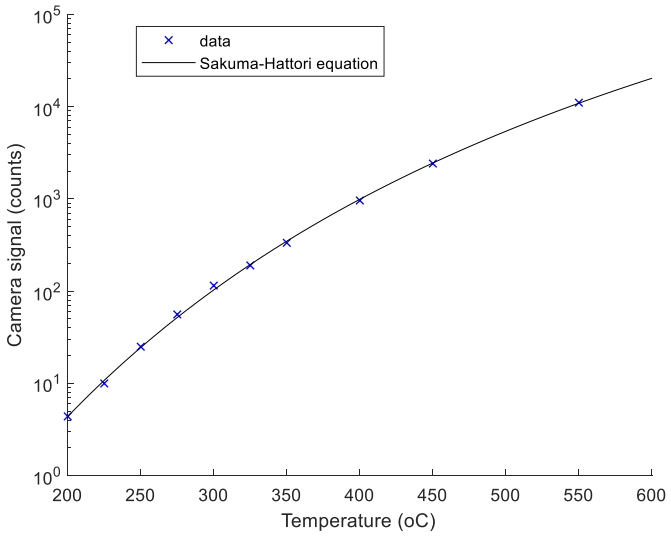

Figure 3.22 The radiometric calibration result using 32ms exposure time.

Also, the results show a good fitting with the Sakuma-Hattori equation, and the fitting coefficients can be calculated as:

$$\boldsymbol{A} = 1.498 \times 10^{-6}$$

$$\boldsymbol{B} = 4.556 \times 10^{-5}$$

$$\boldsymbol{C} = 8.391 \times 10^{8}$$

The temperature residuals by the 32ms exposure time can be obtained, which is shown in Fig. 3.23. The temperature residuals present that the maximum error was around 4.5°C at 300°C. In the temperature measuring range, the error was less than 2% of temperature.

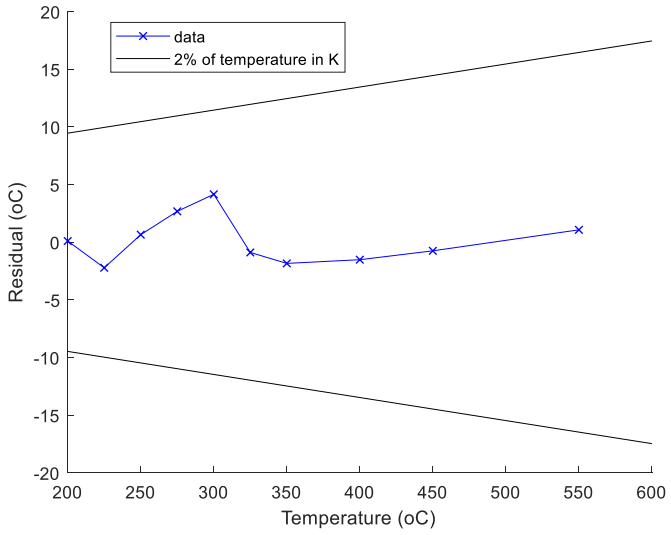

Figure 3.23 The residuals of the measured temperature in 32ms exposure time.

In this study, thermal imaging has been used for measuring the surface temperature of burning wooden rods, which will be presented in Chapter 5 and 6. In particular, the imaging system of exposure time 32 ms will be used in Chapter 5 in order to observe the heat pyrolysis process which will be at lower surface temperature. The imaging system with 16 ms exposure time will be used in Chapter 6 for quantitative analysis about the temperature change under the cross-wind.

3.2.2.3. Testing cases

The calibrated thermal imaging metrology with 32 ms exposure time was tested for measuring the temperature of the burning wood blocks. An injector which filled with water was set above the testing wooden block. When the testing sample was fully ignited, a water droplet will be injected and impacted on the surface of the burning wood. The process had been captured by the InGaAs thermal camera with 32ms exposure time and the calculated temperature is shown in the colour map in Fig. 3.24.

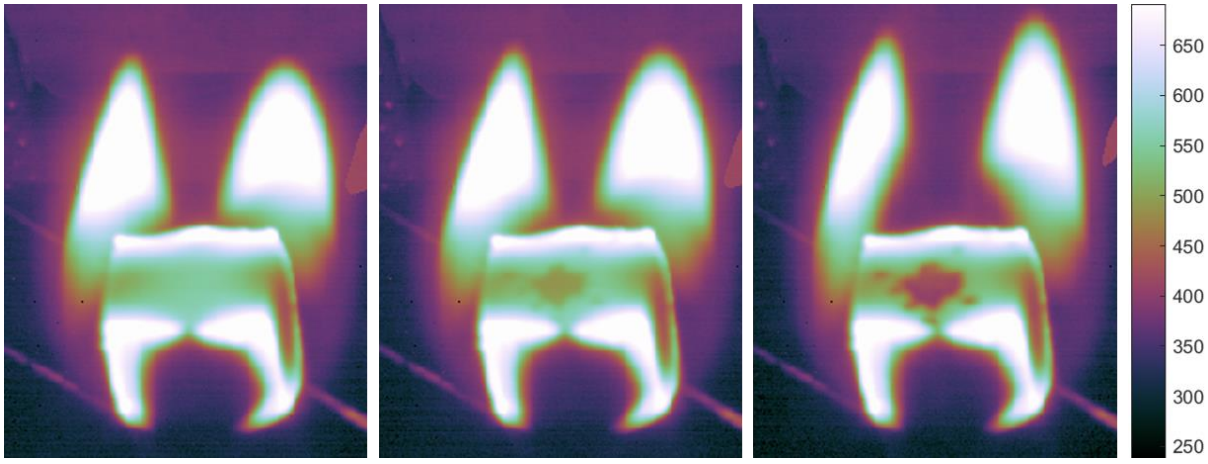

Figure 3.24 The 32ms exposure time testing case of burning wooden block impacted by a water droplet. Left: fully ignited. Middle: just impacted with the water droplet. Right: the moment after the impact of the water droplet.

Fig.3.24 illustrates the different moment of surface temperature distribution. The colour bar indicates the temperature range of the testing zone. The left image represents the moment before the water droplet impacted, the middle one indicates the water droplet just impacted on the surface and the right one represents the moment after the water droplet impacted.

It is found that in the middle of the wood surface, the temperature dropped when the water droplet impacted (middle image of Fig. 3.24) and then the temperature reducing area expanded (right image of Fig.3.24). Based on the calculated temperature map, it is determined that the calibrated thermal imaging system of 32 ms exposure time is able to measure the temperature in a low range, and it was sensitive to the temperature change even if the value is small.

The piloted ignition wooden rod was used for testing the calibrated thermal imaging system with 16 ms exposure time. The wooden rod was fully ignited by a Bunsen burner with the premixed fuel of methane-air. And then a cross-wind produced by the specifically designed fan system would be involved. The InGaAs thermal camera was used to capture the burning

process. The colour temperature map was plotted after data processing. An example is presented in Fig. 3.25.

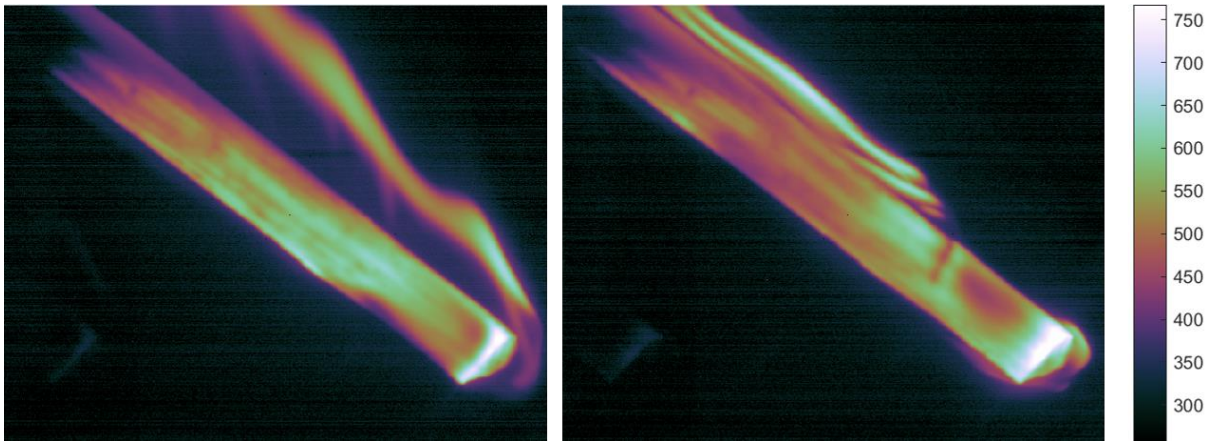

Figure 3.25 The 16ms exposure time testing case of burning wooden rod with/without cross-wind involvement. Left: fully ignited without the cross-wind. Right: the cross-wind involved.

It can be found the calibrated imaging system with 16ms exposure time matched the measuring temperature range well. Although a few areas at the rod end had overexposure, the whole image performed fairly good in the narrow bandpass of wavelength. In addition, the device could sensitively capture the temperature change due to the wind effect. Therefore, thermal imaging metrology could be suitable for the following analysis in the study.

3.3. Schlieren imaging system

Schlieren photography, as one of the most commonly used optical measurement method, has a wide range of applications in the fields involved with any density change upon transmitting media. It can be used to observe the boundary layer of airflow, combustion, and the convection in gas and flow field in tunnels. The basic principle of schlieren photography is based on the property that the refractive index gradient of light in the flow field is proportional to its density.

Schlieren photography was firstly introduced by the German physicist August Toepler in 1864 to study supersonic motion. In 1962, Bland and Pelick used the schlieren method to study the effect of water pressure and temperature and pointed out that the schlieren method could be applied to display the flow field of water tunnels[122]. In 1965, Holde and Norht used a white light splitter prism on a schlieren system to introduce the colour schlieren imaging, which expanded the application scope of schlieren technology[123]. In 1974, Merzkirch classified schlieren technology in the compressible flow field and classified the interferometric schlieren research on the schlieren system, including grating interferometry, prism interferometry and Moire fringe interferometry[124].

The Z-type schlieren imaging system could be easily established in the lab which is basically comprised of two parabolic mirrors, the light source, a knife-edge and the camera. The Schematic representation of the schlieren imaging system is shown in Fig. 3.26. The focal length of the parabolic mirrors was 3.048 m and the diameter of them was 0.3048 m. The light source was designed by a black box which has a Xenon lamp inside the box and a convex lens in the front of the box which is used to concentrate the light.

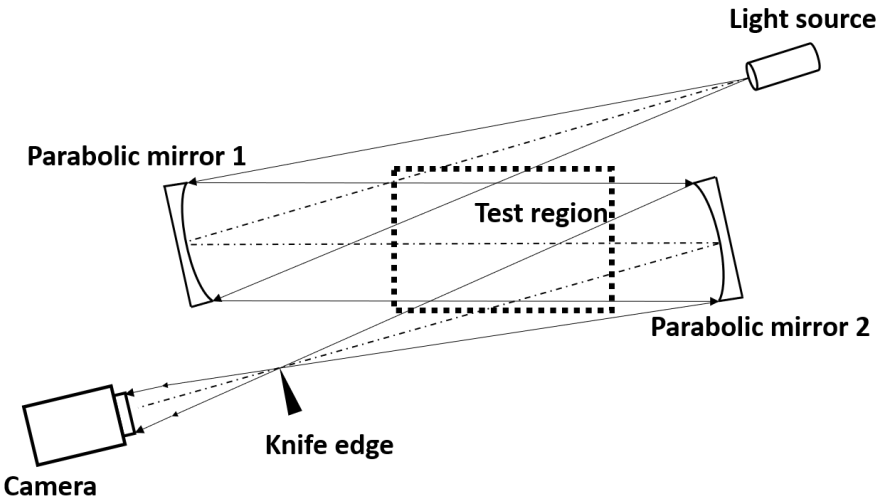

Figure 3.26 Schematic representation of the schlieren system.

In the study, the imaging system based on the schlieren system is shown in Fig. 3.26. This imaging system was synchronised with other imaging system and equipment, including the two colour optical pyrometer, the thermal imaging metrology and the wind diffuser, in order to achieve the various study purposes. An image of a burning wooden rod by the Schlieren system is presented in Fig. 3.27 as an example. The image of schlieren photography is effective to visualise the density change caused by the temperature variations. In Fig. 3.27, it can be seen that the flow field, which cannot be seen by human eyes, had been visualised, including the structure of the fire plume, the hot gas layer and the boundary between surrounding air and the hot gas layer. In this thesis, the Schlieren system was utilised to achieve the analyse of the fire plume in Chapter 4, the underneath convection in Chapter 5 and the effects on the heated gas-phase productions under cross-wind in Chapter 6.

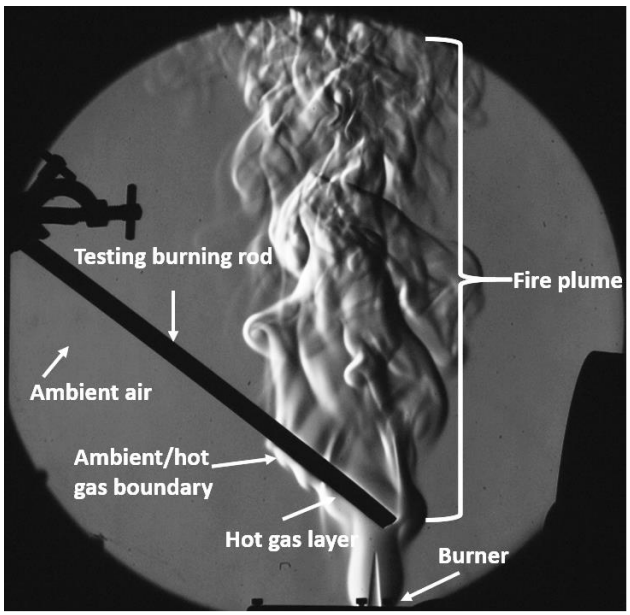

Figure 3.27 Example schlieren image of the burning wooden rod during the piloted ignition by a Bunsen burner.

3.4. Optical flow method for motion estimation

The motion of the flame or the hot gas flow is an important factor in the fire dynamic study. In this study, the optical flow method has been applied to estimate the velocity field of the flame on burning wood and the hot gas flow above the wooden rod.

Optical flow is a concept of object motion detection in the field of vision. It can be used to present the motion of an observed object, surface, or edge. The optical flow method is useful in pattern recognition, computer vision, and other image processing applications. It can be used for motion detection, image segmentation, calculation of collision time and object expansion, or three-dimensional measurement of surfaces and edges of objects[125].

The algorithm of optical flow is developed based on two hypotheses made by Lucas-Kanade: constant brightness hypothesis and near field optical flow similarity hypothesis[126].

It is assumed that the intensities of pixel keep constant between two frames. The assumption is reliable when the illumination condition does not change frequently. It is also assumed that all pixels in the near field have the same optical flow value. Generally, the movement direction and size of pixels in a small image area are basically the same. Therefore, this assumption is also reasonable.

In this study, the optical flow method has been used to estimate the flame edge velocity on the burning wood with the direct images since the flame edge can be seems as continue moving when captured with high frame rate, as well the velocity of hot flow in the fire plume with the schlieren images in Chapter 4. After analysing the various matrix of the processed results, the threshold was set to cut the velocity <0.01mm/s to avoid the background noise and the velocity >2mm/s to cut off the abnormal pixel value in both velocities of the flame

edge and the hot flow. It should be explained that, in order to present the velocity distribution, the results of velocity are shown in normalised percentage instead of the direct pixel numbers. Since the flame or fire plume size varied between the experimental sets, the normalised percentage result was more precise to present the velocity distributions. In addition, due to the weak fluctuation (low-velocity zone <0.1mm/s in the field which is nonsignificant) was accounted for a large proportion to the velocity field, the higher velocity range (>0.1mm/s) has been chosen to present the histogram results in order to better visualise the effect of different experimental parameters on the distribution of flow velocity, such as the inclination angles and the diameters of the rod.

4. The effects of the inclined angle and the diameter of wooden rod on the fire plume

4.1. Introduction

The flame propagation rate of a burning rod, as one of the most important properties, is dependent on various factors including inclined angle, oxygen concentration and moisture content. Among those, the inclined angle of the wood surface could be the dominant factor that affects the flame propagating rate. From Moodie's study in 1992 [127], it is found that the inclined angle of 30° on the wooden escalator strongly enhanced the fire spreading which resulted in the disaster of King's Cross fire. Meanwhile, according to Drysdale's investigation for the flame spread rate on inclined surfaces by using the PMMA slabs, it was found that the flame spread rate could be significantly increased by the side walls [128]. Furthermore, as a new visualization method, the characteristics of the fire plume on an inclined surface was visualised and analysed by using a Schlieren system in Wu's study [71]. From his results, it was observed that there was a critical angle of 24° at where the flame attachment length started to increase sharply in a broad range of inclined angles. Zhang et al. investigated the deceleration of downward flame propagation and determined that the critical angle of fire extinguish was -45°. As well the fire spread rate on the upslope surface in a combustion chamber was measured, he had established an empirical formula to predict the extinction of fire at critical angles [129][130]. Zhou burned single species fuel bed in a metal platform with the side walls mounted at different angles to study if the fires could propagate successfully in certain angles and had highlighted the angle range of the cases with successful fire spread [131]. By using the retroreflective shadowgraph technique, the flame attachments of uphill

flames were qualitatively analysed by Grumstrup et al. [132]. In 2017, Yang et al. [133] studied the flame geometry along the inclined surface by using the grey scale image. It was found that the flame length was increased with the increasing inclination angle at lower angle. From the above literatures, it has been demonstrated that the visualisation analysis is an effective method to investigate the flame dynamics around an inclined surface. However, there is few of publications focusing on the study of inclined-surface-burning with visualisation analysis.

As a new study, the fire plume properties of a single wood rod under various inclination angles are investigated by multiple imaging systems, including a high-speed colour imaging system, a high-speed Schlieren imaging system and the optical flow method. As a great advantage, the Schlieren imaging system can be utilised to visualise the ambient flow field which cannot be observed by direct imaging. Furthermore, the wood rods used in this study can be easily controlled under certain experimental conditions, which could be effective for observing the mechanisms of diameter and inclination effects on the wood burning properties. In this study, a sequence of oak wood rods with different diameters has been ignited at various angles to investigate the effects of inclined angles on fire propagation rate and burning lifetime. A high-speed imaging system with a CMOS camera has been used to capture the direct images of burning rods, as well a Schlieren system has been utilised for visualising the fire-induced flow around the wood rods. In addition, the optical flow method was used for estimating the flame edge velocity as well as the velocity of hot flow above the burning rod.

4.2. Experiments and Methods

4.2.1. Experimental setup

Wood Type	Preconditioning	Length (mm)	Diameter (mm)
Natural Oak	Cylinders shaping	400	6
			7
			8
	Pre-dried for 24h at 150 °C		9
			10
			11
			12

Table 4.1 The properties of the experimental sample

In this study, the oak wood rods of a broad range of diameters have been tested, including 6 mm, 7 mm, 8 mm, 9 mm, 10 mm, 11 mm and 12 mm. The diameters that used in this work were considered from two aspects: firstly, this study needed the fuel surface had enough width to supply the confinement of air entrainment; secondly, one dimension fire propagation is preferred in this work, therefore, the sample should be able to seems as a single element. The properties of the samples are shown in Table.4.1. In order to minimise the effects of cylinder length on flame propagations, all testing samples had been cut into the same length of 400 mm. Before the ignition, the wooden samples had been pre-dried in an electrically controlled furnace for 24 hours at the temperature of 150 °C to neglect the moisture effect.

Diameter (mm)	Inclination angles (°)	Diameter (mm)	Inclination angles (°)
6	-30	12	-30
7			0
8	0		15
9			30
10	30		45
11			60

Table 4.2 The properties of the experimental sample

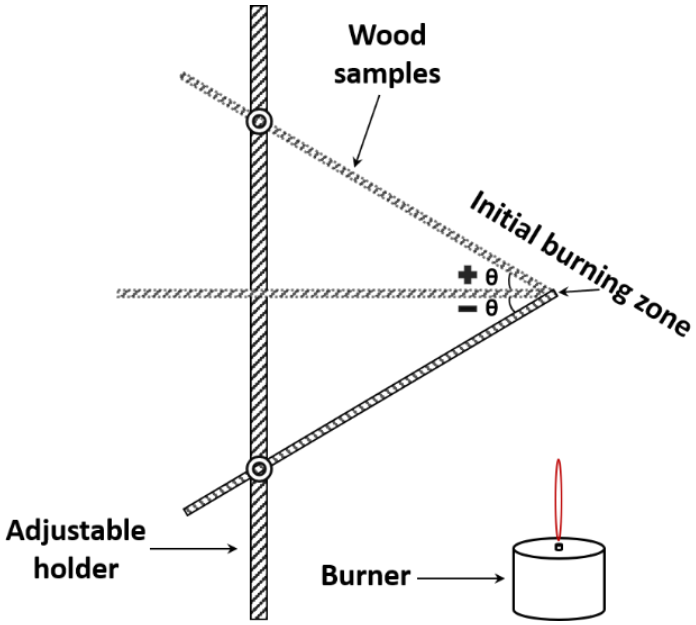

Figure 4.1 Schematic representation of the experimental set-up.

The samples were held above the burner by an adjustable holder at various inclined angles, which is shown in Fig. 4.1. The angle $\boldsymbol{\theta}$ indicates the inclined angle between the rod and horizontal direction. The positive $\boldsymbol{\theta}$ value was used to indicate the downward fire propagation, whereas the negative value indicates the upward direction. The rods of each diameter have been tested to investigate the diameter effects on the combustion properties, including the burning lifetime, the flame propagation rate, the flame attachment, and the fire plume attachment. Furthermore, in order to investigate the inclination effects, the rod of each diameter was tested at different inclined angles, including -15°, 0° and 15°. Considering the 12 mm diameter case performed most stable combustion (longest burning lifetime, strongest flaming and smallest flame propagation speed), the group of 12 mm diameter samples was further tested at six different angles, including -30°, 0°, 15°, 30°, 45°, and 60°, to observe more

details of rod combustion at various inclined angles. The details of experimental objectives are shown in Table.4.2. All cases had been repeated at least 10 times to ensure repeatability, and the results utilised for calculations were averaged values.

For the ignition heat source, a pre-mixed methane and air gas flow was used to ignite the samples. The properties of the premix fuel are shown in Table 4.3. The burner was immediately turned off once the sample was ignited for 20s.

Fuel	Flow rate (L/min)	Equivalence ratio	Ignition time (s)
Methane	0.35	0.612	20
Compressed Air	1.5		

Table 4.3 The properties of the premix fuel

The equivalence ratio $\boldsymbol{\varphi}$ is defined as the ratio of actual fuel/air ratio to the stoichiometric fuel/air ratio, it can be used to estimate the premix combustion status. The equivalence ratio of the premix fuel in this study can be calculated by the equation 4.1 showed below:

$$\boldsymbol{\varphi} = \frac{\boldsymbol{fuel-to-oxidiser\ ratio}}{(\boldsymbol{fuel-to-oxidiser\ ratio})_{\boldsymbol{st}}} = \frac{\boldsymbol{m_{CH_4}/m_{O^2}}}{(\boldsymbol{m_{CH_4}/m_{O^2}})_{\boldsymbol{st}}} = \mathbf{0.612} \qquad (4.1)$$

4.2.2. Imaging system

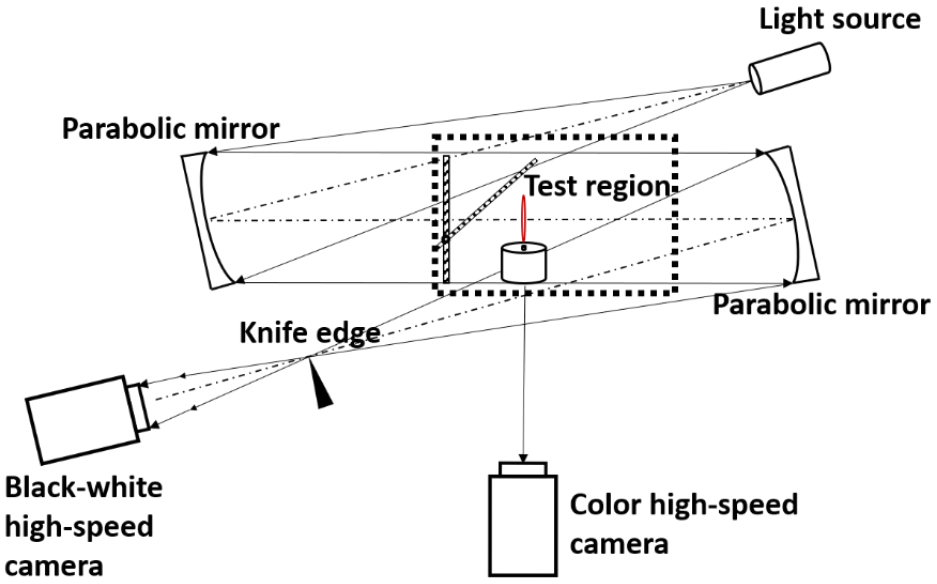

Figure 4.2 The Setup of imaging systems.

A Photron SA-4 high-speed CMOS camera was set in the front of the testing zone to capture the images of burning rods. The camera setting used the aperture of F2.8 and 50 framerates. Furthermore, a black-white high-speed camera was set for the Schlieren imaging system to capture the heated flow during the burning, as shown in Fig.4.2. The schlieren system can be used to observe the ambient flow field around the objects which cannot be seen by the actual imaging system. As well the schlieren imaging system has a high sensitivity which could use into analysing the effect of different diameter wooden rods. In addition, the high-speed colour imaging system can be applied to clearly present the burning status for determining the burning properties. Both imaging systems were synchronised by the frame step, the position

and the size.

4.2.3. Data processing

The burning lifetime and the charring rate were calculated to determine the actual flame properties. The burning lifetime was determined from burning duration, since the self-sustained burning start (ignited by 20s) until flame extinguishment. Meanwhile, the propagation rates of surface charring were calculated to represent the fire propagation rates. The burning images were presented at three different time points: the first 10s of self-sustained burning, the middle-aged of burning and extinguishment (for the 30 degrees inclination, used the 142.5S as the third time point). All the experiments were repeated at least ten times, and the results were averaged. Considering that the charring rates at 30^{o} inclined angle are highest, and it is meaningful to investigate the detailed charring rate for this condition. The detailed charring rates at 30^{o} inclined rods of different diameters were calculated by setting the ten equidistance points when the self-sustained burning began and compared.

The fire plume can be observed from the schlieren images. Due to the fire plume was fluctuated during the burning, the flow attachment phenomenon cannot be quantitatively analysed. In order to analyse the aerodynamics effect on fire propagation. The study focused on the visualisation of the flame and the flow attachment phenomenon. The flow tilt angle was shown as the angle between the wood surface and the middle of the main flow stream. The quantitative flame attachment results will be calculated and presented in the next section, Chapter 5, by a thermal camera.

The optical flow method was used to calculate the velocities of both flame and flow in the

study. The given threshold was used to cancel the background noise. In detail, the regions of flame velocity < 0.01 mm/s and > 2mm/s were cut off to avoid the tiny background noise and the unnormal point. After data processing, the velocity ranged from 0.1mm/s to 2mm/s was presented in the histogram to count the flame edge velocity of the high-velocity zone at different inclination angles. The reason that selecting this velocity range is because only the high-velocity zone is worth notice in the study, the velocity zone which is less than 0.1mm/s was ignored and meaningless. Due to the flame size varied at different inclination angles, the normalised histogram figure could be able to show the percentage of the pixels which had the high velocity. On the contrary, using the direct pixel number cannot present the phenomenon precisely. Similarly, for the calculations based on Schlieren images, the flow velocity was set at the threshold > 0.01 mm/s to avoid background noise. And the histogram shows the velocity ranged from 0.1mm/s to 1mm/s to present the distribution of the turbulent flow at different conditions.

4.3. Results and Discussion

In this section, the results of burning rods at different inclination angles with various rod diameters will be analysed and discussed. In order to visualise the flow field of the burning rod, both the imaging results, including direct images and schlieren images were compared in section 4.3.1; based on the direct images at different timing points, the results of burning lifetime and charring rate will be presented in the section 4.3.2; in the section 4.3.3, the flame attachment phenomenon will be illustrated and demonstrated by the direct images of the burning rods which were respectively ignited from the end and the middle position; further,

the observed attachment phenomenon for the burning rods of different diameters at varied inclined angles will be presented in the section 4.3.4 with the schlieren images; After applying the optical flow method, the flame velocity distribution and the hot gas flow velocity distribution have been calculated to obtain the inclination angle effects on surrounding flow field, they will be discussed in the section 4.3.5 and 4.3.6 respectively.

4.3.1. The fire plume at the beginning of self-sustained burning

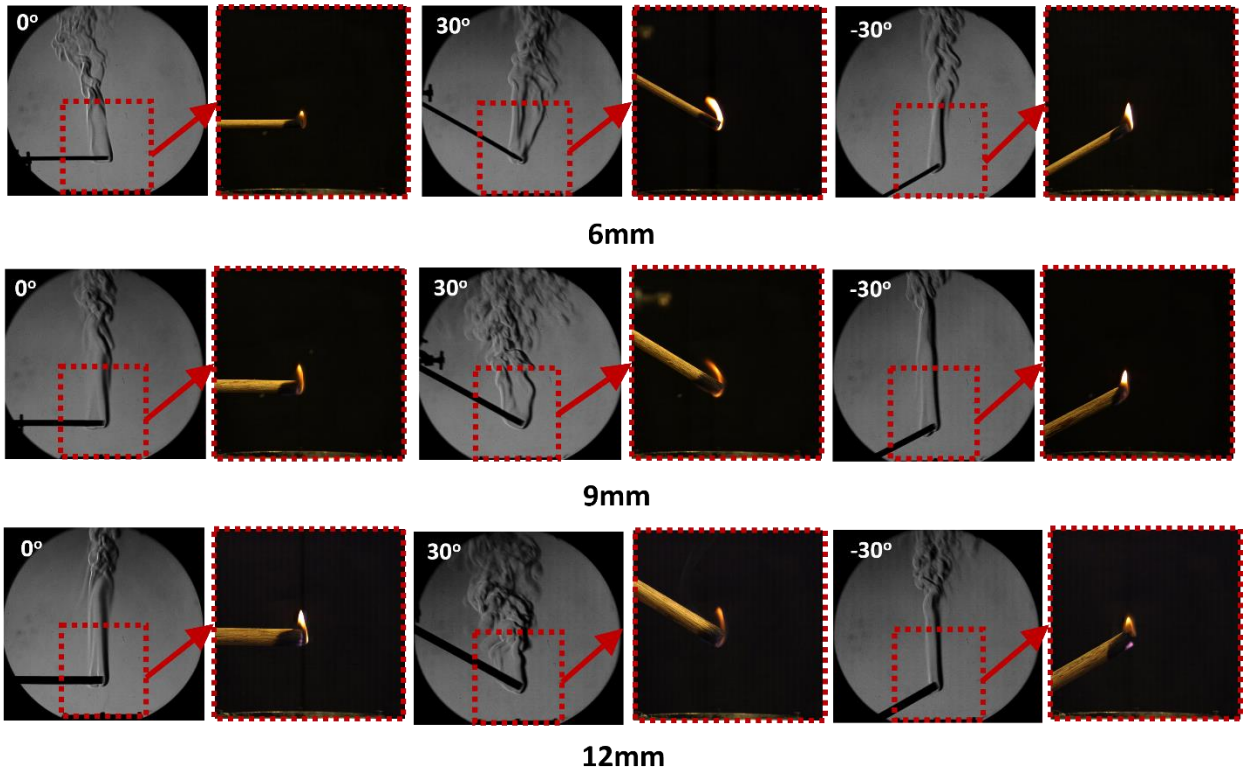

Figure 4.3 The comparison between direct imaging and schlieren imaging at the same time of the wood just ignited.

The comparisons between actual flame images and schlieren images are presented in Fig. 4.3. The schlieren images were synchronised with the actual images at the same time by selecting the reference timing as the burner just turner off. On one hand, the red-dotted frames in direct images illustrate the testing area of the actual flame. The visible images show the actual

flame which indicates the intensity of burning. On another hand, the schlieren images present the surrounding heated flow of the burning woods which contained the burnt gas and the air entrainment. The fire plume above the burning surfaces contained both the actual flame and the buoyant flow. It can be seen that there was no sharp distinction between different cases in the actual images, and the flames were weak at the beginning of the burning. Comparatively, it can be seen that the schlieren imaging system was able to efficiently visualise the fire heated flow around rods. From the results, it can be observed that the ambient flows of the rods at positive angles were much wider than those at the horizontal direction and negative angles. One of the possible mechanisms can be found as more convective heat transfer in positive-inclined-angle-groups due to the larger amount of gas-phase combustion products. In addition, it is worth noting that the flow of positive-inclined-angle-group trended to be more turbulent. The turbulent ambient flow could improve the mixing between the reaction zone and the ambient air. The diffusion flame generated from burning wood performed higher intensity at positive inclination angles by a higher mixing rate of combustible gases and oxygen. The flow velocity will be calculated and analysed in the later section. In addition, since the larger amount of smoke observed from positive-inclined groups, the possible reason can be found that more soot produced in the positive-angle-groups which means higher intensity wood combustion occurred. Although no significant difference among the flames can be observed by direct imaging, the visualisation by the Schlieren system is able to effectively present the effects of the inclined angle and the diameters on the flow around burning rods.

4.3.2. The properties of flame spread

The flame spread speed on burning rods has been determined by the direct image results. The comparisons among the burning status of different diameters and inclinations are presented in Fig.4.4, including the rod diameters of 6 mm, 9 mm and 12 mm, and the inclined angle ranged from -30° to 30°. In Fig. 4.4, three images in each horizontal frame were ranged in the sequence of burning periods, including the beginning of self-sustained burning, the middle-aged flaming and the extinguishment (142.5s in 30^{o} group), whereas the results in vertical direction indicate the different inclined angles of 0°, 30° and -30°. It is found that the burning at 30° had the highest intensity and longest lifetime, which could keep burning until the fire spread through the whole wood. Furthermore, the flame attachment phenomenon could be clearly observed in the positive angle groups, that the flame tilted towards to the unburned surface due to the dynamic effect created by the decreased air entrainment into the fire plume [128]. Comparatively, the cases burning at negative angles were weaker and the flame rarely spread along the rods. Also, the spreading distances of flame were shorter than in other cases. The fire always extinguished in a short period after a slow and short propagation. Comparing the sample of different diameters in positive 30^{o} case, it had been calculated that the 6mm diameter sample had the longest charring distance (77mm) after 142.5s of burning, followed by 9mm (66 mm in charring distance). The 12mm sample had the shortest charring distance of 47 mm, which means the fire on a larger diameter sample would have a lower propagation rate.

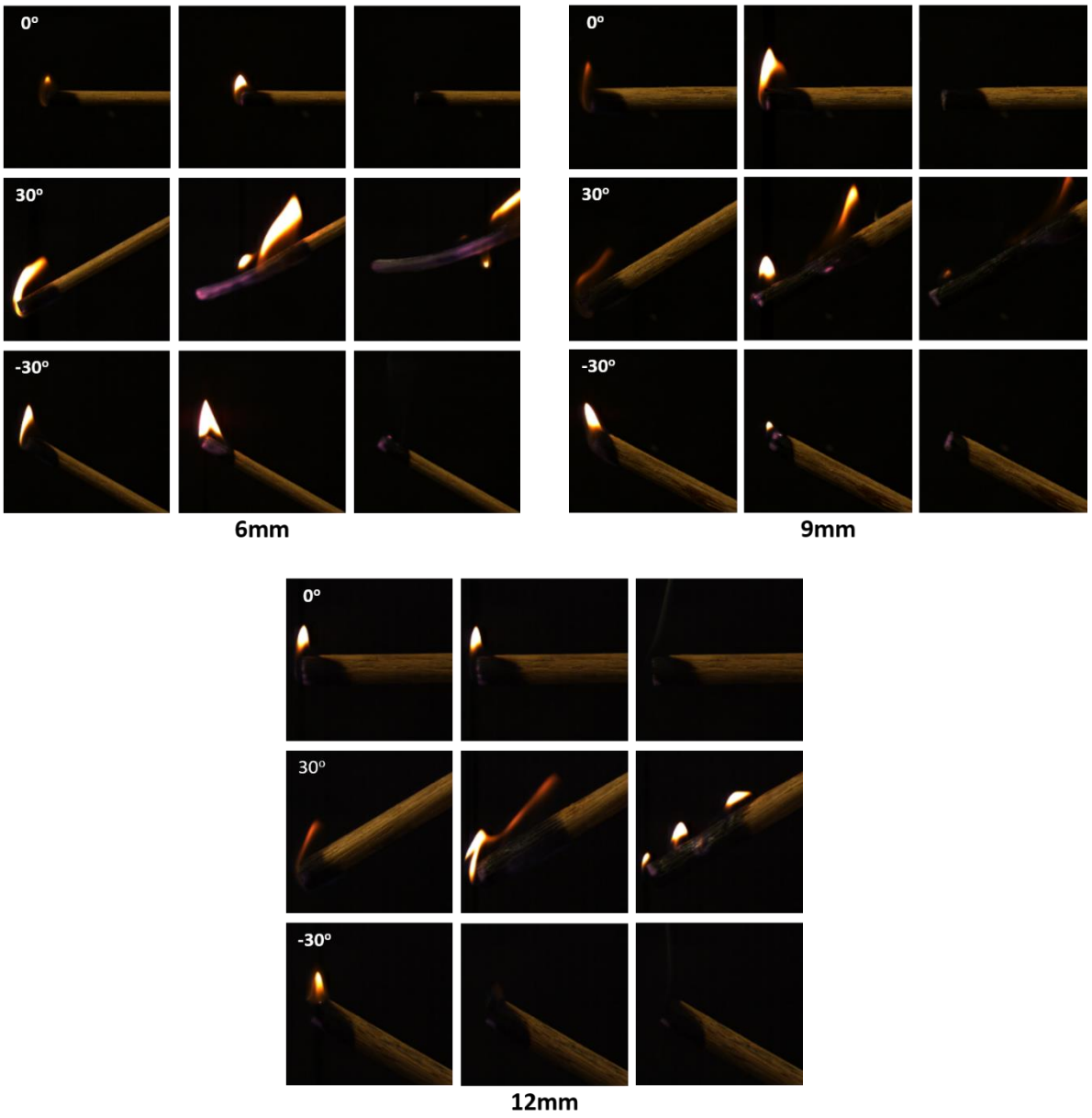

Figure 4.4 The actual burning images of different diameter woods at different inclinations.

The results of the self-sustained burning lifetime of the rods at 0° and -30° are shown in Fig. 4.5. It must be highlighted that the burning time of the rods at 30° was much greater than other cases, which had exceeded 160s as the doubled maximum value of the results of 0° and could keep burning until the fire spread through the whole woods. Comparing the cases of 0° and -30°, it can be seen that the horizontal rods had a longer burning time than the negative ones, averagely about 23.1% longer. Meanwhile, the burning status of the 0° group also was

more stable, that the flame could be easily extinguished on the negative inclined rods. For the effect of rod diameters, it is found that the larger-diameter-group generally could be burnt with a longer lifetime. The combustion was stronger, and the flaming was more stable as well. The surface charring rates in different experimental conditions are presented in Fig.4.6. It is found that the charring rate of 30^{o}-angle-groups reached the largest value up to 0.7 mm/s, whereas the charring rates of the horizontal and negative angle groups were smaller, as 0.23mm/s and 0.18mm/s respectively. For the effects of rod diameter on the charring rate, it is found that the charring rate is decreased with the increasing diameter. The charring rate in 30^{o} groups had a significant decrease from 0.67mm/s to 0.30mm/s with the increased diameters from 7mm to 12mm, decreased by 55%. Moreover, the surface to volume ratio can be calculated by setting a unit length of the sample, and the ratio is presented in the Figure with a black-dotted line showed in Fig.4.6.

As the very similar trending of surface-to-volume ratio comparing for the cases of different diameter and inclinations, a possible mechanism of such effect can be found that the smaller diameter rod sample had a higher surface to volume ratio which means higher efficiency in burning and fire propagation.

Moreover, the time-dependent charring rates were calculated from the beginning of the self-sustained burning at the 30^{o} inclination angle as an example. The results were obtained by calculating the charring rate in every 5 mm charring distance, showed in Fig.4.7. It can be seen that the charring rate was decreased with the increasing diameter of the rod. In addition, the fire propagation tended to be slower with the burning processing in all cases of three diameters. The reason for such phenomenon is that the uniform natural wood fibre caused

the formation of char which could obstruct the combustible gases escape from the wood surface. Lower concentration of produced combustible gases would decrease the following pyrolysis. With more char forming in the wood surface, the gas-phase combustion became weak, eventually extinguish if the rods have sufficient length.

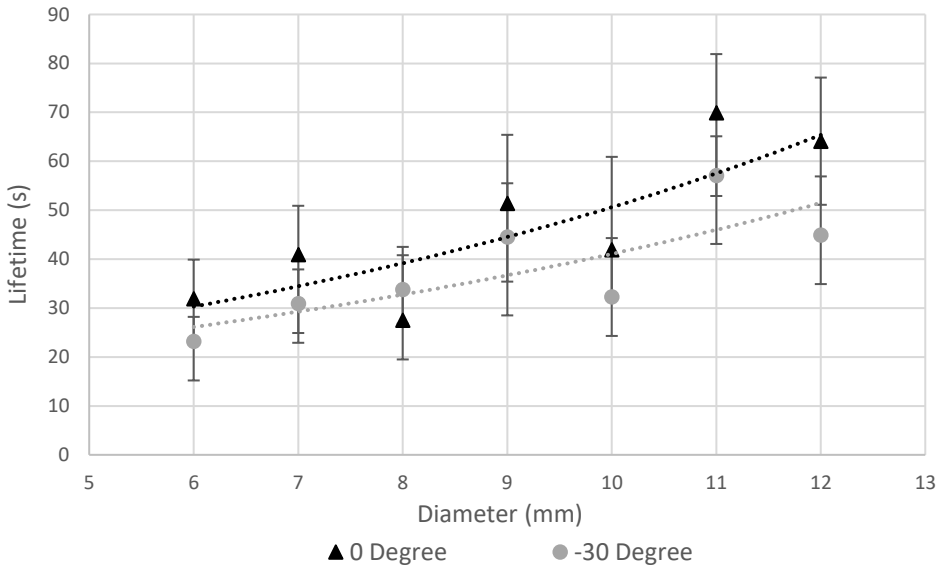

Figure 4.5 The Burning lifetime of different diameters burning wood at 0 degrees and -30 degrees.

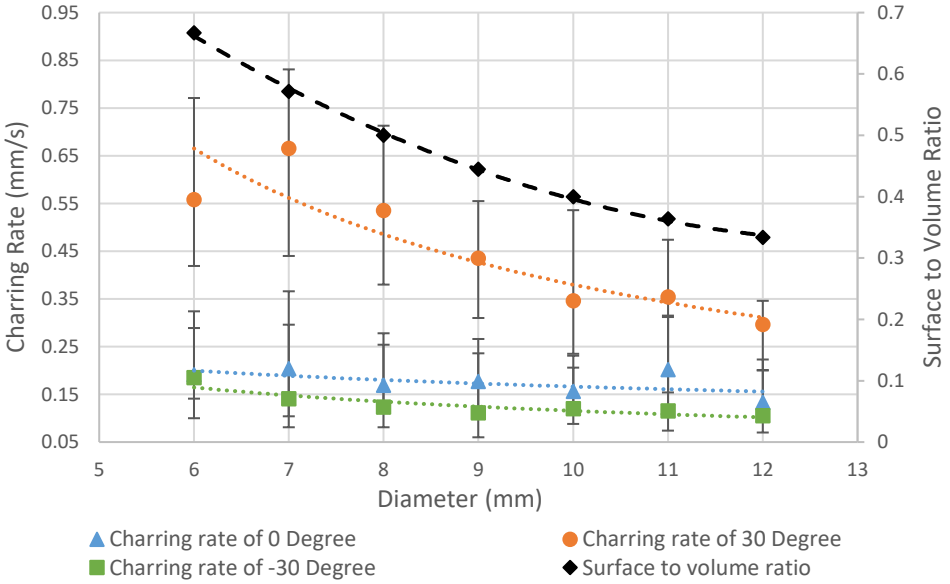

Figure 4.6 The averaged charring rate and surface to volume ratio of different diameters of wooden samples at different inclination angles.

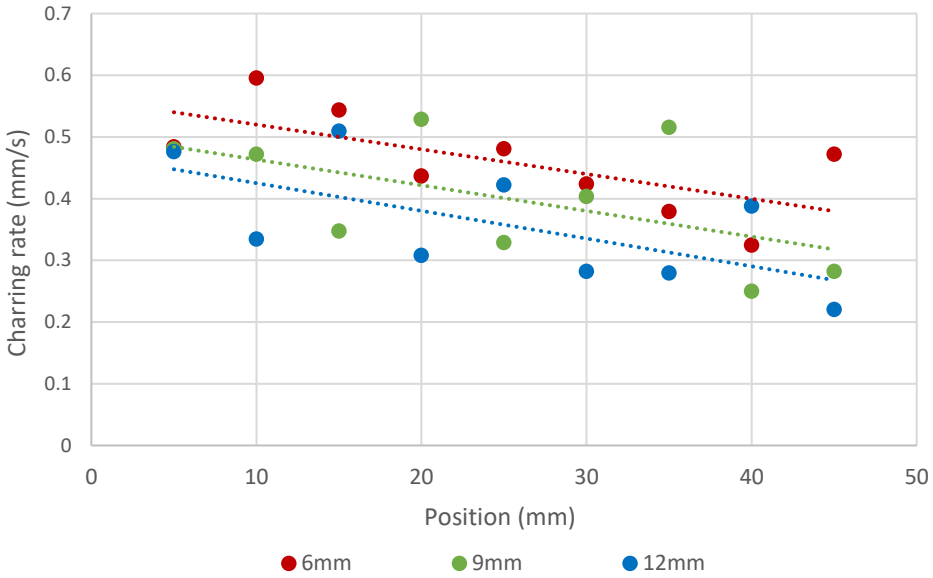

Figure 4.7 An example of the real-time charring rate at 30^{o} inclination angle at different diameter rods at the beginning of self-sustained burning.

4.3.3. The flame attachment phenomenon

In order to illustrate the flame attachment phenomenon more clearly, the wood rods of different diameters had been burned from the middle point of the rod. The flaming at different timing is shown in Fig. 4.8, including the cases of 6mm, 9mm and 12mm in diameter and 0° and 30° of inclinations. It can be observed that the flame on the horizontal wood was smaller than which at 30 degrees. Moreover, the flame burned toward to the vertical direction. On the contrary, the flame burned at 30 degrees bend to the unburned wooden surface, namely, flame attachment. It must be highlighted that the flame tended to propagate in the upward direction which can be found in the second lines of the Figures, such phenomenon is attributed to the effect of buoyancy. The flame attachment phenomenon strongly enhanced the fire propagation and the flame intensity, since more

adjacent unburned wood was taken part in the reaction and the shorter distance between the flame and fuel increased the radiation heat transfer. As the result, the burning rods at 30 inclination angles had a longer lifetime than which at horizontal, the charring rate was higher as well.

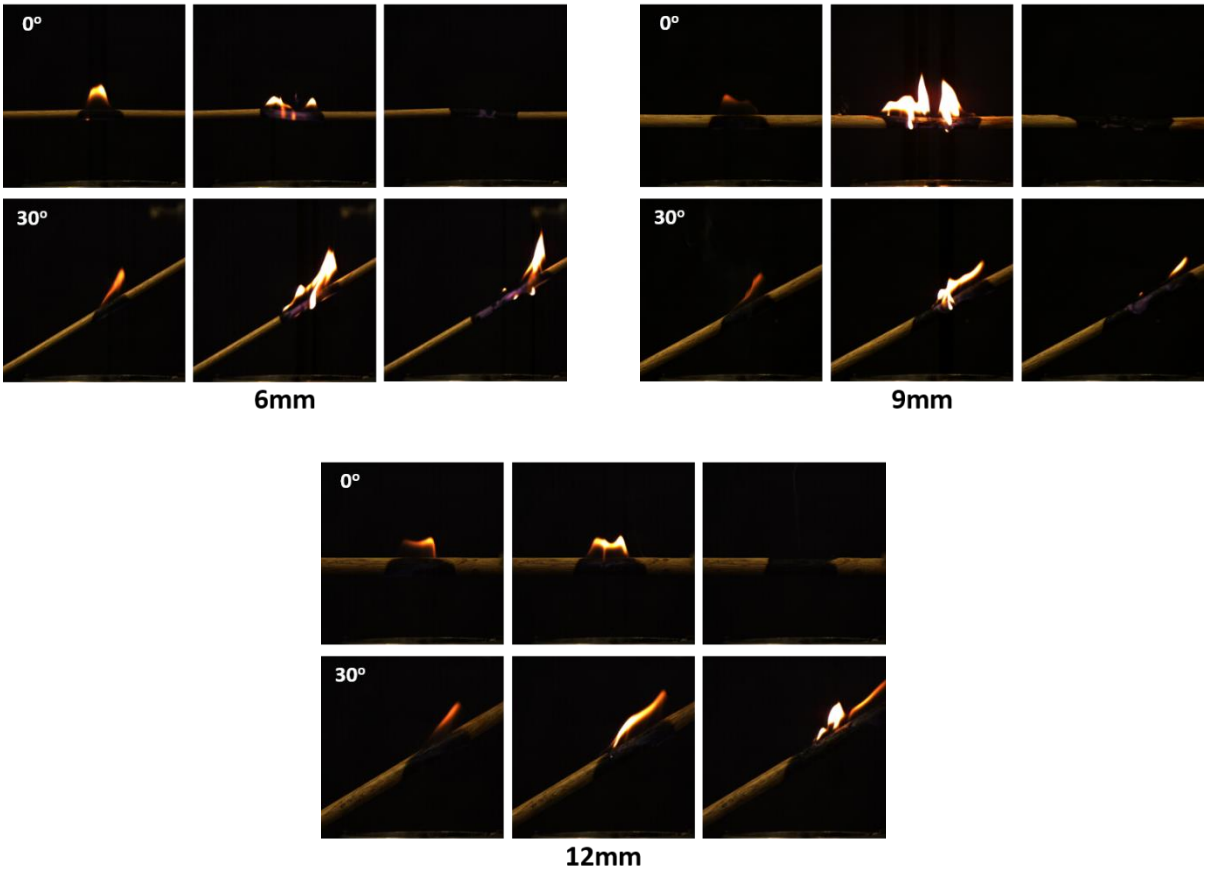

Figure 4.8 The actual flame images of different diameters of wooden rods burned from the middle at different timing and inclination angles.

The mechanism of the flame attachment is illustrated in Fig.4.9, Fig.4.10 and Fig.4.11. As shown in Fig. 4.9, it can be seen that the fire plume is contained by three parts, namely, persistent flame, intermittent flame and buoyant plume. The persistent flame is the zone under steady reaction. The intermittent flame presents the outline of the diffusion flame

which is under exchanging of combustion products with ambient air. The intermittent flame fluctuates and its shape changes. The buoyant plume is contained by the burnt gas of the combustion process, the heated flow and the ambient air. With the help of air entrainment, the ambient air continually replenishes from both sides of the fire plume. It can be observed that the air entrained into the fire plume are from both sides of the fire plume, which keeps the pressure balance.

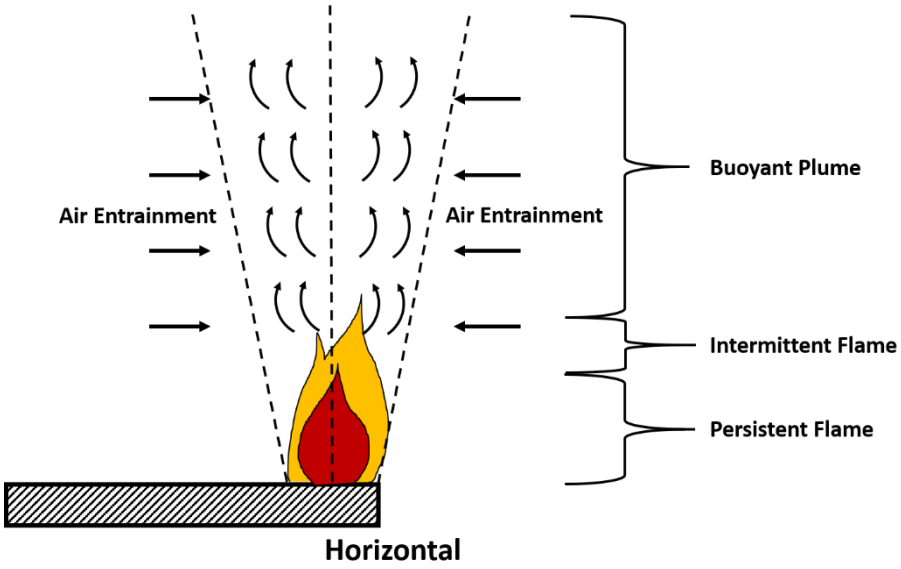

Figure 4.9 The demonstration of fire plume and surrounding air flow burned at horizontal direction.

When the fire plume is generated at an inclination fuel surface, however, the air entrainment is confined by the inclined surface, shown in Fig.4.10 and Fig.4.11. From Fig.4.10, it can be seen that a low-pressure zone has been formed between the flame and the fuel due to the confinement on the one-side air entrainment. As the result, the fire plume bends into the unburned wooden surface. Similarly, after the fire spread at a certain distance downwards, the local imbalanced pressure triggers the fire plume to bend into the burnt wooden surface,

which is illustrated in Fig.4.11. The attachment phenomenon enhances the fire propagation at positive inclination angles, however, decreases the fire spread at negative inclinations. The invisible flow of the fire plume will be visualised and analysed in the next section.

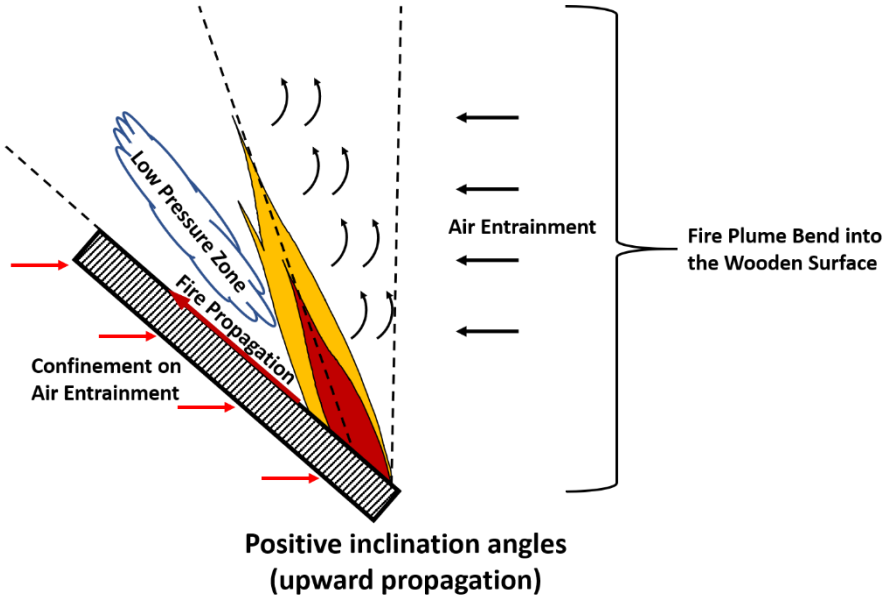

Figure 4.10 The demonstration of fire plume and surrounding air flow burned at positive inclination angle.

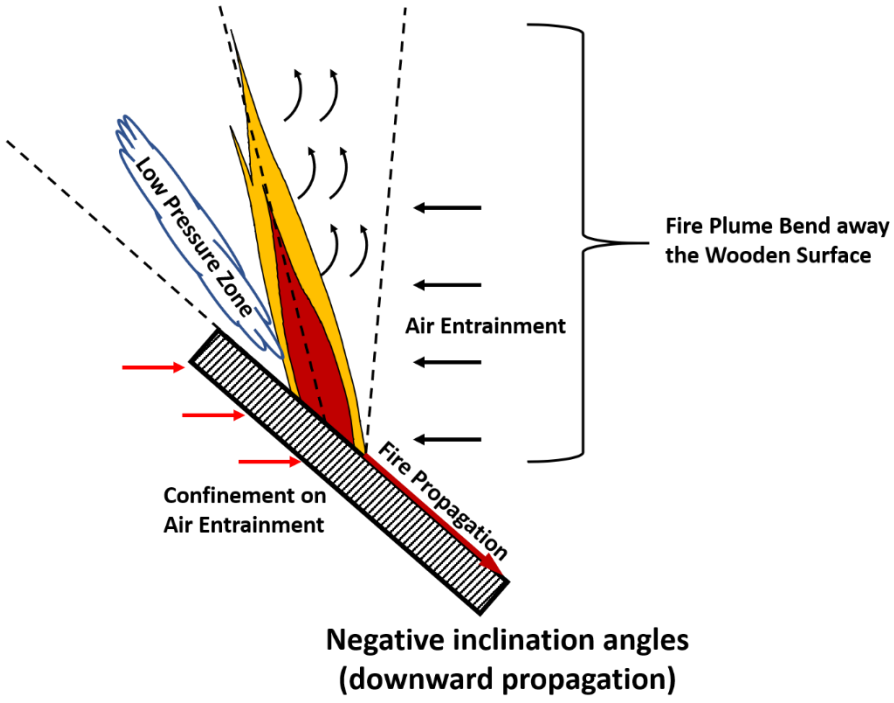

Figure 4.11 The demonstration of fire plume and surrounding air flow burned at negative inclination angle.

4.3.4. The heated flow

In order to observe the flow field of burning rods, the Schlieren imaging system has been applied to visualise the hot gas flow during experiments. The results for the rod of 6 mm, 9 mm and 12 mm in diameter are presented in Fig. 4.12. For each group of the testing cases with the same diameters, the range of the inclined angle was from -30^o to 30^o. Considering the combustion of 12 mm cases had the most stable combustion, the experiments for more inclination have been conducted to obtain the effects of inclined angles on ambient flow, including six chosen inclined angles of -30^o, 0^o, 15^o, 30^o, 45^o, and 60^o, shown in Fig.4.12. It should be clarified that the fire plume fluctuated during the period of burning, which resulted in the unstable flame from the direct images. Therefore, the example Figures were chosen as the time points that could represent the general trend in each case. In addition, the attachment of the fire plume did not occur at the beginning of self-sustained burning but appeared after a few seconds. The example images are chosen from the time point after the high intensity of attachment occurred. The main direction of the fire plume shown in Fig.4.12 represents the general plume direction of all repeat cases.

It can be seen that the combustion of rod trends to be stronger while the increasing inclined angle from -30^o to 30^o, meanwhile the attaching fire plume phenomenon had the similar trending that the strongest occurred at 30^o. The heat flow had been bent into the surface due to the decreased pressure caused by the confinement on air entrainment into the flame front, this could significantly increase the fire spread rate [128][132]. Meanwhile, it is found that the

flow had a slight tilt when the sample burned at 15° inclined angle and the flow tilt angle had significantly increased at 30°. Such finding is similar to Wu's conclusion [71] that the critical angle, which the flame attachment length would increase sharply, was found as 24°. From the results of schlieren images, it could be verified that the heated flow of the fire plume had a similar trend with the actual flame. It should be highlighted that there is no significant increase of the flow tilt angle when the inclined angle was increased from 30° to 60°, although the heat flow attachment length had strongly increased. Moreover, it is found that the intensity of heat flux trended to be stronger with the increasing inclined angle. Comparatively, the heated flows above the rods at the negative inclined angle had a deviation from vertical direction and were away from the surface of the wood, this phenomenon had been explained in Fig.4.11 that the low-pressure zone appeared behind the fire front, such phenomenon would significantly decrease fire propagation rate because of the decreased contact area between the fuel and heat flow. For the reason that the high intensity of fire plume attachment did not occur at the beginning of self-sustained burning, it is because the imbalance air pressure was nonsignificant at the beginning as the burning was weak at the beginning and the fire stilled at the rod end. Along with the fire propagation, more wood on the rod was involved in the heat pyrolysis and the fire became stronger. More importantly, as shown in Fig.4.9 - Fig.4.11, the longer rod involved in the pyrolysis, the higher imbalance air pressure produced. Therefore, the stronger fire plume attachment occurred while the further fire propagation.

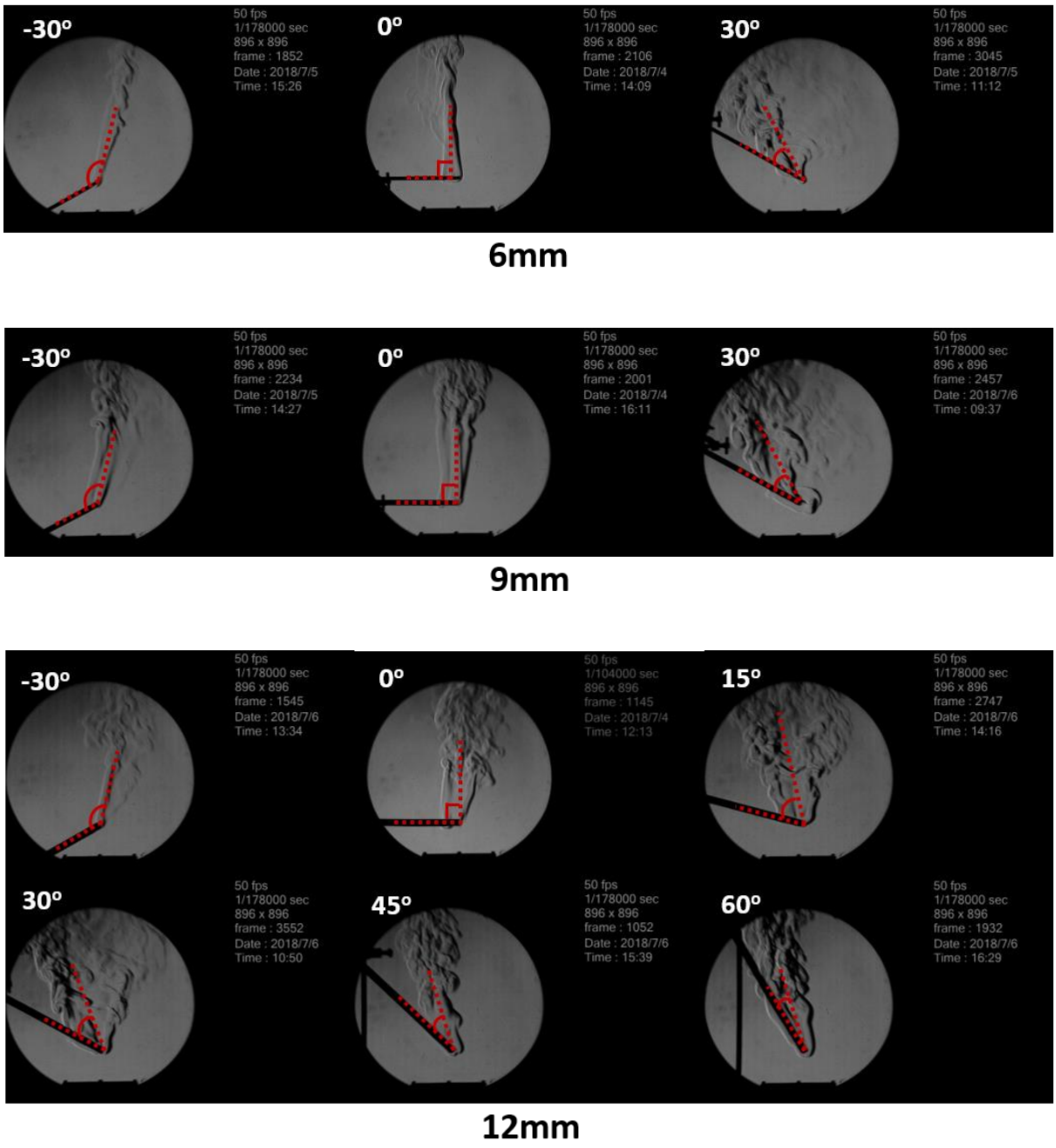

Figure 4.12 The schlieren images of different diameter woods at a set of inclinations.

For the effects of rod diameter on combustion, the cases of different diameters are further compared. It has been observed that the flow around the rods of large-diameter-group became more turbulent and the dimension increased significantly. This is due to the larger amount of fuel were ignited for the larger-diameter-cases, which means a larger amount of

combustible gases produced from the pyrolysis, resulting in means higher mixing rate of combustible gases and ambient air. However, no significant difference of the flow attachment was found. This point explains the find that the fire spread rate was not increased with the increasing diameter of the cylinder. Furthermore, due to the cross-propagation characteristic, the propagation rate of larger-diameter-cases could be smaller than small-diameter-cases.

4.3.5. The flame velocity distribution

The flame velocity can be calculated by the optical flow with a given threshold for noise cancelling. The flame velocity at 0 degrees, 30 degrees and -30 degrees at the first 10 s of the self-sustained burning is illustrated by the blue arrows in Fig.4.13. The direction and magnitude of the arrows present the actual value of flame. It is worth noting that the velocity of the flame at 30 degrees was distinctly larger than the cases at horizontal and negative directions. This phenomenon could further verify the finding that there was more efficient mixing between combustible gases and ambient air in the diffusion flame at a positive inclination. Higher mixing rate could help replenish the oxygen, then increases the efficiency of combustion. Moreover, although the flame fluctuated at 30 degrees, it tended to be bend into the unburned surface. This phenomenon could greatly enhance the continually burning and propagation. Compared to the images of 0 degrees and -30 degrees, it is found that the flame velocity at -30 degrees was larger than 0 degrees case. However, the more violent vibration at -30 degrees made the flame away from the unburned surface. This would decrease the fire propagation since lower heat transfer between the unburned-fuel and the flame.

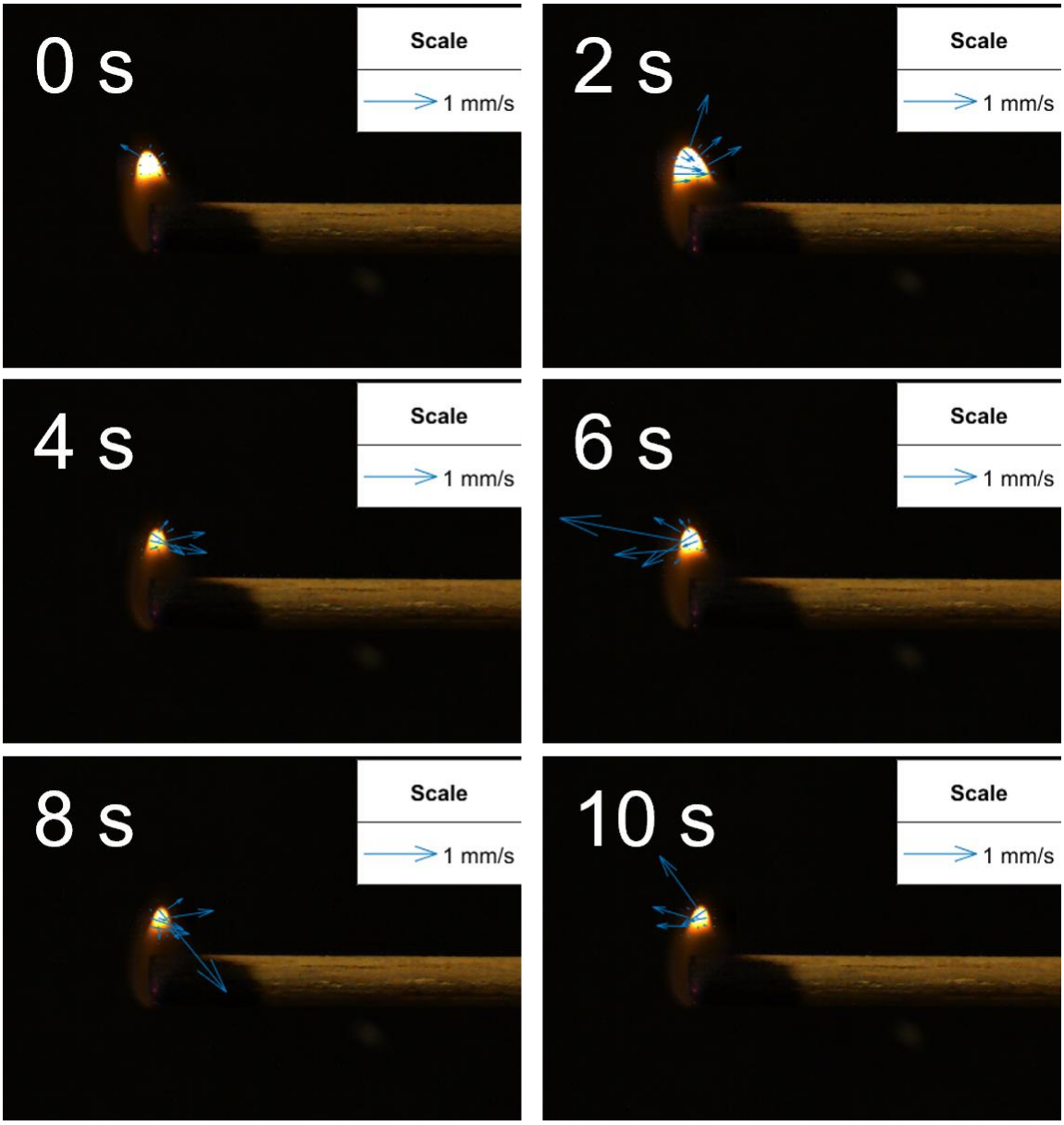
0 s
Scale
1 mm/s
2 s
Scale
1 mm/s
4 s
Scale
1 mm/s
6 s
Scale
1 mm/s
8 s
Scale
1 mm/s
10 s
Scale
1 mm/s

0 Degrees

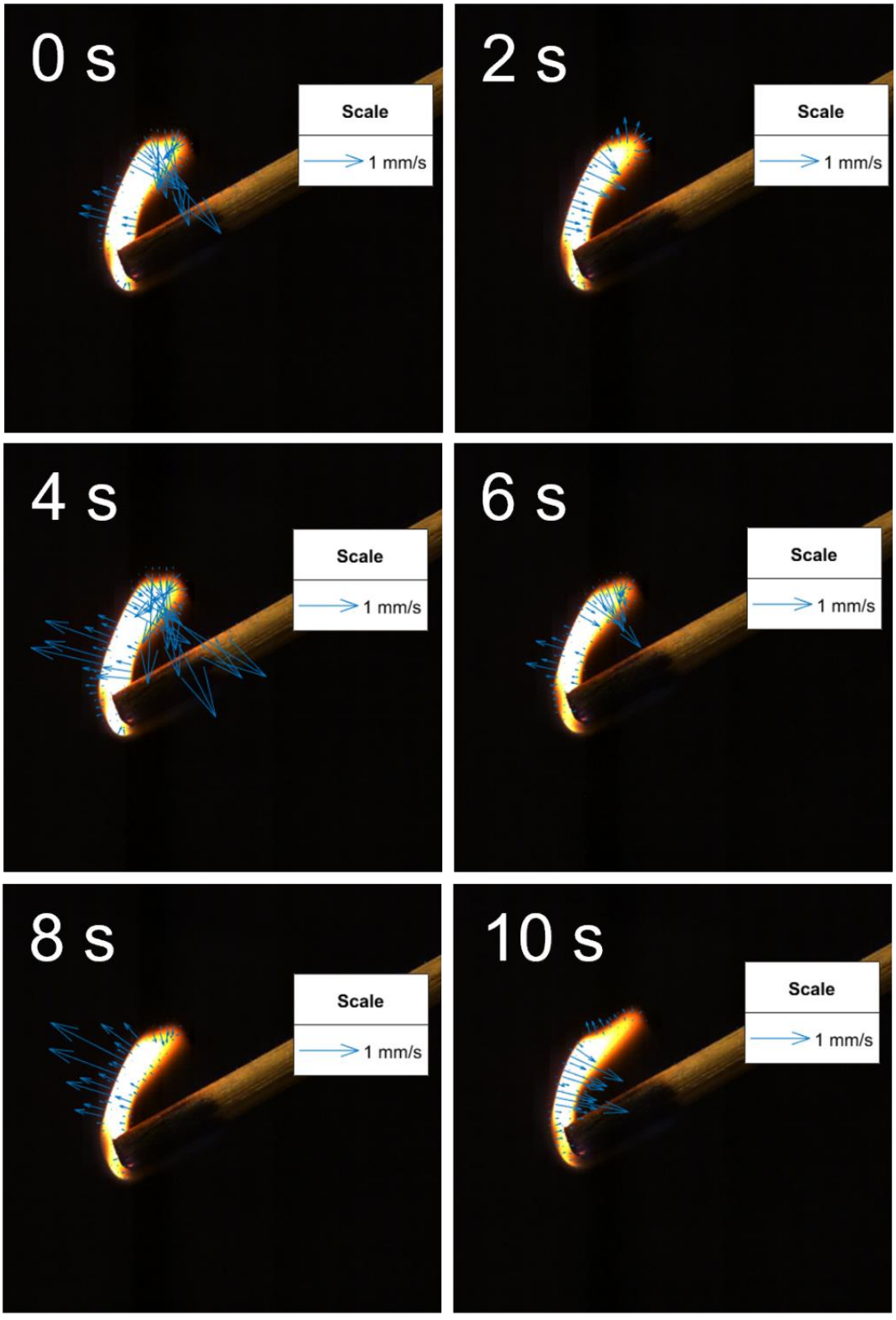
0 s
Scale
1 mm/s
2 s
Scale
1 mm/s
4 s
Scale
1 mm/s
6 s
Scale
1 mm/s
8 s
Scale
1 mm/s
10 s
Scale
1 mm/s

30 Degrees

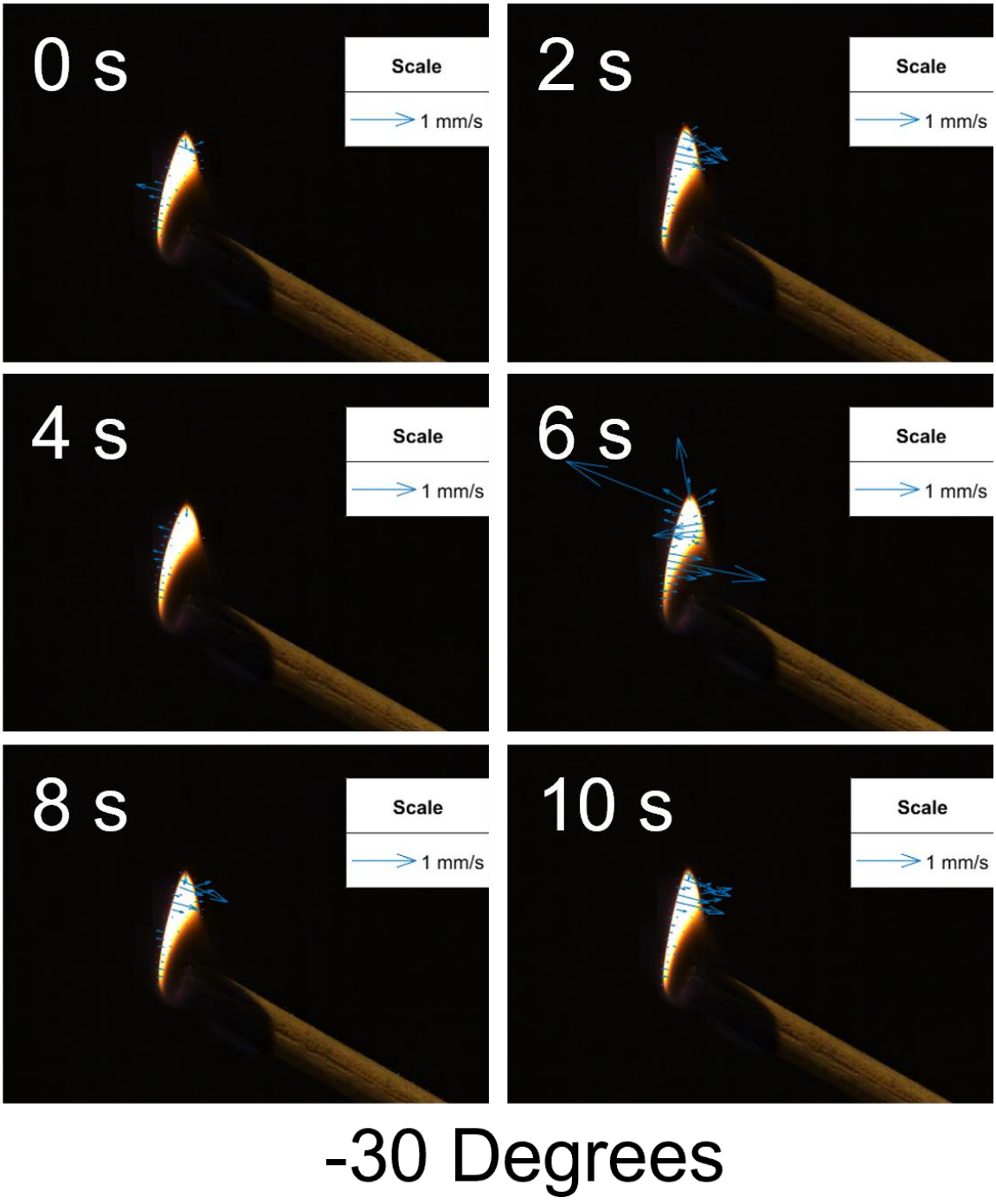

Figure 4.13 The illustration of flame velocity burned at different inclination angles.

Fig.4.14 presents the distribution of flame velocity at 30 degrees, -30 degrees and 0 degrees at different timing. The results of flame velocities were calculated by the optical flow

method with a given threshold to cancel the background noise. The histograms only present the probability of the high-velocity zone because this velocity range could be a better representative of the velocity of the flame edge. It can be seen from Fig.4.14, the velocity at 30 degrees is generally higher than other inclinations, followed by the -30 degrees and 0 degrees. The larger area of the histogram from 30 degrees case means there was a larger area of flame under vibrating. In addition, the flame velocity of 30 degrees had more probability on the high-velocity range (1mm/s- 2mm/s) which indicated the edge of flame violent vibrated at 30 degrees. This means there was a high rate of mixing between the intermittent flame and the ambient flow.

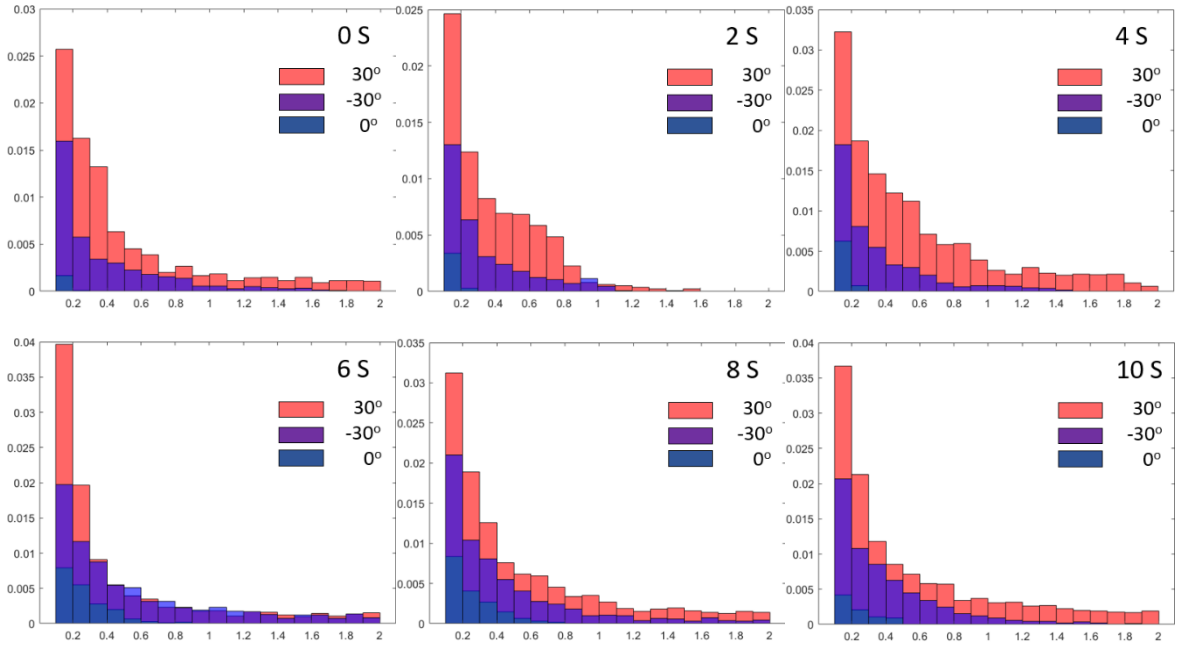

Figure 4.14 The distribution of flame velocity burned at different inclination angles.

4.3.6. The distribution of the heated flow velocity

By applying the optical flow method on the results of schlieren images, the invisible fire

plume vibration can be visualised. Both direction and magnitude of the flow velocity are presented by the white arrows in Fig. 4.15. The timing values on the upper right corner of the Figures indicate the time sequence of results. It should be highlighted that the heated flow at 30 degrees is much more turbulent than in other cases. This means a higher intensity of convection. In addition, the turbulent flow occurred at the area near the burning wood, indicating the oxygen mixing in the diffusion flame was more efficient. Moreover, the dimension of the turbulent flow was wider than other cases, which indicates more wooden fuel had been taken part in, resulting in higher intensity combustion. Comparatively, the size of the fire plume at the horizontal direction and negative inclination angle had no distinguishing difference. Meanwhile, the flow of these two groups was more turbulent at the beginning of self-sustained burning, which indicates there was a high intensity of combustion after turning off the piloted ignition. However, with the burning process, the high intensity of combustion was suppressed and resulted in a shorter burning lifetime.

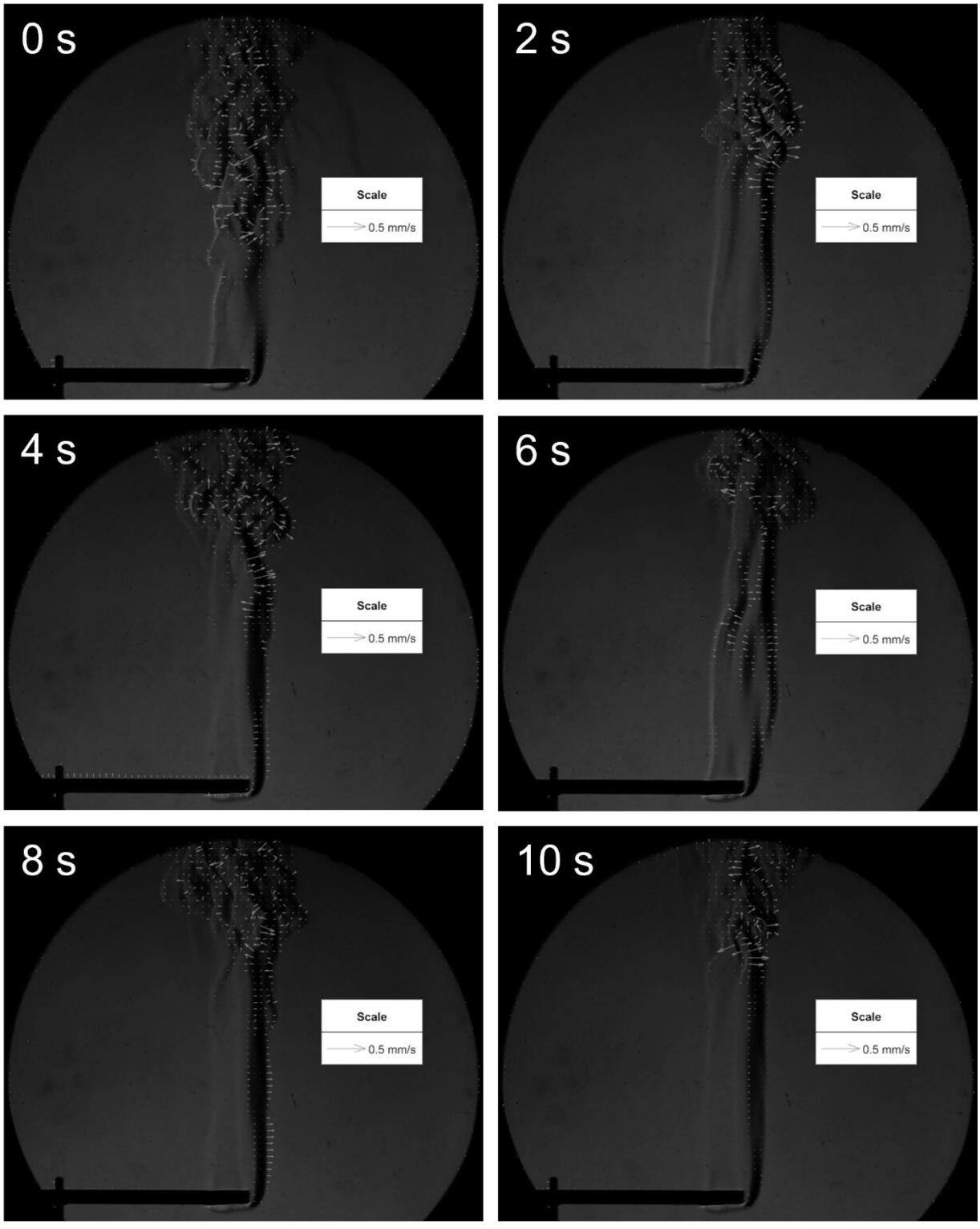
0 s
Scale
0.5 mm/s
2 s
Scale
0.5 mm/s
4 s
Scale
0.5 mm/s
6 s
Scale
0.5 mm/s
8 s
Scale
0.5 mm/s
10 s
Scale
0.5 mm/s

0 Degrees

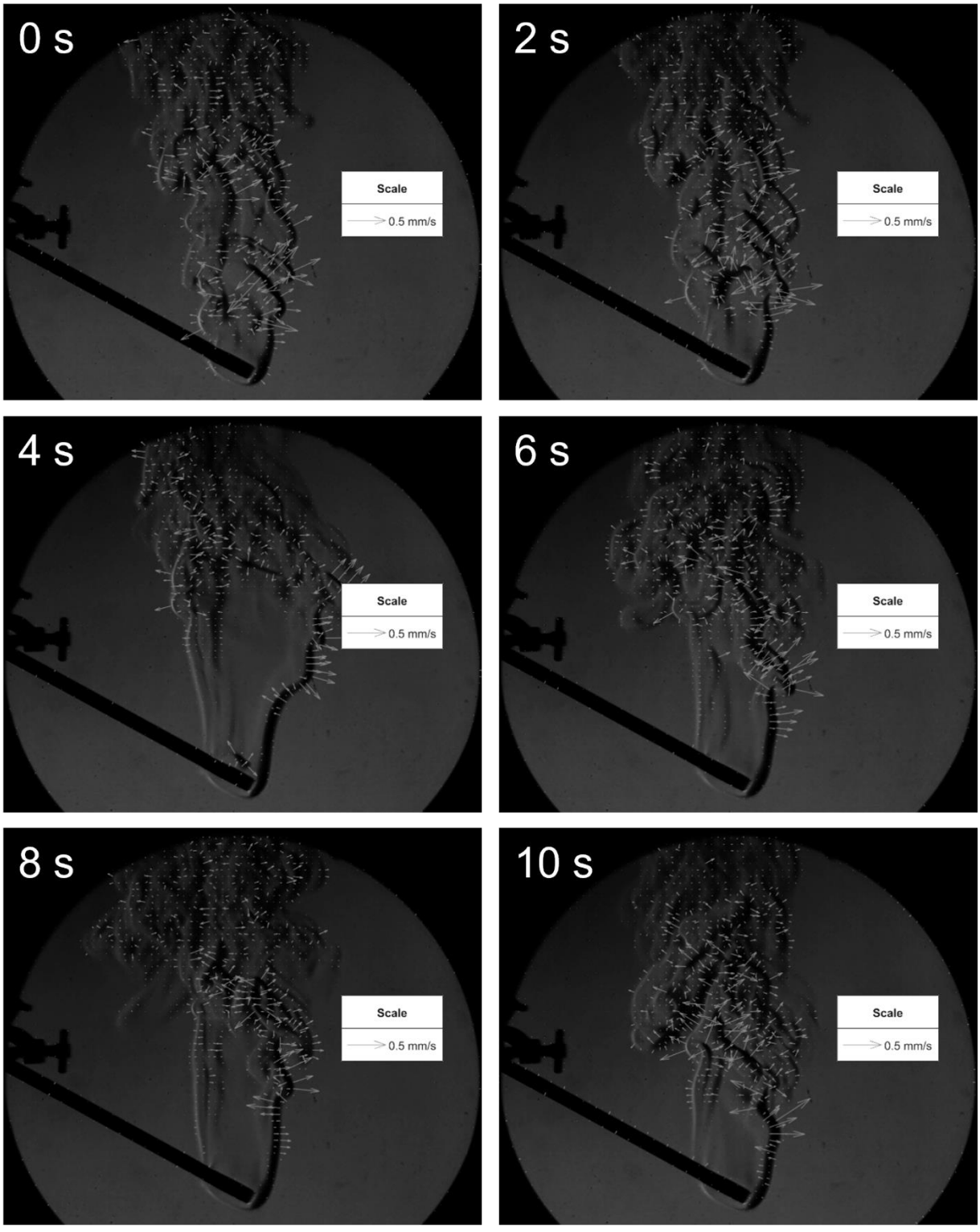
0 s
Scale
0.5 mm/s
2 s
Scale
0.5 mm/s
4 s
Scale
0.5 mm/s
6 s
Scale
0.5 mm/s
8 s
Scale
0.5 mm/s
10 s
Scale
0.5 mm/s

30 Degrees

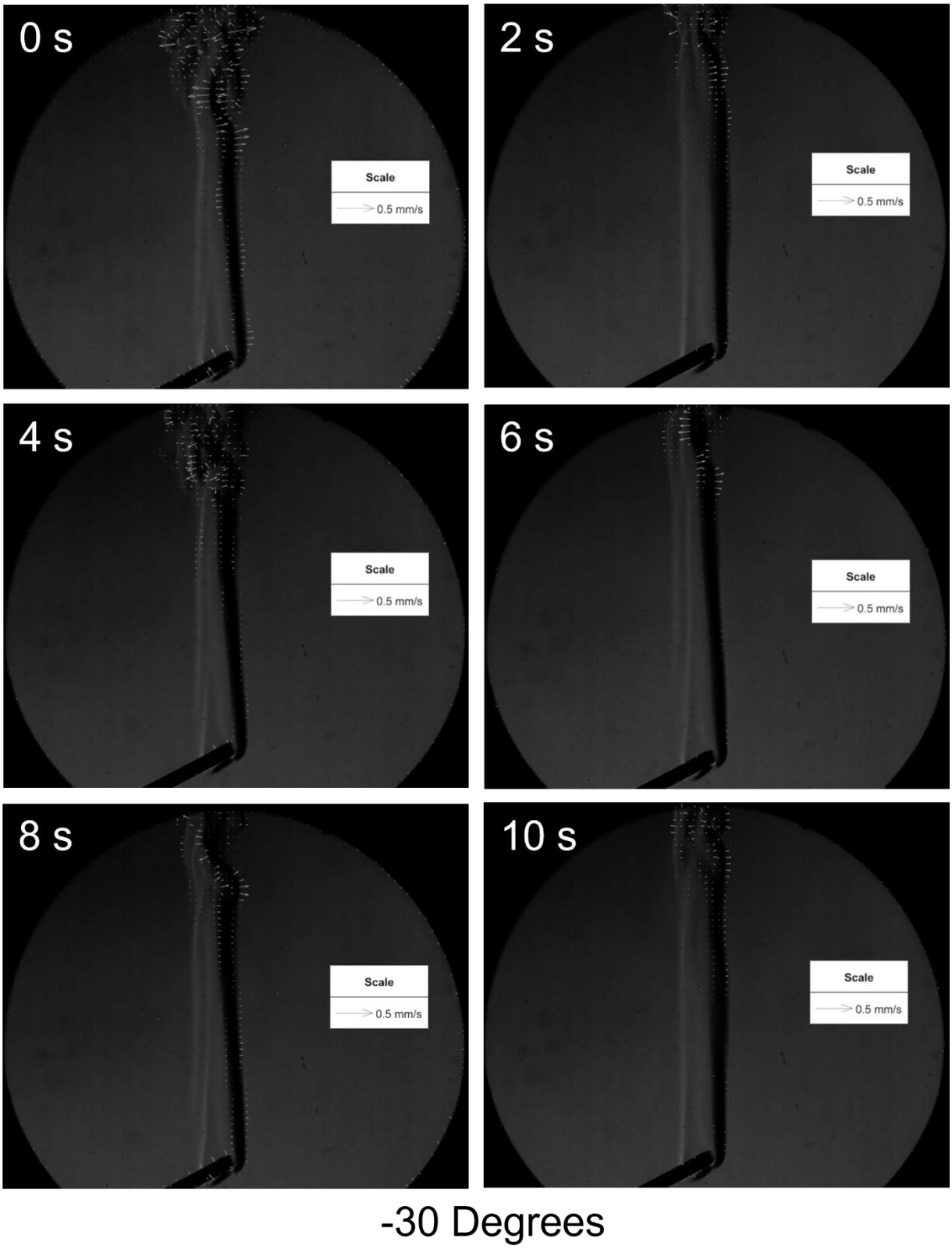

Figure 4.15 The illustration of buoyant heated flow velocity burned at different inclination angles.

Fig.4.16 presents the flow velocity distribution at different timing. The background noise has been cancelled by the given threshold, and only the high-velocity zone has been counted into the histograms. As a common trend, it can be seen that the flow velocity was highest at the beginning and kept decreasing along the burning. With the burning processing, the flow at 30 degrees kept a high velocity whereas the flow velocity at 0 degrees and -30 degrees decreased sharply. At 10 s of self-sustained burning, the probability of high velocity at 0 degrees and -30 degrees decreased at a quite low value, indicating there was no sufficient mixing of oxygen and inefficient convection, therefore, the burning lifetime of these two cases cannot achieve high values. Comparatively, the high velocity of heated flow at 30 degrees indicates that there was a higher intensity of gas-phase combustion as well as more gas-phase combustion products produced. The motion of the heated flow could help increase the heat transfer by convection, further help the thermal pyrolysis on the wood.

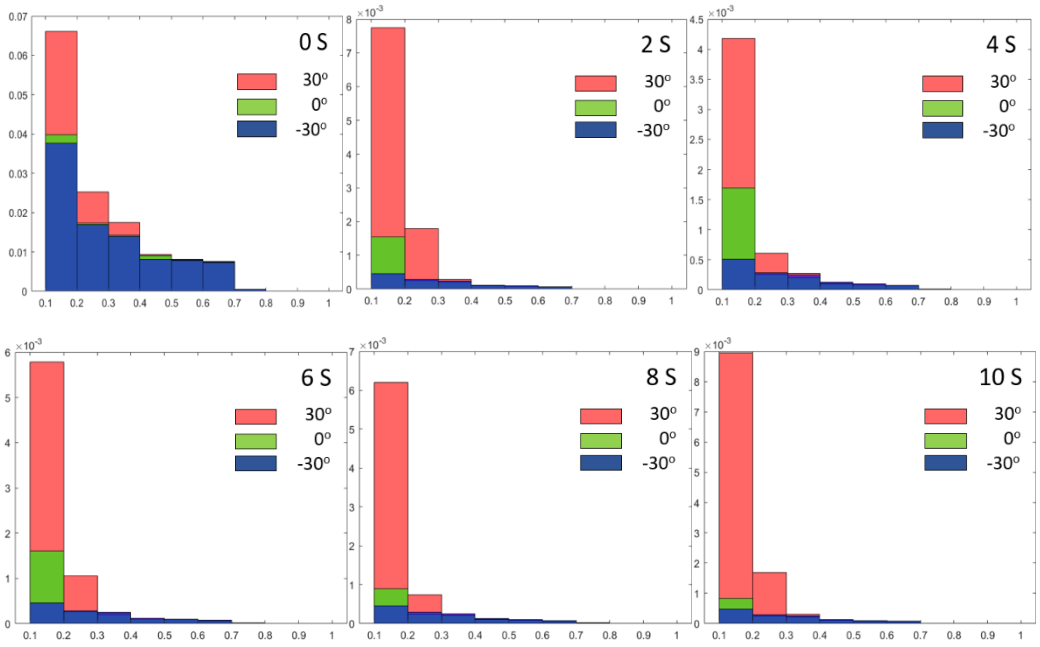

Figure 4.16 The distribution of buoyant heated flow velocity burned at different inclination angles.

4.4. Conclusion

The effects of fire plume aerodynamics at a set of inclination angles and diameters of wooden rods on flame propagation are investigated in this study. In details, study the flaming status of wooden rods at different inclinations have been studied by the direct images method with a high-speed imaging system, including the charring rate and the burning lifetime; meanwhile, after applying the high-speed schlieren imaging system, the attachment phenomenon by both the direct images and schlieren images; and the flame and flow velocity distribution by the optical flow method. Moreover, the ambient flow of burning rods is visualised by a High-speed Schlieren imaging system, of which the results are further compared with the colour images to present the invisible fire plume. From the results, it is found that the positive inclination angle of rods can significantly improve the flame propagation with stronger flaming, higher charring rate and longer burning lifetime, such as the charring rate is increased by 254% when

the inclined angle is increased from -30° to 30°. Meanwhile, it can be observed that the flame propagation is weakened by increasing rod diameter, such as the charring rate has significantly decreased by 55% when the diameter is increased from 6mm to 12mm. The attachment phenomenon of both flame and flow occurred at positive inclinations. The fire plume tilt angles and attachment lengths changed with increasing inclination. Moreover, the burning heated flow above burning rods are tilted forward to the surface when the inclined angle is increased to 30^{o}, and then the heated flow tilt angle would not change much although the inclined angle was continually increased to 60°. The mechanism of the fire plume attachment phenomenon is explained as the local pressure imbalanced. With the help of the optical flow method, the direction and magnitude of flame and flow velocity are illustrated and showed in the histogram. It is found that the flame velocity at 30 degrees is higher than the other cases, which means there is a high rate of mixing the oxygen and fuel in the diffusion flame. By applying the optical flow on the schlieren images, it is found that images of positive angle groups have broader turbulence flow than those of horizontal and negative. Moreover, the larger area of the turbulent flow in the 30 degrees case indicates there is a higher intensity of convection and mixing rate of the oxygen. The flow velocity decreases sharply at 0 degrees and -30 degrees, as the result, these two cases have a shorter burning lifetime, and the combustion is weaker.

5. The effect of the underneath pre-heating on the fire spread

5.1. Introduction

Fire propagation on a fuel surface is a complex process that is affected by many factors, such as the angle of inclination, the moisture content, the ambient flow, and so forth [134]. Among those factors, the inclination can play a dominant role in affecting the fire spread due to its effect on fire dynamics and airflow. In 1992, the investigation of the disaster of King's Cross Fire revealed that wooden beams at 30 degrees enhanced the fire propagation [127]. In order to find out the effect of inclination angle on the fire spread, many researchers studied the effect of geometrical factors on fire spread upon planar surfaces. Drysdale investigated the aerodynamic effect on the fire propagation on PMMA slabs at different inclination angles and stressed on the sharp increase of fire spread rate with the side walls [128]. Yang et al. [133] studied the effect of the inclination angle and trench configuration on the flame geometry by using image processing. Gollner et al. [135] studied the upward flame spread with PMMA slabs, as well the measurements of burning rate and flame spreading rate at different inclination angles.

There are two key factors that influence the fire spread on an inclined surface: flame attachment from the top of the surface (produced by the imbalanced air pressures); the convective preheating of the underside of the fuel. In the research which focused on the effect of inclination on flame spread by Wu et al. [71], the flame attachment length and tilt angle were introduced, and a critical angle of 24 degrees for strong flame attachment was

discovered. Grumstrup et al. [132] studied the aerodynamic effect by qualitatively analysing the flame attachment phenomenon with the retroreflective shadowgraph technique. In addition to the aerodynamic effect, research of the convective heat transfer on combustion has been established. Weber et al. [136] had revealed the importance of underneath convective pre-heating. Hirano et al. [137] studied the fire spread mechanism on paper sheets at different inclination angles, they considered that the heat transfer to the unburned fuel takes place in the front of the pyrolysis zone and mainly occurred from the underneath. In Zhou et al. 's study [131], the effect of convective heat transfer for fire propagation in the case of a metal platform was reported. Moreover, with a set of matchsticks, Hwang et al. [138] investigated the flame propagation on inclined base boards, in which he demonstrated the preheated region increases caused by inclinations.

The investigation of fire spread on individual cellulosic fuels could help in the comprehension of more complex wildfire phenomenon. For example, the fuel bed inside the trench could be seen as comprised of many individual cellulosic fuels. In order to understand the critical condition of fire spreading, Zhang et al. [129], [130] tested different inclination angles and defined four stages of flame propagation, namely acceleration, steady-state, deceleration and extinguishment. Weber et al. [139] used single ponderosa pine needles to investigate the effect of sample orientation on the fire spread rate and modelled the marginal conditions of sustaining flame related to moisture and inclination angles. Hirano et al. [140] used the paper sheets to explore the mechanism of fire spread by using schlieren and fine wire thermocouple. Furthermore, in the research by Lai et al. [141] and Zhou et al. [142], the burning and fire spread on an inclined oak rod surface was studied using visible, schlieren imaging system and

modelling, which showed the importance of local aerodynamic effects on fire spread.

Many previous papers focused on the overall geometric features of fire propagation. Others emphasised how the flow field affected the fire spread. The fire propagation mechanism varies greatly from case to case. However, few published papers have analysed the flame propagation with a specific focus on convective preheating from the underside of the fuel by means of a systematic visualisation of the wood temperature, visible flame and the invisible hot gas simultaneously. Moreover, the importance of convective heat flow from the underside of the fuel has been briefly reported in the studies mentioned above. However, there were no quantitative measurements to explicitly show the difference between preheating length and pyrolysis length. In this study, the use of the schlieren imaging technique provides the visualisation of this invisible hot gas layer, from which the layer length can be measured. The length of the fuel under pyrolysis can be measured by using the selective enhancement technique in combination with thermal temperature distribution. Then, the pre-heating length ahead of the pyrolysis region, which is the difference in those two measured lengths, can be quantified. Wooden rod samples could be used to study the mechanism and help improve the understanding of the large-scale circumstances, the wooden structure of the building and unconsolidated fuel bed in trenches for instance. The cylinder shape sample could show the effect of the pre-heating underneath the surface and on the upper surface separately. In addition, the thickness of the wooden rod allows visualising the longitudinal direction of the pyrolysis process. By synchronising visible, schlieren and thermal imaging systems, a more comprehensive diagnostics of fire propagation on a wood surface has been made in this study. This chapter focuses on the convective preheating of the underside using

quantitative measurements, which is proved to be the driving factor for flame propagation.

5.2. Experiment setup and methodology

5.2.1. Experiment setup

In this study, the same batch of oak wood rods, which were 9 mm in diameter and 400 mm in length were used as samples for tests. To minimise the effect of moisture, all the rods were pre-dried in an electrically controlled furnace over 24 hours at 150^{o}C. An adjustable holder was used to fix the rods at the desired orientation and height. As shown in Fig. 5.1, the inclined angle ϑ is defined as the angle between the horizontal and the rod surface. At negative angles, the fire tends to spread downwards, while it will spread upwards at positive angles. In the experiments, rods at five different inclination angles -30^{o}, 0^{o}, 20^{o}, 25^{o} and 30^{o} were used to investigate the effect of inclination angle on convective heat transfer during fire propagation. The chosen inclined angle covered the critical angle 24^{o}C which is mentioned in Wu's study [71] in order to further study such phenomenon. The rods were subjected to a piloted ignition by a Bunsen burner with pre-mixed fuel (methane and compressed air). For the purpose of consistency, the distances between the burner nozzle and the impact point on the wood were kept the same in all test cases. The piloted ignition flame was controlled with an equivalence ratio (fuel-to-air) of 0.6. All the testing rods were ignited for 20 s to ensure the successful ignition then and the burner was immediately turned off thereafter. The experiment for each case was repeated at least 10 times and all the results were averaged. The samples were made from natural wood and would inevitably cause residuals, considering the repeatability of this work, the averaged results from 10 times experiments could minimum the experimental error.

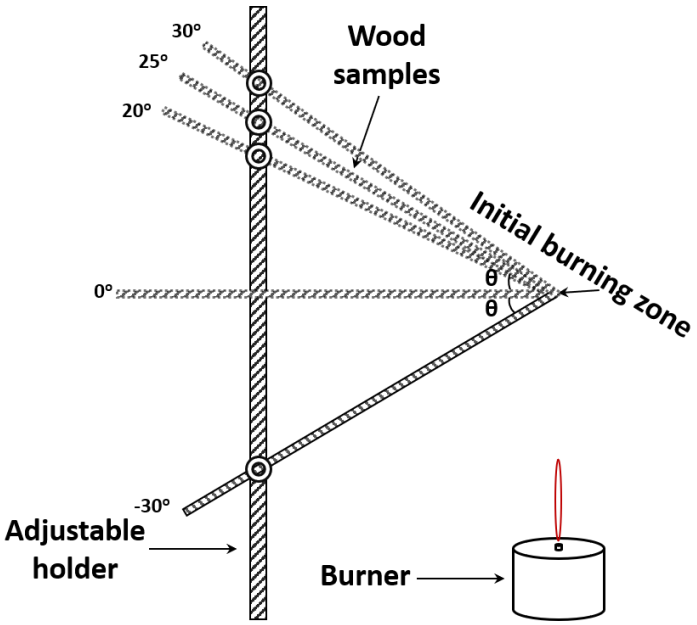

Figure 5.1 Schematic representation of the experimental set-up.

5.2.2. Imaging systems

The setup of the imaging system is illustrated in Fig. 5.2. A Z-type high-speed schlieren system was employed to visualise the hot flow during the combustion. In addition, an InGaAs thermal camera and a high-speed CMOS camera were placed alongside the parallel optical path of the schlieren system. The InGaAs thermal camera was applied with a cut-on filter to restrict its spectral sensitivity within 1550 to 1670 nm and used the fixed exposure time of 32 ms, to ensure that the thermal camera was sensitive to temperatures in the range between 250 and 550 ^{o}C. In total, three types of visualisation were utilised: schlieren imaging, visible-light imaging and thermal imaging. All three imaging systems were synchronised.

From the visible images, the self-sustained combustion lifetime and charring length were measured. Moreover, the difficulty to visualise the blue flame underneath the flame front was selectively enhanced for better visualisation.

The thermal images were used to determine the heated length underneath the rods. Because

of its ability for observing the radiation from objects with a lower temperature, it is effective to study the preheating progress which aids flame propagation. With the measured temperature map under 600 °C, the thermal pyrolysis can be studied. Also, the flame attachment length and flame tilt angle had been determined at 20 s after turning off the burner for each case with the enhanced thermal images.

The schlieren system helps to visualise the hot flow in the combustion zone as well as the preheating zone. Through image processing, it further demonstrates the importance of convective heat transfer for fire propagation.

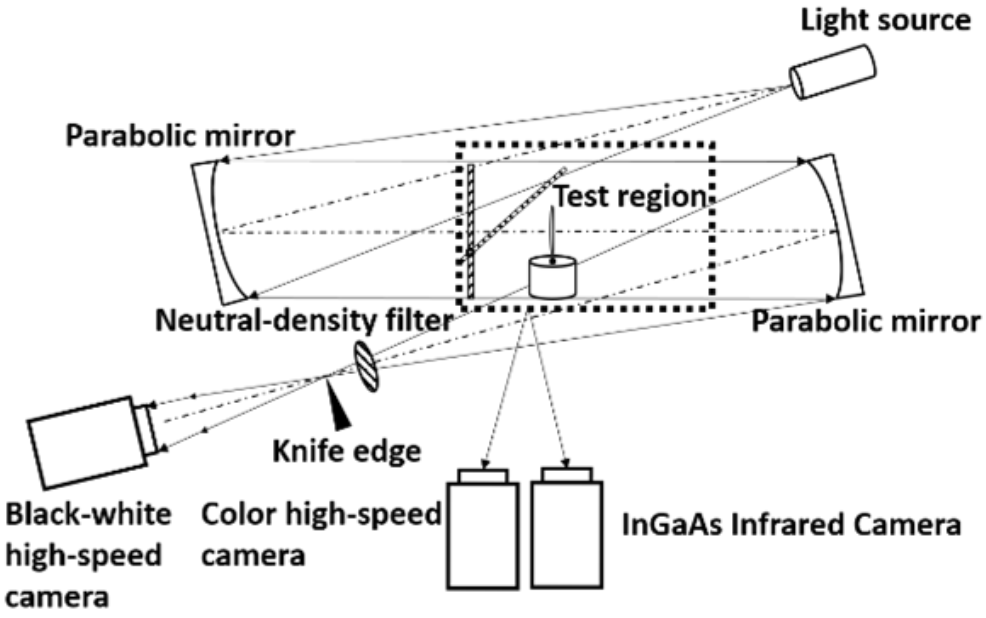

Figure 5.2 The Setup of imaging systems.

5.2.3. Data processing

The burning status is analysed from the actual images of the colour high-speed camera. In the study, the burning lifetime and maximum charring distance were calculated to show the ability of self-sustained burning and fire propagation. In detail, the burning lifetime was defined as

the period from the beginning of self-sustained burning to the extinguishment. And the maximum charring distance was measured as the distance from the end of the initial burning to the furthest point the char moved. The study used the charring distance instead of the charring rate because the fire spread little distance at negative angles and horizontal direction, the calculation of charring rate at these inclinations may cause errors. These two parameters could better represent the intensity of the combustion and the ability of fire spreading.

The radiation intensity from diffusion flame normally is much more intensive than that from premixed flames. In addition, the cameras spectral response is generally low within the premixed flame bands. As a result, the blue flame would be too weak to be discernible for naked eyes. In order to figure out the effect of the inclinations on the gas-phase combustion, by using selective colour enhancement, those weak colours could be selected because the orange sooty flame and the dim blue flame could be easily differentiated in the hue channel of HSV colour space, then according to which V channel is enlarged. As a result, the weak blue flame can be clearly shown in the image. The surface temperature of the burning wood was measured by the InGaAs thermal camera with a narrow band filter of 1550 – 1670 nm. The calibration used a blackbody furnace with emissivity 0.99 from 200 to 550 ^{o}C. The emissivity of wood was set as 0.9 at 1.6μm[143]. The main reason for choosing the narrow band IR camera from 1550 – 1670 nm was because that the spectral emissivity was sensitive to the wavelength. The narrower the selected band, the fewer the errors of the measured temperature. The camera was calibrated by the Sakuma Hattori model[144], which assumed that a single wavelength was used. Hence, a narrow wave band to a single wavelength was approximate. In addition, the reason for the using of the short-wavelength IR camera instead

of the long-wavelength IR camera is because there is more than ten times greater change in signal with the temperature at these wavelengths compared to more conventional cameras. Such kind of setup may increase the accuracy of experiments. With the exposure time of 32 ms, the effective temperature measurement by the NIR camera had covered the general temperature range of wood pyrolysis, which is around 300 °C.

The schlieren imaging system was used to analyse the invisible hot gas flow around the burning rods. The underneath hot gas flow can be considered as a key factor of the longitudinal preheating referred to the work from other researchers[136], [137], [139], [140]. In this experiment, the underneath hot flow length was measured at the beginning of the self-sustained burning ($t = 0\ s$) and the 20s after then ($t = 20\ s$). In addition, the thermal images were able to indicate the area where undergoing heating, the underneath heated length then could be measured at the beginning of the self-sustained burning ($t = 0\ s$) and the 20s after the point ($t = 20\ s$) as well as the thermal images. By combining the values of both lengths, the preheating length can be calculated from the difference between these two lengths, shown in Eq.5.1, where $\boldsymbol{Pre_l}$ is the preheating length, $\boldsymbol{Flow_l}$ indicates the hot flow length and $\boldsymbol{Pyr_l}$ represents the pyrolysis length that measured by thermal camera. Then the effect of the underneath preheating on the fire propagation can be studied. Moreover, the underneath hot flow length and the heated length were recorded every 2 s to track the combustion process, as well the actual image of flame was recorded at the same time.

$$\boldsymbol{Pre_l = Flow_l - Pyr_l} \tag{5.1}$$

The flame attachment could be clearly profiled by the thermal images after a series of imaging enhancements. In detail, the enhancements are including enhancing the contrast, adjusting

the gamma, setting the threshold and correcting the angle. The flame attachment length was measured from the end of the initial ignition point to the maximum contact length between flame and wood. The flame tile angle was measured by the angle between the wood surface and the middle line of the main flame. Since the visual images are confused by the flame going from blue to yellow such as excited plasma emission to conventional thermal emission, the utilisation of thermal images could be a better option for determining the flame attachment length and tilt angle. In addition, the IR image had higher contrast which was easier to draw the flame profile after enhancement. Moreover, the invisible flame can be captured with high sensitivity at low temperature by IR images, further reducing the observational error to some extent.

5.3. Results and Discussion

In this section, the mechanism of fire propagation in an inclined surface will be studied and present in the following subsections. In details, the direct images used for indicating the general combustion status, including the burning lifetime and the maximum charring distance, will be presented in section 5.3.1. The heated flow underneath a burning rod plays a critical role in self-sustaining and propagating the fire, the study of the underneath hot gas parcel will be presented in section 5.3.2. In this part, the preheating zone will be demonstrated by combining the invisible hot gas flow with the enhanced blue flame, and with the help of the thermal images, the pyrolysis length can be calculated and compared with the underneath hot flow length. In section 5.3.3, the flame profile can be obtained by the enhanced thermal images, as an alternative method to measure the flame attachment length and tile angle. In this section, the effect of the topside preheating on the wood combustion will be discussed.

The impact point where was heated during the piloted ignition process had a high concentration of heat while self-sustained burning began, the analysis of the effect of the impact point will be presented in section 5.3.4 by combined the schlieren images with the selective enhanced blue flame.

5.3.1. The general combustion status

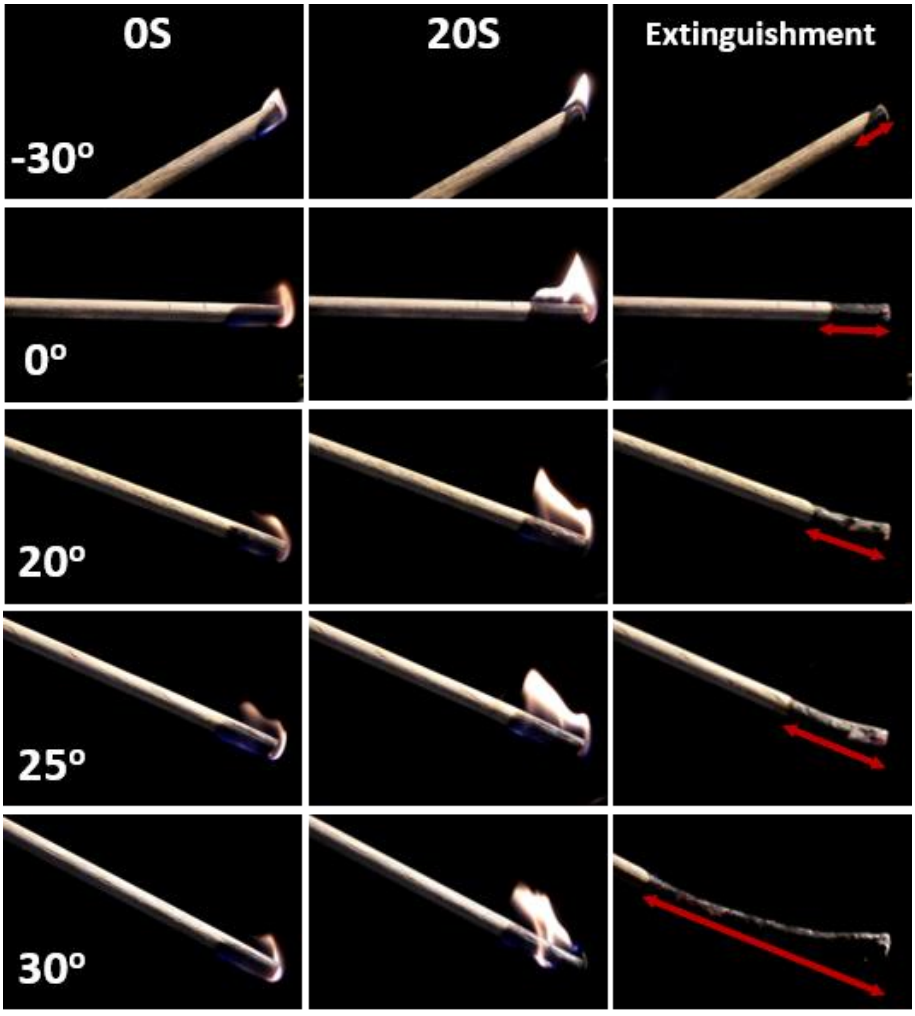

Figure 5.3 The typical burning images at different inclination angles at different time points.

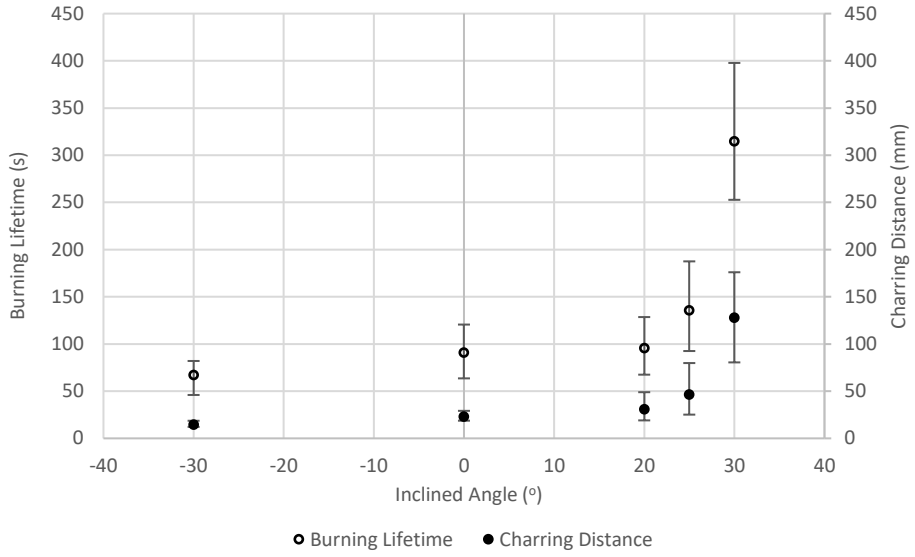

Figure 5.4 The burning lifetime and charring length against inclination angle.

The visible images captured by the high-speed colour camera are presented in Fig. 5.3 Horizontally, three frames are ranged in the time sequence, they are the beginning of self-sustained burning (the time turning off the burner set as 0 S), 20s after self-sustained burning and the extinguishment respectively. Vertically, five different inclination angles have been compared, which are -30°, 0°, 20°, 25°, and 30°. The maximum charring lengths for each case are highlighted with red lines.

In general, it can be found that the charring length and the burning lifetime are increased by increasing orientation angle, as plotted in Fig. 5.4. The burning lifetime is measured as the time duration from turning off the burner to the extinguishment of the wooden rod; the charring length is measured as the maximum charring distance on the wood surface. The data points are plotted based on the averaged value from 10 times repeats for each case. Both, the maximum and the minimum values have been indicated in the Figure. The deviation mainly is caused by material nonuniformity, namely density and grain orientation [57].

From the results, it can be seen that the most sustainable combustion happened in the 30

degrees inclination group, which had the longest combustion lifetime and charring length with an average value of 315 s and 128 mm respectively. It is worth pointing out an abrupt change from 25 degrees to 30 degrees, which covers the critical fire propagation angle [129]. Conclusively, the fire propagation was sensitive to the inclined angle. In the positive angle groups, the flame tended to be lean on the wood surface. The flame attachment phenomenon was due to the pressure difference induced by the surface confinement on the entrainment of the air upslope and down-slope of the fire plume [4] [145]. It also can be observed that, while the flame was burning vigorously, there was a faint blue flame underneath the rod. This blue flame came from gas-phase combustion originating from the pyrolysis of the wood, which is an indication of the source of convective preheating length [146]. For the cases at positive inclination angles, due to the stronger flame attachment and larger contact area, heat convection was more significant for the flame to develop [128].

The radiation from the flame consists of two parts: upper diffusion flame and underneath blue flame. The radiation from the upper part of the flame enhanced the pyrolysis on the top side of the wood because the diffusion flame emitted most radiation. However, it does not play a significant role to help flame propagation. In those short burning-life time cases, although the top side of the wood was still burning, the flame vanished in the absence of underneath pyrolysis. In addition, the radiation from the upper flame to the top side of the wood was assumed to be constant for two reasons: 1. the flame sizes during progression were observed to be similarly small in the test groups; 2. The size of the samples was small. Furthermore, the bottom side blue flame emitted a very short band of radiation; therefore; its effect is negligible. Under these assumptions, the experiments were in a controlled manner to isolate

the effect of convective preheating.

As conclusions, three main effects on sustaining the fire propagation can be found: 1. The presence of hot gas parcel underneath the rod which is generated by the blue flame but with burnt gas extended to the preheating layer, as observed using schlieren imaging; 2. The long preheating length due to the convection which was directly proportional to the inclination angle. 3. Flame attachment generated by the local imbalance air pressure. Through visualisation and image processing, these phenomena can be quantified and analysed in the following sections.

5.3.2. The effect of underneath hot gas parcel

As mentioned in the literature review[136], [140], [137], the underneath hot flow could be a critical factor of sustaining burning and fire propagating. In section 5.3.2.1, the preheating zone, and the effects of underneath hot gas flow on adjacent virgin wood will be explained and illustrated. In section 5.3.2.2, the temperature colour map will be presented to indicate the surface temperature of burning rods at different inclined angles. Further, in section 5.3.2.3, the preheating (underneath the rod) progress will be presented quantitatively based on the hot gas flow length and the pyrolysis length. Moreover, the combustion process diagram in section 5.3.2.4 will be used to present the relationship of the combustion process with both the underneath hot gas length and the bottom heated length.

5.3.2.1. Visualisation of the underneath preheating

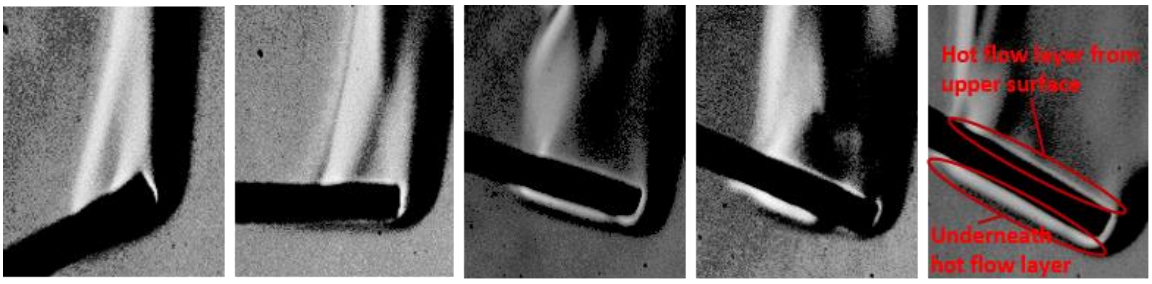

a) -30 degrees b) 0 degrees c) 20 degrees d) 25 degrees e) 30 degrees

Figure 5.5 An example of the surrounding hot flow at different inclination angles at $t=20\ s$.

From Fig. 5.5, it can be seen that the burning rod was enfolded by the hot flow which was generated from the gas phase combustion. In detail, such gas-phase combustion was comprised of the combustible gases produced by thermal pyrolysis and burnt gases. The flow layer underneath the burning rods at positive inclination angles was thicker than those at the negative angle and horizontal direction. Moreover, it can be found that the underneath flow layer was much thicker than what comes from the upper surface. Such thicker hot flow could be considered as an isolation layer which could prevent the convective heat loss from wood surface to ambient cold flow. As well, such layer enhanced the preheating on the unburned part of the wood.

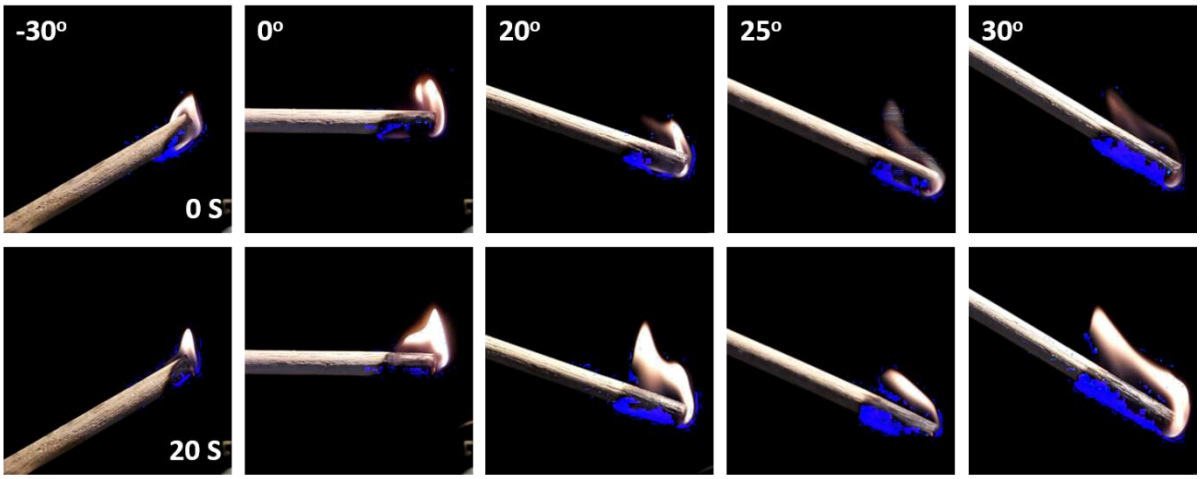

Figure 5.6 An example of the selectively enhanced blue flame at different inclination angles at $t=0$ s and $t=20$ s.

Pyrolysis involves the decomposition of the three main constituents of the wood, namely, hemicellulose, cellulose, and lignin [57]. The decomposition generates combustible gases that are essential for flaming combustion [136]. In order to visualise the surface under pyrolysis, in Fig. 5.6, the dim blue flame of gas-phase combustion from pyrolysis has been selectively enhanced for visualisation. It can be seen that the length and thickness of the blue flame when the rods were inclined at a positive angle were significantly larger than when the rods were inclined at zero and negative which means there are more fuels that had taken part in the rapid pyrolysis at positive inclinations than other cases. In addition, related to the premix flame, the blue flame also could present there are more combustible gases produced from the thermal pyrolysis of the burning wood since the high rate of premixing there. Moreover, the blue flame appeared at underneath the rod also indicated there was laminar flow underneath the burning rod. It is found that there are blue flame presenting at $t = 0\ s$ in all inclination angles. This is the initial of the self-sustained burning, all the burning rods had the high intensity heat concentrated near the impact point. However, with the burning process,

the blue flame almost disappeared at -30 degrees and 0 degrees at $\boldsymbol{t} = 20\ s$. This means the combustion at these angles tended to be weak and cannot develop further since the less combustible gases produced from the thermal pyrolysis. Comparatively, the area of blue flame increased after 20 s of ignition at positive inclination angles. This means the flame became stronger after the 20s at positive inclination angles. The visualisation of the selectively enhanced blue flame could be a piece of evidence to support that the burning at positive angles could have a longer lifetime and intensity.

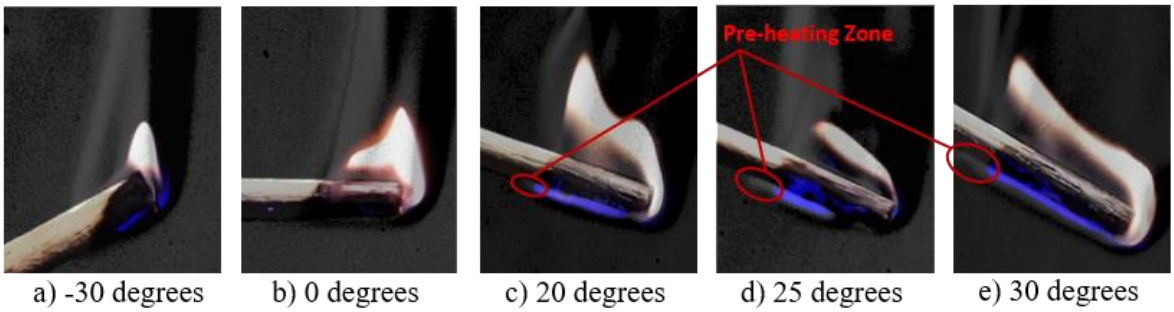

Figure 5.7 The illustration of underneath preheating zone related to the selectively enhanced weak blue flame with schlieren imaging at $\boldsymbol{t}=20\ s$.

The thick hot flow underneath the rod in the schlieren image is longer than the pyrolysis length. The difference in length is the preheating zone. The preheating of the unburnt rod is significant in sustaining the flame. In order to present the pre-heating zone, the schlieren images and the selectively enhanced blue flame are synchronised, shown in Fig.5.7 the hot flow enclosing the visible flames was observed to have a much longer coverage of the rod. These areas namely, preheating zone, had been highlighted in the Figures. At such zone, the heated flow would preheat the adjacent unburned wood increase the temperature and remove the moisture, make them more readily for the continued pyrolysis progress. As well,

it can be seen that the hot gas layer ahead of the combustion zone became longer with increasing inclinations from -30 to 30. The reason is that the burnt gas flow extended further due to the buoyancy at positive angles. Thus, a conclusion can be drawn that, due to the preheating effects by the hot gas flow on adjacent wood, the pyrolysis progress which is important for fire propagation could be enhanced, especially for the cases at positive inclined angles.

5.3.2.2. The temperature distribution of the burning surface

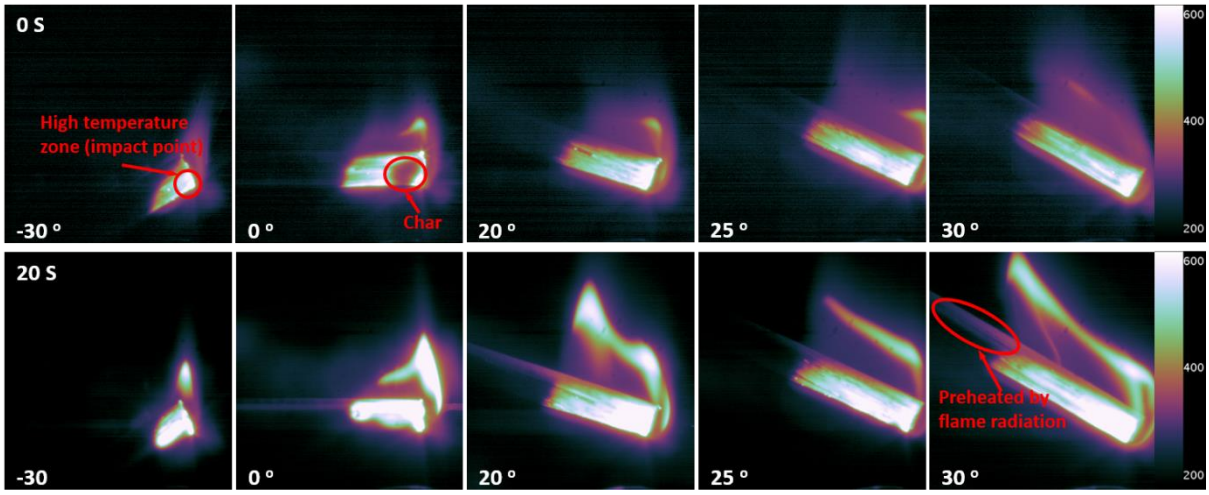

Figure 5.8 An example of the temperature distribution of the burning surface at different inclination angles at $t=0$ s and $t=20$ s.

In Hirano et al. 's study [140], the blackening of the paper is used to measure the pyrolysis, which is less accurate. The pyrolysis cannot be fully indicated by the blackening. In order to trigger the rapid pyrolysis progress, the certain temperature must be reached. The reason for using the InGaAs camera to determine the temperature distribution is because its measurable range overlaps with the temperature of typical wood pyrolysis. The temperature map produced by the infrared camera provides a more precise indication of pyrolysis. The temperature distribution measured by the InGaAs thermal camera can indicate the region

undergoing pyrolysis. As examples, the temperature maps of a burning rod at ranged inclined angles are presented in Fig.5.8. The measured temperature in Fig.5.8 shows the heated area that had exceeded the temperature point for rapid pyrolysis started occurring from other research which is around 300 ^{o}C [55], [147]. This covered almost the whole bright area that the thermal images captured. It is worth noting that the temperature of the surface underneath is higher than the temperature on the upper surface at $\boldsymbol{t} = 0\ s$. The thermal gradient through the wood leads to the upper surface becoming heated. The results could verify the theory from Weber et al. [136] and Hirano et al. [137], that the underside pre-heating is crucial to flame spread along the fuel sample, they set thermocouple at top and bottom of the fuel separately and recorded the thermocouple from the bottom reached the high temperature faster than the one from the top. Unfortunately, it is hard to obtain the accurate temperature response from the thermocouple, especially on the small samples. Comparatively, the use of thermal images with the temperature map in this study could get more reliable results.

It is also found that the high temperature concentrated in the impact point at $\boldsymbol{t} = 0\ s$, however, there are divergences between positive-angle groups and other inclinations at $\boldsymbol{t} = 20\ s$. After the 20s the area underneath the rods at the horizontal and negative angle became dark, meaning that the underneath pyrolysis had almost gone. The temperature at the upper side on the surface was higher. On the contrary, the underneath temperature had a high intensity at positive inclination angles. In addition, the underneath pyrolysis length was increased with the increasing inclination angles. It also can be observed that the upper side flame attachment increased the radiation heat transfer on the upper surface as the upper side

preheating occurred at larger inclination angles. The upper side preheating mainly improved the vertical pyrolysis. With sufficient underneath heating, the fire could propagate further. This phenomenon will be analysed with the synchronised schlieren images and thermal images in the next section.

5.3.2.3. The effect of the underneath preheating on the fire propagation

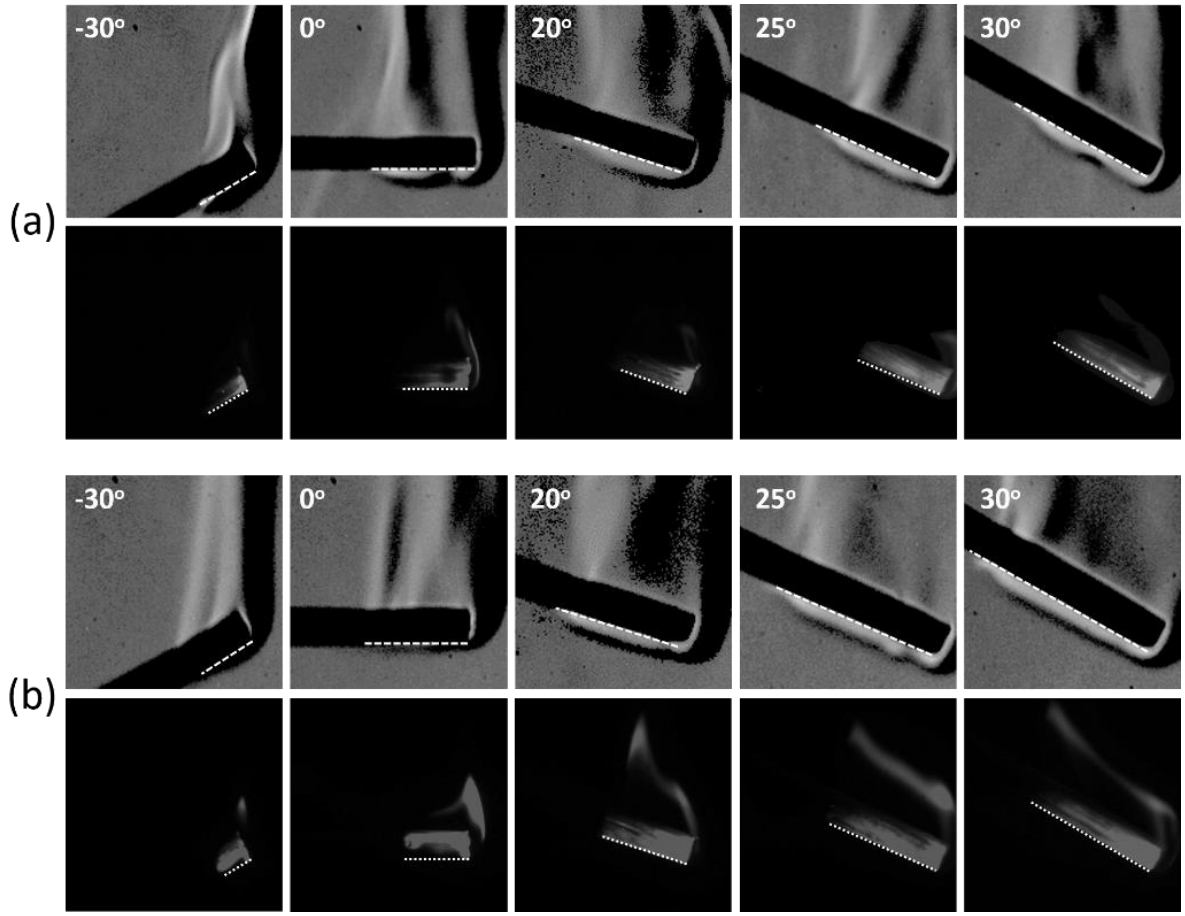

Figure 5.9 The visualisation of the bottom heated area at (a) the point when the piloted ignition is turned off (***t=0 s***) and (b) 20s after piloted ignition is turned off (***t=20 s***). For each time point, top: the schlieren images of different inclination angles; bottom: the corresponding thermal images.

In order to further investigate the underneath preheating is a crucial factor that helps the fire

propagation, the synchronised images of schlieren and thermal images are presented in Fig.5.9. It is worth noting that the hot gas parcel underneath the rod had a significant increase of length when the inclined angle increased from -30^{o} to 30^{o}, which has been marked by the white-dotted line at Fig.5.9. It is found that longer preheating length helps to remove moisture content and to raise the temperature, which makes it more readily for subsequent pyrolysis to sustain the flame.

From Fig.5.9, the comparison of the flow field between the beginning of self-sustained combustion and the 20 seconds after shows this effect. It is notable that the underneath hot gas flow at 0 s was thicker than the topside from the schlieren images. Weber et al. [136] found that the underneath temperature gradient was larger than the one at the topside from the interferometry pattern in their study. Under the hypothesis of constant pressure, it is similar to the density gradient which is obtained by the schlieren image according to the Ideal Gas Law. The thicker hot flow could be considered as an isolation layer which could prevent the convection heat loss from the wood surface to the ambient cold flow, resulting in a higher temperature which is showed in Fig.5.8.

The thermal images have been utilised to present the heated area of the rods. The measured temperature in Fig. 5.8 indicates that the temperature at underneath heated area had exceeded the trigger value for rapid pyrolysis which was around 300 ^{o}C [55], [147]. Longer heated length at positive angles indicated that a larger part of the rod was undergoing the rapid pyrolysis. At $\boldsymbol{t} = 0\ s$, the tips of the rods had hot gas parcels, which indicated the onset of self-sustained combustion. However, at $\boldsymbol{t} = 20\ s$, the hot flow in 0 and -30 degrees angles were almost gone; while the hot flow underneath was longer along the rod for positive angle

groups. The subsequent pyrolysis followed the hot flow direction because the underneath hot gas flow drove the convection upward due to the lateral pressure gradient created by the buoyancy [57] [136]; therefore, instead of propagating along the rod, it progressed from bottom to top. From the thermal images at 0 and -30 degrees at $\boldsymbol{t} = 20\ s$, it can be seen that the top fibre was bright and bottom fibre was dark. With no convective preheating in longitudinal direction, the pyrolysis was limited. This is the main reason that these two cases have a short burning lifetime.

By contrast, at positives angles, hot convection from the longer pre-heating zone ahead of the pyrolysis area improve the flame propagation, then supplying more heat flux for further pyrolysis, not only along the rod but also in deeper layers. This can be observed from thermal images of the positive angle groups in Fig. 5.9, where the bottom fibre was still bright even when there was the presence of char. For understanding the mechanism of burning lifetime, it is found that the charring was the main factor that affects the burning lifetime of wood combustion. Since the lower thermal conductivity of char than wood [57], the charring part acted as a barrier for the pyrolysis in deeper layers. Therefore, higher heat flux was required in order to generate combustible gases from deep layers.

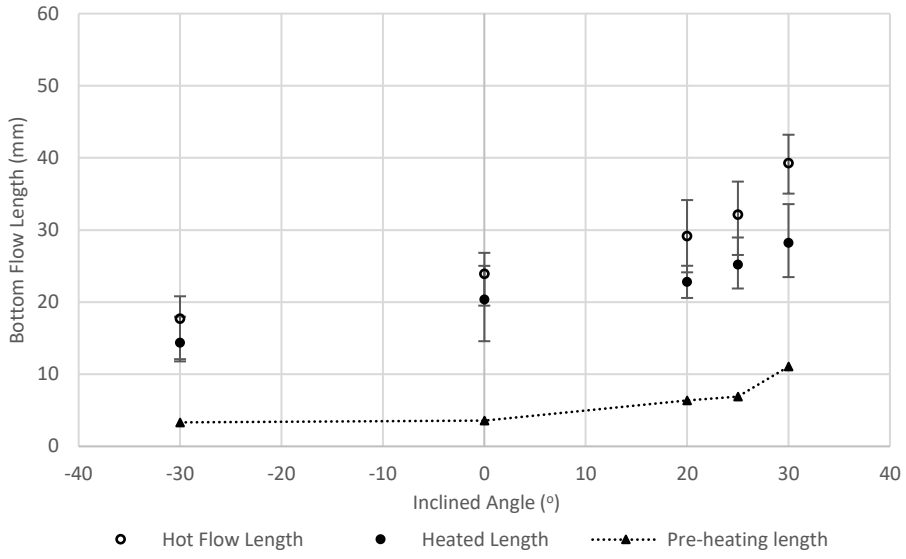

Figure 5.10 The underneath hot gas flow length and the heated length against the inclination angle at the beginning of self-sustained burning.

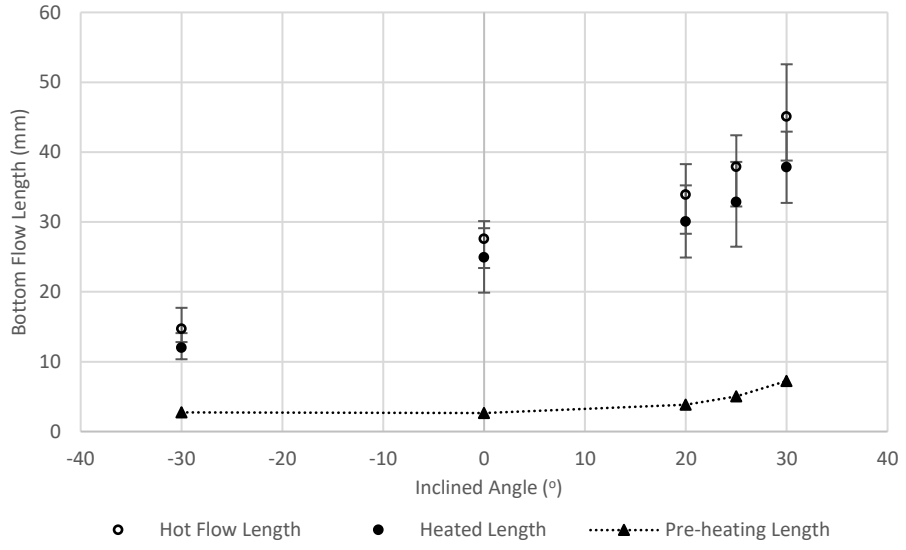

Figure 5.11 The underneath hot gas flow length and the heated length against the inclination angle at 20 s after the start of self-sustained burning.

the comparisons of measured convective hot flow length and heated length are presented in Fig. 5.10 and 5.11. The pre-heating length was calculated by the differences between the hot flow length and the heated length. It is obvious that both hot flow length and heated length

were increased with increasing inclination angle. Meanwhile, it can be observed that the pre-heating length was increased significantly with the increasing positive inclination angle while it remained constant at horizontal and negative angle. The flame spread process requires an amount of fuel pre-heating ahead of the flame[136]. The longer pre-heating length at positive angles enhanced the fire spread and resulted in a longer burning lifetime and charring distance. By contrast, for horizontal and negative angle groups, the heat conduction played the main role in fire spread due to the limited pre-heating length. Under such circumstance, the fire could not spread effectively and result in a shorter burning lifetime and charring distance. In addition, the pre-heating length at $\boldsymbol{t = 0\ s}$ (shown in the Fig. 5.10) was larger than that at $t = 20\ s$ (shown in the Fig. 5.11). The reason can be found that the high-temperature region was concentrated near the impact point after turning off the piloted impinging heat flux.

By comparing Fig. 5.10 and Fig. 5.11, it can be found that the heated length of rods at positive angle cases had larger increases after 20 s of self-sustained burning than those at negative and horizontal inclinations. The larger increase of the heated area suggested there was a higher pyrolysis rate when the rod was inclined at a positive angle. A possible mechanism might be that the larger extent of the hot gas parcel underneath the rod drove the convection upward and then increased the thermal pyrolysis [57]. Overall, in positive inclination groups, a longer preheated length ahead of the pyrolysis area indicated that more virgin wood was readily available for subsequent pyrolysis. More water content had been removed and the temperature had been raised up.

5.3.2.4. The burning process of the wooden rods related to underneath heated area

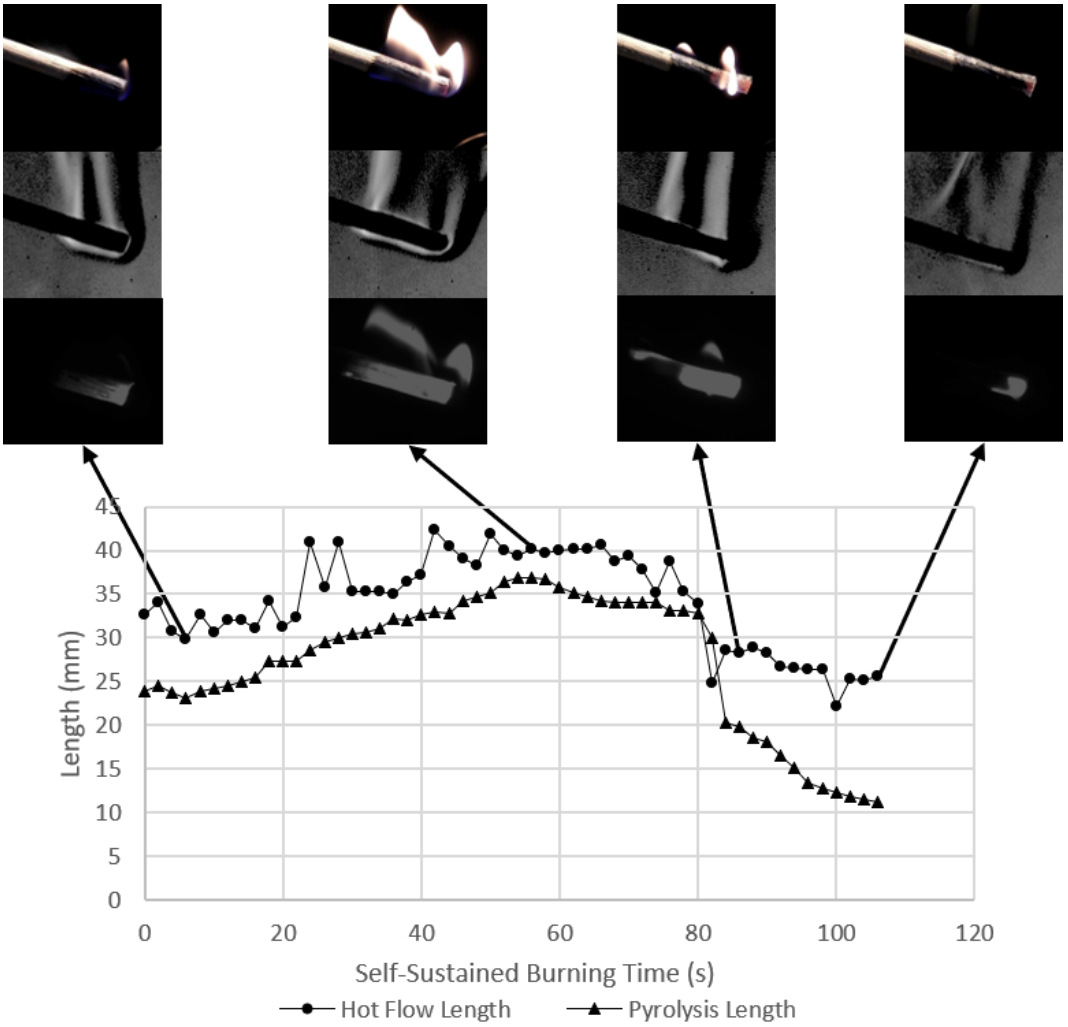

Figure 5.12 The combustion process at 20^{o} inclination angle.

Since the relationship between the fire propagation and the underneath pre-heating, the underneath hot flow length and pyrolysis length can be used to track the combustion process of burning woods. Based on the results in Fig. 5.12, the wood combustion can be summarised with three stages: the acceleration, the deceleration and the extinguishment. At the first stage, both the hot flow length and pyrolysis length had increased from the start of self-

sustained burning to around 60 s, while the heat convection at this moment was the strongest. Although the actual flame was weak, the subsequent combustion would be accelerated due to the long pre-heating zone ahead of the pyrolysis area. The preheating had strongly promoted the pyrolysis progress. After the peak point, the hot flow length rarely increased, as a consequence, the fire propagation stopped. After 80 s of self-sustained burning, both the hot gas length and the pyrolysis length shrank, indicating a weakening combustion because of the lack of sustainable pyrolysis gases. It can be seen that the top fibre was bright while the bottom fibre was dark. As the decreased heat convection was insufficient to sustain the combustion, the longitudinal pyrolysis was limited and the wood burning gradually extinguished.

5.3.3. The effect of flame attachment phenomenon

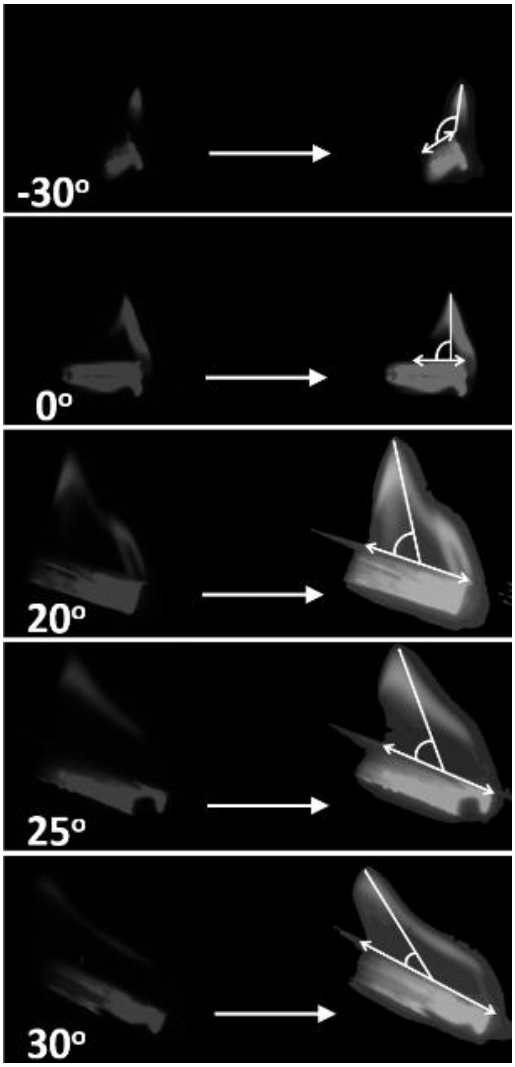

Figure 5.13 The thermal images at different inclination angles at 20 s after the turning off the burner, the original images (left column) and the enhanced images (right column)

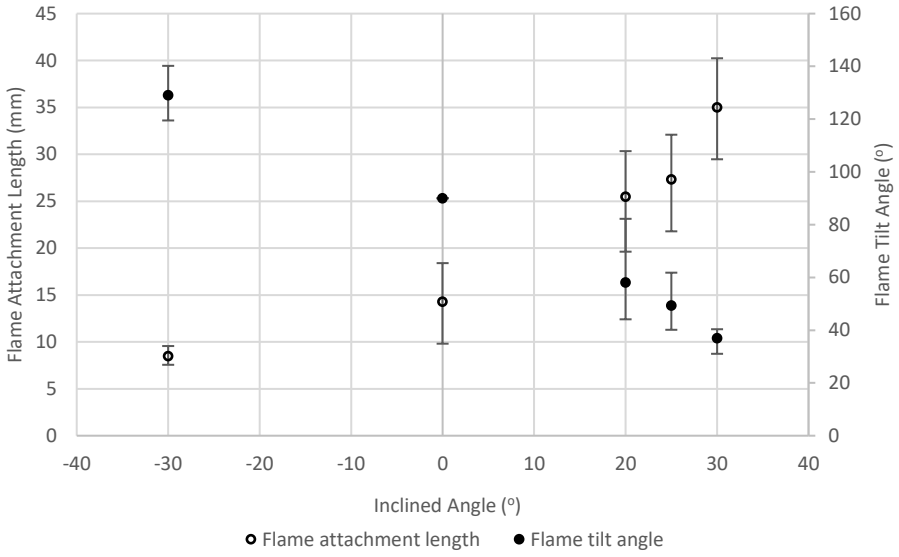

Figure 5.14 Flame attachment length and flame tilt angle against inclination angles.

Be different from the blue flame underneath the rod which helps the flame propagation longitudinal, the attachment of the flame on top of the rod improves the combustion in the perpendicular direction. As the inclination angle increases, the difference in air entrainment between both sides (caused by the buoyancy) produces a local pressure imbalance [141]. As a result, the flame is more prone to lean onto the rod, which helps with flame propagation. Such phenomenon can be proved by the experimental results presented in Fig. 5.13. More specifically, the attachment of the flame increased the length of the rod submerged into the hot convective flow.

As indicated in Fig. 5.13, the flame attachment length was measured as the contacting area of the flame and rod; the flame attachment tile angle was measured as the angle between the connecting line and the rod, whereas such connecting line was defined from the frontmost tip to the midpoint of attachment length. From the results in Fig. 5.14, it can be seen that the attachment length was directly proportional to the inclination angle. There was an abrupt change in this length from 25 degrees to 30 degrees, in details, 1.536mm/^{o} in averaged, as

three times larger than the results at other inclinations. This phenomenon shows good agreement with the previously reported critical inclination angle [71]. The longer flame attachment length could significantly increase the convective heat transfer between the flame and the fuel and then enhance the burning [148].

Moreover, the flame tilt angle was sharply decreased with the increasing angle. A smaller attachment angle led to the higher radiative heat transfer which was from the diffusion flame above the rod, because of the increased the view factor and shorter distance which could enhance the pre-heating on the upper surface. With the aid of perpendicular propagation, it is very probable that the rate of decomposition for combustible gases is higher; therefore, the flame is more likely to be sustained [71].

5.3.4. Observation on the impact point of piloted impinging heat flux

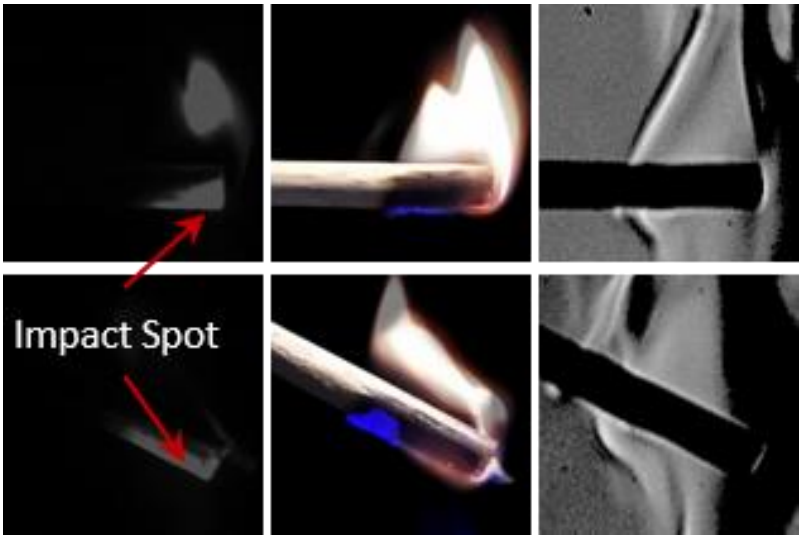

Figure 5.15 The comparison between 0 degrees and 30 degrees at 1 second before the piloted impinging heat flux is turned off. Top row: 0 degrees; Bottom row: 30 degrees.

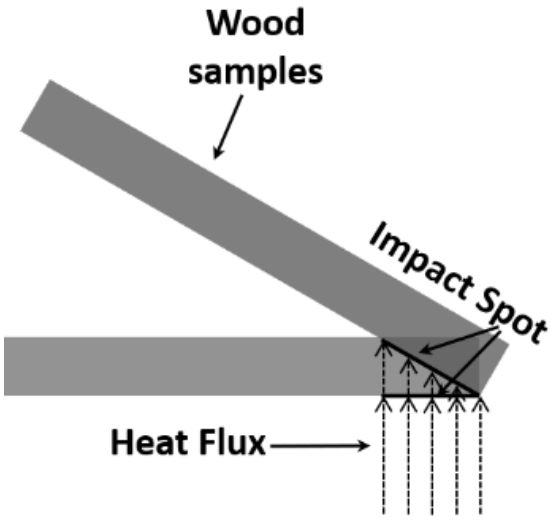

Figure 5.16 Demonstration of the effect of inclination on impact spot.

The self-sustained combustion starts from the location other than the contact spot with the impinging heat flux. As indicated by the red arrow in Fig. 5.15, the impact spot was subjected to the intense heat flux during piloted ignition. Rapid pyrolysis and char formation took place in deep layers, causing a locally fuel rich diffusion flame. The temperature at this spot was much higher than the adjacent regions in the thermal images. Combustible gases produced were quickly ignited by the piloted heat flux. By contrast, in the vicinity of the impact spot, the temperature gradient was less sharp; the deep layers gradually reached pyrolysis temperature, which can be observed from the selectively enhanced blue flame. This phenomenon was observed from most cases at inclined angles.

By comparing the images of 0 degrees and 30 degrees, it is found that the longer length of the rod was heated by the impinging heat flux during the ignition at an inclination of 30 degrees, as well more combustible gases were produced. For positive inclination angles, more inclination means a longer length submerged in the impinging heat flux which is demonstrated

by Fig. 5.16. Consequently, the rods inclined at large positive angles have a strong initiation for self-sustained flame propagation.

5.4. Conclusion

With a systematic visualisation, the influences of the inclination angle on fire propagation were investigated. The schlieren imaging revealed the hot convective flow field both above and underneath the oak rods. Its propagation mechanism was visualised. Meanwhile, thermal imaging gave the temperature distribution of the surface of the rods, which was affected by the preheating of the convective flow field. Despite uncertainties caused by texture variation and discrepancies of wood rod production, the experimental results showed a general trend that fire propagation and flame attachment length increase as the inclination angle increases; the sharp increase from 25 degrees to 30 degrees corresponded to the critical point beyond which the flame propagates more rapidly. The physical mechanisms as to how the flame propagated were studied by means of combined visualisation.

The effects of the inclination angle on improving the flame propagations were attributed to three main effects. Firstly, convective preheating is essential for longitudinal pyrolysis, hence aids to the fire propagation longitudinal; for positive inclinations, the larger is the angle, the longer will be the preheating length, which in turn resulted in a longer progression of flame along the rod. Secondly, the increased flame attachment length at positive inclinations helps pyrolysis in the perpendicular direction to the rod. Thirdly, in the case with piloted impinging heat flux, the inclination affects the initiation of the self-sustained flame propagation; because a longer length of the rod is submerged in the heat flux at ignition for positive inclination

angles, from which more combustible gases are produced at the start of self-sustained flaming.

6. The study of the fire spread under different cross-wind conditions

6.1. Introduction

The burning of wood behaviour in still air has been extensively studied in the aspects of burning rate[14], [149], aerodynamics[150], flame dynamics[151], and radiation[152], the researchers have achieved remarkable progress[79]. The burning in the still air condition is easy to control due to the burning being buoyancy-driven solely. However, the fire disaster mainly occurs with the involvement of wind flow. The study becomes much more complicated with the presence of wind, as the involvement of wind flow significantly changes the flow field, flame morphological characteristics, ways of heat transfer and more[79]. The study of the burning of wood with wind flow mainly focuses on the effects of the cross-wind, which is the air flow in the direction parallel to the fire propagation of in the lateral side of the flame. The cross flow, which influences the burning behaviour mainly, is attributed to the horizontal momentum generated by the flow counteracts with vertical buoyancy generated by the fire[15].

The effects of the cross-wind are complicated and involved various aspects. Researchers have studied the burning behaviours under forced wind flow from multiple aspects, such as the burning rate, the geometry of flame, mass loss rate, flow field, effects on the heat transfer, and temperature.

As one of the basic parameters representing the burning behaviours is the burning rate under a forced air flow has been extensively studied. Welker et al. [153] found that the burning rate of methanol fire decreased with the increasing wind speed. The phenomenon that the burning

rate decreases with higher wind speed is similarly found in the researches of Apte et al. [153], Saito et al.[154] and Carvel et al.[155] as well. However, with a more detailed experimental study, Woods and Kostiuk [156] found the change of burning rate depends on the size of the square pool, which could show monotonic increase, constant, or non-monotonic response. In the study of McAllister et al. 's [157], the non-monotonic change of burning rate with increasing wind speed had been found from the different design of wood cribs, and the change of burning rate with increasing wind speed depends on the types of various design cribs. In addition, from the works of Hu et al. [158], it is also found there were turning points of wind speed inside various sizes of the pool, in which the monotonicity of burning rate changes.

As another aspect, it has been found that the geometry of flame can be significantly affected by the cross-wind. Lin et al. [15] had studied the behaviours of pool fire on the inclined surface under the cross-wind, they had concluded that the flame height decreases with the increasing wind speed, while the larger inclined angles increase the flame height. Concerning the flame tile angle, it is wildly acknowledged that the tilt angle of the flame increases with the increasing wind speed[158][159][160]. The changes of flame geometry under cross-wind are mainly caused by the existence of the negative pressure zone generated by the wind[15].

Regarding the effects of cross-wind on temperature, Himoto[161] used a series of thermocouples to read the temperature distribution on different height and distance of fire plume. From his research, it is found that the temperature along the trajectory of the fire plume is the highest, and the temperature influenced by the cross-wind depends on the location of the fire plume. Luan et al. [162] utilised an experimental wind tunnel to simulate the effects of canyon cross-wind on the temperature of smoking progress. They used

thermocouples to read the smoke temperature inside the wind tunnel and found the temperature changed with the different positions and wind speed with a general decrease with increasing wind speed. In the work of Salvagni et al.[159][160], the thermography was used for re-building the temperature map of flame under various wind speed. It is found that the temperature in the reaction region was increased with increasing temperature due to the additional air mixing, while the temperature was decreased in the edge of the flame because of the higher heat loss rate.

Besides the experiments, the air flow field had been simulated by CFD (Computational Fluid Dynamics) as well. In Eftekharian et al.'s work[163], the computed results indicated that the cross-wind acted as a driving force to accelerate the flow and cause the wind enhancement downstream of the fire source. From the simulation results of Zhu et al.'s [164], it is found the flow fields near the fuel pan varied from horizontal surface to inclined surface.

Many researchers focused on the wind effects on the geometry flame, burning rate, and mass loss, which are the general properties of wood combustion. Others studied the flow field change under cross-wind by computing simulation. However, according to the literature reviews, it is found that there are few publications focused on how the cross-wind influences the fire spread along the wood surface. Besides, as one of the most important parameters, the surface temperature of the wood surface under cross-wind has not been studied. The challenge can be considered that the invasive temperature measurement devices are hard to be applied due to the high temperature at the burning zone and the disturbance produced by the installation of devices. Meanwhile, the flow field, especially the underneath flow layer, could be a crucial factor in sustaining burning and spreading the fire, studied in the previous

work under the still air condition[165]. However, there is no publication that visualising the hot flow layers under the cross-wind. As these research gaps mentioned above, a novel imaging system which synchronised the visible, schlieren and thermal images with the temperature measurement by thermal imaging metrology and two-colour method has been developed for studying the effects of cross-wind on the fire spread on a single wooden rod. The use of single element fuel could be easy for experimental control, in addition, the underneath hot gas layer is achievable by using a single rod. This study uses two inclinations which are horizontal and 30 degrees, for simulating the different circumstances in practice. The non-invasive temperature measurement is suitable for the study of wood combustion as the temperature can be obtained from a distance. The two-colour method is suitable for reading the soot flame temperature and the thermal imaging is sensitive to a slight change of temperature which is adequate for the burning surface temperature measuring. With the help of the schlieren imaging system, the flow field around the burning wood can be visualised. By synchronising the different images, the mechanisms of the cross-wind effects on fire spread can be studied.

6.2. Experiments method and setup

6.2.1. Sample setup

The samples were made of oak wood, of which the density is higher than the samples utilised in Chapter 4 and 5. This change ensures the longer burning lifetimes of samples and improves the accuracy of results. All the samples were cylinder-shaped of 9.5 mm in diameter and 400 mm in length. All the samples have been pre-dried in an electrical furnace for 24 hours at the temperature of 150 ^{o}C to reach the minimum humidity.

In the study of this chapter, the samples were fixed at the horizontal direction and 30 degrees by an adjustable holder, shown in Figure 6.1. Each test was operated at 40 mm above the burner to ensure the same burning conditions. The fuel of premixed methane-air was used to ignite the samples for 40 s. An adjustable fan with five different wind speed set was set in front of the initial burning zone to provide the cross-wind with the same direction of the fire propagation, where the details of wind speed are presented in Table 6.1. For the measurements. The wind speed was measured at the end of rods and 20 tests were made for the averaged measurements. The fan would be turned on once the burner turned off (the stage of self-sustained burning began). In order to provide a relative homogenous cross-wind, a designed wind diffuser with five mesh layers was set in the front of the fan.

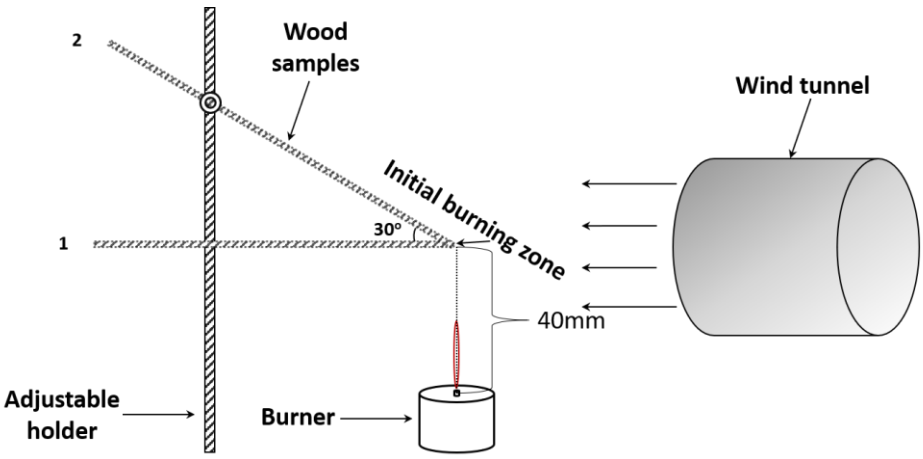

Figure 6.1 Schematic representation of the experimental set-up.

Orientation (º)	Premix fuel (L/min)		Ignition time (s)	Cross-wind speed (m/s)	
0	Methane	0.34	40	Speed 0	0
				Speed 1	0.40
				Speed 2	0.49
30	Compressed air	0.9		Speed 3	0.62
				Speed 4	0.71
				Speed 5	0.77

Table 6.1 The parameters of experiment setup

6.2.2. Imaging system

The imaging system of this study comprised of multiple cameras, including a black-white high-speed camera which is used for a Z-type schlieren system; a CMOS high-speed colour camera which is used to measure the soot flame temperature after a calibration process; an InGaAs thermal camera which could capture the 60 frame rates thermal image with a cut-on filter to restrict its spectral sensitivity to 1550-1670 nm for measuring the temperature on the wooden surface. In this study, the camera was calibrated with the fixed 16 ms exposure time to measure the temperatures in the range 300-750 ^{o}C. A raspberry pi camera that could record the 30 fps videos was applied for capturing the actual images. All the cameras were synchronised with each other and corrected with the same angle and position. The illustration of the imaging system is shown in Fig.6.2 below.

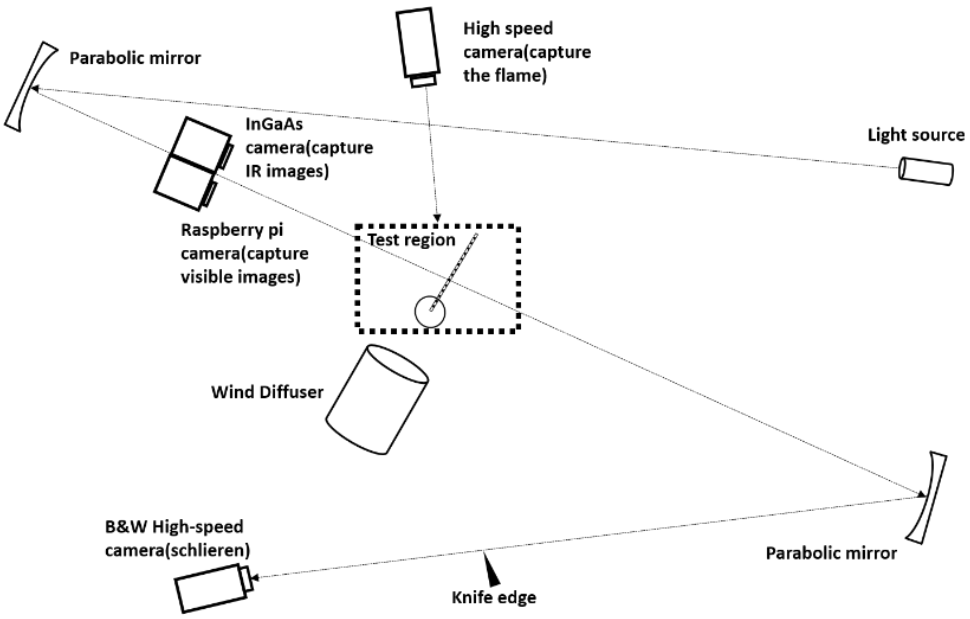

Figure 6.2 The top view imaging system and experimental setup.

6.2.3. Data processing

In this study, the results obtained from experiments have been analysed in three aspects: the general burning status including the burning lifetime and the charring rate; the temperature distribution including both the flame and the surface of the burning rod; and the invisible hot gas flow around the burning rods. Besides, the results of two different inclination angles are analysed separately and then compared with each other to determine the different mechanisms. The techniques, including the two-colour method, thermal imaging metrology and the schlieren imaging system, have been utilised in this chapter. The details are shown below:

- For the burning status of rods, the results can be analysed from the actual images captured by the raspberry pi camera. Similar with the Chapter 5 and 6, the self-sustained burning lifetime and averaged charring rate were calculated to represent the ability of self-sustained burning and fire propagation.

- For the flame temperature measurements, the two-colour method was used. The two colour temperature method can be used to measure the temperature of solid objects. As one of the important applications of this method, the temperature of soot flame can be well measured by two colour method. Since the product of wood combustion has a high concentration of soot particles which was well-distributed in the flame [88]–[90]. The high-speed colour camera was pre-calibrated and was able to measure the temperature above 850 ^{o}C to cover the flame temperature range of burning. Further, by analysing the flame temperature distribution, the effects of cross-wind on how to enhance or cool the burning as well as the combustion products can be studied.
- For the rod surface temperature, the single wavelength temperature measurement method was utilised to obtain the surface temperature whose spectral emissivity is known. In the study, the InGaAs thermal camera was calibrated in the temperature range from 300-750 ^{o}C. Based on the temperature map of the wooden surface, the burning on the wooden rods can be studied by both quantitative and qualitative analysis.
- In addition, combined with the different type of images, the burning process can be studied by visualisation, such as the burning front, the preheating from the hot gas and the cooling.

6.3. Results and discussion

The results about the effects of wind on self-sustained burning and the fire spread on the 0^{o} and 30^{o} wood surface are presented in Section 6.3.1 and 6.3.2 respectively. In Section 6.3.3, the difference of cooling mechanism between the inclination of 0^{o} and 30^{o} will be discussed.

During the experiments, all the cases had been repeated 6 – 10 times depending on their repeatability. Although there were a few cases that were abnormal from others, such as the sudden flaming distinguishment and the blockage of fire propagation, most cases in a group showed good repeatability and had a similar combustion performance. In order to achieve more realistic simulations, the samples were selected from the real natural wood rod which has a complicated and inhomogeneous internal structure [54] which resulted in the deviation from the results, the deviation of these experiments are natural and acceptable based on the repeatability of experiments. In order to further improve the accuracy of this study, each experiment was repeated as many times as possible to verify these abnormal cases. There were a few abnormal cases which suddenly extinguished during the burning, it is highly possible that such phenomenon is caused by the interior fibrous structure of wood which has a very high density when fire propagated into these areas, the combustible gases cannot escape to the surface then led to the lack of burning fuel which stopped the chemical burning process. In addition, the fire was harder to spread through these zones due to low hear conduct. After checking these abnormal samples, the most possible reason is the internal structure was damaged by the machining process. Therefore, these abnormal cases were highlighted from the results, but not counted in the averaged values.

In this section, all the experimental results are presented with the averaged and shown both the maximum and the minim values are provided as reference. Regarding the visualisation results and temperature colour map, the results of one case in a group will be used as an example to illustrate the experimental phenomenon, the chosen case was decided as the most representative case while the others showed good repeatability to the chosen ones.

6.3.1. The cross-wind effects on the self-sustained burning at 0^o

6.3.1.1. The burning status

The direct images of burning in the horizontal direction are shown in Fig.6.3. The images in each row images indicate different burning times, including the start of self-sustained burning, 10s and 20s after it (15s in the speed 5 case). The burning with different wind speeds is presented in different lines, including speed set of 0, 1, 2, 3, 4, and 5, where the details of these cross-wind have been introduced in Table 6.1 in Chap. 6.2.1.

It can be seen that the flame was perpendicular to the horizontal surface without the cross-wind, shown as the Figure at the first row in Fig.6.3. When the cross-wind of the same direction of fire propagation was involved, it can be seen that the flame bent into the wood surface. As a general trend, it can be found that the flame tilt angle tended to be smaller with the increasing wind speed. Especially when the wind speed was increased into the speed 4 and 5, the flame attached tightly onto the wood surface. For the burning status, it can be seen that the flame became weaker after the 20s of self-sustained burning (15s in speed 5) at the speed 0, 4 and 5. However, at the speed 1, 2 and 3, the flame became stronger. In particular, the intensity and size of the flame under wind speed 2 dramatically increased after the 20s. This means under such cross-wind speed, the flame was enhanced. Moreover, in the case of speed 2, there was blue flame appeared on the underside of the wood rod. The appearance of blue flame indicated that there was a high concentration of flammable gases which was explained in Chapter 5. It can be found that, as one of the important parameters which affect the burning, the surrounding wind field is not only able to suppress the combustion, but also able to enhance the flaming. Proper flow conditions, as the speed from 0 to 0.6 m/s would

strongly enhance the burning on the wood rod in diameter of 9.5 mm. Any flow speed beyond this range would have negative effects on the combustion.

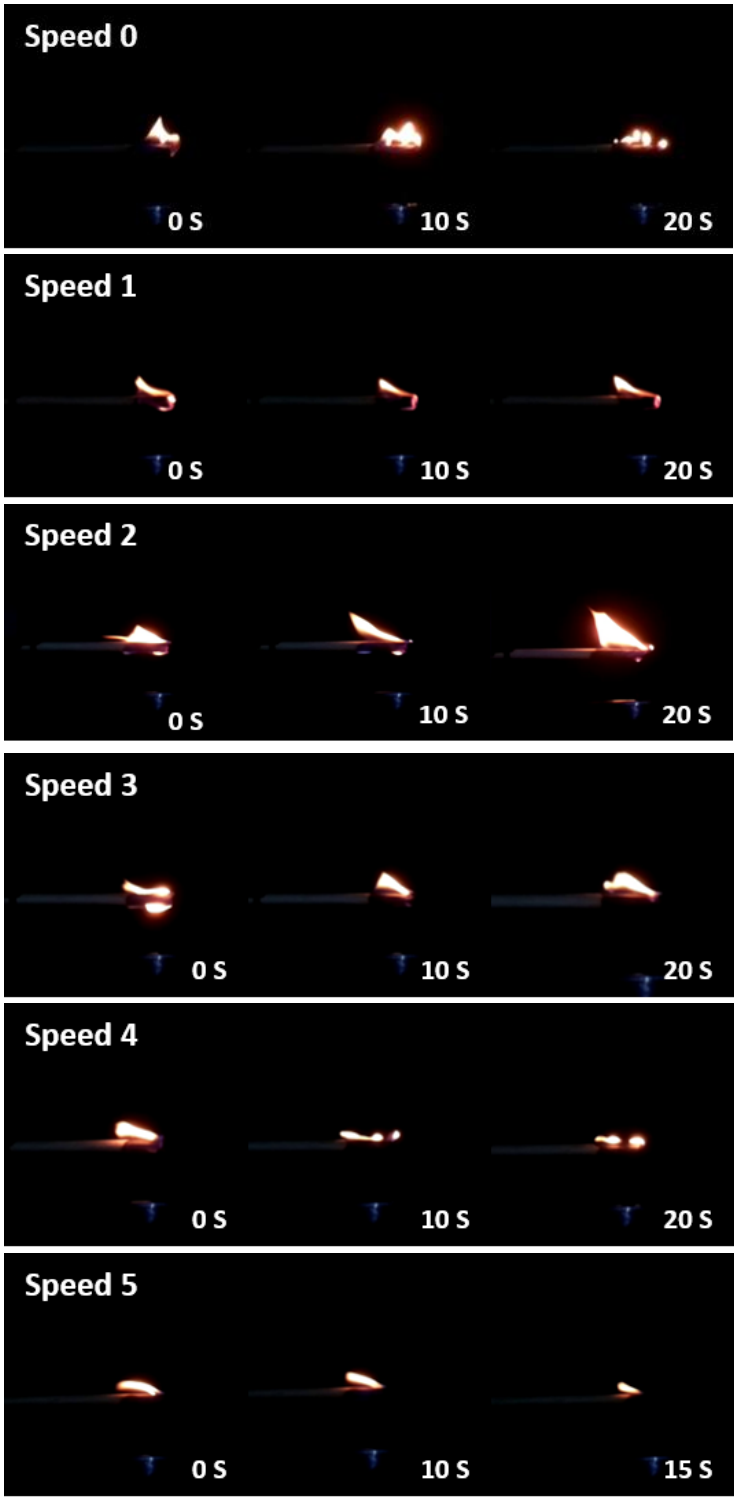

Figure 6.3 The direct images of self-sustained burning at the different timing at the 0 degrees inclination with different speed of cross-wind.

6.3.1.1.1. Burning lifetime

The burning lifetime was calculated from the time period since turning off the burner (the beginning of self-sustained burning) until the fire completed extinguishment. Fig.6.4 presents the averaged burning lifetime under different cross-wind speed. Both the maximum and the minimum values of the burning lifetime for each case are presented in the Figure to introduce the value range as well. It can be seen that the burning lifetime at the wind speed set 1 and 2 were significantly increased by comparing with no wind case, namely 'enhanced group'. Also, these two cases had a relatively higher deviation of results, this is because the inhomogeneity of internal wood structure could emerge more frequently. The speed 2 case of 0.49 m/s could be considered as the 'turning point' of the experiments, that the burning lifetime tends to be decreased while the wind speed beyond this value. Comparing with the results of speed 0, 1 and 2, it can be found that the burning at speed 3 and 4 became weak with the increasing wind speed, called as 'reduced group'. For the case at speed 5, all the cases in the group extinguished within the 20s since the extreme strong flow field, called as 'extinguishment group' which means the fire is unable to be sustained under such wind speed.

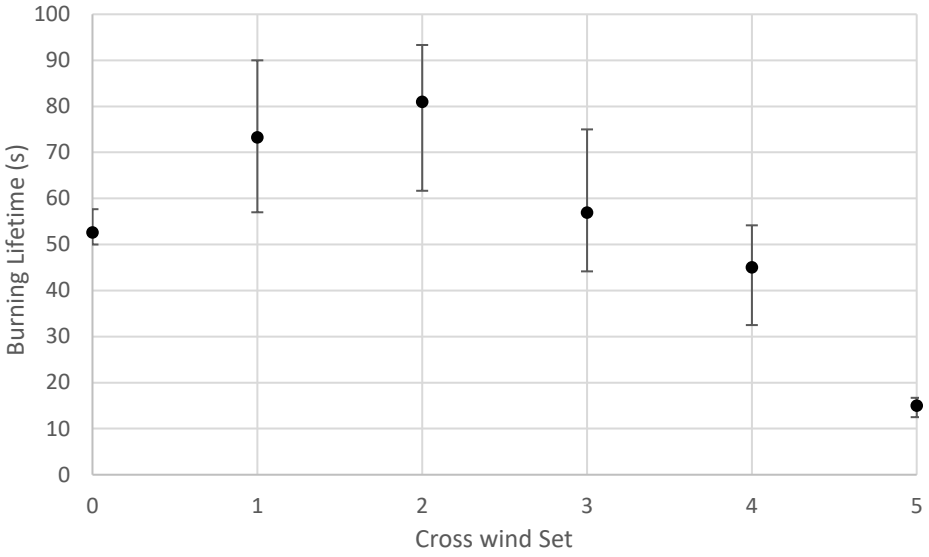

Figure 6.4 The averaged burning lifetime against different cross-wind set at 0 degrees.

6.3.1.1.2. Charring rate

The charring rate was calculated by the averaged charring front moving speed during the first 20s from the beginning of self-sustained burning (the case at speed 5 was averaged from 0s to the extinguishment), shown in Fig. 6.5. The results of the charring rate have a similar trend with the burning lifetime in Fig.6.4, that the burning was enhanced at the lower wind speed until the peak at speed 2, then the charring rate was decreased with the larger wind speed. It is worth noting that the high velocity of the cross-wind had negative effects on both the lifetime of burning and the charring rate. It is attributed to multi factors, and the following section will study the mechanism of wind effects from the surface temperature and the invisible hot gas flow around the rods.

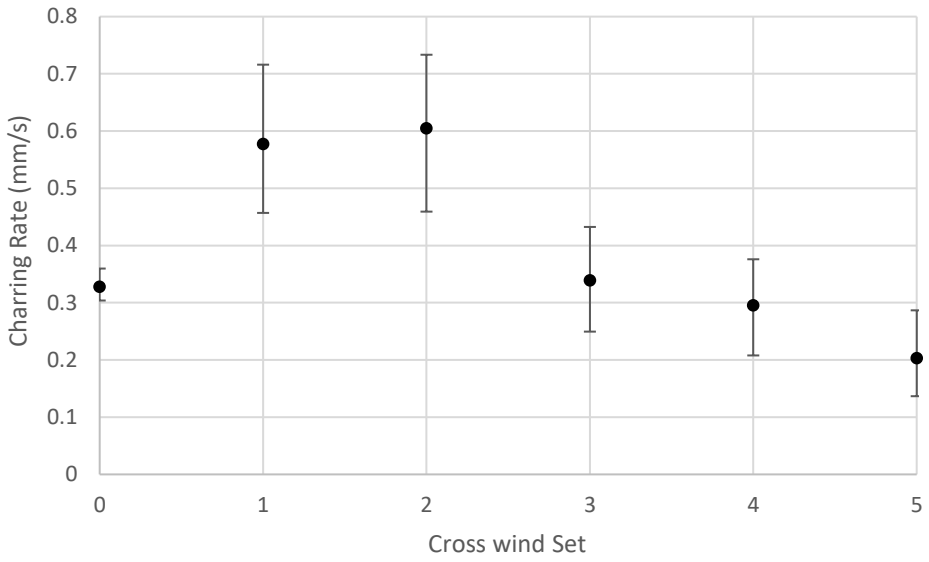

Figure 6.5 The averaged charring rate against different cross-wind set at 0 degrees.

6.3.1.1.3. Flame temperature

Due to the small size of the flaming on the horizontal surface, the number of image pixels captured by the camera was small. The flame temperature distribution of such small burning on the horizontal surface at one single flame profile might be not critical enough. Instead, the results of flame temperature in every single frame were averaged in order to determine the wind effect during the whole burning progress.

The averaged soot temperature was calculated by the two colour method with an IR cut off filter and assumed as the wood flame temperature, and equation 3.12 of RG channels were used to calculate the temperature. The results of soot flame temperature during the first 20s of self-sustained burning is shown in Fig.6.6. It is found that the flame of the control group (no cross-wind) had the highest temperature. With the cross-wind involving, the flame temperature was decreased at all the wind speed cases. The cross-wind increased the heat

loss of the flame to the surrounding cold air. However, the flame temperature was not affected by the wind speed significantly at 0 degree. The reason is that although the heat loss was increased under the higher velocity of cross-wind, the stronger flame attachment under this condition made the larger area under heat pyrolysis. In addition, the higher speed of wind increased the mixing rate of fuel and oxygen[159]. Moreover, due to the smaller flame tile angle in the higher wind speed case, a smaller area was contacted with the surrounding cold air. Therefore, these reasons counteracted the temperature reduction. Besides, the flame burned on the 0 degrees surface only appeared on the topside under the sets of wind flow in this study. The different wind speed did not strongly change the property of the flame, which is another reason the different wind speed did not affect the flame temperature significantly.

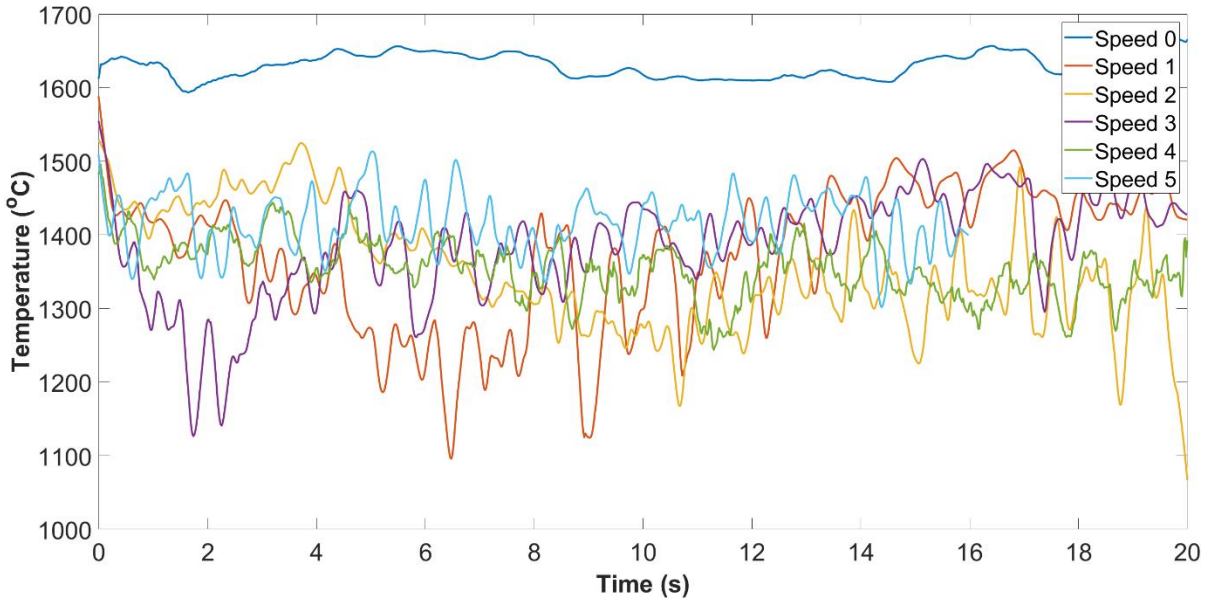

Figure 6.6 The time-dependant averaged flame temperature of 0 degrees group under different cross-wind speed during the first 20s.

6.3.1.2. The temperature of the wood surface

In order to study the effects of the cross-wind on the self-sustained burning in the horizontal

direction, the temperature of the wood surface had been calculated and shown in the temperature colour map in Fig.6.7. The three different frames in each row present the burning at different timing, including 0 s (the fan starts to be applied), 10 s and 20 s respectively (in the case of speed 5, 0s, 10s and 15s are chose considering its extreme short burning lifetime).

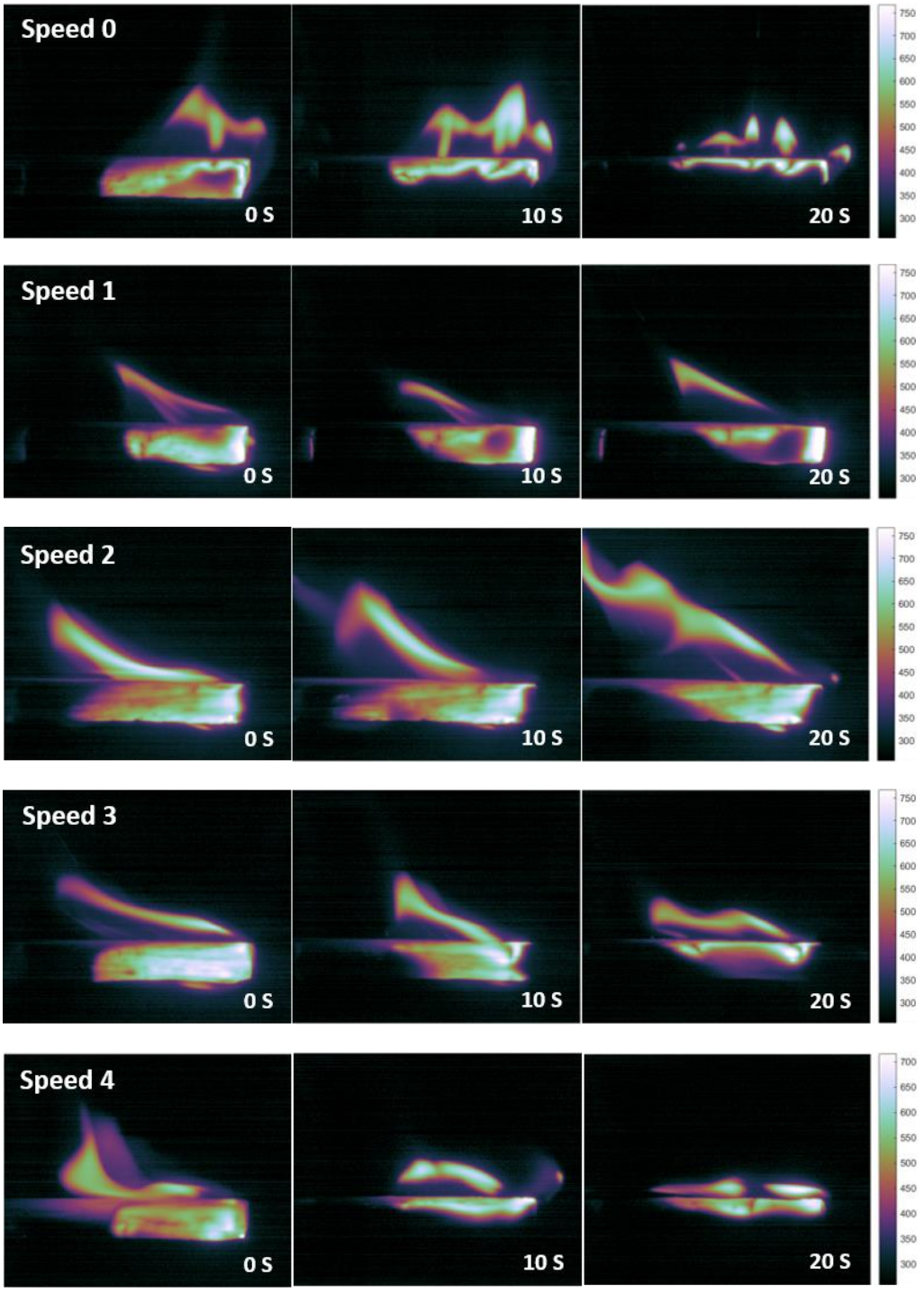

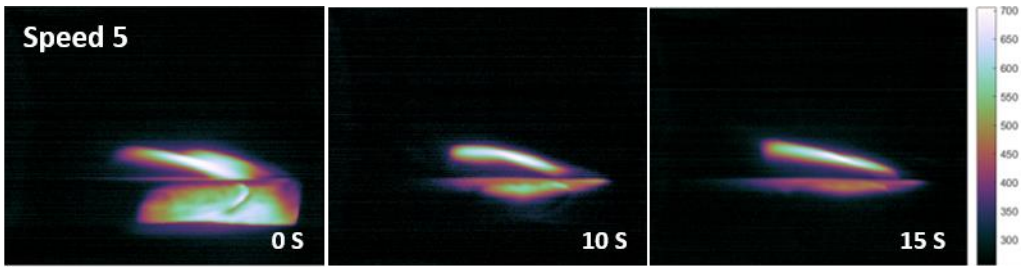

Figure 6.7 The surface temperature map at the 0 degrees inclination with different speed of cross-wind and timing.

It can be seen that at the 0s, although there were a few areas whose temperature is lower than the average (charred points, results in high density of the fibre[57]), the wood rods had been completely heated at both the topside and the bottom. After applying the cross-wind, the temperature of the surface of the rod started to be decreased from the bottom side. From the speed 0 case as the control group, it can be seen that the bottom temperature had been cooled under 300^{o}C (seen as the rapid pyrolysis temperature of the wood[57][59][60]) within 10s and continued to decrease the deeper layer from the bottom at the 20s. A conclusion can be drawn that the cooling mechanism of the burning at the horizontal surface is derived from the underneath. This phenomenon is attributed to the lack of the underneath hot gas parcel which had been discussed in Chapter 5. The insufficient convective heat transfer from the underneath hot flow resulted in a short burning lifetime and less ability of fire spread in the horizontal direction.

Comparatively, with the involving a lower speed cross-wind, it can be found that the temperature on the bottom side of the surface decreased slower than the speed 0 case, such as the results of speed 1,2 and 3 at 10s. The second images (t=10 s) in different lines showed that the bottom surface still had a relatively high temperature which was higher than 500^{o}C

at 10s of burning time. The high temperature indicates there was still a high rate of thermal pyrolysis and gas-phase combustion. At the 20s, the bottom temperatures at speed 1 and speed 2 were still high enough for the rapid thermal pyrolysis. In contrast, the bottom temperature at speed 3 was decreased nearly to the pyrolysis temperature which is 300^{o}C. The possible reason for this phenomenon is that the low speed of wind could enhance the underneath hot gas flow, then prevent the cooling from the bottom side. In addition, the increased mixing rate of oxygen and fuel enhanced pyrolysis. With the increasing speed of cross-wind, such as the cases of speed 4 and 5, a large area of the surface from the bottom side had been cooled within 10s, the cooling rates were higher than the control group (speed 0).

Moreover, at the 20s of burning time at speed 4 and 15s at speed 5, all the bottom surface had been cooled and extinguished. The rapid thermal pyrolysis just happened in a few areas near the top flame. The possible reason for the accelerated cooling with higher wind speed was that the high velocity of cross-wind blew off the underneath hot parcel, and the wind increased the heat transfer from the wood surface to the cool air. Meanwhile, it can be found that the cooling was started from the bottom side of the self-sustained burning on the horizontal surface. When the temperature decreased lower than 300 ^{o}C, the reaction was mainly in the solid-phase oxidation and favoured to produce the char[57], which further impeded the heat transfer. Comparatively, the low-speed cross-wind could enhance the intensity of the burning by decreasing the bottom side cooling. The continuous heating from underneath helps keep the temperature, resulting in a higher gas-phase combustion rate. Speed 2 was the turning point of this experiment set, with the increasing wind speed, the

underneath surface accelerated the cooling. The wind speed of set 5 significantly accelerated the cooling of the surface both on the bottom side and the topside, then extinguished the burning in a short time.

In order to achieve a better understanding of how the wood rod was cooled down at the different speed of cross-wind. The temperature during the first 20 s of burning time at a selected line on the wood surface had been presented as 3-D Figures. Fig.6.8 indicates the position of the chosen line which is 5 mm in length from the rod end. The selected line locates on the position near the impact point where has a higher heat concentration. This temperature at the selected position could better represent the cooling condition of the whole wood.

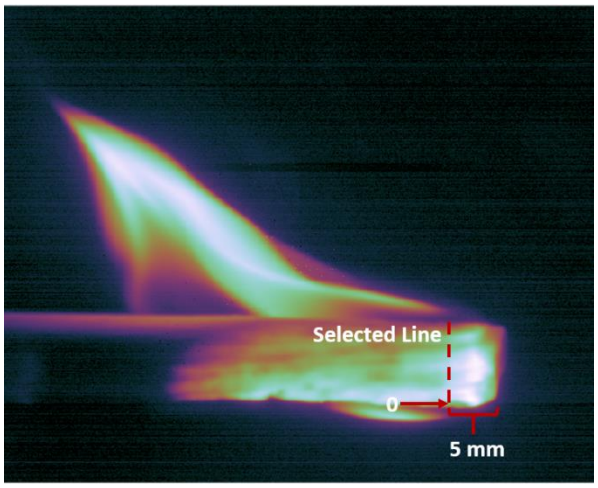

Figure 6.8 The illustration of the selected line position.

Fig.6.9 presents the selected line temperature against time. The x-axis indicates the burning time from 0 s to 20 s, the y-axis indicates the position which is from 0 mm (the bottom) to 10 mm (the topside), and the z-axis indicates the surface temperature. It can be seen that at the beginning of the self-sustained burning (0 s), all the five groups had a high temperature

underneath. This is because the ignition came from underneath, there also was a high concentration of heat around underneath at the beginning. As the Speed 0 shown in the temperature map in Fig.6.9 (a) which is the basic group without the cross-wind, it can be seen that the surface temperature decreased from underneath. It verifies the conclusion drawn in Chapter 6, that the underneath preheating plays an important role in sustaining the burning as well as the heat transfer from fire propagation. Since the heat from the underneath would transfer upward along the wood (due to buoyancy) to keep sustaining the burning. In addition, the fire could propagate forward if there was sufficient underneath convective preheating. With the involvement of the cross-wind, there were significant changes in the temperature distributions.

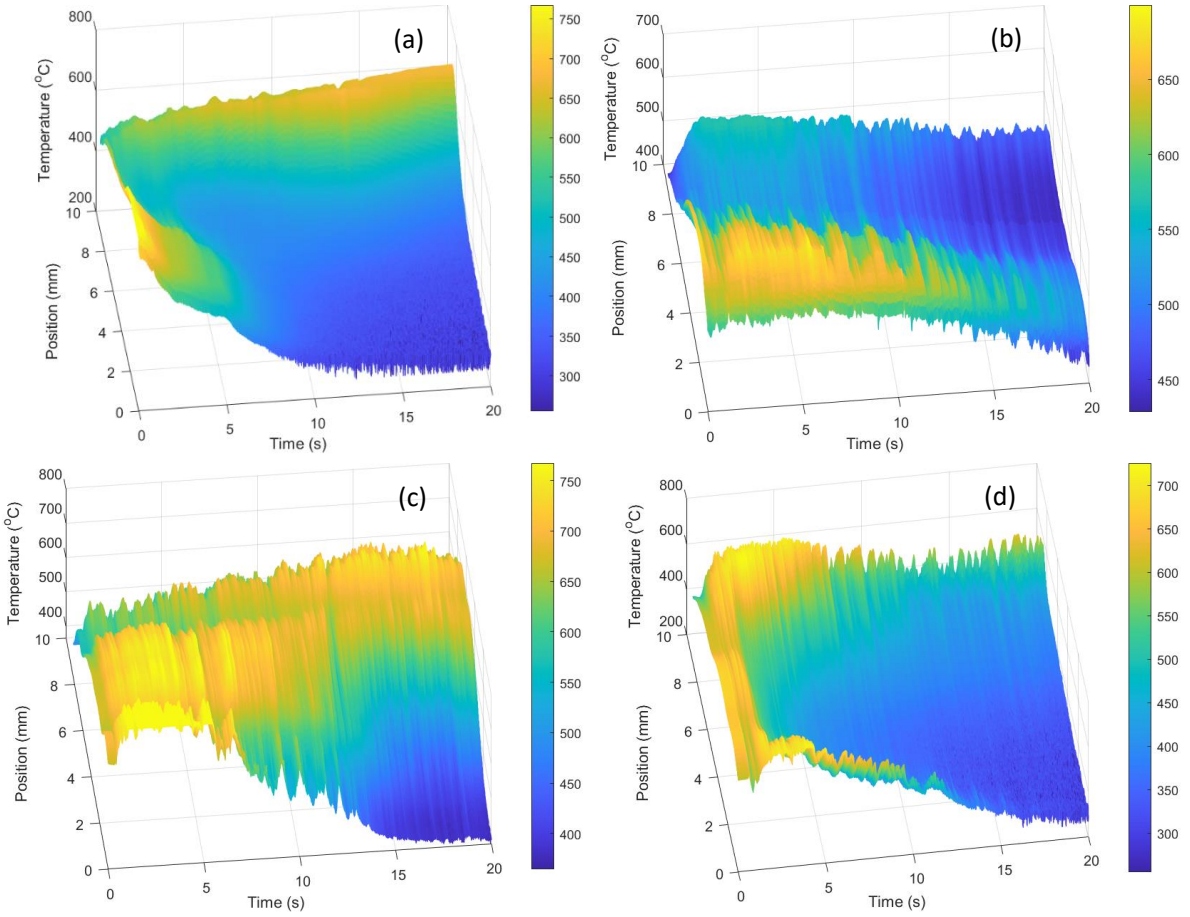

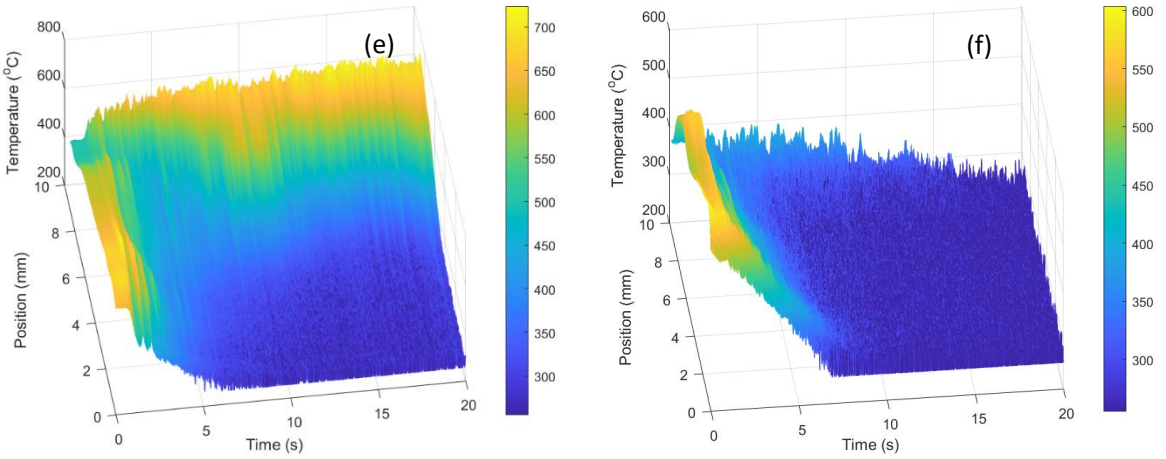

Figure 6.9 The selected-line temperature map against time at the 0 degrees inclination with different speed of cross-wind. (a) presents speed 0; (b) presents speed 1; (c) presents speed 2; (d) presents speed 3; (e) presents speed 4; (f) presents speed 5.

As one of the findings in previous sections that the small wind field had strongly positive effects on the fire propagation, the temperature map at Speed 1 and 2 are presented in Fig.6.9 (b) and (c). It can be found that the slower velocity of cross-wind delayed the cooling from the bottom side of the wood rod and contributed to a larger area where kept a high temperature compared to the group without wind. Meanwhile, the cooling rate also decreased in these two groups. This phenomenon is due to the increased convective heating from the underneath hot gas flow. As the influence by cross-wind, the hot gas-phase products were brought into the underneath of the rod and kept heating the wood on the bottom side. In addition, the cross-wind brought the oxygen from the surrounding air and the combustible gases produced from the impact point to the unburned wood. With the enhanced heat pyrolysis, the more heated gas flow appeared underneath the rod. Moreover, a reasonable hypothesis can be made that the wind took the heat from the impact point along the wooden rod.

When the wind speed increased to the speed set 3, the underneath cooling rate increased once again, and only a small layer kept in a high temperature on the bottom side. This could illustrate that there was convectively heated underneath, however, the thickness of the hot gas flow was insufficient to heat the deeper layer of the wood from the underneath.

When the cross-wind speed increased to speed 4, shown in Fig.6.9 (e), the cooling of the underneath surface had been significantly increased and was more significant than the control group (Fig.6.9 a). From the Fig.6.9 (e), it can be seen that most area was cooled to extinguishment before 10s except the tiny part on the top surface. For the wind speed 5 group (Fig.6.9 f), not only the bottom side, but the topside temperature also decreased fast under this wind speed. The fast cooling of these two cases attributed to two aspects: the first reason is that the high velocity of cross-wind significantly increased the heat transfer to the cold air, such as the case shown in Fig.6.9 (f), the topside of the wood cooled dramatic fast even if there was continuously heated by the flame. The second reason is that the hot gas flow around the burning wood was blown off by the high velocity of wind, the incompact hot flow cannot effectively heat the wood and sustain the temperature. The decreased temperature under high wind speed contributed to a more volume of char formation, further decreased the pyrolysis.

6.3.1.3. The cross-wind effects on the underneath hot gas parcel

As discussed in Chapter 5, the convective preheating from the hot gas flow plays a critical role in sustaining the burning and the fire spread, the underneath preheating particularly. In consideration of the cross-wind effects on the underneath hot gas parcel, the schlieren

imaging system has been applied to further verify the effects of cross-wind on underneath hot flow and heat convection. Fig.6.10 presents the schlieren images of hot gas flow around the burning wood with different cross-wind speed at 0s, 10s and 20s respectively (0s, 10s and 15s in the case of speed 5). Similar to the findings in Chapter 5, it is found that the underneath parcel existed at the beginning of self-sustained burning in all the cases. This is because the high intensity of the heat was concentrated on the impact point after ignition spread along the rods. The attached hot flow was essential for the continued burning and propagation.

While the burning processing, at the control group (without wind), the underneath hot gas parcel disappeared at 10s, no sufficient heat convection supplied from the underneath resulted in the graduate cooling from the bottom side. That is why the temperature dropped fast in Fig.6.9 (speed 0). Comparatively, in the cases of speed 1 and 2, the underneath hot gas layers existed during the first 20s of self-sustained burning. In particular, the hot gas parcel became larger than the beginning with the involving wind speed 2. It was a complicated phenomenon about the appearance of the underneath hot gas parcel in these two cases. Many factors had contributed to this phenomenon, such as the movement of the hot gas flow, the radiative heat transfer according to the flame attachment angle, the change of the heat transfer coefficient and so on. Of those, the most distinguishing factor was the cross-wind which supplied a horizontal force in the underneath flow and made it able to move forward. It is illustrated in Fig. 6.11. Under the natural circumstances, the heated flow from underneath only moved upward (the red line) because of the buoyancy. The lengthwise preheating mostly by the conduction along the rod. With the involvement of the cross-wind, the heated flow in the impact point could move forward (the green line) and preheat the adjacent unburned

wood. The new produced gas-phase combustion products by the adjacent wood would supply the underneath hot gas parcel again. In addition, a part of the gas-phase combustion products which came from the whole burning wood waw blown into the bottom of the rods. The cross-wind would apply the horizontal force on the combustion products together with the buoyancy and push them into the underneath hot gas flow, to some extent. When the cross-wind increased to speed 3, it can be found that the underneath hot gas parcel had begun to decrease. Under this velocity of cross-wind, the heat convection between the hot gas flow and the surrounding cold air was increased. Therefore, the cooling rate of the hot gas flow increased, further decreased the underneath flow gas parcel. Besides, according to the surface temperature in Fig.6.9, the surface temperature decreased fast, as a result, more char formed while less gas-phase produced. As another reason, it is the high velocity of wind that blew off a part of the hot flow layer. In the high wind speed cases (4 and 5), it is found that all the underneath hot flow layer was blown off by the wind. Without underneath convective heating, in addition to the increased cooling attributed to the crosswind, the burning under wind speed 4 and speed 5 had dramatically weakened.

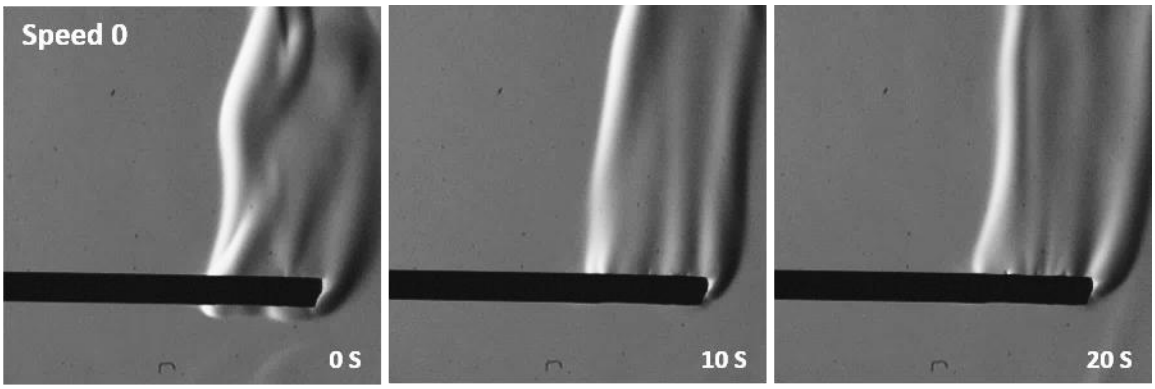

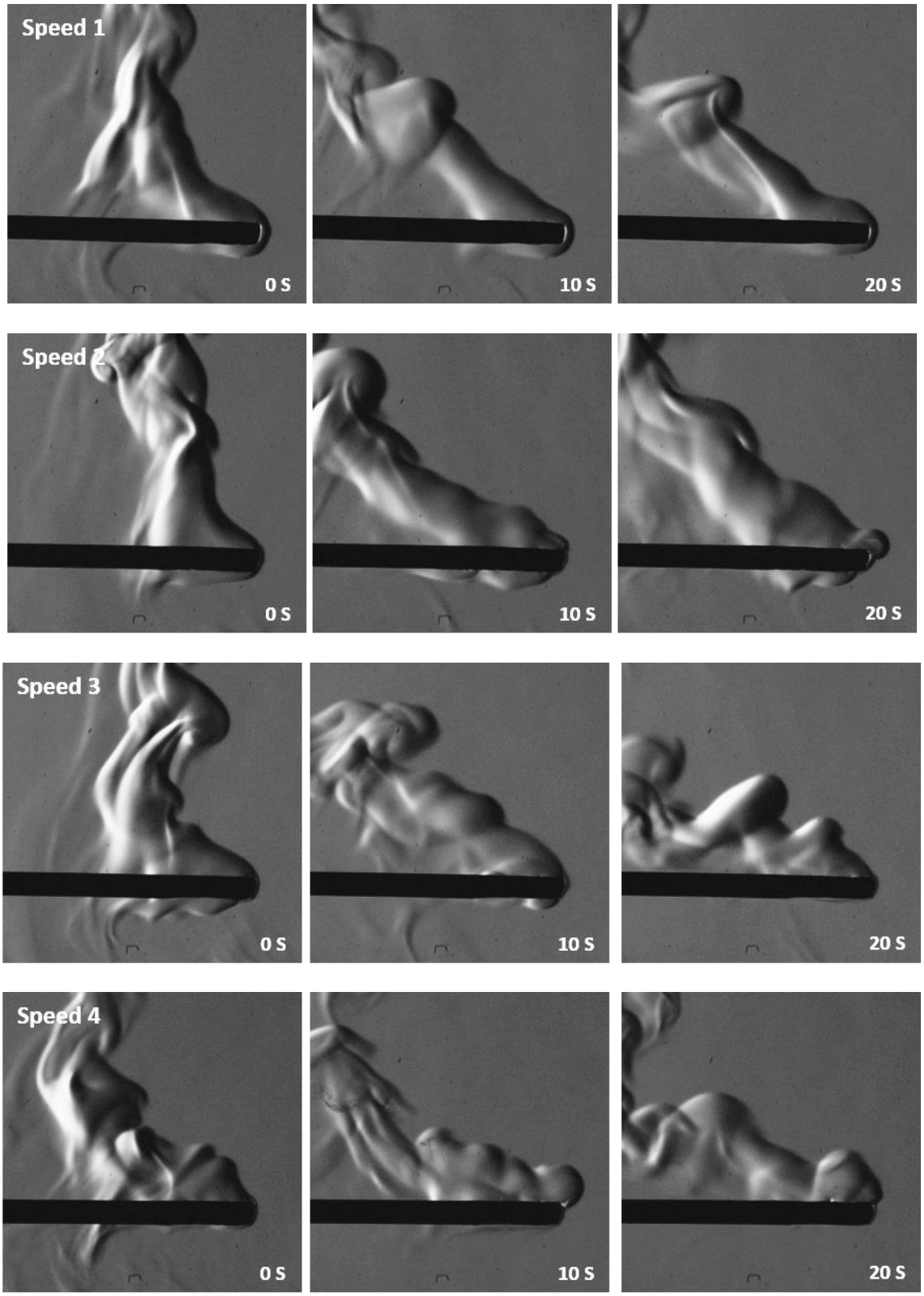
Speed 1
0 S
10 S
20 S
Speed 2
0 S
10 S
20 S
Speed 3
0 S
10 S
20 S
Speed 4
0 S
10 S
20 S

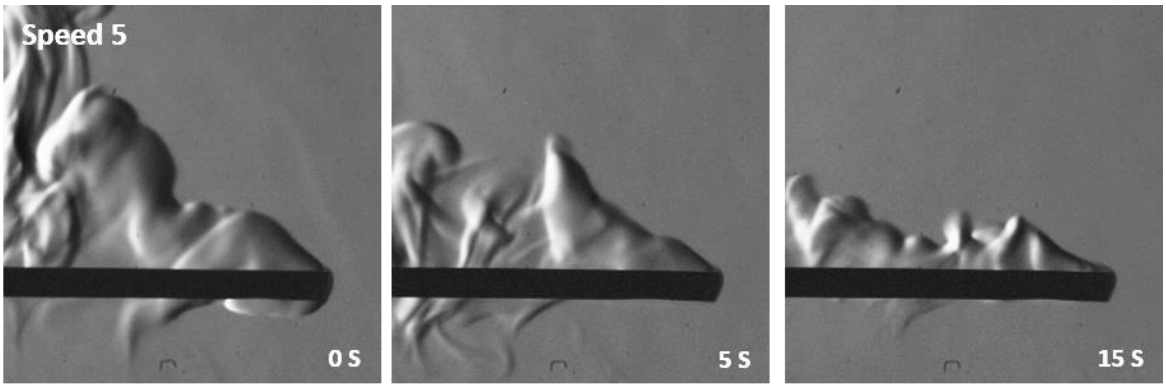

Figure 6.10 The illustration of underneath hot gas flow at 0 degrees inclination at different timing under different cross-wind speed set.

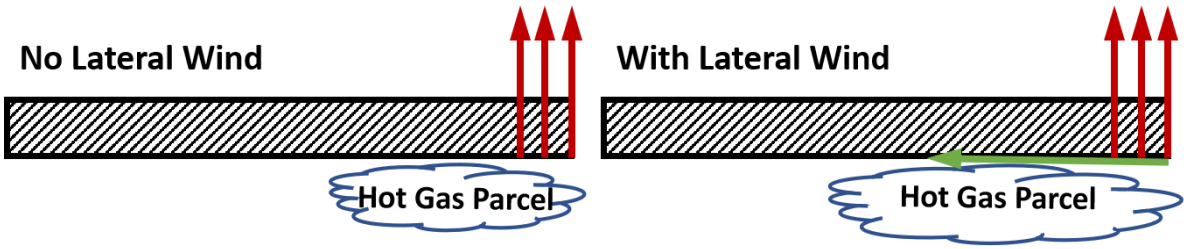

Figure 6.11 The illustration of the effect of the cross-wind on the underneath hot gas flow in the horizontal direction.

6.3.2. The cross-wind effects on the self-sustained burning at 30°

6.3.2.1. The burning status

It had been demonstrated that the inclination angle would play an important role in the fire propagation in Chapter 4 and 5. The positive inclined angle could enhance the fire spread by affecting the surrounding flow field and the flame attachment. In Chapter 5, it had been proved that the 25° is the critical angle for enhancing the burning[165]. Therefore, 30° inclined angle has been used in this section as a high-intensity burning group for the study of the cross-

wind effects.

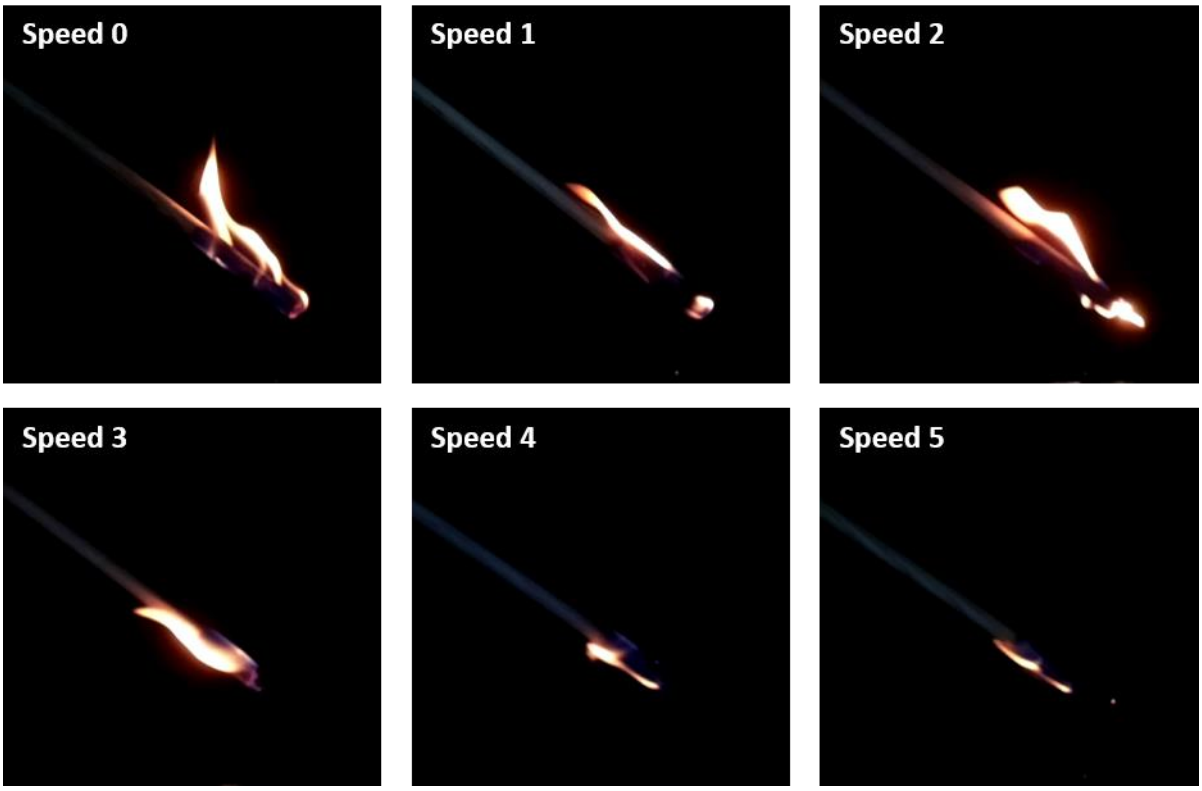

Figure 6.12 The direct images of self-sustained burning at 10 s on the 30 degrees inclination.

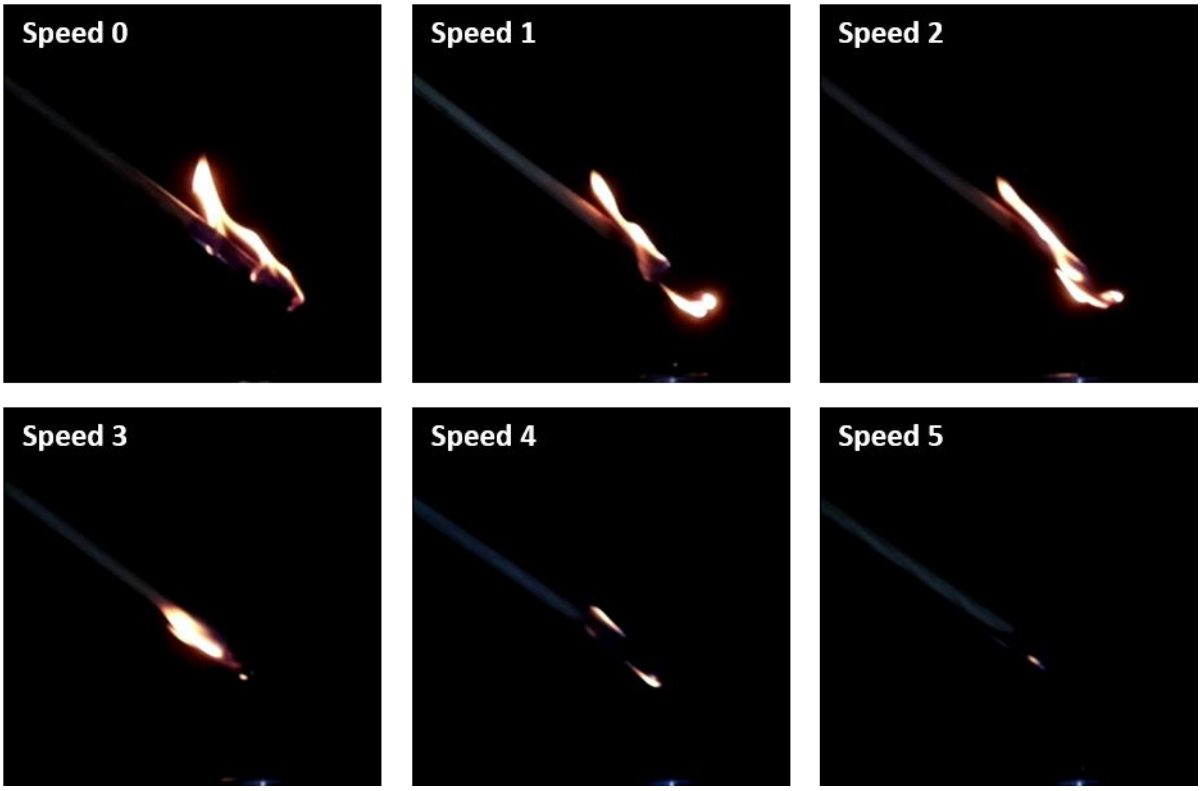

Figure 6.13 The direct images of 20 s self-sustained burning at the 30 degrees inclination with different speed of cross-wind.

Fig.6.12 and Fig.6.13 present the flame under different cross-wind speed at 10s and 20s respectively. By comparing Fig.6.12 and Fig.6.13 with Fig.6.3, it is found that the flame on the 30^o inclined surface had a longer attachment length and a smaller tilt angle than the cases at 0^o. In addition, the size and the intensity of the flame on the 30^o were much higher than which on the horizontal surface. The larger values of both size and intensity of flame could influence the burning status greater due to the larger amount of heat transfer from the flame to the surface in both radiation and conduction.

With the increasing crosswind speed, both Fig.6.12 and Fig.6.13 indicate that the flame had a greater attachment phenomenon, the flame was enfolded the wooden rod under wind speed 1 and speed 2. The appearance of the flame indicates that the gas-phase combustion occurred, the larger size of the flame thus means there was a larger volume of gas-phase products. As the flame appeared on both sides of the rod under wind speed 1 and 2, the thermal pyrolysis rate is the highest in these two cases. When the wind speed increased to speed 3, the whole flame attached to the bottom side of the wood surface. Moreover, the flame intensity had significantly decreased when the wind speed increased to speed 4 and 5. After 20 s of self-sustained burning, the flame was weakened and dimmed under wind speed 4 and 5, shown in Fig.6.13.

6.3.2.1.1. Burning lifetime

The averaged burning lifetime from the beginning of self-sustained burning is shown in Fig.6.14 below with the maximum and minimum values. The x- and y-axis indicates the wind speed sets and the burning lifetime, respectively. It was found that the burning under the cross-wind speed 1 and 2 cases was strong, and most cases could keep burning until the flame propagated to the end of wooden rods, which was about 300 s until the flame spread thoroughly. Therefore, the results in Fig.6.14 only show the minimum burning lifetime value in these two groups which represent these exceptional cases extinguished before burned out the whole rod. The main cases under wind speed 1 and 2 were counted in Fig.6.14 in the black-dotted line 'burned out the whole rod' which is around 300s.

Overall, it is found that the burning lifetime firstly increased at the slower speed of cross-wind, then significantly decreased after the turning point which is wind speed 2. By comparing with the burning lifetime of the cases at the horizontal direction, shown in Fig.6.4, the tendency and the turning point of the burning lifetime with increasing wind speed is similar to those at the inclination of 30 degrees. Since the similar conditions, including similar material, ignition conditions and burning environment, the effects of cross-wind speed on the burning of a wood surface may contribute to the study of the fire safety scopes.

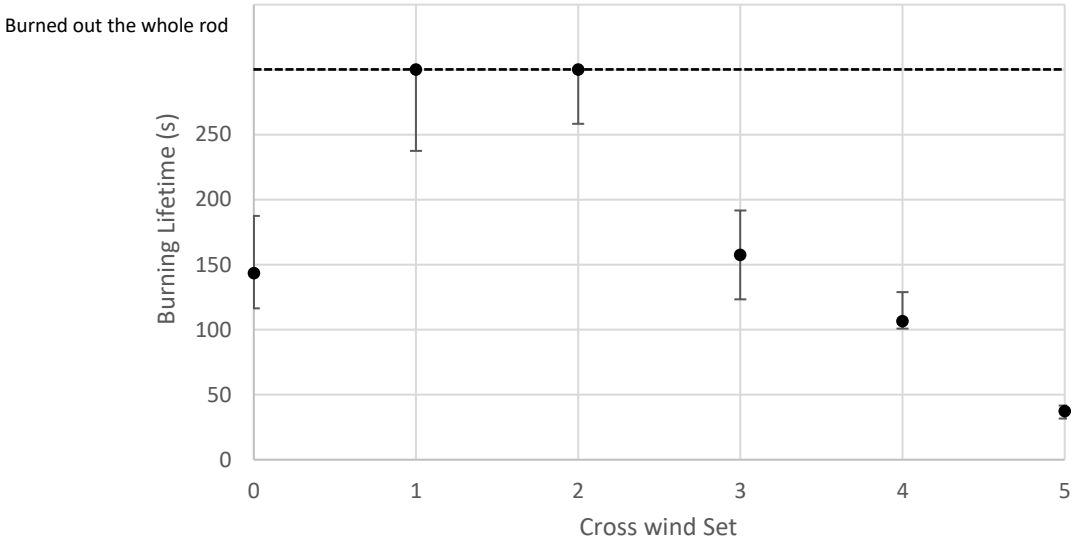

Figure 6.14 The averaged burning lifetime against different cross-wind set at 30 degrees.

6.3.2.1.2. Charring rate

The averaged charring rate at the first 20 s of burning under vary cross-wind speed is shown in Fig.6.15. It should be highlighted that all the groups involved with the cross-wind, had a higher charring rate than the control group (without wind). Comparatively, the charring rate on the horizontal surface which is shown in Fig.6.5 was reduced under the higher velocity of wind speed. The increased charring rate on 30 degrees inclined surface was because the higher speed wind pushed the flame and hot gas flow into the bottom side of the rods, which helped the burning. Although there was significant cooling under high wind speed cases which resulted in the lack of perpendicular propagation of burning and heat transfer, the longitudinal preheating was still enhanced. This is the reason that even the speed 5 group had a higher charring rate than the case without cross-wind.

Combined with the results of the burning lifetime, shown in Fig.6.14, the burning at 30 degrees surface was significantly enhanced when the wind speed 1 or 2 was involved, in both

the intensity of burning and the fire propagation. In Fig.6.12 and Fig.6.13, it can be seen the enhanced burning had attributed to the enfolded flame and hot gas flow (such finding will be discussed in the later section) on both the topside and underneath of the rods, which could enhance the perpendicular combustion and longitudinal propagation respectively. With the increasing wind speed, although the intensity of flame was decreased, shown as results of the speed 3, 4 and 5 in Fig.6.12 and Fig. 6.13, benefitted by the flame attached on the bottom side of the rods, the burning front moved faster than the group without wind due to the increased underneath preheating. In the meantime, the stronger cooling under the higher wind speed and the insufficient perpendicular combustion resulted in a shorter burning lifetime under these cross-winds.

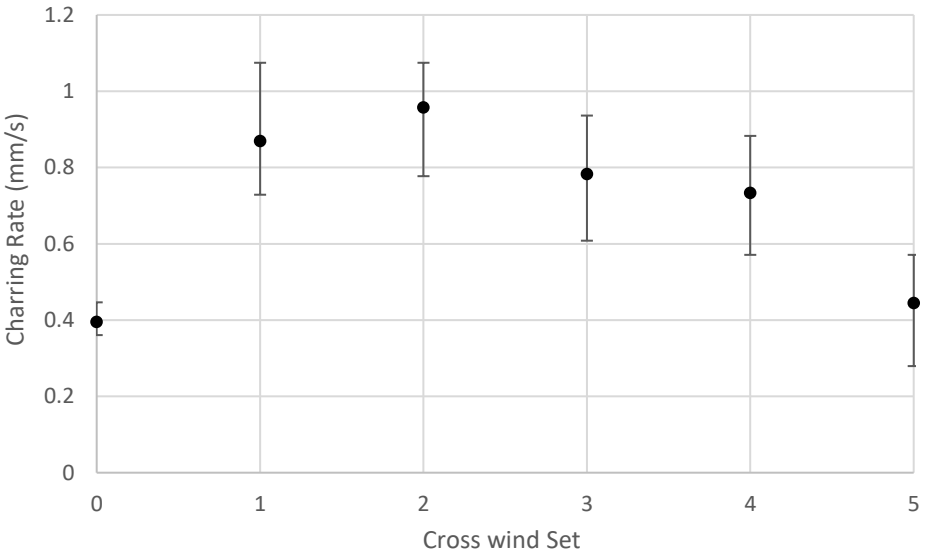

Figure 6.15 The averaged charring rate against different cross-wind set at 30 degrees.

6.3.2.2. Temperature analysis

Other than the horizontal surface, the burning at the 30 degrees surface had a much more stronger flaming behaviour in both the intensity and the flame size. Consequently, the flame

temperature could be a more important factor in the self-sustained burning. In details, the large size of flame could produce more conductive and radiative heat transfer and impact on a large area. Besides, the two colour method is good at calculating the temperature for a relatively larger flame. Therefore, in this section, the flame temperature will be calculated in the colour map to understand the mechanism of the burning under the cross-wind which is the same direction to the fire propagation.

As the temperature change of the 30 degrees inclined burning rod was a complicated process, which comes from both the longitudinal and perpendicular directions. Therefore, the surface temperature recorded by the InGaAs thermal camera will be used to analyse the different points and different select lines temperature to study the crosswind effects on the surface temperature.

6.3.2.2.1. Flame temperature

As discussed before, the flame on the 30 degrees surface would play an important role in sustaining the burning. The wood flame could be considered as the uniform distribution of a high concentration of soot particle[88], [92]–[94], [100], therefore, the two colour method can be a suitable tool for the temperature measuring as its non-induced and instantaneity property. The calculation range of this method is well-matched with the temperature range of flame as well. After the calibration process, the flame temperatures at 10 s under different cross-wind speed are presented by the colour maps in Fig. 6.16. The original flame images are shown in the left columns for comparisons. The minimum testing temperature in this experiment was 900^{o}C.

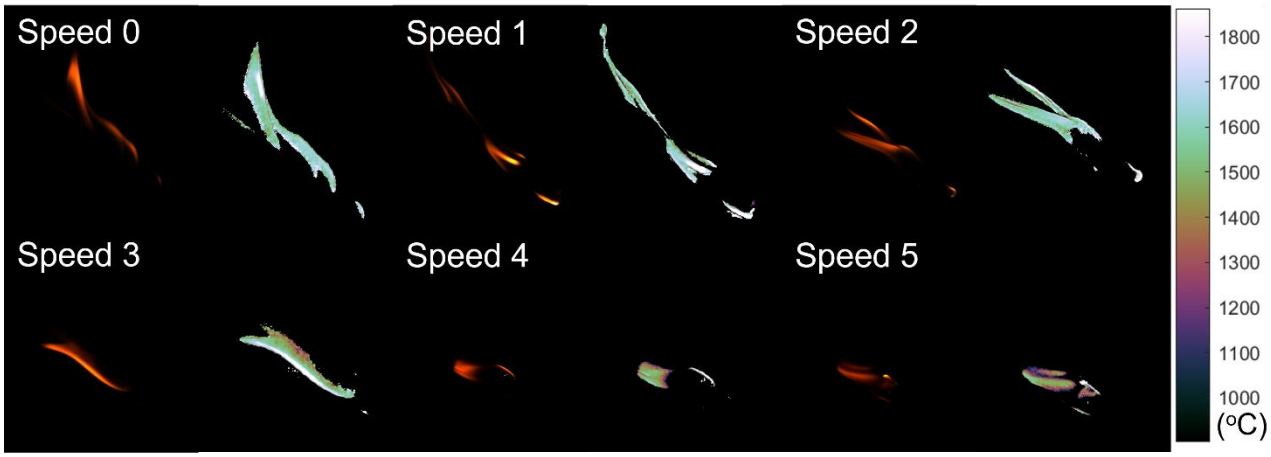

Figure 6.16 The actual flame and temperature map of 10 s self-sustained burning at the 30 degrees inclination with different speed of cross-wind. Left: the actual flame; right: the temperature colour map.

It is found that in the speed 0, 1 and 2, the flame mainly attached on the top side while the flame concentrated on the bottom side in the cases of speed 3, 4 and 5. Although there was flame on the underneath in the cases at speed 1 and 2, their temperature was too low to capture. Aiming at the full observation, the invisible flame and hot gas flow have been visualised by the schlieren imaging system in the later section. It is worth noting that there were areas which had the very high temperature in the cases speed 1, 2 and 3. On the contrary, the main area of the flame in the cases speed 4 and 5 concentrated in the low-temperature range.

The temperature distributions under the different speed of cross-wind at 10s are presented in Fig.6.17 below. The red-dotted lines represent where the peak value appeared. Fig.7.16 indicates the normal temperature distribution of the control group (speed 0) and its mean value was around 1600 ^{o}C. With the involvement of the cross-wind, the temperature showed abnormal distribution. It is worth noting that the average flame temperature slightly increased

when the cross-wind of speed 1 and 2 was applied, then decreased with the higher velocity of wind speed and dropped fast when the cross-wind speed increased to speed 4 and 5. There was an interesting phenomenon found in the flame temperature distributions, in details there were high volume pixels of flame concentrated in the high-temperature range (beyond the temperature of the peak value), in the cases of speed 1, 2 and 3. The reason for the phenomenon is attributed to the increased oxygen supplement. Another reason for this phenomenon is that the thermal pyrolysis rate is higher under low wind speed. As the high rate of thermal pyrolysis under wind speed 1 and 2, the reactions are in the gas-phase combustion more than the solid-phase oxidation, more flammable gases combined with larger oxygen supply made the flame temperature higher. In addition, the thinner char layer under these two cases made the water evaporating faster, with lower moisture content, the flame temperature tended to be in the high-volume zone.

In the meantime, the crosswind cooled part of the flame by increasing the convective heat loss to the surrounding cold air. Therefore, the temperature showed more fluctuant than those in the control group (without wind). On the contrary, the flame rarely appeared in the high-temperature range in the cases at speed 4 and 5. This phenomenon is attributed to the high rate of solid-phase oxidation, as the surface temperature decreased fast under the high wind speed, the thermal pyrolysis tended to be slower under the temperature lower than 300 ^{o}C. In addition, the pyrolysis favoured producing solid products, like the carbon char. The less combustible gases products under these cases made the flame temperature decreased and concentrated in a low volume zone. Another reason is that the high speed of wind increased the convective heat transfer coefficient between the flame and the cold air, the heat loss was

increased.

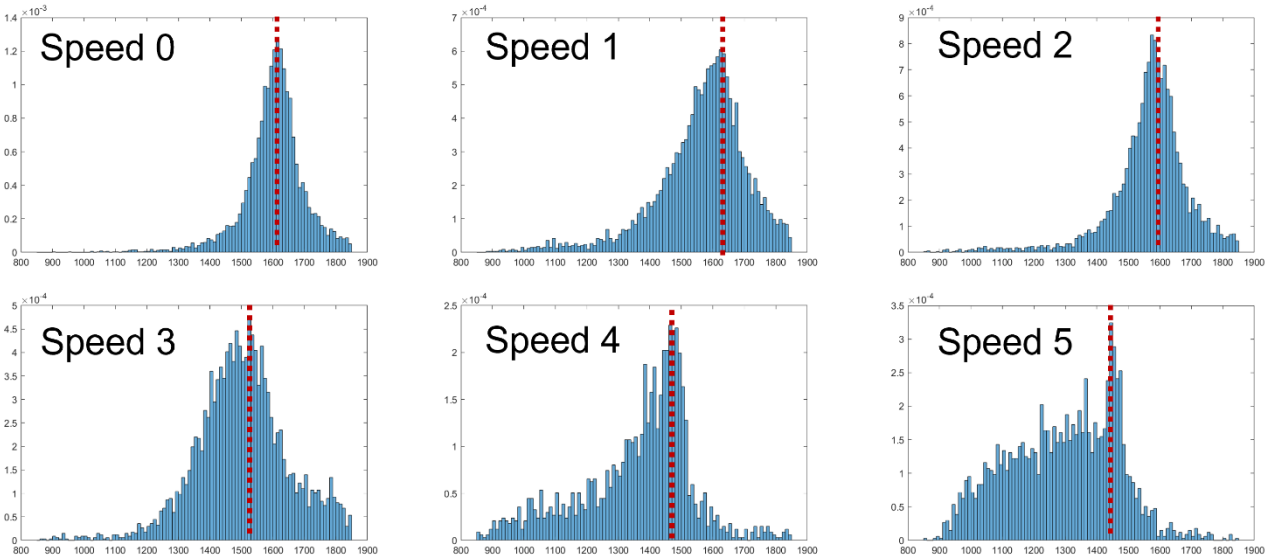

Figure 6.17 The flame temperature distribution of 10 s self-sustained burning at the 30 degrees inclination with different speed of cross-wind.

Similar to the 0 degrees group, the flame temperature of 30 degrees was averaged in each frame and compared the results at different cross-wind speed, which is shown in Fig.6.18. It is worth noting that averaged flame temperature slightly increased under wind speed 1 and 2 than the control group (the blue line in Fig.6.18), which is dramatically different from the results of 0 degrees group that the ambient wind decreased the temperature for all testes. Further, the flame temperature started to decrease when the wind speed increased to speed 3, and fast dropped when the speed increased to 4 and 5. This phenomenon is because the lower speed of wind made the flame enfolded around both sides of the rod. The larger area involved in the heat pyrolysis, the more combustible gases were produced from the pyrolysis progress, resulted in a higher intensity of combustion. In addition, the more area enfolded the burning rod means there was less area contacted directly with the surrounding cold air in the cases of speed 1 and 2, resulted in the decreasing heat loss of the flame. Therefore, the flame

slightly increased under wind speed 1 and 2.

On the contrary, the wind at high velocity blew the flame and made it attached only on the bottom side of the rod, the cooling of the increased heat loss made the flame temperature decreased under the high wind speed. Unlike the horizontal groups that wind speed did not show a significant effect on the flame temperature, the flame temperature decreased with the increasing wind speed on the 30 degrees group. This is due to the flame on the 30 degrees had an initial strong attachment due to the imbalance of air pressure, which can be seen in the flame in the control group. Consequently, the increased wind speed did not enhance the intensity of flame attachment significantly but only influenced on cooling the flame by the increasing heat loss under the cases of speed 3, 4 and 5. As a results, the flame temperature decreased with the higher cross-wind speed.

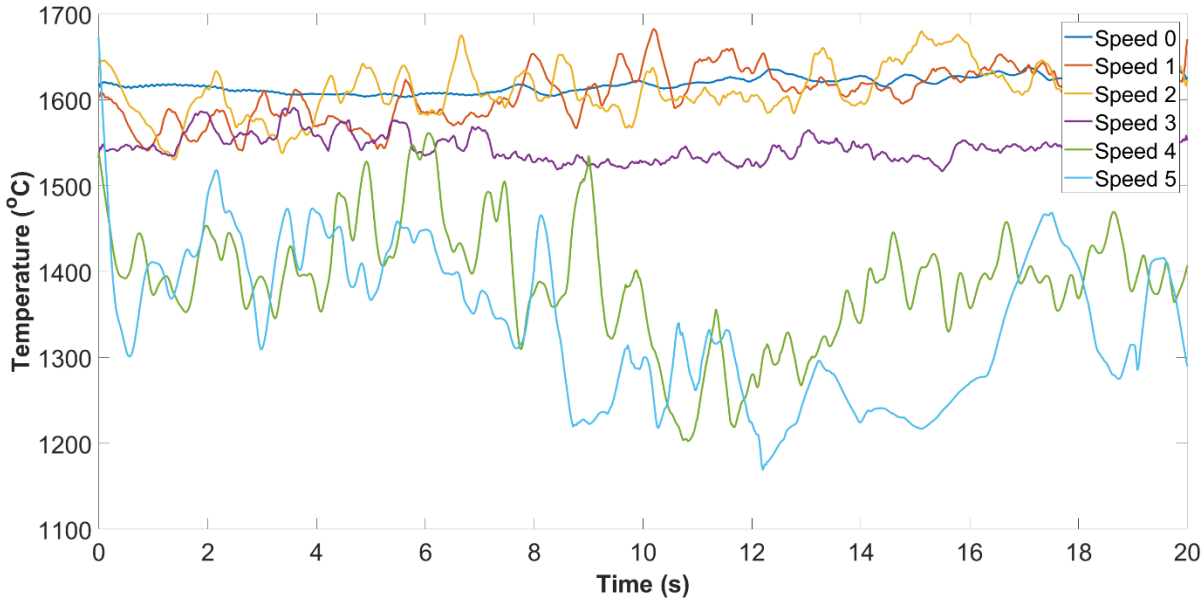

Figure 6.18 The time-dependant averaged flame temperature of 30 degrees group under different cross-wind speed during the first 20s.

6.3.2.2.2. The temperature of wooden surface

6.3.2.2.2.1. The lengthwise cooling

By comparing with the direct images in Fig.6.12 and Fig.6.13, it can be seen that, with the increased cross-wind speed, there was observably lengthwise cooling start from the rod end under the high velocity of wind speed. In order to determine the differences between cases quantitatively, the surface temperature of the cross line was calculated. The temperature at the cross line represents the temperature distribution at a crossing line in the middle of the wooden surface, an example is presented in Fig.6.19.

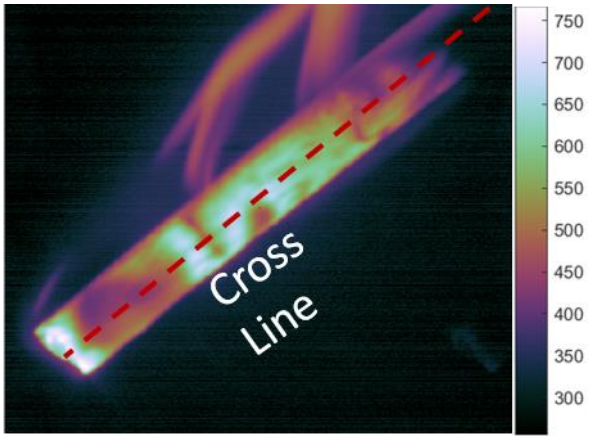

Figure 6.19 The surface temperature map and cross line position.

In consideration of the fast cooling and short burning lifetime of the case under wind speed 5, the temperature at the time point when the self-sustained burning started 10s was chosen for comparison on account of the good representativeness of the whole burning status. The temperature at the cross line at 10s as well as the same time temperature colour map are presented in Fig.6.20 below. The x-axis represents the different positions starting from the rod end while the y-axis represents the temperature.

It is found that the averaged surface temperature was slightly decreased with the increasing wind speed. This means the involvement of the cross-wind increased the convective heat loss on the burning surface. Regarding the lengthwise cooling, it can be seen that the lengthwise cooling from the rod end was not significant under the speed 0, 1 and 2. Although there was a temperature drop at the area near the impact point (high-temperature zone) in the speed 0 case, the temperature in this area was still high enough for the heat pyrolysis. From the crossline temperature in the right Figure, it can be found the temperature drop occurred at the position around 10mm from the rod end, which indicates that the cooling still came up due to the decreased invisible hot gas flow.

Comparatively, the temperature drop was not significant under wind speed 1 and 2. The fast cooling from the rod end was started when the cross-wind speed increased to speed 3, it can be observed that there were areas where cooled down to under 300 ^{o}C in the cases of speed 3, 4 and 5. The low temperature means this area had already ended the fast thermal pyrolysis[57]. The pyrolysis occurring under 300^{o}C favours to produce the char, leaving the thicker layer which prevented the transfer of heat flux into the deep surface of the wood, results in extinguishment eventually. Meanwhile, the area became larger with the increasing wind speed. From the crossline temperature in the right, it is found that the high-temperature concentration at the impact point almost disappeared in the speed 3 case and completely disappeared under wind speed 4 and 5. In addition, the lengthwise cooling processed approximately 15 mm from the rod end under wind speed 3 while this length significantly increased to around 20mm and 30mm in the speed 4 and 5 cases, respectively. The averaged cooling rate under these three cases could then be approximately calculated as 1.5mm/s,

2.0mm/s and 3.0mm/s in the lengthwise direction. The cooling rate was much higher than the burning front move rates which were shown in Fig.6.15. From this point of view, it is understandable that the cases under the high velocity of cross-wind had a shorter burning lifetime.

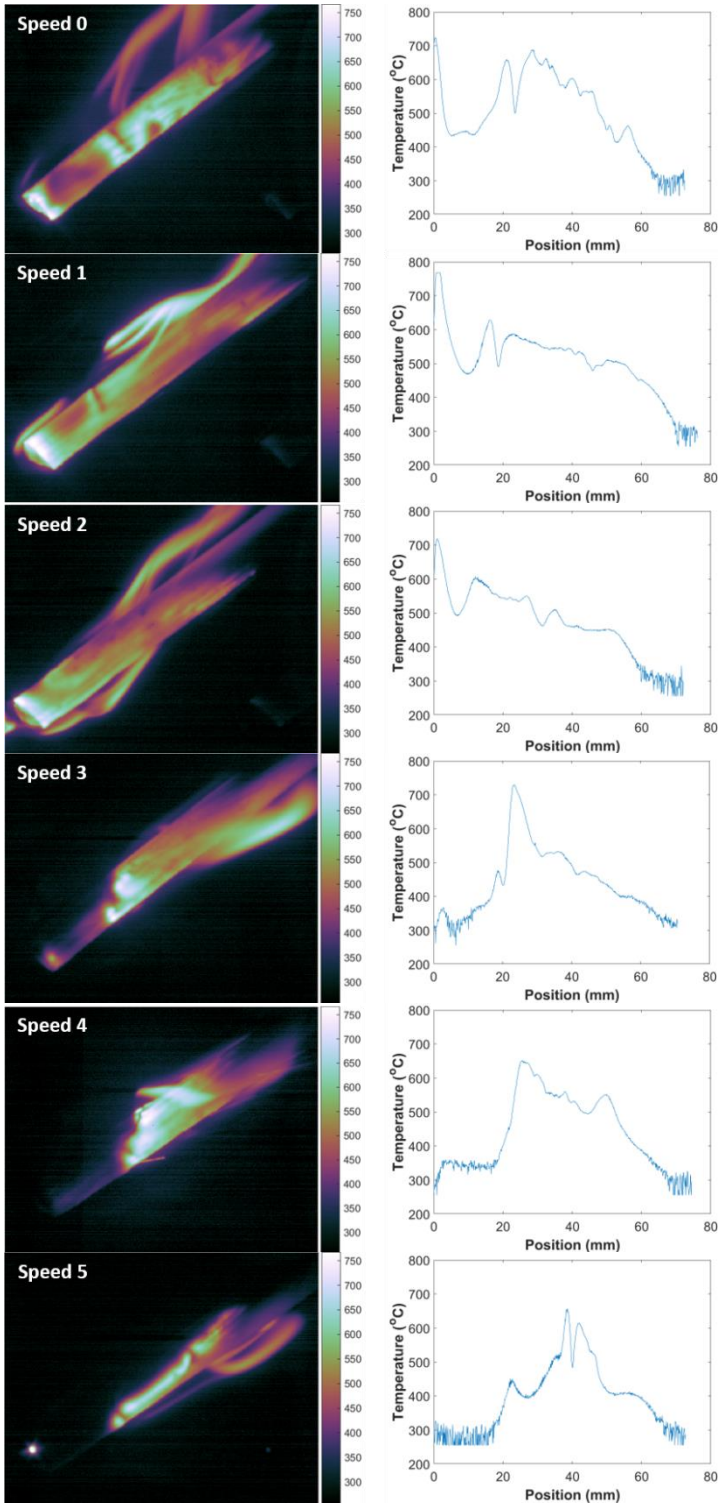

Figure 6.20 The surface temperature map and the cross-line temperature of 10 s self-sustained burning at the 30 degrees inclination with different speed of cross-wind.

Furthermore, during the experiment, it was found that the cooling did not occur when the cross-wind involved, but a few seconds delay. In order to demonstrate the different timing of

the fast-cooling start, four points at the crossline were set, which are demonstrated in Fig.6.21. The first point (point 0) is set at the very edge of the rod end representing the impact point where a high volume of heat is concentrated. Point 1 locates on the boundary of the high-temperature area. And point 2 and 3 represents the areas adjacent to the impact point area. The distance between each point is 3 mm.

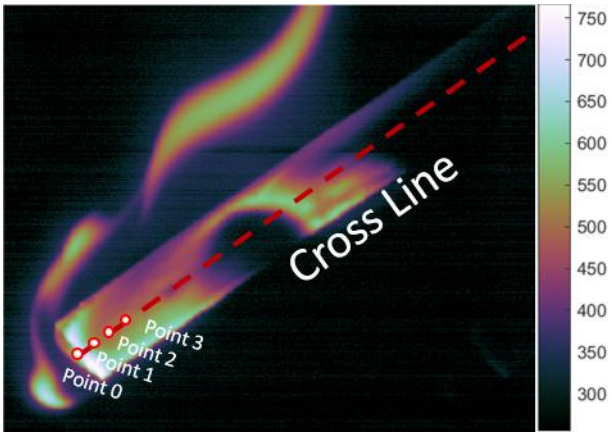

Figure 6.21 The demonstration of the point temperature positions.

The temperature change at point 0 and point 2 during the first 20s of self-sustained burning under different cross-wind speed is shown in Fig.6.22. The temperature at point 0 could represent the high-temperature area (impact point) and represent how it changed over time. Point 2 could represent the point just near the impact point. It can be seen that the temperature at point 0 kept in high value at the first 20s in the cases of speed 0, 1 and 2. This signifies that under these conditions, the impact point could keep the high temperature for at least 20s instead of natural cooling or cooling by the wind. On the contrary, the temperature at point 0 decreased quickly under wind speed 3, 4 and 5. This could demonstrate that the heat loss was significantly higher under these high wind speed conditions than others.

From the results of point 2 (in the right of Fig.6.22), it is worth noting that the temperature

decreased with the increasing wind speed at the first 20 seconds. The temperature change of the no wind condition represents the natural cooling of this area, it was slowly decreased with time. The high velocity of cross-wind increased the convective heat loss then resulted in the fast temperature drop. It can be highlighted that the cases of speed 1 and 2 remained in high temperature at point 2 during the 20 s burning. In addition, the temperature at point 2 slightly increased under wind speed 1 and 2 compared with the temperature at the beginning. The temperature increasing indicated the low velocity of cross-wind which enhanced the thermal pyrolysis, by means of supplying the oxygen and increasing the convection heat transfer along the wood.

On the contrary, the point temperature in the cases under wind speed 3, 4 and 5 had dramatically dropped during this period. It should be highlighted that the fast cooling did not occur at the beginning but slightly later after the wind involving. In addition, it can be observed that the time for the quick drop of temperature would be different under wind speed 3, 4 and 5. The temperature of high wind speed case would cool earlier than of those under low wind speed case. Besides, the extinguishment points had a similar trend: the speed 5 cases extinguished fast (under 300^{o}C, few gas-phase combustion products, seem as the extinguishment, hereinafter inclusive) the point 2 extinguished in a later time under wind speed 3.

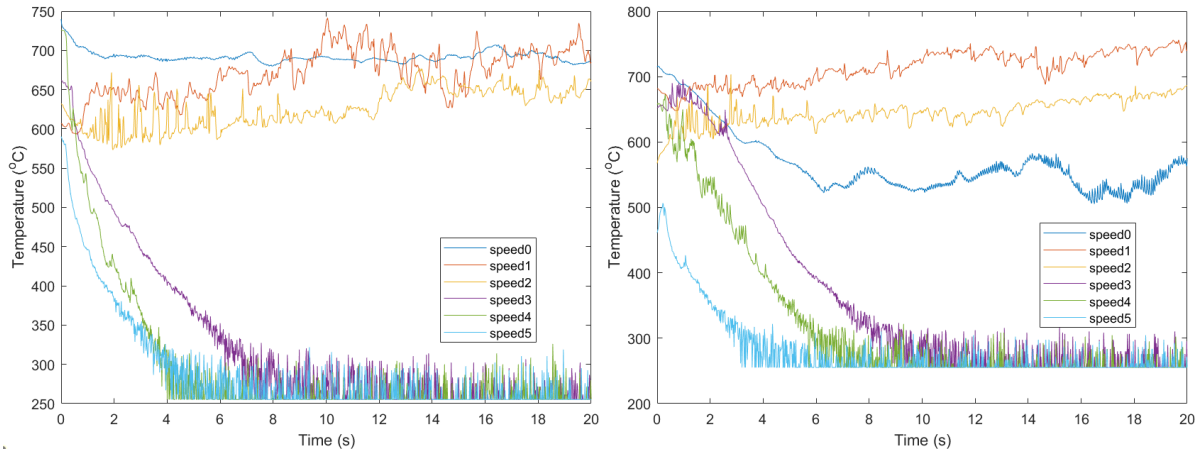

Figure 6.22 The first 20s from the self-sustained burning temperature at point 0 (left) and point 2 (right) with different cross-wind speed.

In order to figure out the difference between the cooling under the high wind speed groups, the temperature at four points against time is presented in Fig.6.23. For the reason that the cases of speed 1 and 2 did not present a significant lengthwise cooling at the first 20s, the Figure only showed the temperature under high velocities of wind (speed 3, 4 and 5) and the control group (no wind condition). The no wind case (speed 0) could represent the natural cooling condition. From the results of the speed 0 case, it is found that all four points had a slow temperature decrease from the beginning of the self-sustained burning. The point 0 and 1 under no wind condition decreased slowly than those at point 2 and 3, this is due to the high concentration of combustible gases around this area and remained at high-intensity combustion.

As discussed before, the fast cooling did not start from the beginning but a few seconds later under the high speed of the wind, the red-dotted line is used to indicate this period in Fig.7.21. It is found that the temperature at point 0 which indicates the impact point had a high value when the self-sustained burning began. Then, after the involvement of cross-wind, the

temperature of point 0 decreased immediately which is presented by the blue line in Fig.7.21. However, the temperature of point 1, 2 and 3 did not decrease once the cross-wind was involved.

On the contrary, the temperature at point 1, 2 and 3 increased at the beginning and then kept the high temperature before the fast cooling. This comes from two reasons: firstly, the high volume of heat concentrated at the impact point during the ignition, the heat was brought towards the rods at the beginning by the cross-wind and remained the high the temperature; secondly, there was a high concentration of combustible gases near the impact point which was proved in Chapter 5, the blowing cross-wind could bring the gas-phase fuel in addition with the oxygen supply to the unburned wood which helped enhance the combustion at the beginning. The fast cooling would start when the high-temperature zone was consumed. More importantly, the time period when the temperature fast dropped was affected by the wind speed. The higher the wind speed, the earlier cooling will occur. In detail, the fast cooling occurred at around 2.75 s under wind speed 3, at 0.4 s in the case of speed 4 and at 0.2 s under wind speed 5. The earlier time of fast cooling start signifies that the high-volume heat in the impact point was cooled down faster under the condition of high wind speed.

In terms of the cooling rate, it is clearly shown that the temperature dropped faster under the high wind speed. In detail, it took about 5.75 s for the flame temperature to decrease to the extinguishment point (under 300^{o}C) from the beginning of fast cooling at wind speed 3, around 4.5 s under wind speed 4 and 3 s under wind speed 5 respectively. The high wind speed could significantly increase the convective heat loss which then resulted in the increasing heat transfer coefficient.

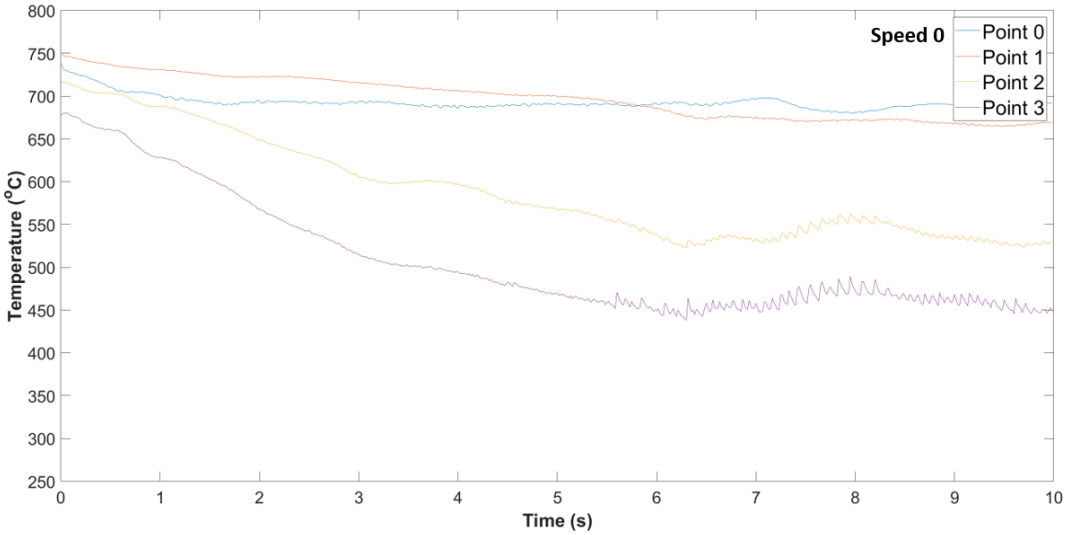
Speed 0
Point 0
Point 1
Point 2
Point 3
Temperature (°C)
Time (s)

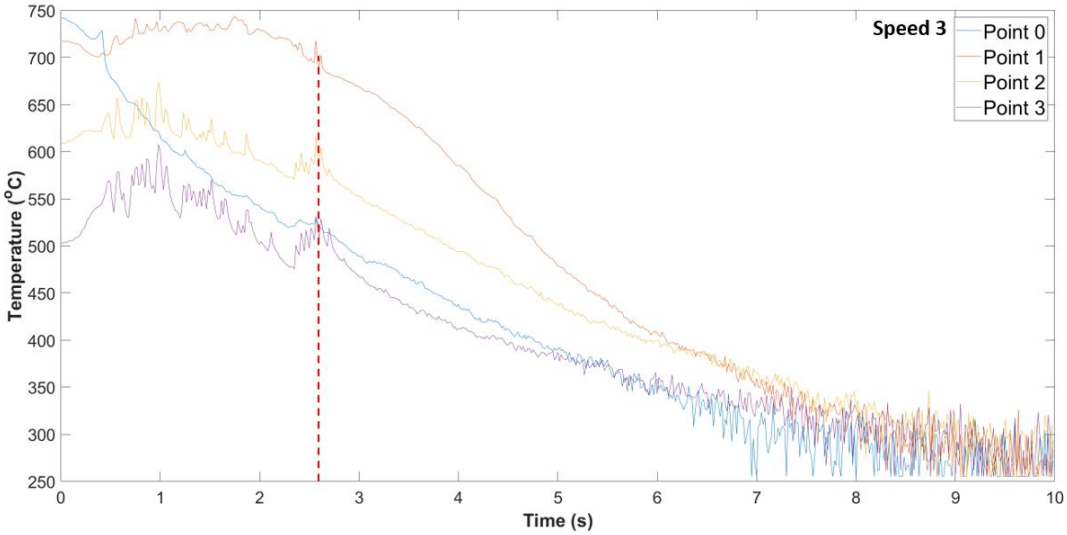
Speed 3
Point 0
Point 1
Point 2
Point 3
Temperature (°C)
Time (s)

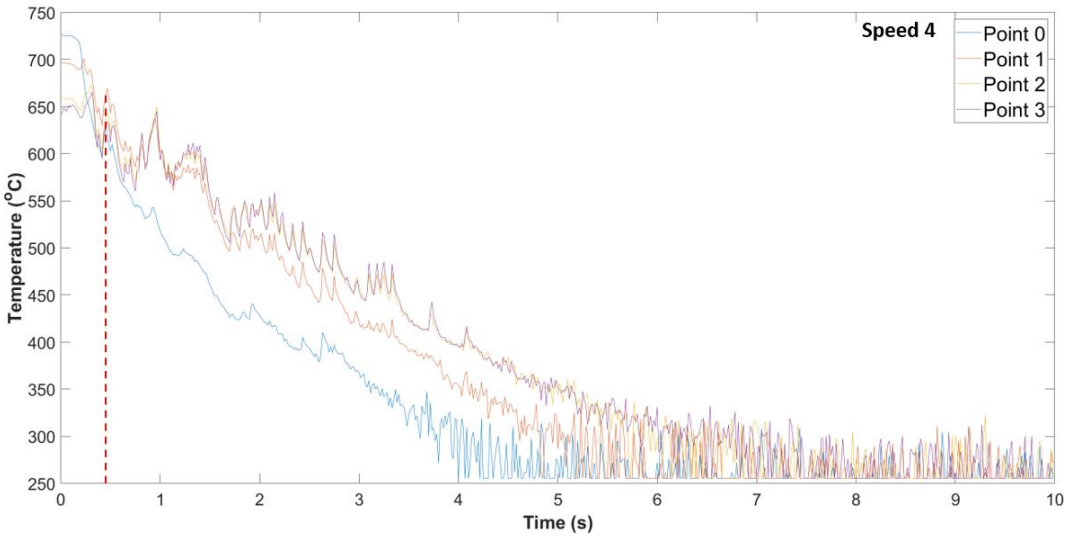
Speed 4
Point 0
Point 1
Point 2
Point 3
Temperature (°C)
Time (s)

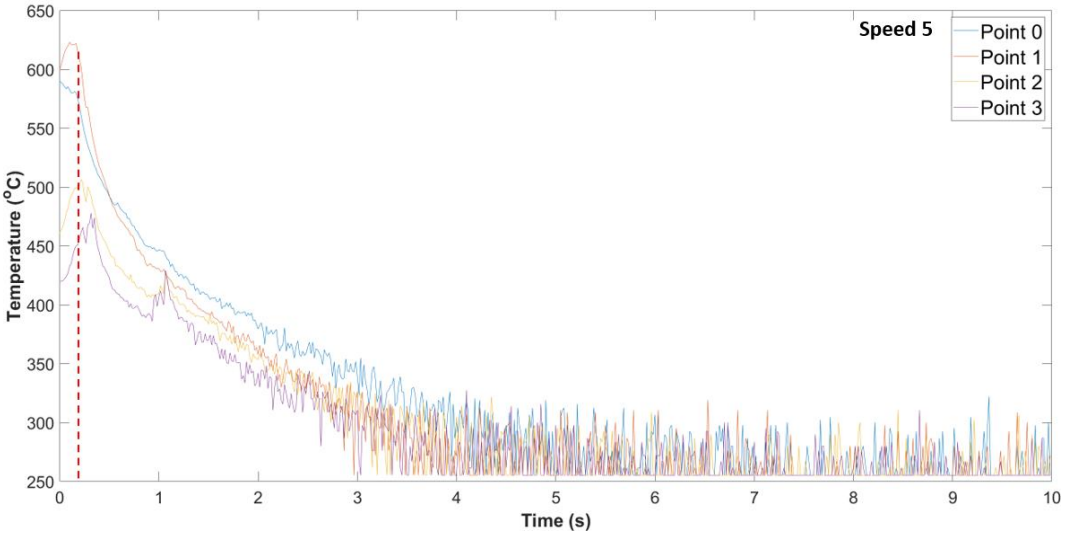

Figure 6.23 The first 10s from the self-sustained burning temperature at different positions with wind speed set 0, 3, 4 and 5.

6.3.2.2.2.2. The combustion along the thickness wise

As discussed in earlier sections, the fire propagation on the wood surface in two directions: longitudinal combustion and perpendicular combustion. The longitudinal preheating was proved as the critical factor of the burning on the wood surface under the piloted ignition at the horizontal direction and with inclination angles. On the other side, although the perpendicular combustion showed insignificant impact on the fire propagation, it helped the sustaining of burning. With regards to the burning under crosswind, as discussed in Section 6.3.1, the wind did not significantly impact the perpendicular combustion on the horizontal surface. This is because the flame on the 0 degrees surface was small and the flame only appeared on the topside of the rods. Unlike the 0 degrees inclination, the involved cross-wind dramatically changed how the perpendicular combustion proceeded on the 30 degrees surface. It can be seen from the temperature map in Fig.6.20, that the wood pyrolysed along the thickness-wise of the wood in the no-wind case as well as the low-speed wind cases, while

the pyrolysis mainly concentrated near the bottom side in the high wind speed cases. From the direction images in Fig.6.12 and Fig.6.13, it is found that most of the flame in the high wind speed cases were attached on the bottom side of the rods. The attached visible flame could be one of the possible reasons which affected the thickness wise combustion.

In order to figure out how the crosswind changed the way that the perpendicular combustion proceeded, the vertical line, which is in a similar position to the selected line in the 0 degrees cases (shown in Fig.6.8) was set to present the temperature on it. Fig.6.24 presents the selected line temperature changed in the period of the first 20s under different wind speed. From Fig.7.1 (a), it can be seen that in the control group, the high temperature concentrated in the underneath and decreased slowly with time, standing for the underneath hot gas parcel and the heat transfer from the bottom to top. Besides, the top side temperature remained at a high value, this is because the flame kept heating the topside surface and the heat flux continuedly transfers from the bottom to the top due to the buoyancy.

With regard to the cases under the cross-wind, in the cases of wind speed 1 and 2 see Fig.6.24 (b) and (c), the most significant change is the bottom side of the surface was heated and had a higher temperature than the control group. The large area from underneath the wooden rod remained at a high temperature in the first 20 s, the combustion of the whole surface was distinctly enhanced under these conditions. The flame could play an important role in enhancing combustion. The flame under these wind speeds had a stronger attachment phenomenon and enfolded around the burning rod. In addition, according to the flame temperature distribution in Fig.6.17, the flame temperature increased slightly under wind speed 1 and 2, and it was more likely to concentrate in the high-temperature zone. With the

increased radiative and conductive heating from the flame, therefore, the thickness wise combustion under these two groups was significantly enhanced. Another reason that the wooden rods had a higher temperature in the cases of speed 1 and 2 is that the wind supplied the additional oxygen and combustible gases produced from the pyrolysis of the impact point. The heat pyrolysis was significantly enhanced with the efficient oxygen and gas-phase fuel. Moreover, the invisible underneath heated gas flow could help the thickness combustion, which has been proved in Chapter 5. The discussion of the invisible hot gas will be discussed in section 6.3.2.3. Therefore, it can be seen the temperature of the cross-section of the rods under wind speed 1 and 2 was the highest.

Wind speed 3 is a turning point, which could be seen in Fig.6.24 (d). The underneath temperature under wind speed 3 remained at a high value at the beginning. However, the temperature on the top side dropped quickly after a few seconds. Under this wind condition, the temperature in the bottom side decreased after the extinguishment of the top side and extinguished around 10s. There are three reasons that caused this phenomenon, the first is the flame only attached underneath the rod, insignificant heating in the top side weaken the thickness wise combustion; the second is the crosswind prevented the upward heat transfer by affecting the hot gas flow direction; the third is the heat loss of the wood surface became significantly high under this wind condition. Continue to increase the wind speed, it is found that the cooling of the surface increased. Moreover, the thickness of the high-temperature layer from the bottom side decreased with the increasing wind speed. Under the wind speed 5, there was only a small thickness of layer where was heated. This can be explained with the thicker layer of char formed under high speed of the wind, the fast cooling of underneath

surface results in a high rate of solid-phase oxidation, therefore, the heat transfer is decreased due to the prevention of char layer. It is worth noted that although the visible flame all attached underneath the rod under wind speed 3, 4 and 5, the thickness of the heated surface was quite different between these cases. This could be attributed to another factor that comes from the invisible hot gas flow and will discuss in the next section.

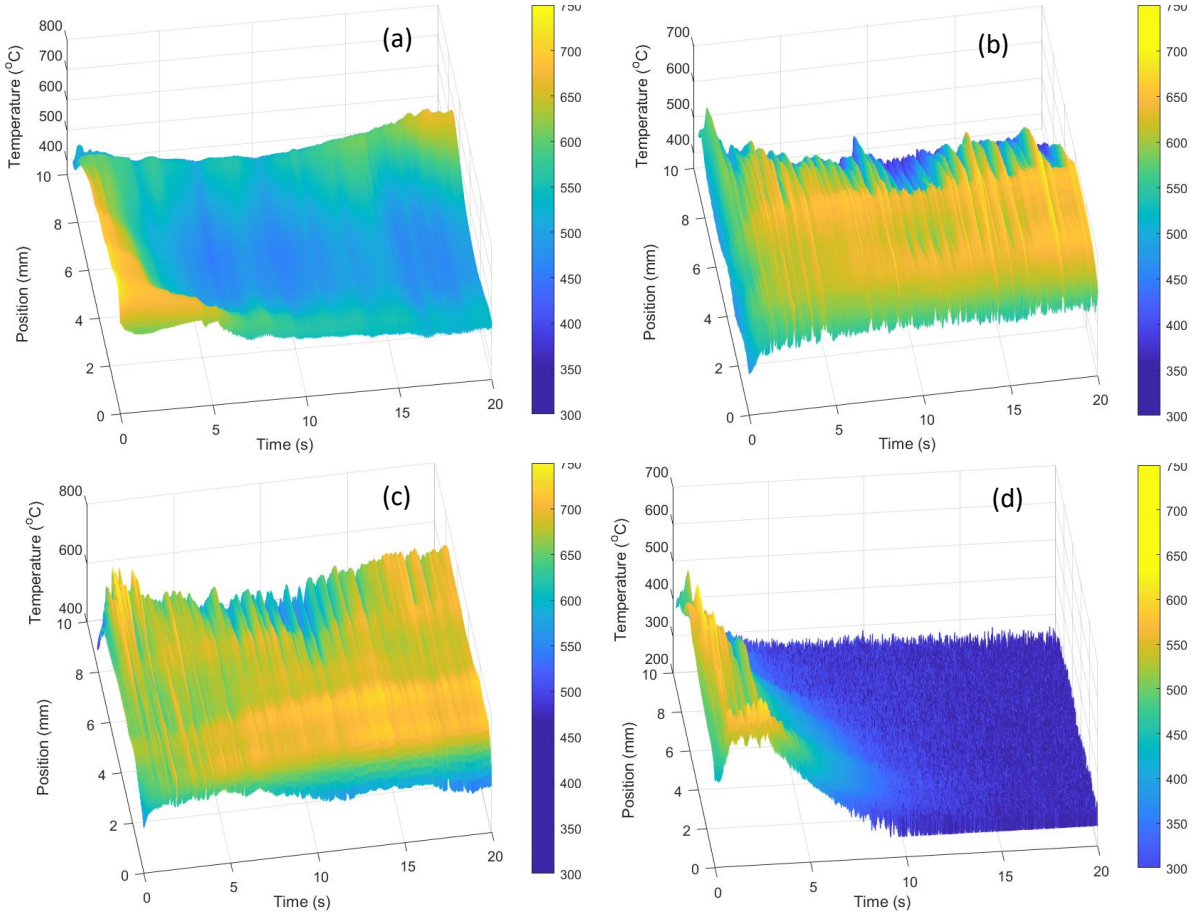

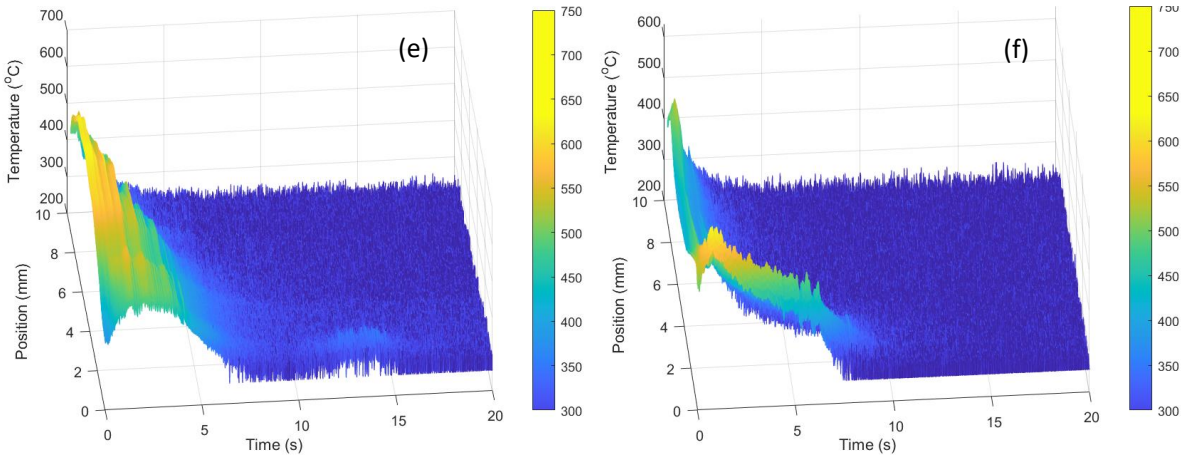

Figure 6.24 The selected-line temperature map against time at the 30 degrees inclination with different speed of cross-wind. (a) presents speed 0; (b) presents speed 1; (c) presents speed 2; (d) presents speed 3; (e) presents speed 4; (f) presents speed 5.

6.3.2.3. Visualisation analysis

Based on the previous chapters, it has been found that the surrounding hot gas flow is the crucial factor of sustaining burning and propagating flame which had been demonstrated in Chapter 4 (focus on the hot flow on the topside) and Chapter 5 (focus on the underneath hot gas parcel). In order to study the effect of the cross-wind speed on the invisible hot gas flow around the burning rods, the schlieren imaging technique will be applied for visualising and analysing the how field along with the surface temperature map.

6.3.2.3.1. Effects of the invisible hot gas flow on the surface temperature

Fig.6.25 shows the schlieren images matched with the surface temperature map at 10s of self-sustained burning under the different crosswind conditions. The temperature map from the thermal images was corrected in the size, position, and angle to synchronise with the schlieren images. With the synchronised images, the heat pyrolysis status on the wood surface could

be clearly visualised.

From the image of the control group (speed 0), it can be seen that the invisible hot gas flow appeared on both the underneath and the topside of the rod. It is worth noting that the hot flow on the tops side was much larger than the visible flame, it covered the rod from the impact point to the pyrolysis front and extended to the adjacent unburned area. To the underneath hot gas flow, it attached closely to the bottom side of the rod. As well it can be clearly observed that the underneath hot gas parcel extended further than the pyrolysis front which is showed in the temperature map and preheated the adjacent unburned wood.

From the images of speed 1 and 2, the flame under these two wind conditions blew into the top side of the wooden surface. It is found that the flame moved faster than the no-wind case. In the cases of speed 1 and 2, the flame attached tightly on the surface and had a smaller flame tile angle than which in the no-wind case. It should be noted that there was a large area where no flame appeared on the topside in these two cases. More importantly, even there was no flame on the topside of this area, the surface remained at the high-temperature range. The schlieren image could explain this interesting phenomenon. There was thick invisible hot gas flow attached surrounding the no flame area surface both in the topside and the bottom. The underneath flow layer represents there was kept heating from the underneath, with the effect of both the buoyancy and the slow crosswind, the heat could be transferred upward to heat the wood surface deeply. Around the top side of the no flame area, the attached hot flow layer shows the pyrolysis proceeded and the gas-phase products formed the hot layer to keep the temperature of the wood. With the increased wind speed, in the cases of speed 3, 4 and 5, the flame tended to attach the bottom side of the rods due to the blowing of the high-

speed wind, which indicates the gas-phase combustion only occurred on the bottom side. Meanwhile, there were no flame areas observed under the high wind speed conditions, and the area became larger with the increased wind speed. It should be highlighted that the cooling in the high wind speed cases was along with the direction of crosswind and started from the top to the bottom. In the case of speed 3, the area near the end of the rod had completely extinguished while the temperature at the bottom side still was high enough for the rapid pyrolysis. The conclusion can be drawn from the images of speed 4 and 5 as well, that the topside always extinguished before the underneath. Combined with the schlieren images, it is found that the area where already cooled to extinguishment had no significant hot flow layer attached both in the top and bottom side. This is attributed to the bottom side, the underneath hot flow layer of the extinguished area was blowing off and cannot attach to the bottom side. No attached hot gas parcel underneath means there was no sufficient convective heating from the underneath, in addition to the heat loss from the crosswind, which resulted in fast cooling of the deep rod surface. On the other side, there was no hot flow around the topside means the pyrolysis stopped in the area. Neither hot gas flow from the combustion production nor the convective heating from underneath, the wood in these areas showed a quick cooling and extinguishment.

Regarding the underneath preheating, it is found the preheating length was significantly increased under wind speed 1 and 2. There was a large area enfolded in the thick hot flow layer in these wind conditions. In the high wind speed cases, although the hot gas flow was blowing further in the adjacent virgin wood than the no wind condition, the flow did not attach tightly to the underneath surface. The scatted underneath hot flow cannot keep

preheating the unburned wood effectively than those under wind speed 1 and 2. In addition, the larger speed of the cross-wind, the more dispersal can be found in the underneath hot flow. This phenomenon explains the charring rate decreasing, which is shown in Fig.6.15.

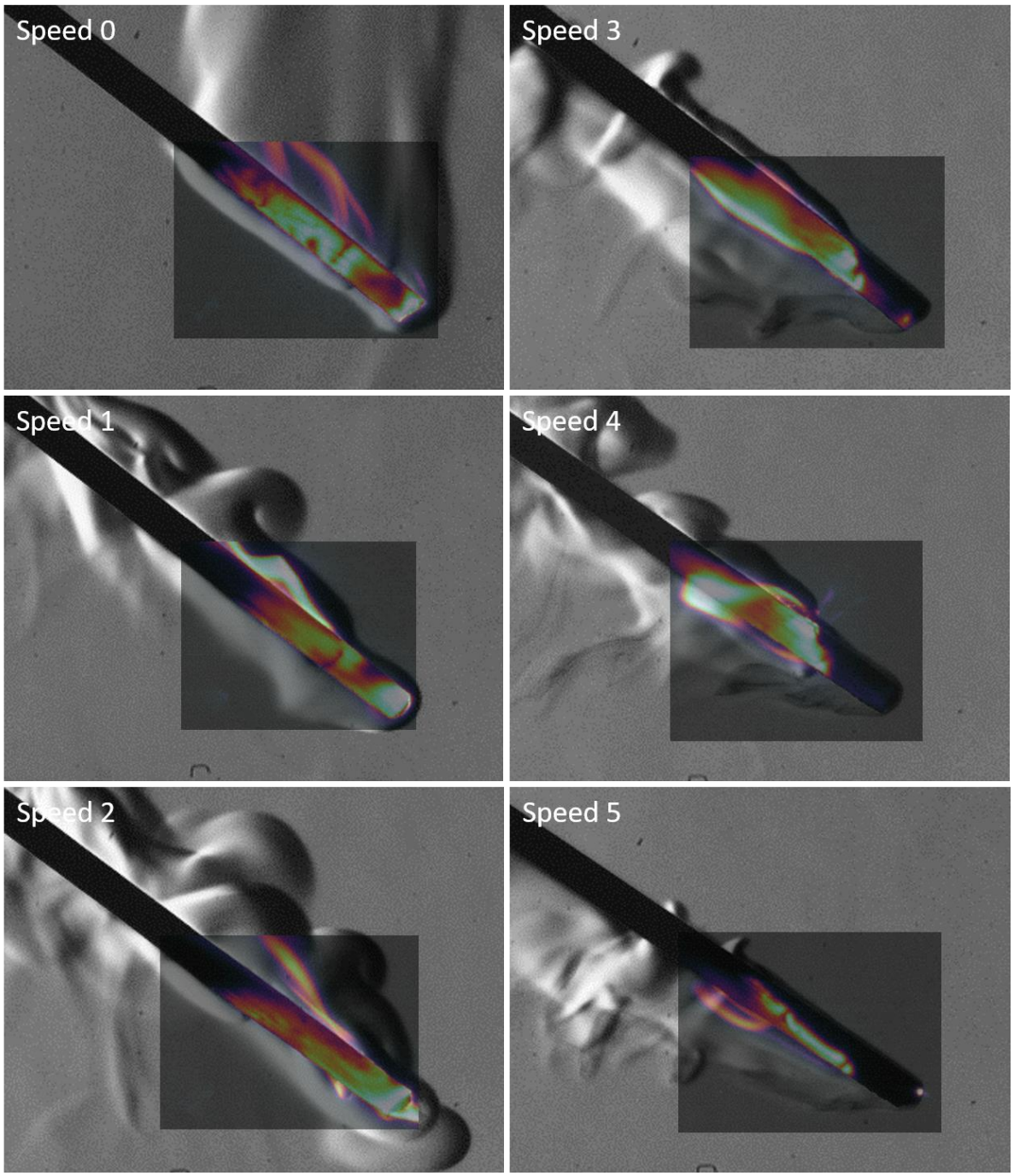

Figure 6.25 The schlieren image matches the surface temperature map after 10 s of self-sustained burning started with different cross-wind speed.

6.3.2.3.2. The effects of cross-wind speed on the hot gas flow

In order to further study the effect of the cross-wind on the invisible hot gas flow, the schlieren images under different wind speed set at 0s, 10s and 20s are shown in Fig.6.26. At the beginning of self-sustained burning, all the six cases had the thick hot flow parcel underneath. With the cross-wind involving, the invisible hot flow was more likely to attach the burning rod. Under wind speed 1 and 2, it covered both sides of the rod, while it was more likely to attach underneath the rod under wind speed 3, 4 and 5.

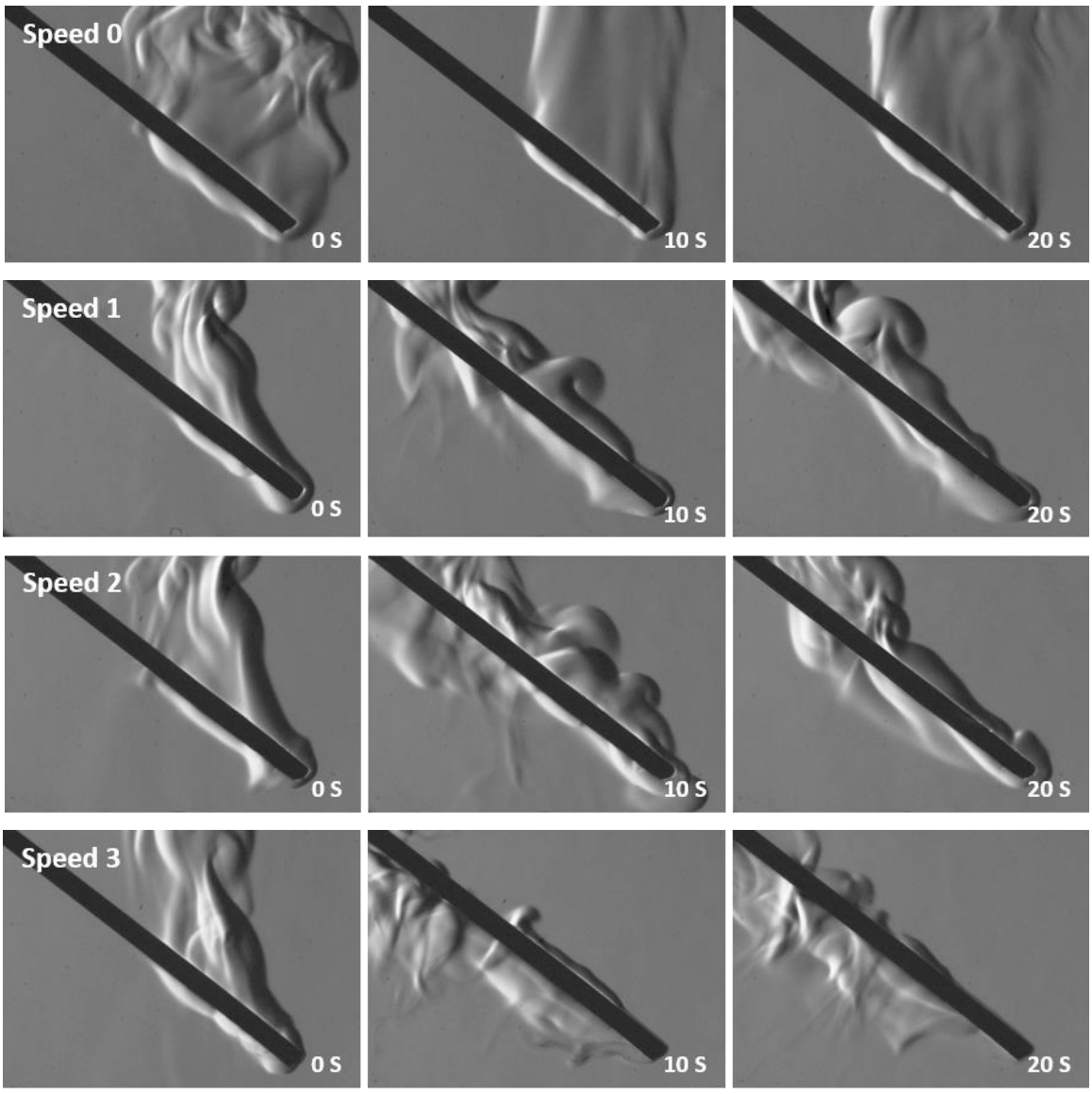

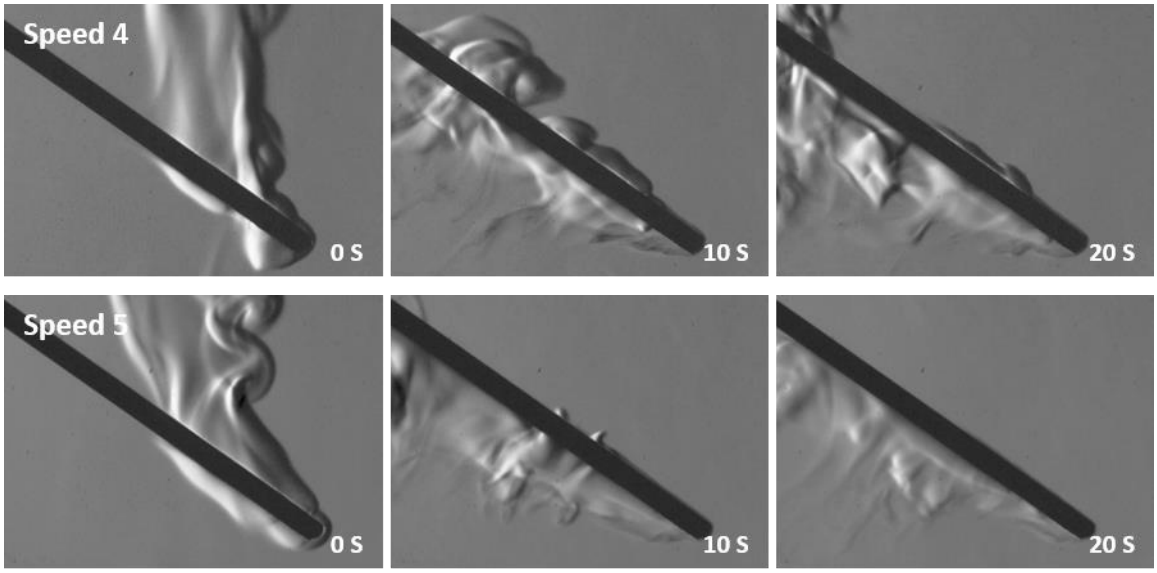

Figure 6.26 The illustration of underneath hot gas flow at 30 degrees inclination at 0 s,10 s and 20 s under different cross-wind speed set.

As discussed in Section 6.3.2.4, the preheating length was longer under a cross-wind than under no cross-wind, especially in the cases of speeds 1, 2, 3 and 4, where a large area was heated by the hot gas layer. However, by comparing the images between the cases with the crosswind, the hot gas layer was blown away from the underneath surface under the higher speed wind. There was no obvious layer of the underneath hot flow under the wind speed 5. The schlieren image could reflect the density of the air by the contrast of the image. The hot flow under higher wind speed shows in a low contrast than in the control group case. This represents that the crosswind blew away the combustion products and cooled the temperature of the invisible layer by increasing the heat loss to the surrounding cold air. On the contrary, the underneath hot gas parcel kept in relatively high contrast and could obviously be attached to the bottom surface in the cases of speeds 1 and 2. This is attributed to two aspects: the first is due to the heat transfer from the high-temperature area (impact point) was increased by the crosswind; the second is that the wood combustion (both rapid thermal

pyrolysis and gas-phase combustion) was enhanced under these wind conditions by both the larger area of hot flow enfolded and the increased flame attachment phenomenon, further the gas-phase combustion products increased with the enhancing burning.

After the 20s of self-sustained burning, the hot gas flow in the cases of speeds 1 and 2 became larger in size and stronger in intensity. It indicates that the combustion was significantly enhanced under these wind conditions, and more combustion products were produced. A mutual promotion relationship might be found between the enhanced combustion and the increased gas-phase combustion products since the more combustion products produced, the more hot gas layer was supplied. With the help of the crosswind, the gas-phase combustion products that came from the top side could be transferred into the adjacent underneath and continued to heat the deep surface.

On the contrary, the contrast of the hot flow under the higher wind speed decreased, of those, the hot flow in the speed 5 case decreased dramatically and almost disappeared. Moreover, the hot flow under wind speeds 3, 4 and 5 mainly concentrated near the combustion front while few appeared near the rod end. This is because the direction of the hot flow transferred was significantly changed by the strong crosswind, resulted that it cannot effectively transfer upward to heat the deep surface. Therefore, the topside would be cooled quickly, results in less flammable gasses produced in the pyrolysis. Few hot gas flow supply from the gas-phase combustion products into the bottom side and the incompact underneath hot gas parcel resulted in the bottom side cooling afterwards.

Fig.6.27 illustrates how the hot gas flow moves and how the underneath hot gas parcel supply from the gas-phase combustion products of the deep surface burning. The first image in

Fig.6.27 presents the natural circumstance (no cross-wind), that the hot gas flow came from the impact point moved in two ways: the red line represents that the heated flow moved upward due to the buoyancy; the green line shows that the part of the upward hot flow moved along the underneath surface because of the Coanda Effect[166]. The upward hot flow could heat the deep layer of the surface and the flow in the longitude direction could preheat the adjacent wood. The black line indicates the gas-phase combustion products which came from the deep surface of the rod similarly moved in two ways: upward and along the rod. The part of heat flow that came from the burned surface could extend along the rod and preheat the same layer of the wood. In the low-speed crosswind cases: speed 1 and 2, the hot gas flow of the impact point still moved in two directions. However, due to the involvement of crosswind, the movement slightly tilts in the direction along with the wind. It can be seen that the underneath hot gas parcel (the green line) was blowing off the bottom surface slightly, which is the reason why the underneath hot flow turned to be stronger under wind speed 1 and 2 in Fig.6.26. In addition, the hot gas flow moving upward (the red line) had a tilted angle with the wooden rod instead of the vertical direction. This would increase the fire propagation rate due to the faster heat transfer along the rod. It is worth knowing that the gas-phase combustion products with a high temperature tended to move downward due to the crosswind and supplied to the underneath hot gas flow (the black line). The more supply of the underneath hot gas parcel, the higher intensity self-sustained combustion would have. That is why the combustion was strongest under these two sets of wind speed. However, with the increasing wind speed, as shown in the third image of Fig.6.27, the larger amount of the underneath hot flow was blowing away from the bottom surface (the green line), the high

velocity of wind made the hot flow unable to attach on the surface. Moreover, the upward moving hot flow (the red line) was significantly affected by the crosswind and cannot be transferred upward effectively. As a result, a large area on the topside cannot be heated, cooled fast, more char formed while less flammable gases were produced as a consequence, as shown in the blue colour area in the third image. This is the reason that the high wind speed cases (speed 3, 4, 5) had a relatively higher charring rate than the control group but a shorter burning lifetime, as shown in Fig.6.14 and 6.15. Another reason is the hot flow supply from the deep surface, due to the larger area fast cooled under the high velocity of wind, there were less gas-phase combustion products supply into the underneath. As result, the underneath hot gas parcel became thinner with time, as shown in Fig.6.26 at the 20s.

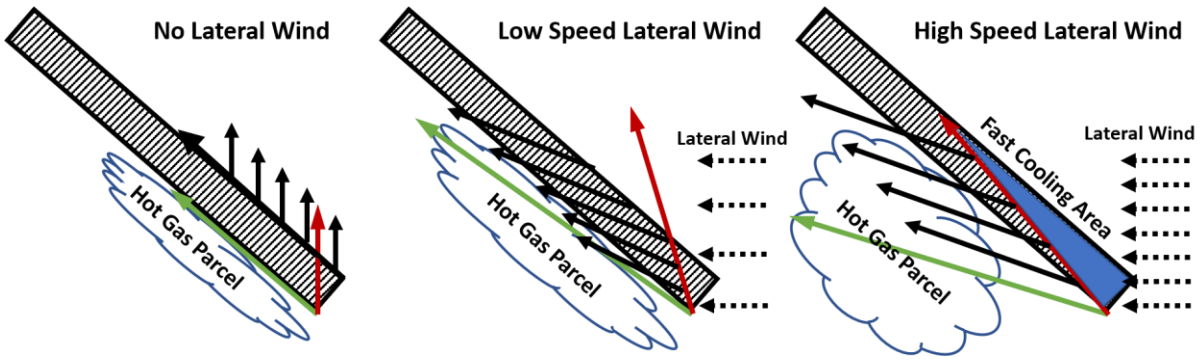

Figure 6.27 The illustration of the convective heat transfer and the supply of the hot gas flow underneath.

Overall, the crosswind significantly affected the surrounding hot gas flow, especially for the underneath hot gas layer. In the cases of speeds 1 and 2, the crosswind blew the gas-phase products of combustion into the adjacent underneath side and enhanced the burning. In the higher wind speed cases, since the incompact underneath hot flow cannot transfer the heat

effectively to the deep surface, the topside wood was extinguished fast. Without sufficient gas-phase combustion products supply, the combustion was weakening under these conditions.

6.3.3. The comparisons of the cross-wind speed effects between 0^o and 30^o

From the results and discussion above, it is found that the effects of crosswind on the combustion of the rod have different mechanisms between the inclination at 0^o and 30^o. Fig.6.28 shows the burned wood at 0^o and 30^o under the natural wind circumstances, enhanced group (speed 2 as an example) and the weakened group (speed 4 as an example). It can be clearly seen that the combustion status on the horizontal surface and the 30^o surface are different since different convective hot gas flow occurred during the burning process.

In detail, it is found that the underneath hot gas parcel is thinner at 0^o than which at 30^o, as well the gas parcel disappeared quicker when self-sustained burning begins. This is because the underneath hot gas parcel could be effectively supplied at 30^o, rather than 0. As the impact from the buoyancy and the Coanda Effect (illustrated in Fig.6.27), the hot gas flow trended to move upward rather than the horizontal direction (shown in Fig.7.10). As a result, in natural wind circumstances, the cooling comes from underneath at 0^o cases. It can be seen from the image of 0^o (a) in Fig. 6.28, the char in the bottom side gradually decreased until extinguishment after piloted ignition. At the end of the charring, there was only char that appeared at the topside.

Comparatively, the char moved uniformly at 30^o inclination, as shown in Fig.6.28 30^o (a), which means the surface pyrolysis proceeded in the deep surface. When the crosswind was applied,

the high concentrate heated flow at the impact point was brought along the rod and supply the underneath hot gas flow. It is found that the char from the bottom side of the rod moved longer under wind speed 2 (Fig.6.28 0^o (b)); due to the insufficient heated gas supply from the deep surface combustion products, the charring distance in the bottom side eventually shorter than which in the top side. Similar to the horizontal direction, the combustion at 30^o under speed 2 significantly enhanced, the heat pyrolysis proceeded along the whole wooden rod, see Fig.6.28 30^o (b). The mechanism of how the wind affects the hot gas flow supply was demonstrated in the section picture of Fig.6.27. At the higher wind speed group, the intensity of combustion at both orientations was decreased. However, it is quite different from the way they cooled by the wind. At 0 degrees, the cooling still came from underneath, this is mainly attributed to the increased convective heat loss to the surrounding cold air. At 30 degrees, the cooling came from the top side of the rod, although there was a faster charring rate underneath than those under no crosswind condition, the heat pyrolysis of the whole wood became weaker. The reason for that was explained in the third picture of Fig.6.27, which comes from three sides: the first reason is the high-velocity wind blew away the underneath hot gas parcel, made it hard to attach on the surface; the second one is the topside cannot be effectively heated because the upward heat transfer was impeded by the crosswind; the third reason is the high concentration of char formed under low surface temperature, as a result, the supply of the underneath hot gas flow which generated from the deep surface significantly decreased.

The flame was another factor that impacted the combustion status. At the horizontal direction, the flame was small in size and relatively low intensity compared with those at 30 degrees.

Besides, the flame only appeared at the top side of the rod. Although the applying of crosswind decreased the flame temperature, the effects of flame on the wood burning under different wind speed was insignificant. Comparatively, the flame was much larger and stronger at 30 degrees inclination, therefore, it is meaningful to study the differences of flame between various crosswind speeds. In fact, from the results of flame temperature distribution in Fig.6.17, it is found the flame temperature concentrated in the high-temperature zone in the low wind speed cases, in contrast, it was concentrated in the low-temperature zone under the high velocity of the wind. In addition, the flame at low wind speed cases enfolded around the whole wooden rod, see Fig.6.12 and 6.13, while it was mainly attached on the bottom side at high wind speed cases. The larger area of heat pyrolysis made the flame temperature slightly increased in the cases of speeds 1 and 2. On the contrary, few flame appearances at the topside under the higher velocity of crosswind decreased the ability of the heat pyrolysis on the deep surface. As a result, the char mainly appeared on the bottom side under high wind speed.

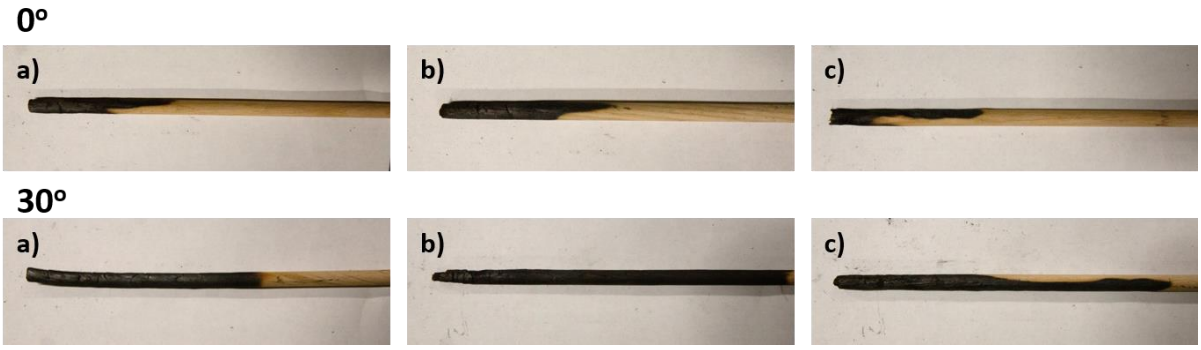

Figure 6.28 The burned wooden rod examples from different cases: a) represents speed 0; b) represents speed 2 and c) represents speed 4.

6.4. Conclusions

With the improved imaging system of direct, schlieren, thermal and flame images, the influence of the crosswind on fire propagation and self-sustained burning at 0^o and 30^o was investigated. The results could be concluded in the following points:

A) To the wind effects on the burning at 0^o:

- The burning lifetime and charring rate were increased under wind speed set 1 and 2 then decreased with higher wind speed.
- The flame temperature decreased when the crosswind was applied. However, the wind speed did not significantly affect the flame temperature.
- The cooling came from underneath the rod, the underneath cooling became slowly under wind speed 1 and 2 while the cooling became faster under wind speeds 3, 4 and 5.
- From the schlieren images, it is found the underneath hot gas flow was significantly increased under wind speed 1 and 2. Although the underneath hot gas parcel started to decrease with higher wind speed, the underneath flow under these groups was still more than those under no crosswind condition.

B) To the wind effects on the burning at 30^o:

- The burning lifetime and charring rate were increased under wind speed set 1 and 2 then decreased with higher wind speed. The burning under wind speed 1 and 2 could self-sustained and burned out the whole rod. It is noticed that the charring rate under all the cases with the crosswind was higher than which under natural wind circumstances.

- The flame was enfolded around the burning rod under wind speeds 1 and 2, while the flame was mainly attached under the bottom side under wind speeds 3, 4 and 5.
- The averaged flame temperature slightly increased under wind speed 1 and 2, while it decreased at higher wind speed.
- The flame temperature was distributed mainly in the high-temperature zone under wind speed 1 and 2. With the crosswind speed increasing, the flame temperature tended to concentrate in the low-temperature range.
- It is noticed that the wooden rod under wind speed 1 and 2 did not show significant cooling. In other groups, the cooling came from the rod end and along with the wood lengthwise. With no crosswind condition, the cooling started from the beginning of the self-sustained burning, while it started a few whiles after the piloted ignition end under wind speed 3, 4 and 5. This is attributed to the heat transferred from the impact point by the crosswind. Besides, the lengthwise cooling started earlier with the increasing wind speed and cooled faster in a higher velocity of crosswind.
- By analysing the temperature on a vertical line, it is found that the underneath heating was stronger at wind speeds 1 and 2 compared with other cases. In the high wind speed cases (speed 3, 4 and 5), the topside surface started cooling early and dropped temperature faster than those of the bottom side. In addition, with the increasing wind speed, the layer where it was heated became thinner, and the temperature dropped faster in the high wind speed cases.
- With the help of schlieren images, the invisible heated gas flow can be visualised. It is found that the hot gas flow surrounded the burning rod attached the burning rod more

tightly under wind speed 1 and 2 than in other cases. In addition, the underneath preheating length was longer in these wind conditions. Comparatively, there were only a few heated gas flows on the topside in the cases of speeds 3, 4 and 5. Moreover, the underneath hot gas flow attached incompact under these wind conditions and disappeared soon with time.

C) The different mechanism of how the wind affects on the burning at 0^o and 30^o was compared. The wind affects the burning wood at 0^o mainly on the convective heat loss and the movement of the underneath hot gas flow. At 30^o cases, the wind effects on the flame position and temperature, the heat transfer from bottom to top and the supply into the underneath hot gas flow came from the deep surface.

7. Conclusions and Future works

7.1. Conclusions of the thesis

The main objective of this thesis is to study the mechanism of fire propagation on an inclined wooden surface by means of combustion diagnostics and imaging systems. Various methodologies of combustion diagnostics have been developed in this study, including the two-colour temperature measurement, the thermal imaging metrology, the schlieren imaging system and the optical flow motion estimation. The two means of temperature measuring methods have been well calibrated in various settings of the imaging system, and the most suitable setting has been used in the experimental studies in this thesis.

The various imaging systems and equipment have been used for achieving the study aims. In details, in Chapter 4, the imaging system which synchronises the direct and schlieren imaging has been used for the study of fire plume of the burning wood; the thermal imaging system has been introduced and synchronised with both the direct and schlieren imaging system in Chapter 5 in order to analyse the effect of underneath hot gas flow on preheating the wooden rods; in Chapter 6, total four cameras have been used for the imaging system, they are: high-speed colour camera for the flame temperature measuring, raspberry pi camera for capturing the direct images of the burning wood, high-speed black and white camera for the schlieren imaging and InGaAs thermal camera for reading the wood surface temperature. The contributions of this research are summarised in detail as below together with the suggestions for the future work in the field of research.

7.1.1. Developed optical pyrometers

In this part, the two means of temperature measurement, including the two-colour method

and the thermal imaging method, have been developed to cover the request of study and minimise the residuals. In detail, the contributions can be concluded as:

- The two-colour optical pyrometer is calibrated with a black body furnace in the temperature range of 700 – 1500 ^{o}C. In order to minimise the interference from the infrared radiation, an infrared cut off filter is applied. The calibrated results together with the residuals of two imaging settings including with the IR blocker filter and without any filter have been compared and analysed. The results show that using the infrared blocker filter together with the ratio of Red/Green channels reaches the minimum error, which is under 10 K in the whole range. In addition, the effect of infrared on the camera response has been studied in the chapter.
- The thermal imaging metrology is calibrated with a black body furnace in the temperature range from 200 – 750^{o}C. The wavelength bandpass which is in the range of 1550nm – 1670nm is achieved by a long-pass filter together with the response range of the camera sensor in order to get a high sensitivity in the requested temperature range. The size of source effect (SSE) has been calibrated firstly with an adjustable aperture, which shows the minimum size of the testing objective is 3 mm with the imaging system. In order to achieve a wider testing range of temperature, two different exposure time: 16 ms and 32 ms have been used for calibration. The results show the maximum error with 16 ms is about 4K in the temperature range 300 – 750^{o}C while the maximum error with 32 ms is about 4.5K in the range of 200 – 550^{o}C.

7.1.2. The effect of the diameter of wooden rods and the inclination angle on the fire plume

Based on the synchronised schlieren imaging and the visible imaging system, the fire plume of the burning rods can be visualised. With the help of optical flow, the motion of the flame and the heated flow above the burning rod can be estimated. The main conclusions in this chapter can be summarised as below:

- The inclination angle of the burning surface significantly affects the burning properties including the lifetime of burning and the charring rate. In detail, the burning on the positive 30^o surface has the longest burning lifetime which could burn out the whole wooden rod in this study. Followed by the burning on the horizontal surface, while the burning lifetime is the shortest on the minor 30 degrees surface. Similarly, the fastest charring occurs in the 30^o case, followed by the horizontal direction while the charring rate is the slowest in negative 30 degrees.
- The distinct flame attachment phenomenon is visualised in the 30o inclination angle case, and become stronger when igniting the wooden rod from the middle. The mechanism of the flame attachment is explained, which is caused by the imbalance of air pressure caused by the confinement on the one side air entrainment. The appearance of flame attachment could significantly enhance the burning and fire propagation.
- From the schlieren images, the fire plume can be visualised. Similar to the flame attachment phenomenon, the main direction of the fire plume tends to deviate from the vertical direction. The attachment phenomenon of fire plume does not appear at

the beginning of the self-sustained burning but a while after the ignition off. The results show that the fire plume has a slight deviation away from the rod while the fire plume has attached to the rod surface with the positive inclined angles when the attachment phenomenon occurs. In addition, the tile angle of the fire plume significantly increased when the inclined angle increased to 30^{o}, the tile angle has indistinctive change when the inclined angle continuedly increases.

- The velocity field is estimated by the optical flow method in this chapter. For the velocity of flame edge, the results show that the flame velocity at 30 degrees is higher than the other cases, which means there is a high rate of mixing the oxygen and fuel in the diffusion flame. For the velocity field in the schlieren images, the velocity distributions show that the velocity of the heated flow in the 30 degrees case is more likely in the high-velocity range which means the fire plume in the positive angle in more turbulence. The assumption can be made from these that the convection is more effectively and the mixing rate of the oxygen and fuel is higher when burns on the positive angle surface.

7.1.3. The effect of the underneath preheating on the fire propagation

In this chapter, the thermal imaging system is introduced and synchronised with direct imaging and schlieren imaging system. The importance of the underneath preheating by the invisible hot gas parcel on the bottom side has been systematically studied for the first time. The contributions made in this research can be listed as below:

- The underneath preheating zone has been visualised by the novel imaging system. In

detail, the dim blue flame could be enhanced for visualising by the selective enhancement method in HSV space, the wooden surface which is under heat pyrolysis can be visualised. In addition, the hot gas flow can be visualised in the schlieren imaging system. By synchronising the two imaging systems, the pre-heating zone can be obtained which is the difference between the pyrolysis zone and the zone of hot gas flow.

- The flame attachment phenomenon was usually analysed by visible images. In this chapter, the flame attachment is quantitatively analysed by the enhanced thermal images for the first time. The enhanced thermal images can be more accurate to determine the flame attachment length and the tile angle than the direct images. From the results, it is found that the flame attachment length increases with the inclined angle, and the critical angle at which the sharp increase occurs is about 25°. In addition, the tile angle decreases when the inclined angle increase, similar to the flame attachment length, the critical angle is 25° for the sharp decrease of the tile angle.
- The importance of the underneath preheating has been proved by three means of method. Firstly, the hot gas layer on the bottom side is much thicker than which on the top side. Secondly, the surface temperature on the bottom side is higher than which on the top side. Thirdly, by analysing both the thermal and schlieren images at different timing, it is found that the heat pyrolysis process from the bottom to the top. From these pieces of evidence, it can be concluded that the underneath preheating is essential for the fire propagation along the rods. In addition, with the

combustion process diagram, it is clearly found the intensity of burning depends on the underneath hot gas parcel.

- From the quantitative results of underneath preheating, it is found that the preheating length increases with the increasing inclined angle. In addition, there is a critical angle of 25^{o} at which, the underneath preheating length significantly increases. The longer burning lifetime and larger charring rate of burning at the positive inclined angle are attributed to its longer preheating length underneath the wooden rod.
- The impact point is defined as the area where is immerged with the piloted ignition. The impact area has a high concentration of heat and combustible gases. The wooden rods which ignited at the positive inclined angle have a larger impact area which means a higher intensity initial combustion occurring at the positive inclined angles.

7.1.4. The effects of the cross-wind on the self-sustained burning

In this chapter, a designed wind system is introduced to supply the five sets of cross-wind along with the fire propagation. Four cameras are utilised to build an imaging system that could measure the flame and wood surface temperature and visualise the invisible hot gas and the actual burning of the rod at the same time. Two inclined angles: 0^{o} and 30^{o} are chosen to represent the different circumstances. The mechanisms of the burning under the cross-wind have been analysed and concluded as below:

- From the results of the general properties, it is found the cross-wind enhances the burning of the speed 1 and 2, under these wind conditions, both the burning lifetime and the charring rate have increased. The wind speed 2 in this study is defined as the

'turning point', beyond which the intensity of burning decreases. The cross-wind impacts various aspects of the burning, including the oxygen supply, the temperature of flame and surface, the heat transfer, and the movement of the combustion products.

- The results of the flame temperature show that the flame temperature decrease with the cross-wind involves in the 0^o case, while it increases at speed 1 and 2 then decreases with the increasing wind speed in the 30^o case. The different trend of 0^o and 30^o is due to the larger area under pyrolysis in the 30^o case when applies the wind of low speed. In addition, by analysing the temperature distribution on the 30 degrees inclination, it is found the flame tends to be concentrate in the high-temperature zone with the wind speed 1, 2 and 3 while it is more likely in the low-temperature range when the wind speed increases to speed 4 and 5.
- From the results of the surface temperature in the 0^o case, it is found that the cooling starts from the bottom side. With the involvement of the cross-wind, the cooling from the underneath decreases, the temperature remains in the high value for a longer time with the wind speed 1, 2 and 3 than the no wind condition. The cross-wind could enhance the convective heat transfer of the bottom side. In addition, the gas-phase combustion produces can be brought into the underneath flow layer with the cross-wind. However, the higher velocity of cross-wind significantly increases the heat loss, results in a fast temperature dropping under these wind conditions.
- The schlieren images are used to analyse the mechanism of the cooling in the 0^o case. The underneath hot gas flow disappears quickly under the natural wind condition,

while the thicker underneath hot gas parcel appear under the cross-wind. This is due to the cross-wind applies a horizontal pressure to the gas and makes the heated flow including the gas-phase combustion products moving forward. However, when the wind speed is too high, such as the speed 4 and 5, the heat loss is significantly increased, results in an incompact flow layer underneath the rod.

- From the results of the surface temperature in the 30^{o} case, a different phenomenon is found comparing with the 0^{o} case. The cooling starts from the end and moves along the rod under the high speed of cross-wind. Under wind speed 1 and 2, the whole burning rod remains at a high temperature, while increases the wind speed, the temperature of the topside surface decreases earlier than which of the bottom side.
- From both the results of the surface temperature and the schlieren images of the 30^{o} case, it is found the cooling direction under the 30^{o} inclined angle is attributed to multiple factors. Firstly, the flame is enfolded around the burning wood with the wind speed 1 and 2, while it only attaches on the bottom side when the wind speed is higher than speed 3; secondly, the high velocity of cross-wind impedes the heat transfer to the topside; thirdly, the combustion products could supply the underneath hot gas flow when the cross-wind is slow, while the fewer gas-phase combustion products have produced when the cross-wind has a high velocity.

7.2. Suggested future works in this field

- The high-speed colour imaging system could be used for spectral emissivity measuring with full calibration by the objects with a standard emissivity, for example, the SiC fibre. An example for the calibration to a standard SiC fibre is shown in Fig.7.1, the red, blue and green points represent the emissivity calculated by the R/G/B channels respectively, consider that the emissivity of the SiC fibre is 0.88, the calibration results are reliable. Due to the good compatibility with the two-colour method, the colour imaging system can measure the temperature and the emissivity of a solid object at the same time. To be specific, calculate the temperature by the two-colour method first, then calculate the black body radiation at the same temperature of the testing object by a pre-calibration curve. The spectral emissivity of the testing can be obtained by the ratio of the pixel response of red/green/blue channels with the black body radiation. Some examples are shown in Fig.7.2. The testing object is an electrically heated coil under different power, the Figures show that the temperature (black points) can be obtained with its emissivity (red, green and blue points) in real-time. As the emissivity is changing with the various circumstances such as the temperature, the oxidation degree, the view angle and so on. Real-time emissivity measuring can be a useful measuring tool in the field where the emissivity changes a lot. In addition, this methodology could measure the emissivity in an open place instead of inside the black body furnace, it is able to measure the emissivity for large-scale objects.

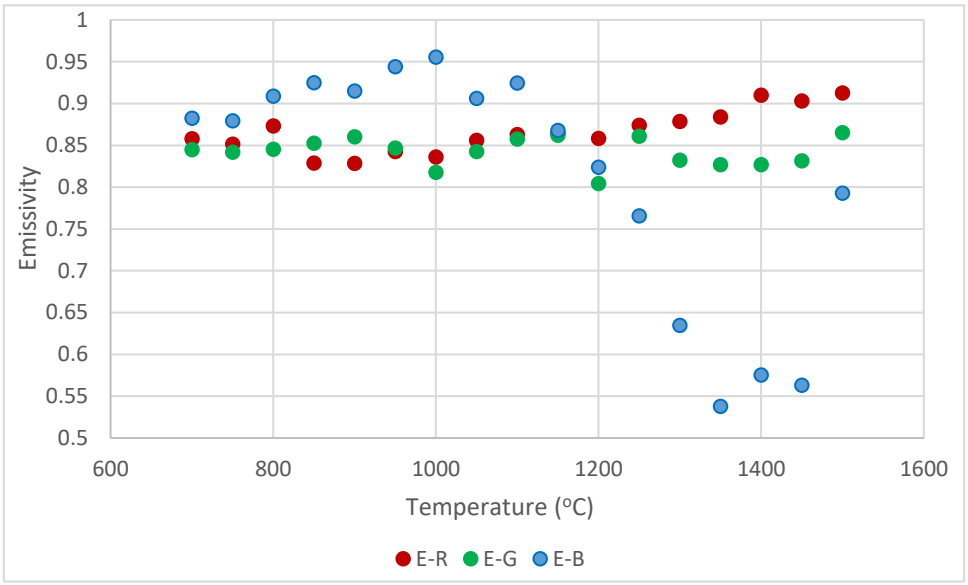

Figure 7.1 An example of the validation of the spectral emissivity of a SiC fibre. The colours represent the calculating channels: red is R channel; green is G channel and blue is B channel.

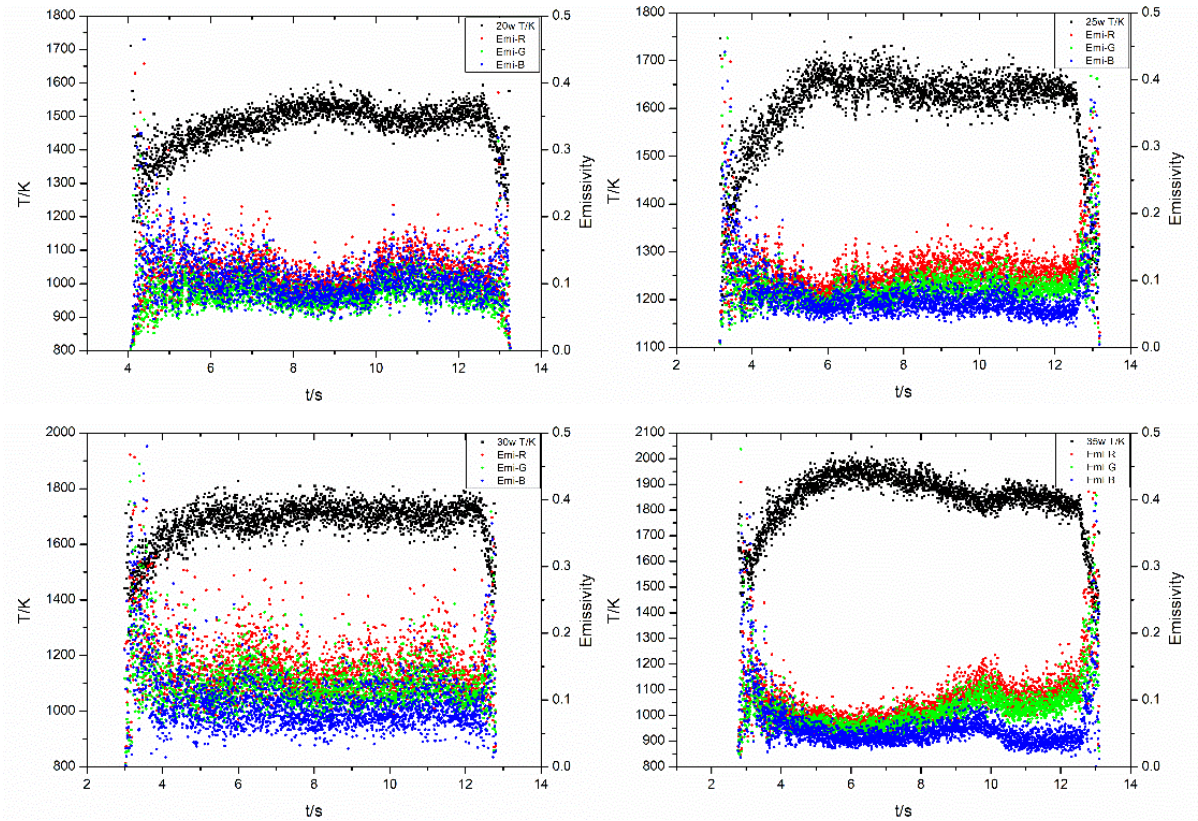

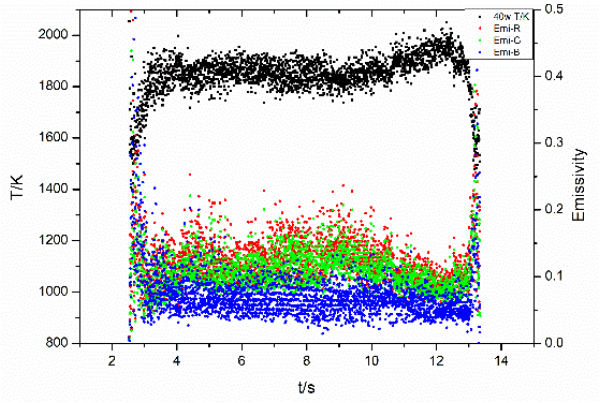

Figure 7.2 Some examples of the real-time emissivity/temperature measuring of electrically heated coils at different power (20w, 25w, 30w, 35w and 40w). The colours represent the results calculated by different colour channels: red indicates the R channel; green indicates the G channel and blue indicates the B channel. The black points represent the temperature measured by the two-colour method.

- The other kinds of non-invasive temperature measurement, such as measuring temperature by density change in schlieren images can be very useful in some circumstances. For example, the schlieren imaging system which is used for visualising the hot flow gas around the burning wood in this study can be synchronously utilised for reading the flow's temperature. To achieve this objective, the calibration of the density relating to the temperature is required. To be specific, the schlieren image of a fluid calibration source that has a certain temperature can be analysed by its pixel intensity distribution, combined with the relative equations of the Gas Law, the fitting curve of temperature measuring can be obtained.
- The wood combustion is significantly influenced by the moisture of the wood, as the wood will be heated to remove the moisture before the pyrolysis occurring. In addition, the evaporation of water could dramatically decrease the temperature of the flame temperature. Therefore, the study of the effects the moisture on the flame

temperature is meaningful. As the two-colour method can easily read the wood flame temperature, the experiments can be set by control the moisture content of the wood in a humidity cabinet, and calculate the flame temperature by the two-colour method. The results can be used for the study in fire safety both in the field and the structure of the indoor buildings.

- Regarding the wind effects on the fire propagation, this study only focuses on the cross-wind with the same direction along with the fire propagation as this direction could significantly influence the charring rate and fire spread. However, the cross-wind with the opposite direction of the fire propagation could affect the self-sustained burning as well, and it is hard to predict how the results could be. Therefore, the burning under the opposite direction could be an interesting study by using the imaging system developed in this thesis. Moreover, the burning under the wind which is vertical to the wooden surface could be another worth studying project, as the wind in this direction would not affect the fire propagation directly but in the convective heat transfer. Thus, this could be another meaningful field to study.
- A more accurate wind supply system is needed to further improve the experimental result. In detail, a powerful fan that could supply a large amount of the airflow is needed, a long enough wind tunnel is required to obtain the laminar flow, and the simulation process will be used for validating the wind system. With a decent wind supply system, quantitative results such as the heat transfer coefficient between the wood and flame or the flame and air can be achieved. It is meaningful to utilise these imaging systems and techniques in this thesis to further study the fire propagation

phenomenon.

- To help improve the understandings of the burning of natural wood, the developed imaging system with techniques in this thesis could be used to test various kinds of wood, especially the wood species used in the building structure, such as balsa, pine, birch and so on, with or without the bark. As the methodologies in this thesis could cover the main study aspects during the burning, it is easy to apply the methodologies to other species of wood and collect more useful information for fire safety research.

References

[1] F. A. Williams, “Mechanisms of fire spread,” *Symp. Combust.*, vol. 16, no. 1, pp. 1281–1294, 1977.

[2] R. B. milan sonka , vaclav Hiavac and, *Milan Sonka_ Václav Hlavác_ Roger Boyle-Image processing, Analysis, and Machine Vision-Cengage Learning (2015)*. .

[3] M. Takeda, “Applications of MEMS to industrial inspection,” *Proc. IEEE Micro Electro Mech. Syst.*, vol. 00, pp. 182–191, 2001.

[4] Z. Liu, H. Ukida, P. Ramuhalli, and K. Niel, “Integrated imaging and vision techniques for industrial inspection: Advances and applications,” *Integr. Imaging Vis. Tech. Ind. Insp. Adv. Appl.*, pp. 1–536, 2015.

[5] F. Sullivan, “Current Medical Diagnosis and Treatment 1998,” *Bmj*, vol. 318, no. 7185, p. 743, 1999.

[6] J. Molleda *et al.*, “An improved 3D imaging system for dimensional quality inspection of rolled products in the metal industry,” *Comput. Ind.*, vol. 64, no. 9, pp. 1186–1200, 2013.

[7] C. Y. Fang, S. W. Chen, and C. S. Fuh, “Automatic change detection of driving environments in a vision-based driver assistance system,” *IEEE Trans. Neural Networks*, vol. 14, no. 3, pp. 646–657, 2003.

[8] H.-W. Huang and Y. Zhang, “Flame colour characterization in the visible and infrared spectrum using a digital camera and image processing,” *Meas. Sci. Technol.*, vol. 19, no. 8, p. 085406, 2008.

[9] H. W. Huang and Y. Zhang, “Digital colour image processing based measurement of premixed CH 4 + air and C2H4 + air flame chemiluminescence,” *Fuel*, vol. 90, no. 1, pp.

48–53, 2011.

[10] J. Yang, F. M. S. Mossa, H. W. Huang, Q. Wang, R. Woolley, and Y. Zhang, “Oscillating flames in open tubes,” *Proc. Combust. Inst.*, vol. 35, no. 2, pp. 2075–2082, 2015.

[11] R. Shang, Y. Zhang, M. Zhu, Z. Zhang, D. Zhang, and G. Li, “Laminar flame speed of CO2 and N2 diluted H2/CO/air flames,” *Int. J. Hydrogen Energy*, vol. 41, no. 33, pp. 15056–15067, 2016.

[12] S. W. Turner, J. Thompson, and R. M. Rosser, “The kings cross fire,” in *International handbook of traumatic stress syndromes*, Springer, 1993, pp. 451–459.

[13] X. Zhou, S. Mahalingam, and D. Weise, “Experimental study and large eddy simulation of effect of terrain slope on marginal burning in shrub fuel beds,” *Proc. Combust. Inst.*, vol. 31 II, pp. 2547–2555, 2007.

[14] J. Zhao, H. Zhu, J. Zhang, H. Huang, and R. Yang, “Experimental study on the spread and burning behaviors of continuously discharge spill fires under different slopes,” *J. Hazard. Mater.*, vol. 392, no. December 2019, p. 122352, 2020.

[15] Y. Lin, L. Hu, X. Zhang, and Y. Chen, “Experimental study of pool fire behaviors with nearby inclined surface under cross flow,” *Process Saf. Environ. Prot.*, vol. 148, pp. 93–103, 2021.

[16] R. T. Sataloff, M. M. Johns, and K. M. Kost, *Combustion*, 4th ed. 2006.

[17] G. Irvin and A. Y. Richard, *Combustion*. 2008.

[18] I. Glassman, R. A. Yetter, and N. G. Glumac, “Chapter 4 - Flame phenomena in premixed combustible gases,” in *Combustion (Fifth Edition)*, Fifth Edit., I. Glassman, R. A. Yetter, and N. G. Glumac, Eds. Boston: Academic Press, 2015, pp. 147–254.

[19] W. M. Rohsenow and J. R. Hartnett, *Handbook of heat transfer*, vol. 36, no. 06. 1999.

[20] R. M. Manglick, *Heat trnsfer Enhancement*. 2003.

[21] Y. A. Cengel, “Heat Transference a Practical Approach,” *MacGraw-Hill,* vol. 4, no. 9, p. 874, 2004.

[22] C. K. Batchelor and G. K. Batchelor, *An introduction to fluid dynamics*. Cambridge university press, 2000.

[23] W. Bethell, “Dynamics of surf-zone turbulence in a spilling breaker,” *Notes Queries*, vol. s7-VI, no. 140, p. 169, 1888.

[24] D. H. Sliney, “What is light? the visible spectrum and beyond,” *Eye*, vol. 30, no. 2, pp. 222–229, 2016.

[25] G. K. Pal, *Textbook Of Practical Physiology-2Nd Edn.* Orient Blackswan, 2006.

[26] M. Beckers, S. Plasmon, S. P. Resonance, D. Material, R. Index, and E. Field, “Basics of light guidance Electromagnetic Wave.”

[27] A. Stockman and L. T. Sharpe, “The spectral sensitivities of the middle- and long-wavelength-sensitive cones derived from measurements in observers of known genotype,” *Vision Res.*, vol. 40, no. 13, pp. 1711–1737, 2000.

[28] A. G. Kirk and J. F. O’Brien, “Perceptually based tone mapping for low-light conditions,” *ACM SIGGRAPH 2011 Pap. - SIGGRAPH ’11*, p. 1, 2011.

[29] X. Yang and B. Wei, “Exact research on the theory of the blackbody thermal radiation,” *Sci. Rep.*, vol. 6, no. 6, pp. 1–5, 2016.

[30] A. Ford and A. Roberts, “Colour space conversions,” *Westminster Univ. London*, vol. 1998, pp. 1–31, 1998.

[31] J. Zhu, M. Y. Choi, G. W. Mulholland, S. L. Manzello, L. A. Gritzo, and J. Suo-Anttila, “Measurement of visible and near-IR optical properties of soot produced from laminar flames,” *Proc. Combust. Inst.*, vol. 29, no. 2, pp. 2367–2374, 2002.

[32] J. Jarosinski and B. Veyssiere, *Combustion phenomena: Selected mechanisms of flame formation, propagation and extinction*. CRC press, 2009.

[33] L. Zheng, “Combustion Visualisation Monitoring Using High Speed Imaging.” University of Sheffield, 2018.

[34] R. Hobbs, “Digital video and HD algorithms and interfaces.” Morgan Kaufmann, 2010.

[35] M. Brown, *Advanced Digital Photography*. Media Publishing, 2004.

[36] A. El Gamal and H. Eltoukhy, “CMOS image sensors,” *IEEE Circuits Devices Mag.*, vol. 21, no. 3, pp. 6–20, 2005.

[37] T. Moynihan, “CMOS Is Winning the Camera Sensor Battle, and Here’s Why,” *TechHive.[online]*, 2011.

[38] J. Morlet, “Sampling theory and wave propagation,” in *Issues in acoustic Signal—image processing and recognition*, Springer, 1983, pp. 233–261.

[39] J. Byrnes, *Unexploded ordnance detection and mitigation*. Springer Science & Business Media, 2008.

[40] Markus Tarin, “Choosing a camera for infrared imaging,” 2016. [Online]. Available: https://www.vision-systems.com/cameras-accessories/article/16736873/choosing-a-camera-for-infrared-imaging.

[41] Teledyne, “InGaAs Cameras: The Basics.”

[42] R. T. Balmer, *Modern engineering thermodynamics*. 2011.

[43] G. A. W. Rutgers and J. C. De Vos, “Relation between brightness, temperature, true temperature and colour temperature of tungsten. Luminance of tungsten,” *Physica*, vol. 20, no. 7–12, pp. 715–720, 1954.

[44] T. Kirchho, T. H. E. I. B. Model, and H. A. The, “Black-body radiation,” 1860.

[45] P. R. N. Childs, J. R. Greenwood, and C. A. Long, “Review of Temperature Measurement,” *Rev. Sci. Instrum.*, vol. 71, no. 8, pp. 2959–2078, 2000.

[46] E. R. Cohen and B. N. Taylor, “The 1973 Least-Squares Adjustment of the Fundamental Constants,” *J. Phys. Chem. Ref. Data*, vol. 2, no. 4, pp. 663–734, 1973.

[47] T. D. McGee, *Principles and methods of temperature measurement*. John Wiley & Sons, 1988.

[48] L. Michalski, K. Eckersdorf, and J. McGhee, *Temperature measurement*. Wiley, 1991.

[49] R. R. Corwin and A. Rodenburgh, “Temperature error in radiation thermometry caused by emissivity and reflectance measurement error,” *Appl. Opt.*, vol. 33, no. 10, pp. 1950–1957, 1994.

[50] K. L. Cashdollar, “Three-wavelength pyrometer for measuring flame temperatures,” *Appl. Opt.*, vol. 18, no. 15, p. 2595, 1979.

[51] S. D. Alaruri, “Integrating sphere method for determining the effective spectral emissivity of superalloys at high temperatures using a single wavelength pyrometer,” *Opt. Eng.*, vol. 35, no. 9, p. 2736, 1996.

[52] C. Alvarez-Herrera, D. Moreno-Hernnápticadez, and B. Barrientos-García, “Temperature measurement of an axisymmetric flame by using a schlieren system,” *J. Opt. A Pure Appl. Opt.*, vol. 10, no. 10, 2008.

[53] A. R. Colclough, “Primary acoustic thermometry: principles and current trends,” *Temp. Its Meas. Control Sci. Ind. (American Inst. Physics, New York, 1992)*, vol. 6, pp. 65–75, 1982.

[54] V. K. R. Kodur and T. Z. Harmathy, *Handbook of Fire Protection Engineering*. 2016.

[55] D. Drysdale, *An introduction to fire dynamics*. John Wiley & Sons, 2011.

[56] A. Yasemin, M. Doğan, and E. Bayramlı, “The effect of red phosphorus on the fire properties of intumescent pine wood flour – LDPE composites Yasemin,” *Finnish-Swedish Flame Days 2009*, no. August 2008, p. 4B, 2009.

[57] A. I. Bartlett, R. M. Hadden, and L. A. Bisby, “A Review of Factors Affecting the Burning Behaviour of Wood for Application to Tall Timber Construction,” *Fire Technol.*, vol. 55, no. 1, pp. 1–49, 2019.

[58] C. Di Blasi, E. Gonzalez Hernandez, and A. Santoro, “Radiative pyrolysis of single moist wood particles,” *Ind. Eng. Chem. Res.*, vol. 39, no. 4, pp. 873–882, 2000.

[59] H. W. Emmons and A. Atreya, “The science of wood combustion Howard W Emmons and Arvind Atreya heat ’ heat transfer fuel mass transfer,” vol. 5, no. December, pp. 259–268, 1982.

[60] C. Di Blasi, “Modeling chemical and physical processes of wood and biomass pyrolysis,” *Prog. Energy Combust. Sci.*, vol. 34, no. 1, pp. 47–90, 2008.

[61] K. W. Ragland, D. J. Aerts, and A. J. Baker, “Properties of wood for combustion analysis,” *Bioresour. Technol.*, vol. 37, no. 2, pp. 161–168, 1991.

[62] R. H. White and M. A. Dietenberger, “Wood Products: Thermal Degradation and Fire,” *Encycl. Mater. Sci. Technol.*, pp. 9712–9716, 2001.

[63] Arne Inghelbrecht, “Evaluation of the burning behaviour of wood products in the context of structural fire design,” 2014.

[64] A. F. Roberts, “Problems associated with the theoretical analysis of the burning of wood,” in *Symposium (international) on combustion*, 1971, vol. 13, no. 1, pp. 893–903.

[65] A. H. Buchanan and A. K. Abu, *Structural design for fire safety*. John Wiley & Sons, 2017.

[66] J. Schmid, A. Just, M. Klippel, and M. Fragiacomo, “The reduced cross-section method for evaluation of the fire resistance of timber members: discussion and determination of the zero-strength layer,” *Fire Technol.*, vol. 51, no. 6, pp. 1285–1309, 2015.

[67] V. Babrauskas, “Structural fire protection: ASCE Manuals and Reports on Engineering Practice No. 78. Edited by TT Lie. American Society of Civil Engineers, New York, August 1992, 241 pp. ISBN 0-87262-888-4. Laminated paper over boards. Price: US $56.00.” Elsevier, 1993.

[68] E. L. Schaffer, “Charring Rate Of Selected Woods - Transverse To Grain,” *FPL Res. Pap. 69*, no. April, 1967.

[69] P. C. R. Collier, *Charring rates of timber*. Building Research Association of New Zealand, 1992.

[70] C. P. Butler, “Notes on charring rates in wood,” *Fire Saf. Sci.*, vol. 896, no. November, p. 1, 1971.

[71] Y. Wu, H. J. Xing, and G. Atkinson, “Interaction of " re plume with inclined surface,” vol. 35, pp. 391–403, 2000.

[72] B. Moghtaderi, V. Novozhilov, D. F. Fletcher, and J. H. Kent, “A new correlation for bench-scale piloted ignition data of wood,” *Fire Saf. J.*, vol. 29, no. 1, pp. 41–59, 1997.

[73] C. S. Tarifa, P. P. del Notario, A. R. Villa, A. L. Martinez, and E. Mezquida, “Open fires and transport of firebrands,” 1966.

[74] A. Tohidi, N. Kaye, and W. Bridges, “Statistical description of firebrand size and shape distribution from coniferous trees for use in Metropolis Monte Carlo simulations of firebrand flight distance,” *Fire Saf. J.*, vol. 77, pp. 21–35, 2015.

[75] A. Filkov *et al.*, “Investigation of firebrand production during prescribed fires conducted in a pine forest,” *Proc. Combust. Inst.*, vol. 36, no. 2, pp. 3263–3270, 2017.

[76] S. L. Manzello *et al.*, “On the development and characterization of a firebrand generator,” *Fire Saf. J.*, vol. 43, no. 4, pp. 258–268, 2008.

[77] H. Zhou, “Interaction of big particles with flow- A study of the spotting distances of the firebrands by modelling and simulations,” 2020.

[78] E. Koo, P. J. Pagni, D. R. Weise, and J. P. Woycheese, “Firebrands and spotting ignition in large-scale fires,” *Int. J. Wildl. Fire*, vol. 19, no. 7, pp. 818–843, 2010.

[79] L. Hu, “A review of physics and correlations of pool fire behaviour in wind and future challenges,” *Fire Saf. J.*, vol. 91, pp. 41–55, 2017.

[80] H. C. Hottel and F. P. Broughton, “Determination of True Temperature and Total Radiation from Luminous Gas Flames,” *Ind. Eng. Chem. Anal. Ed.*, vol. 4, no. 16, pp. 166–175, 1932.

[81] D. C. Corporation and D. C. Corporation, “Advantages of 2-Color Pyrometry in Temperature Measurement of the Claus Reaction Furnace,” pp. 1–8.

[82] M. Alhuda, K. Yamada, and T. Ueda, “Measurement of Temperature of CBN Tool in Turning of High Hardness Steel.,” *J. Japan Soc. Precis. Eng.*, vol. 64, no. 11, pp. 1684–

1688, 1998.

[83] J. Thevenet, M. Siroux, and B. Desmet, “Measurements of brake disc surface temperature and emissivity by two-color pyrometry,” *Appl. Therm. Eng.*, vol. 30, no. 6–7, pp. 753–759, 2010.

[84] Y. taik Han, K. hyeon Lee, and K. doug Min, “A study on the measurement of temperature and soot in a constant-volume chamber and a visualized diesel engine using the two-color method,” *J. Mech. Sci. Technol.*, vol. 23, no. 11, pp. 3114–3123, 2010.

[85] F. Payri, J. V Pastor, J. M. García, and J. M. Pastor, “Contribution to the application of two-colour imaging to diesel combustion,” *Meas. Sci. Technol.*, vol. 18, no. 8, pp. 2579–2598, 2007.

[86] H. Zhao and N. Ladommatos, “Optical diagnostics for soot and temperature measurement in diesel engines,” *Prog. Energy Combust. Sci.*, vol. 24, no. 3, pp. 221–255, 1998.

[87] L. Wang and J. Wang, “Application of Two-color Method in Combustion Diagnosis of IC Engine,” *Small Intern. Combust. Engine Mot.*, vol. 36, 2007.

[88] G. Lu, Y. Yan, G. Riley, and H. Chandr Bheemul, “Concurrent measurement of temperature and soot concentration of pulverized coal flames,” *IEEE Trans. Instrum. Meas.*, vol. 51, no. 5, pp. 990–995, 2002.

[89] H. C. Zhou *et al.*, “Experimental investigations on visualization of three-dimensional temperature distributions in a large-scale pulverized-coal-fired boiler furnace,” *Proc. Combust. Inst.*, vol. 30, no. 1, pp. 1699–1706, 2005.

[90] W. Li, C. Lou, Y. Sun, and H. Zhou, “Estimation of radiative properties and temperature distributions in coal-fired boiler furnaces by a portable image processing system,” *Exp. Therm. Fluid Sci.*, vol. 35, no. 2, pp. 416–421, 2011.

[91] S. M. Godoy and F. C. Lockwood, “Development of a two-colour infrared pyrometer for coal particle temperature measurements during devolatilisation,” *Fuel*, vol. 77, no. 900, pp. 995–999, 1998.

[92] Gang Lu, Yong Yan, S. Cornwell, and G. Riley, “Temperature Profiling of Pulverised Coal Flames Using Multi-Colour Pyrometric and Digital Imaging Techniques,” *2005 IEEE Instrumentationand Meas. Technol. Conf. Proc.*, vol. 3, no. 4, pp. 1658–1662, 2005.

[93] T. S. Draper, “Application of Two-Color Pyrometry to Characterize the Two-Dimensional Temperature and Emissivity of Pulverized-Coal Oxy-Flames,” *BYU Master*, 2012.

[94] Z. W. Jiang, Z. X. Luo, and H. C. Zhou, “A simple measurement method of temperature and emissivity of coal-fired flames from visible radiation image and its application in a CFB boiler furnace,” *Fuel*, vol. 88, no. 6, pp. 980–987, 2009.

[95] S. Simonini, S. J. Elston, and C. R. Stone, “Soot temperature and concentration measurements from colour charge coupled device camera images using a three-colour method,” *Proc. Inst. Mech. Eng. Part C J. Mech. Eng. Sci.*, vol. 215, no. 9, pp. 1041–1052, 2001.

[96] B. F. Magnussen and B. H. Hjertager, “On mathematical modeling of turbulent combustion with special emphasis on soot formation and combustion,” *Symp. Combust.*, vol. 16, no. 1, pp. 719–729, 1977.

[97] J. Zhang, W. Jing, W. L. Roberts, and T. Fang, “Soot temperature and KL factor for

biodiesel and diesel spray combustion in a constant volume combustion chamber," *Appl. Energy*, vol. 107, pp. 52–65, 2013.

[98] K. I. Svensson, A. J. Mackrory, M. J. Richards, and D. R. Tree, "Calibration of an RGB , CCD Camera and Interpretation of its Two-Color Images for KL and Temperature," *SAE Int.*, vol. 2005-01–06, no. 724, 2005.

[99] Y. Gong, Q. Guo, Q. Liang, Z. Zhou, and G. Yu, "Three-dimensional temperature distribution of impinging flames in an opposed multiburner gasifier," *Ind. Eng. Chem. Res.*, vol. 51, no. 22, pp. 7828–7837, 2012.

[100] Y. Huang, Y. Yan, and G. Riley, "Vision-based measurement of temperature distribution in a 500-kW model furnace using the two-colour method," *Meas. J. Int. Meas. Confed.*, vol. 28, no. 3, pp. 175–183, 2000.

[101] Z. Zhou, D. Tian, Z. Wu, Z. Bian, and W. Wu, "3-D Reconstruction of Flame Temperature Distribution Using Tomographic and Two-Color Pyrometric Techniques," *IEEE Trans. Instrum. Meas.*, vol. 64, no. 11, pp. 3075–3084, 2015.

[102] M. Planck, *The theory of heat radiation*. Courier Corporation, 2013.

[103] Z. Yan, Q. Liang, Q. Guo, G. Yu, and Z. Yu, "Experimental investigations on temperature distributions of flame sections in a bench-scale opposed multi-burner gasifier," *Appl. Energy*, vol. 86, no. 7–8, pp. 1359–1364, 2009.

[104] L. Metek, "a Range of Temperature Calibration Sources." .

[105] "Fastcam SA4 High-Speed Imaging System," vol. 048. pp. 2–3.

[106] J. Chouinard, "The Fundamentals of Camera and Image Sensor Technology Digital Cameras."

[107] C. C. Ndubizu, R. Ananth, P. A. Tatema, and V. Motevalli, “On water mist fire suppression mechanisms in a gaseous diffusion flame,” *Fire Saf. J.*, vol. 31, no. 3, pp. 253–276, 1998.

[108] F. Cignoli, S. De Iuliis, V. Manta, and G. Zizak, “Two-dimensional two-wavelength emission technique for soot diagnostics,” *Appl. Opt.*, vol. 40, no. 30, p. 5370, 2001.

[109] Q. He, Z. Su, Z. Xie, Z. Zhong, and Q. Yao, “A novel principle for molten steel level measurement in tundish by using temperature gradient,” *IEEE Trans. Instrum. Meas.*, vol. 66, no. 7, pp. 1809–1819, 2017.

[110] B. Lane, E. Whitenton, V. Madhavan, and A. Donmez, “Uncertainty of temperature measurements by infrared thermography for metal cutting applications,” *Metrologia*, vol. 50, no. 6, pp. 637–653, 2013.

[111] E. M. Vuelban *et al.*, “Radiometric techniques for emissivity and temperature measurements for industrial applications,” *Int. J. Thermophys.*, vol. 36, no. 7, pp. 1545–1568, 2015.

[112] Dong-Ho Lee, “Thermal analysis of integrated-circuit chips using thermographic imaging techniques,” *IEEE Trans. Instrum. Meas.*, vol. 43, no. 6, pp. 824–829, 1994.

[113] K. S. Chang *et al.*, “Precise temperature mapping of GaN-based LEDs by quantitative infrared micro-thermography,” *Sensors*, vol. 12, no. 4, pp. 4648–4660, 2012.

[114] Z. M. Zhang, “Surface temperature measurement using optical techniques,” *Annu. Rev. Heat Transf.*, vol. 11, 2000.

[115] D. L. Blackburn, “Temperature measurements of semiconductor devices - a review,” in *Twentieth Annual IEEE Semiconductor Thermal Measurement and Management Symposium (IEEE Cat. No.04CH37545)*, 2004, pp. 70–80.

[116] M. J. Hobbs *et al.*, “InAs/GaSb Type-II Superlattice for Radiation Thermometry,” *IEEE Trans. Instrum. Meas.*, vol. 64, no. 2, pp. 502–508, 2015.

[117] X. Zhou, X. Meng, A. B. Krysa, J. R. Willmott, J. S. Ng, and C. H. Tan, “InAs Photodiodes for 3.43 $μ\text{m}$ Radiation Thermometry,” *IEEE Sens. J.*, vol. 15, no. 10, pp. 5555–5560, 2015.

[118] F. Sakuma and S. Hattori, “Establishing a practical temperature standard by using a narrow-band radiation thermometer with a silicon detector,” 1983.

[119] S. Soldan, J. Rangel, and A. Kroll, “More Info at Open Access Database www.ndt.net/?id=17665,” *Conf. Quant. InfraRed Thermogr.*, 2014.

[120] G. Grgić and I. Pušnik, “Analysis of Thermal Imagers,” *Int. J. Thermophys.*, vol. 32, no. 1, pp. 237–247, 2011.

[121] P. Saunders and H. Edgar, “Size-of-source effect correction for a thermal imaging radiation thermometer,” *High Temp. High Press.*, vol. 31, no. 3, pp. 283–292, 1999.

[122] R. E. Bland and T. J. Pelick, “The schlieren method applied to flow visualization in a water tunnel,” 1962.

[123] S. Weintroub, “The National Physical Laboratory, Teddington.” Nature Publishing Group, 1965.

[124] W. Merzkirch, “Generalized Analysis of Shearing Interferometers as Applied for Gas Dynamic Studies,” *Appl. Opt.*, vol. 13, no. 2, p. 409, 1974.

[125] J. L. Barron, D. J. Fleet, and S. S. Beauchemin, “Performance of optical flow techniques,” *Int. J. Comput. Vis.*, vol. 12, no. 1, pp. 43–77, 1994.

[126] B. D. Lucas and T. Kanade, “Iterative Image Registration Technique With an Application

To Stereo Vision.," vol. 2, pp. 674–679, 1981.

[127] K. Moodie, "The King's Cross fire: damage assessment and overview of the technical investigation," *Fire Saf. J.*, vol. 18, no. 1, pp. 13–33, 1992.

[128] T. K. Buildings, "Flame Spread on Inclined Surfaces," vol. 18, pp. 245–254, 1992.

[129] Y. Zhang, X. Chen, Y. Song, X. Huang, Y. Niu, and J. Sun, "The deceleration mechanism and the critical extinction angle of downward flame spread over inclined cellulosic solids," *Appl. Therm. Eng.*, vol. 124, pp. 185–190, 2017.

[130] Y. Zhang, J. Ji, Q. Wang, X. Huang, Q. Wang, and J. Sun, "Prediction of the critical condition for flame acceleration over wood surface with different sample orientations," *Combust. Flame*, vol. 159, no. 9, pp. 2999–3002, 2012.

[131] X. Zhou, S. Mahalingam, D. Weise, and U. F. Service, "Experimental Modeling of the Effect of Terrain Slope on Marginal Burning," pp. 863–874, 2005.

[132] T. P. Grumstrup, S. S. Mcallister, M. A. Finney, M. Fire, and U. S. F. Service, "Qualitative Flow Visualization of Flame Attachment on Slopes," pp. 1–6, 2017.

[133] Z. Yang, H. Chen, Z. Yang, and H. Chen, "Experimental Study on Flame Geometry along the Protection Inclined Surface with Experimental and Study on Flame Geometry along the Inclined Surface with Fire Burner without Sidewalls by Using a the Gas Experimental Study on Flame Geometry along Inclined S," *Procedia Eng.*, vol. 211, pp. 925–933, 2017.

[134] A. Atreya, C. Carpentier, and M. Harkleroad, "Effect of Sample Orientation on Piloted Ignition and Flame Spread.," pp. 97–109, 1986.

[135] M. J. Gollner, X. Huang, J. Cobian, and A. S. Rangwala, "Experimental study of upward flame spread of an inclined fuel surface," *Proc. Combust. Inst.*, vol. 34, no. 2, pp. 2531–

2538, 2013.

[136] R. O. Weber and N. J. De Mestre, “Flame Spread Measurements on Single Ponderosa Pine Needles: Effect of Sample Orientation and Concurrent External Flow,” *Combust. Sci. Technol.*, vol. 70, no. 1–3, pp. 17–32, 1990.

[137] T. Hirano, S. E. Noreikis, and T. E. Waterman, “Measured velocity and temperature profiles near flames spreading over a thin combustible solid,” *Combust. Flame*, vol. 23, no. 1, pp. 83–96, 1974.

[138] C. C. Hwang and Y. Xie, “Flame Propagation Along Matchstick ArraysOn , Inclined Base Boards,” vol. 2202, no. May, 2007.

[139] R. O. Weber, “The moist strand and the burning bed,” *Can. J. For. Res.*, vol. 20, no. 6, pp. 845–848, 1990.

[140] T. Hirano, S. E. Noreikis, and T. E. Waterman, “Postulations of flame spread mechanisms,” *Combust. Flame*, vol. 22, no. 3, pp. 353–363, 1974.

[141] Y. Lai, H. Zhou, and Y. Zhang, “Experimental Investigation of the Fire Spread on Inclined Wooden Rods,” pp. 1–6, 2019.

[142] H. Zhou, Y. Lai, Y. Li, Y. Zhang, and S. Yorkshire, “Modelling the propagation of one-end-burning cylindrical firebrand based on the measured regression rates,” pp. 1–6, 2019.

[143] P. O. Pt, “Technical Information Data Bulletin,” *Build. Constr. Mater.*, no. 914, p. 10710, 1999.

[144] L. R. Stanger, T. C. Wilkes, N. A. Boone, A. J. S. McGonigle, and J. R. Willmott, “Thermal imaging metrology with a smartphone sensor,” *Sensors (Switzerland)*, vol. 18, no. 7, 2018.

[145] J. J. J. J. Sharples, a. M. M. Gill, and J. W. J. W. Dold, “The trench effect and eruptive wildfires: lessons from the King’s Cross Underground disaster,” *Proc. AFAC 2010*, no. August 2015, pp. 1–9, 2009.

[146] S. J. Ritchie, K. D. Steckler, A. Hamins, T. G. Cleary, J. C. Yang, and T. Kashiwagi, “The effect of sample size on the heat release rate of charring materials,” *Fire Saf. Sci.*, vol. 5, pp. 177–188, 1997.

[147] C. Lautenberger, S. Sexton, and D. Rich, “Understanding long term low temperature ignition of wood,” in *international symposium on fire investigation science and technology, College Park, MD, September*, 2014, pp. 22–24.

[148] X. Xie *et al.*, “Upslope fire spread over a pine needle fuel bed in a trench associated with eruptive fire,” *Proc. Combust. Inst.*, vol. 36, no. 2, pp. 3037–3044, 2017.

[149] H. C. Tran and R. H. White, “Burning rate of solid wood measured in a heat release rate calorimeter,” *Fire Mater.*, vol. 16, no. 4, pp. 197–206, 1992.

[150] K. Hiroshi and Y. Taro, “Air entrainment and thermal radiation from heptane pool fires,” *Fire Technol.*, vol. 24, no. 1, pp. 33–47, 1988.

[151] B. J. McCaffrey, “Purely Buoyant Diffusion Flames (NBSIR 791910),” no. October, 1979.

[152] M. Muñoz, J. Arnaldos, J. Casal, and E. Planas, “Analysis of the geometric and radiative characteristics of hydrocarbon pool fires,” *Combust. Flame*, vol. 139, no. 3, pp. 263–277, 2004.

[153] J. R. Welker and C. M. Sliepcevich, “Burning rates and heat transfer from wind-blown flames,” *Fire Technol.*, vol. 2, no. 3, pp. 211–218, 1966.

[154] N. Saito, “Experimental study on fire behavior in a wind tunnel with a reduced scale

model," in *Proc. of the 2 nd Int. Conference of Safety in Road and Rail Tunnels*, 1995, pp. 303–310.

[155] R. O. Carvel, A. N. Beard, and P. W. Jowitt, "A Bayesian estimation of the effect of forced ventilation on a pool fire in a tunnel," *Civ. Eng. Environ. Syst.*, vol. 18, no. 4, pp. 279–302, 2001.

[156] J. A. R. Woods, B. A. Fleck, and L. W. Kostiuk, "Effects of transverse air flow on burning rates of rectangular methanol pool fires," *Combust. Flame*, vol. 146, no. 1–2, pp. 379–390, 2006.

[157] S. McAllister and M. Finney, "The Effect of Wind on Burning Rate of Wood Cribs," *Fire Technol.*, vol. 52, no. 4, pp. 1035–1050, 2016.

[158] L. Hu, C. Kuang, X. Zhong, F. Ren, X. Zhang, and H. Ding, "An experimental study on burning rate and flame tilt of optical-thin heptane pool fires in cross flows," *Proc. Combust. Inst.*, vol. 36, no. 2, pp. 3089–3096, 2017.

[159] R. G. Salvagni, M. L. S. Indrusiak, and F. R. Centeno, "Biodiesel oil pool fire under air crossflow conditions: Burning rate, flame geometric parameters and temperatures," *Int. J. Heat Mass Transf.*, vol. 149, 2020.

[160] R. G. Salvagni, F. R. Centeno, and M. L. S. Indrusiak, "Burning rate, flame geometry and temperature of convection-controlled circular diesel oil pool fire under air crossflow conditions," *J. Hazard. Mater.*, vol. 368, no. December 2018, pp. 560–568, 2019.

[161] K. Himoto, "Quantification of cross-wind effect on temperature elevation in the downwind region of fire sources," *Fire Saf. J.*, vol. 106, no. January, pp. 114–123, 2019.

[162] D. Luan *et al.*, "Experimental investigation of smoke temperature and movement

characteristics in tunnel fires with canyon cross wind," *J. Wind Eng. Ind. Aerodyn.*, vol. 210, no. September 2020, p. 104531, 2021.

[163] E. Eftekharian, Y. He, K. C. S. Kwok, R. H. Ong, and J. Yuan, "Investigation of fire-driven cross-wind velocity enhancement," *Int. J. Therm. Sci.*, vol. 141, no. March, pp. 84–95, 2019.

[164] P. Zhu, X. S. Wang, Y. P. He, C. F. Tao, and X. M. Ni, "Flame characteristics and burning rate of small pool fires under downslope and upslope oblique winds," *Fuel*, vol. 184, pp. 725–734, 2016.

[165] Y. Lai, X. Wang, T. B. O. Rockett, J. R. Willmott, H. Zhou, and Y. Zhang, "The effect of preheating on fire propagation on inclined wood by multi-spectrum and schlieren visualisation," *Fire Saf. J.*, vol. 118, 2020.

[166] D. J. Tritton, *Physical fluid dynamics*. Springer Science & Business Media, 2012.